NASA CR-120886
ASRL TR 154-4

# FINITE-ELEMENT ANALYSIS OF LARGE TRANSIENT ELASTIC-PLASTIC DEFORMATIONS OF SIMPLE STRUCTURES, WITH APPLICATION TO THE ENGINE ROTOR FRAGMENT CONTAINMENT/DEFLECTION PROBLEM

(NASA-CR-120886) FINITE ELEMENT ANALYSIS
OF LARGE TRANSIENT ELASTIC-PLASTIC
DEFORMATIONS OF SIMPLE STRUCTURES, WITH
R.W. Wu, et al (Massachusetts Inst. of
Tech.) Jan. 1972 326 p CSCL 20K G3/32
N72-22915
Unclas
24986

Richard W-H Wu
Emmett A. Witmer

AEROELASTIC AND STRUCTURES RESEARCH LABORATORY
DEPARTMENT OF AERONAUTICS AND ASTRONAUTICS
MASSACHUSETTS INSTITUTE OF TECHNOLOGY
CAMBRIDGE, MASSACHUSETTS 02139

January 1972

Prepared for
AEROSPACE SAFETY RESEARCH AND DATA INSTITUTE
LEWIS RESEARCH CENTER
NATIONAL AERONAUTICS AND SPACE ADMINISTRATION

NASA Grant NGR 22-009-339

REPRODUCED BY
NATIONAL TECHNICAL
INFORMATION SERVICE
U. S. DEPARTMENT OF COMMERCE
SPRINGFIELD, VA. 22161

| | | |
|---|---|---|
| 1. Report No.<br>NASA CR-120886 | 2. Government Accession No. | 3. Recipient's Catalog No. |

4. Title and Subtitle
FINITE-ELEMENT ANALYSIS OF LARGE TRANSIENT ELASTIC-PLASTIC DEFORMATIONS OF SIMPLE STRUCTURES, WITH APPLICATION TO THE ENGINE ROTOR FRAGMENT CONTAINMENT/DEFLECTION PROBLEM

5. Report Date
January 1972

6. Performing Organization Code

7. Author(s)
Richard W-H Wu and Emmett A. Witmer

8. Performing Organization Report No.
ASRL TR 154-4

9. Performing Organization Name and Address
Aeroelastic and Structures Research Laboratory
Department of Aeronautics and Astronautics
Massachusetts Institute of Technology
Cambridge, Massachusetts 02139

10. Work Unit No.

11. Contract or Grant No.
NGR 22-009-339

13. Type of Report and Period Covered
Contractor Report

12. Sponsoring Agency Name and Address
National Aeronautics and Space Administration
Washington, D.C. 20546

14. Sponsoring Agency Code

15. Supplementary Notes
Technical Monitor: Patrick T. Chiarito, Aerospace Safety Research and Data Institute
Technical Advisor: Richard H. Kemp, Materials and Structures Division
NASA Lewis Research Center, Cleveland, Ohio

16. Abstract

This study had as one of its principal objectives a contribution to the finite-element (FE) method for predicting the large-deformation elastic-plastic transient responses of structures where efficient and accurate strain predictions are of particular interest to the aerospace designer/analyst; here one is concerned with conditions such that it is desired to have a minimum weight structure absorb as much energy by plastic work as possible before fracture occurs. Because of the relative ease and versatility with which the FE method can be applied by designer/analysts to geometrically complex branched and/or stiffened structures, as well as its potential for more accurate strain predictions with a limited number of degrees of freedom than other available methods provide, the FE method is investigated in this study. However, being a first step in this development, the present study is devoted largely to planar structures. Having now demonstrated the successful development of the FE method for planar structures undergoing large-deformation elastic-plastic transient responses, one can now confidently extend this type of analysis to "complex non-planar structures".

Based upon the Principle of Virtual Work together with D'Alembert's Principle, assumed-displacement versions of the finite-element method are developed to predict large-deformation elastic-plastic transient deformations of structures; both the "conventional" and a new improved finite-element variational formulation are derived. These formulations are then developed in detail for straight-beam and curved-beam elements undergoing (a) Bernoulli-Euler-Kirchhoff or (b) Timoshenko deformation behavior, in one plane. For each of these categories, (a) and (b), several types of assumed-displacement finite elements are developed, and transient response predictions are compared with available exact solutions for small-deflection, linear-elastic transient responses. The present finite-element predictions for large-deflection elastic-plastic transient responses are evaluated via several beam and ring examples for which experimental measurements (of transient strains and large transient deformations) and independent finite-difference predictions are available; very good agreement is noted.

The new improved finite-element method developed in this study and applied to simple structures is found to be both more efficient and more convenient than the conventional finite-element formulation. Further, this new method when used in conjunction with the lumped-mass matrix is found to be competitive from the efficiency/accuracy standpoint with the finite-difference method for predicting transient responses for this category of problems (large-deformation, elastic-plastic behavior).

As an example of the application of the present finite-element (FE) method to problems of current practical interest, the transient responses of containment and deflection rings to impact from an engine-rotor blade are analyzed. Energy and momentum considerations are employed in an approximate analysis to predict the collision-induced velocities which are imparted to the blade and to the affected ring segment. This collision analysis is combined with the present improved FE analysis to predict the resulting large-deformation transient responses of containment/deflection rings. Comparisons with limited experimental data are given.

17. Key Words (Suggested by Author(s))
Transient Structural Response
Large Deflections
Structural Mechanics
Elastic-Plastic Behavior; Stress Analysis
Finite-Element Method
Turbojet Rotor Containment
Aircraft Safety
Aircraft Hazards

18. Distribution Statement
Unclassified, Unlimited

| | | | |
|---|---|---|---|
| 19. Security Classif. (of this report)<br>Unclassified | 20. Security Classif. (of this page)<br>Unclassified | 21. No. of Pages<br>326 | 22. Price* |

*For sale by the National Technical Information Service
Springfield, Virginia 22151

AEROELASTIC AND STRUCTURES RESEARCH LABORATORIES
DEPARTMENT OF AERONAUTICS AND ASTRONAUTICS

Richard W-H Wu
Emmett A. Witmer

PRECEDING PAGE BLANK NOT FILMED

# FOREWORD

This report has been prepared by the Aeroelastic and Structures Research Laboratory (ASRL), Department of Aeronautics and Astronautics, Massachusetts Institute of Technology, Cambridge, Massachusetts under Grant No. NGR 22-009-339 from the Lewis Research Center, National Aeronautics and Space Administration, Cleveland, Ohio 44135. Mr. Patrick T. Chiarito of the Lewis Research Center served as technical monitor and Mr. Richard H. Kemp served as technical advisor.

The cooperation and helpful suggestions of Mr. Chiarito and Mr. Kemp throughout this research program are deeply appreciated. The authors are also indebted to Messrs. G.J. Mangano and R. DeLucia of the Naval Air Propulsion Test Center, Philadelphia, Pa. for helpful discussions and for supplying certain experimental data.

The authors especially wish to acknowledge the careful reviewing of this report and the many constructive suggestions contributed by Dr. John W. Leech of the MIT-ASRL. Mr. Raffi P. Yeghiayan of the MIT-ASRL carried out and furnished a number of finite-difference transient response predictions for comparison with the present finite-element predictions, and also contributed to helpful discussion. Also, Professors T.H.H. Pian and P. Tong of the Department of Aeronautics and Astronautics, MIT, provided stimulating discussion and valuable suggestions during this study.

The use of SI units (NASA Policy Directive NPD 2220.4, September 14, 1970) was waived for the present document in accordance with provisions of paragraph 5d of that Directive by the authority of the Director of the Lewis Research Center.

CONTENTS

Section Page

1 INTRODUCTION 1

1.1 Purpose of Study 1

1.2 Synopsis of Investigation 3

2 GENERAL FORMULATION 5

2.1 Introduction 5

2.2 Governing Equations 6

2.2.1 The Strain-Displacement Relations 6

2.2.2 Descriptions of Stresses and Forces on a Deformed Continuum Element 9

2.2.3 Conservation of Mass 11

2.2.4 The Principle of Virtual Work 11

2.2.5 Thermodynamic Equations 18

2.3 Constitutive Relations 20

2.3.1 Thermoelastic Material Behavior 22

2.3.2 Thermoelastic-Plastic Material Behavior 24

2.3.3 Strain-Rate Effect 31

3 GENERAL OUTLINE OF METHOD OF ANALYSIS 33

3.1 Background and Survey of Pertinent Literature 33

3.2 Variational Derivation of the Equations of Motion Utilizing the Finite-Element Approximation 40

3.2.1 Improved Formulation 42

3.2.2 Conventional Formulation 49

3.3 Timewise Solution of the Governing Equations 53

3.3.1 Solution Process 54

3.3.1.1 Improved Formulation 58

3.3.1.2 Conventional Formulation 62

3.3.2 Evaluation of Stress Increments, Stresses, Plastic Strain Increments, and Plastic Strains 63

CONTENTS CONTINUED

Section Page

3.3.3 Comparison of Storage and Computing Requirements for the Improved versus the Conventional Formulation 68
3.3.4 Selection of a Temporal Finite-Difference Operator 69

4 FORMULATION FOR A CURVED BEAM 74
4.1 Introduction 74
4.2 Geometry Description for a Curved Beam Element 74
4.3 The Bernoulli-Euler-Type Curved Beam Element 76
4.3.1 Displacement Field 76
4.3.2 Strain-Displacement Relations 80
4.3.3 The Discrete-Element Property Matrices 83
4.3.4 Stress-Strain Relations 88
4.4 The Timoshenko-Type Curved Beam Element 91
4.4.1 Displacement Field 91
4.4.2 Strain-Displacement Relations 91
4.4.3 The Discrete-Element Property Matrices 94
4.4.4 Stress-Strain Relations 96

5 EVALUATION AND DISCUSSION 99
5.1 Introduction 99
5.2 Small-Deflection Linear-Elastic Transient Responses of Mechanically Loaded Beams 99
5.2.1 Small-Deflection Linear-Elastic Responses of a Beam with Bernoulli-Euler-Type Deformation Behavior 100
5.2.2 Small-Deflection Linear-Elastic Transient Responses of a Beam with Timoshenko-Type Deformation Behavior 100
5.3 Large-Deflection Elastic-Plastic Transient Responses of Impulsively-Loaded Simple Structures 104

CONTENTS CONTINUED

Section Page

5.3.1 Example Problems Analyzed 104
5.3.2 Effects of Using Various Timewise Integration Operators: Central-Difference Method, Houbolt's Method, and Newmark's β-Method 105
5.3.3 Comparison of the Conventional Formulation Versus the Improved Formulation for the Dynamic Equilibrium Equations 110
5.3.4 Comparison of LC Versus CC Assumed Displacement Functions for the Bernoulli-Euler-Type of Ring Element 111
5.3.5 Comparison of the Use of a Consistent Mass Matrix Versus a Lumped Mass Matrix 112
5.3.6 Assessment of Some Features of the Method 113
  5.3.6.1 Effects of Using Various Initial Nodal Velocities to Approximate the Impulse Loading 114
  5.3.6.2 Effects of the Number of Spanwise and Depthwise Gaussian Integration Points 115
  5.3.6.3 The Effect of Strain-Rate Sensitivity 116
  5.3.6.4 The Effects of Including Transverse Shear Deformation 117
5.3.7 Comparison of Accuracy and Efficiency of Finite-Element Solutions Versus Finite-Difference Solutions 118
  5.3.7.1 Scope of Comparisons 118
  5.3.7.2 Comparison of Experiment with FE and FD Predictions 119
  5.3.7.3 Convergence and Efficiency Comparisons 122

CONTENTS CONTINUED

Section | Page

6 APPLICATION: CONTAINMENT/DEFLECTION RING RESPONSES TO ENGINE ROTOR BLADE FRAGMENT IMPACT 128

- 6.1 Introduction and Problem Definition 128
- 6.2 Approximate Collision Analyses 133
  - 6.2.1 Collision-Imparted Velocity Method (CIVM) 133
    - 6.2.1.1 Consistent-Mass Collision Model 135
    - 6.2.1.2 Lumped-Mass Collision Model 141
    - 6.2.1.3 Governing Equations 142
    - 6.2.1.4 Solution Procedure 145
  - 6.2.2 Outline of the Collision-Force Method (CFM) 150
- 6.3 Application and Evaluation of the CIVM Approach 153
  - 6.3.1 Definition of Example Problems and Calculations 153
  - 6.3.2 Effect of Type of Idealized Collision Model 155
  - 6.3.3 Effect of Coefficient of Restitution 158
  - 6.3.4 Strain-Rate Effect 160
  - 6.3.5 Comparison of Predictions with Experiment for a Complete Free Ring Subjected to Rotor Blade Impact 162
  - 6.3.6 Responses of a Variously-Supported Ring Quadrant to Rotor Blade Impact 164
- 6.4 Comments on Potential Extensions of the CIVM Approach to More Complex Problems 165

7 SUMMARY AND CONCLUSIONS 168

- 7.1 Summary 168
- 7.2 Conclusions 171
- 7.3 Suggestions for Further Study 173

REFERENCES 176

TABLES 195

ILLUSTRATIONS 200

## CONTENTS CONCLUDED

Appendices — Page

A DESCRIPTION OF THE MECHANICAL SUBLAYER MODEL FOR STRAIN-HARDENING, STRAIN-RATE SENSITIVE MATERIAL BEHAVIOR 287

B DEFINITION OF FINITE ELEMENT MATRICES INDICATED SYMBOLICALLY IN THE TEXT 294

- B.1 Bernoulli-Euler-Type Deformation Behavior 294
  - B.1.1 Bernoulli-Euler-Type Curved Beam Element with CC Assumed-Displacement Functions 294
  - B.1.2 Bernoulli-Euler-Type Curved Beam Element with LC Assumed-Displacement Functions 299
- B.2 Timoshenko-Type Curved Beam Element 303

C MIXED FINITE-ELEMENT MODEL BASED UPON REISSNER'S VARIATIONAL PRINCIPLE 310

## LIST OF TABLES

Table

1 Data Characterizing NAPTC Ring Tests 88 and 91 195

2 Summary of CIVM Calculation Cases for Single-Blade Fragment Impact Against a Free Complete Circular Ring 196

3 Summary of CIVM Calculation Cases for Single-Blade Fragment Impact Upon a Supported Partial Ring 197

4 Blade Motion and Impact Data for Case CR-5B(EL-PP) vs. Case CR-7B(EL-PP-SR) 198

## LIST OF ILLUSTRATIONS

| Figure | | Page |
|---|---|---|
| 1 | Nomenclature for Space Coordinates and Deformation | 200 |
| 2 | Nomenclature for Stress Tensors | 201 |
| 3 | Nomenclature for a Possible Finite Element Representation of a General Two-Dimensional Structure | 202 |
| 4 | Flow Chart for Solution Process of Structural Large Deflection Elastic-Plastic Transient Responses | 203 |
| 5 | Nomenclature for Geometry, Coordinates, and Displacements of a Curved-Beam Finite Element | 205 |
| 6 | Comparison of Finite-Element with Exact Normal Mode Solution for the Small-Deflection Response of a Mechanically Loaded Linear-Elastic Simply-Supported Beam | 206 |
| 7 | Geometry and Nondimensional Quantities for a Free-Free Beam Subjected to an Applied Concentrated Transient Load at its Midspan | 207 |
| 8 | Transverse Shear Responses of the Mechanically Loaded Small-Deflection Linear-Elastic Free-Free Beam | 208 |
| 9 | Moment Responses of the Mechanically Loaded Small-Deflection Linear-Elastic Free-Free Beam | 210 |
| 10 | Transverse Deflection Responses of the Mechanically Loaded Small-Deflection Linear-Elastic Free-Free Beam | 212 |
| 11 | Test Studies of Large-Deflection Elastic-Plastic Transient Responses of Impulsively-Loaded Simple Structures | 214 |
| 12 | Maximum Natural Frequencies for Small Vibrations of the Clamped Beam | 215 |
| 13 | Comparison of Dynamic Responses of the Clamped Beam Calculated by Using Various Temporal Finite-Difference Operators: Central-Difference, Houbolt's, and Newmark's | 217 |
| 14 | Effects of Using Inexact Strain Increments on the Predicted Dynamic Responses of the Clamped Beam | 220 |

## LIST OF ILLUSTRATIONS CONTINUED

| Figure | | Page |
|---|---|---|
| 15 | Comparison of Dynamic Responses of the Clamped Beam Calculated by the Conventional and the Improved Formulation of Dynamic Equilibrium | 223 |
| 16 | Comparison of Dynamic Responses of the Free Ring Obtained by Using CC Versus LC Assumed Displacement Functions | 224 |
| 17 | Comparison of Dynamic Responses of the Free Ring (Including Strain-Rate Effect) Obtained by Using LC Versus CC Assumed Displacement Functions | 227 |
| 18 | Comparison of Dynamic Responses of the Clamped Ring Calculated by Using CC Versus LC Assumed Displacement Functions | 229 |
| 19 | Comparison of Dynamic Responses of the Clamped Beam Calculated by Using the Lumped Mass Matrix and the Consistent Mass Matrix | 230 |
| 20 | Comparison of Dynamic Responses of the Free Ring Calculated by Using the Lumped Mass Matrix and the Consistent Mass Matrix | 232 |
| 21 | High Explosive Edge Effects on the Distribution of Imparted Impulse and Nodal Initial Velocities | 235 |
| 22 | Effects of Various Initial Nodal Velocities on Dynamic Responses of the Clamped Beam | 236 |
| 23 | Effects of Initial Nodal Velocities and Discrete Element Size on Dynamic Responses of the Free Ring | 237 |
| 24 | Effects of Number of Spanwise Gaussian Integration Stations on Dynamic Responses of the Clamped Beam | 238 |
| 25 | Effects of Number of Depthwise Gaussian Integration Points on Dynamic Responses of the Clamped Beam | 239 |
| 26 | Effects of Strain-Rate on Dynamic Responses of the Clamped Beam | 240 |
| 27 | Effects of Strain-Rate on Dynamic Responses of the Free Ring | 241 |
| 28 | Effects of Strain-Rate on Dynamic Responses of the Clamped Ring | 242 |

## LIST OF ILLUSTRATIONS CONTINUED

| Figure | | Page |
|---|---|---|
| 29 | Comparison of the Maximum Natural Frequency of the Clamped Beam Calculated by Using Timoshenko-Type Elements Versus Bernoulli-Euler-Type Elements | 243 |
| 30 | Comparison of the Maximum Natural Frequency of the Free Ring Calculated by Using Timoshenko-Type Elements Versus Bernoulli-Euler-Type Elements | 244 |
| 31 | Comparison of Dynamic Responses of the Clamped Beam Calculated by Using the Timoshenko-Type Element Versus the Bernoulli-Euler-Type Element | 245 |
| 32 | Comparison of Dynamic Responses of the Clamped Ring Calculated by Using Timoshenko-Type Elements Versus Bernoulli-Euler-Type Elements | 246 |
| 33 | Comparison of Finite Element with Finite Difference Predicted Transient Responses for the Impulsively-Loaded Free Ring | 247 |
| 34a | Convergence Behavior of FE-Predicted Peak Relative Centerline Deformation for the Free-Ring Example | 252 |
| 34b | Approximate Convergence Behavior of FE-Predicted Peak Circumferential Strains for the Free-Ring Example | 253 |
| 35a | Convergence Behavior of FD-Predicted Peak Relative Centerline Deformation for the Free-Ring Example | 254 |
| 35b | Approximate Convergence Behavior of FD-Predicted Peak Circumferential Strains for the Free-Ring Example | 255 |
| 36 | Schematics of the Fragment Containment and Fragment Deflection Problems | 256 |
| 37 | Schematics of Some Types of Failed-Rotor Fragments | 257 |
| 38 | Schematic of a Containment Ring Subjected to Single-Fragment Impact | 258 |
| 39 | Schematics of Fragment-Ring Collision Models | 259 |
| 40 | Exploded Schematics of Idealized Collision Models at the Instant of Impact | 260 |

## LIST OF ILLUSTRATIONS CONTINUED

| Figure | | Page |
|---|---|---|
| 41 | Schematics for Free and Restrained Complete Rings | 261 |
| 42 | Schematics for Free and Restrained Partial Rings | 262 |
| 43 | Inspection for Determining a Collision of the Fragment with the Ring | 263 |
| 44 | Information Flow Schematic for Predicting Ring and Fragment Motions in the CIVM Approach | 265 |
| 45 | Schematics of Example Problems Analyzed by the CIVM Approach | 266 |
| 46 | Ring Quadrant and Blade-Fragment Responses Predicted by Using the CM Collision Model | 267 |
| 47 | Ring Quadrant and Blade Fragment Responses Predicted by Using the LM Collision Model | 269 |
| 48 | Comparison of CM with LM Collision Model Predictions for the Complete Free Ring Subjected to Single-Blade Impact | 271 |
| 49 | Effect of the Coefficient of Restitution on the Predicted Inner-Surface and Outer-Surface Circumferential Strains of a Blade-Impacted Free Complete Ring | 273 |
| 50 | Effect of the Coefficient of Restitution on the Accumulated Number of Impacts of a Blade-Impacted Free Complete Ring | 274 |
| 51 | Comparison of Predictions with Experiment for the Free Complete Ring Subjected to Single-Blade Impact in NAPTC Test 88 | 275 |
| 52 | Comparison of Predictions with Experiment for the Free Complete Ring Subjected to Single-Blade Impact in NAPTC Test 91 | 278 |
| 53 | Comparison of Predictions with Experiment for the Free Complete Ring Subjected to Single-Blade Impact in NAPTC Test 91, with a Revised Instant of Initial Impact | 281 |
| 54 | Comparison of the Responses of Ring Quadrants with Ideally-Clamped and Smooth-Hinged Ends to Single-Blade Impact | 283 |

## LIST OF ILLUSTRATIONS CONCLUDED

| Figure | | Page |
|---|---|---|
| 55 | Illustration of the Response of a Quadrant Ring Smoothly Hinged at $\theta = 27°$ to Single-Blade Impact | 285 |
| A.1 | Approximation of a Uniaxial Stress-Strain Curve by the Mechanical Sublayer Model | 290 |
| A.2 | Schematic of Strain-Rate Dependent Uniaxial Stress-Strain Curves | 292 |
| B.1 | Simple Circular Ring Element | 309 |
| B.2 | Straight Beam Element | 309 |

# SECTION 1

# INTRODUCTION

## 1.1 Purpose of Study

In recent years, with accelerated developments in aerospace technology, the needs for accurate and rapid methods for flight-vehicle-safety analysis and for structural design have been keenly felt. In design, one must account for the interaction of the structural system with various types of environmental dynamic conditions such as landing, maneuvering, gust, blast, etc. Also of interest is the interaction of a high-velocity fragment with the structure which is intended to contain and/or to deflect the fragment; uncontained fragments which may be generated from the failure of high-speed rotating turbojet aircraft engine parts could damage equipment and threaten passenger safety [1]*.

For efficient minimum weight (optimum) design, it is often necessary to take full advantage of the load-carrying capacity of available materials by permitting the material to proceed well into the plastic range; thus, nonlinear material behavior must be accounted for in some design analyses. Also, frequently, it is necessary in predicting structural responses to consider geometric nonlinearities, specifically, when the deflections are large enough. Multilayer structures involving composite materials which have high strength and low density properties are becoming useful in aerospace structures as well as in other applications. The complex and nonlinear character of such structural problems, however, makes it almost impossible for one to carry out a conventional analytical solution in closed form. In order to provide a practical means of obtaining meaningful predictions for this kind of complex problem, numerical analysis procedures have been developed.

The general numerical methods of structural analysis may be divided conveniently into two categories. The first category, "numerical solution of the governing algebraic and/or differential equations" is based on mathematically approximating and solving the governing differential equations either by finite-differences [2, 3, for example] or by forward integration[+] [4, 5, 6, for example]. The second category is the "finite-element method" which is most systematically based on variational principles. In this method, the solid continuum is represented by a finite number of regions which are connected at a finite number of nodes along interelement boundaries; the geometric and the material properties of the continuum may be faithfully retained in the idealized structural assembly. In the past several years, the finite-element method of analysis has undergone intensive development and has proved to be a very effective and powerful method for analyzing certain classes of problems, especially for a continuum or structure with complicated boundary conditions, geometric shape, and material properties. The relative ease and versatility with which the finite element (FE) method can be applied to complex structural shapes in comparison with the finite-difference (FD) method is often regarded as an important attribute of the finite-element method. Accordingly, the assumed-displacement version of the finite-element method of analysis for large-deflection elastic-plastic transient responses of simple structures is developed in the present study*. Various aspects of the present development are given in Sections 2 through 5; for convenience, a review of the pertinent literature on this topic is given in Subsection 3.1.

---

*Numbers in brackets [ ] refer to references cited at the end of the text.

Discussed in Section 6 is a timely problem to which the present method of analysis has been applied; this concerns rotor-blade fragment impingement upon (a) a complete circular structural containment ring or (b) a segment of a circular structural ring which is supported in one of several ways. Sought for (a) is a prediction of the motion and structural deformation of the containment ring, as well as the motion of the (idealized-as-rigid in the present first-approximation analysis) rotor blade; suitably accurate engineering predictions of strains are desired. Similar data in category (b) are sought, but there is greater interest in observing the "diverted trajectory" of the rotor

---

[+] This method is applicable to problems in one space variable such as beams and shells of revolution.

[*] Principal emphasis has been devoted to employing the assumed-displacement type of finite-element model; however, other types of finite-element models such as equilibrium-stress models, hybrid models, and mixed models [7] could also be used for this type of problem.

blade -- the idea of interest being to divert the blade to a new "harmless direction". Further background on the rotor fragment containment/deflection problem and on alternate or supplementary methods for its analysis is given in Subsection 6.1. Section 6 is devoted to discussing the rotor burst fragment containment/deflection problem, and the application of a method of analysis developed in this study to analyze some simple cases of fragment impingement upon containment and/or deflection structures.

## 1.2 Synopsis of Investigation

The present study is devoted to developing and validating a method to analyze the large deflection transient responses of simple structures, including elastic-plastic material behavior. The assumed-displacement finite-element approach which is based upon the Principle of Virtual Work and D'Alembert's Principle (or equivalently, Hamilton's Principle) is used to formulate the governing equations. The resulting equations of motion are solved by a direct timewise numerical integration scheme. This method has been evaluated (see Section 5) by applying it to a sequence of transient response examples having reliable independent analytical or experimental results, for a definitive comparison. This development is then applied to the rotor fragment containment/deflection problem. A simplified fragment structure interaction model which utilizes momentum and energy considerations of the system is employed to predict the collision-induced velocities imparted "instantaneously" to the affected ring segment and to the fragment.

Sections 2 through 5 pertain to the development and evaluation of the present finite-element method for predicting both small-deflection and large-deflection elastic and/or elastic-plastic transient responses of simple structures. The general equations which govern large elastic-plastic dynamically-induced deformations of a continuum are presented in Section 2 in general three-dimensional tensor form. Section 3 is devoted to the development of an overall method of solution, following a review of the pertinent literature dealing with this class of problems; the spatial finite-element approximation together with the temporal finite-difference approximation are used. Also in Section 3, the equations of motion for the finite-element treatment are derived from a variational statement consisting of the Principle of Virtual Work and

D'Alembert's Principle; the resulting equations are developed in two forms: (a) the "conventional form" (see Eq. 3.1), and (b) an "improved" unconventional form (see Eq. 3.2). The new improved formulation (b) is shown (in Section 5) to be more efficient and economical for computing the large-deflection elastic-plastic transient responses of simple structures than is the conventional finite-element formulation (a). In Section 4, the general formulation discussed in Section 3 is developed in detail for an arbitrarily curved beam having (a) zero and (b) non-zero transverse shear deformation. Finally, Section 5 contains an assessment of this method of analysis by means of a sequence of problems for beam and ring example structures which are subjected to transient mechanical loading or to initial impulsive loading; comparisons of the present predictions are made with reliable experimental data and/or independent predictions (finite-difference and/or analytical).

In Section 6, the problem of burst-rotor fragments interacting with either a complete or a partial containment/deflection structural ring is discussed. Energy and momentum considerations are employed to predict the collision-induced velocities which are imparted to the colliding fragment and to the affected ring segment (the associated analysis method is termed the collision-imparted velocity method, CIVM). This collision analysis is combined with the earlier-developed FE analysis to permit one to predict the resulting large deformation responses of containment/deflection rings. Comparisons with limited experimental data are also given.

The entire study is summarized and pertinent conclusions are drawn in Section 7.

Also, three appendices are included. Appendix A contains the description of the mechanical sublayer model for strain-hardening, strain-rate sensitive material behavior. In Appendix B, all of the matrices used in the present analysis for the assumed displacement finite-element formulations are listed. Appendix C contains, for purposes of illustration, the formulation of the equations of motion based on a mixed finite-element method (1) by assuming a displacement field which is continuous over the entire solid and (2) by using an assumed-stress field for the individual element; however, no evaluation of this model has been made in this report.

## SECTION 2

## GENERAL FORMULATION

### 2.1 Introduction

In this section, the equations which govern the large deflection dynamic and/or static responses of a continuum are presented. Elastic-plastic strain-rate-dependent material behavior is considered, but not viscoelasticity. The equations are derived in general tensor form for convenience and generality and, therefore, any coordinate system can be employed for defining the three-dimensional space containing the continuum. These equations are later specialized to treat simpler classes of problems.

The terminology "large deflections" as used here indicates, for example, that the lateral deflections of beams and/or plates are large compared with the thickness of the structure; the change in geometry is significant. Through the strain-displacement relations and the equilibrium equations, the geometric nonlinearities are introduced into the theory. It should be noted, however, that in the present analysis, the strains (extension and shear) are treated as being small compared with unity.

In a finite-strain analysis, there are various possible types of definitions of stresses and strains (Refs. 8, 9, 10) based on either the predeformed or post-deformed configurations of the continuum, and the distinctions between them cannot be neglected; whereas, they may be indistinguishable in small-strain theory. The constitutive relations for cases involving finite elastic-plastic strain are uncertain (not well established), primarily because of the lack of adequate experimental data. However, finite-strain predictions have been of increasing interest recently, for instance, in connection with explosive forming of structural shapes. The analysis tools for this class of problem are much desired, and further research is required.

In this study, the indicial notation and summation convention associated with vector and tensor analysis are used.

## 2.2 Governing Equations

### 2.2.1 The Strain-Displacement Relations

Consider the continuum in its process of deformation from an initially undeformed state which exists at time $t_o$ (Fig. 1). Each material point in the 3-dimensional space can be identified by a general curvilinear coordinate system (termed Lagrangian) $\xi^j$ and an inertial Cartesian rectangular coordinate system $Y^j$ fixed in space. Let the position vector of a given material point in the initial undeformed state be $\bar{r}(\xi^j, t_o)$ and the position vector of the same material point in the deformed* state at any instant of time t be $\bar{R}(\xi^j, t)$.

Base vectors for the coordinate system $\xi^j$ may be defined in both the undeformed state and the deformed state of the continuum, respectively, as

$$\bar{g}_j = \frac{\partial \bar{r}}{\partial \xi^j} \qquad \text{and} \qquad \bar{G}_j = \frac{\partial \bar{R}}{\partial \xi^j} \tag{2.1}$$

The metric tensor $g_{ij}$ associated with the undeformed state and the metric tensor $G_{ij}$ associated with the deformed state are defined, respectively, by:

$$g_{ij} = \bar{g}_i \cdot \bar{g}_j \quad , \quad G_{ij} = \bar{G}_i \cdot \bar{G}_j \tag{2.2}$$

The contravariant metric tensors $g^{mn}$ and $G^{mn}$ are defined, respectively, through the relations**

$$g_{mp}\, g^{mn} = \delta_p^n \quad , \quad G_{mp}\, G^{mn} = \delta_p^n \tag{2.3}$$

where $\delta_p^n$ is the Kronecker delta defined as

$$\delta_p^n = \begin{cases} 1 & \text{if } n = p \\ 0 & \text{if } n \neq p \end{cases} \tag{2.4}$$

The respective contravariant base vectors are defined by

$$\bar{g}^i = g^{ij}\, \bar{g}_j \quad , \quad \bar{G}^i = G^{ij}\, \bar{G}_j \tag{2.5}$$

---

*Quantities associated with the deformed state are represented by capital letters, and lower case letters denote the initial undeformed state.

**Index quantities such as i, j, p, m, n, k, etc., take on values 1, 2, and 3.

The deformed position vector $\bar{R}$ and the undeformed position vector $\bar{r}$ are related by the displacement vector $\bar{v}(\xi^j, t)$ as follows:

$$\bar{R}\,(\xi^i, t) = \bar{r}\,(\xi^i, t_0) + \bar{v}\,(\xi^i, t) \tag{2.6}$$

The displacement vector $\bar{v}$ may be expressed in component form with respect to the base vector system of the undeformed state at time $t_o$ as

$$\bar{v} = v^i \bar{g}_i = v_i \bar{g}^i \tag{2.7}$$

The Lagrangian strain tensor associated with the deformation process is defined by

$$\gamma_{ij} = \frac{1}{2}\,(G_{ij} - g_{ij}) \tag{2.8}$$

and can be written in terms of the displacement components as

$$\gamma_{ij} = \frac{1}{2}\,(v_{i,j} + v_{j,i} + v^k_{,i}\, v_{k,j}) \tag{2.9}$$

where $v_{i,j}$ denotes covariant differentiation of $v_i$ with respect to $\xi^j$ using the metric tensor of the undeformed state and is defined as

$$v_{i,j} = \frac{\partial v_i}{\partial \xi^j} - \left\{ {k \atop i\;j} \right\}_o v_k \tag{2.10}$$

where $\{i^k j\}_o$ is the Christoffel symbol of the second kind associated with the undeformed state (subscript "o") and is defined by

$$\left\{ {k \atop i\;j} \right\}_o = \frac{\partial \bar{g}_i}{\partial \xi^j} \cdot \bar{g}^k = \frac{\partial \bar{g}_j}{\partial \xi^i} \cdot \bar{g}^k \tag{2.11}$$

Differentiating Eqs. 2.7 and 2.9 with respect to time t which is a monotonically increasing quantity, and using the fact that $\bar{g}_i$ and $\{i^k j\}_o$ are not functions of time (fixed quantities with respect to the initial state), one may obtain the following expression for the displacement rate:

$$\dot{\bar{v}} = \dot{v}^i \bar{g}_i = \dot{v}_i \bar{g}^i \tag{2.12}$$

Hence, the strain rate $\dot{\gamma}_{ij}$ which is related to the displacement and displacement rate is given by

$$\dot{\gamma}_{ij} = \frac{1}{2}\left[(\delta_i^k + v^k_{,i})\,\dot{v}_{k,j} + (\delta_j^k + v^k_{,j})\,\dot{v}_{k,i}\right] \tag{2.13}$$

where $(\dot{\ })$ denotes partial differentiation with respect to time t.

In the problem of interest, expressions are required for the strain increment $\Delta\gamma_{ij}$ and the displacement increment $\Delta\bar{v}$ which occur when the continuum is deformed incrementally from one deformed state at time $t_1$ to another deformed state at time $t_2$, where $t_2 = t_1 + \Delta t$ (the solution procedure is to be discussed later for transient-response behavior of a continuum). If the time-step $\Delta t$ between these two instants is small, the displacement (denoted by ${}^2\bar{v}$) at time $t_2$ can be constructed by employing the Taylor series expansion involving the finite increment $\Delta t$ in time*:

$${}^2\bar{v} = {}^1\bar{v} + \int_{t_1}^{t_2} \dot{\bar{v}}\,dt = {}^1\bar{v} + {}^1\dot{\bar{v}}(\Delta t) + {}^1\ddot{\bar{v}}\,\frac{(\Delta t)^2}{2} + o(\Delta t)^3 \tag{2.14}$$

or in component form

$${}^2v_i = {}^1v_i + {}^1\dot{v}_i\,(\Delta t) + {}^1\ddot{v}_i\,\frac{(\Delta t)^2}{2} + o\,(\Delta t)^3 \tag{2.15}$$

and correspondingly, the Lagrangian strain ${}^2\gamma_{ij}$, at time $t_2$ may be expressed as

$${}^2\gamma_{ij} = {}^1\gamma_{ij} + \int_{t_1}^{t_2} \dot{\gamma}_{ij}\,dt = {}^1\gamma_{ij} + {}^1\dot{\gamma}_{ij}\,(\Delta t) + {}^1\ddot{\gamma}_{ij}\,\frac{(\Delta t)^2}{2} + o(\Delta t)^3 \tag{2.16}$$

In Eq. 2.16 terms of the order of $(\Delta t)^3$ and higher are neglected because of the smallness of the time-step $\Delta t$.

It perhaps should be mentioned that the displacement vector $\bar{v}$ can be expressed alternatively in terms of components with respect to the deformed base vectors at time t as

$$\bar{v} = V^m\,\bar{G}_m = V_m\,\bar{G}^m \tag{2.17}$$

and the corresponding strain tensor (termed Almansi, see Ref. 11) has the form

---

*Note that prescripts, both sub and super, are used here to identify quantities associated with particular instants in time.

$$\gamma_{mn} = \frac{1}{2}\left( V_m|_n + V_n|_m - V^k|_m \, V_k|_n \right) \tag{2.18}$$

where $V_{m|n}$ indicates also covariant differentiation but with respect to the metric tensor of the deformed state and is defined as

$$V_m|_n = \frac{\partial V_m}{\partial \xi^n} - \left\{ {k \atop m\,n} \right\} V_k \tag{2.19}$$

where

$$\left\{ {k \atop m\,n} \right\} = \frac{\partial \bar{G}_m}{\partial \xi^n} \cdot \bar{G}^k = \frac{\partial \bar{G}_n}{\partial \xi^m} \cdot \bar{G}^k \tag{2.20}$$

Since $\bar{G}_m$ as well as $\left\{ {k \atop mn} \right\}$ are functions of time, the displacement vector rate and the strain rate expressed in terms of components with respect to the deformed base vector system will not take as simple a form as Eqs. 2.12 and 2.13 in which the components are expressed with respect to the undeformed base vector system. Hence, the strain-displacement relations represented by Eq. 2.9 are chosen for use.

### 2.2.2 Descriptions of Stresses and Forces on a Deformed Continuum Element

Consider the geometry and the forces acting upon an arbitrary parallelepiped element on its path of deformation (see Figs. 1 and 2). In the initial undeformed state, it has the volume $dV_o$ bounded by surfaces $dA_{om}$ (having edges $d\xi^n \bar{g}_n$ and $d\xi^p \bar{g}_p$, where $m \neq n \neq p$). After deformation, this Lagrangian parallelepiped has a volume $dV$ and is bounded by surfaces $dA_m$ (having edges $d\xi^n \bar{G}_n$, $d\xi^p \bar{G}_p$). Thus,

$$dV_o = \sqrt{g}\, d\xi^1 d\xi^2 d\xi^3 \quad , \quad dV = \sqrt{G}\, d\xi^1 d\xi^2 d\xi^3$$

$$dA_{om} = \sqrt{g\, g^{mm}}\, d\xi^n d\xi^p \quad , \quad dA_m = \sqrt{G\, G^{mm}}\, d\xi^n d\xi^p \tag{2.21}$$

where g and G are the determinants of $g_{ij}$ and $G_{ij}$, respectively.

In the following, convenient descriptions for stresses and forces acting upon the deformed parallelepiped element are to be discussed as a prelude for their use in the Principle of Virtual Work from which the equations of motion and boundary conditions will be obtained.

Let $\bar{\sigma}_o^i$ denote the stress vector associated with the $\xi^i$ surface (at $\xi^i$ = const) in the deformed state measured per unit initial undeformed area. The Kirchhoff stress tensor $S^{ij}$ is defined by (Fig. 2):

$$\bar{\sigma}_o^{\,i}\sqrt{g^{ii}} = S^{ij}\,\bar{G}_j = S^{i}_{j}\,\bar{G}^{j} \tag{2.22}$$

or

$$\bar{\sigma}_o^{\,i}\sqrt{g^{ii}} = S^{ij}\,(\delta^k_j + V^k_{,j})\,\bar{g}_k \tag{2.22a}$$

The stress resultant $\bar{T}^i$ exerted on the deformed surfaces $dA_i$ by the neighboring element of the continuum may be expressed in the form

$$\bar{T}^{i} = \bar{\sigma}_o^{\,i}\sqrt{g\,g^{ii}} = \sqrt{g}\;S^{ij}(\delta^k_j + V^k_{,j})\,\bar{g}_k \tag{2.23}$$

Alternatively, let $\bar{\sigma}^i$ be the stress vector associated with the $\xi^i$ surface in the deformed body but measured per unit deformed area; thus, the Eulerian stress tensor, $\tau^{ij}$, is defined by (Fig. 2):

$$\bar{\sigma}^{i}\sqrt{G^{ii}} = \tau^{ij}\,\bar{G}_j = \tau^{i}_{j}\,\bar{G}^{j} \tag{2.24}$$

Then the stress resultant, $\bar{T}^i$, may be expressed as

$$\bar{T}^{i} = \bar{\sigma}^{i}\sqrt{G\,G^{ii}} = \sqrt{G}\;\tau^{ij}\,\bar{G}_j \tag{2.25}$$

Likewise, the body force, $\bar{F}$ (inertia, gravitational, magnetic, etc.) per unit mass acting on the deformed body may be described in component form either with respect to the undeformed base vector of the coordinate system $\xi^i$ as

$$\bar{F} = f^{i}\,\bar{g}_i = f_i\,\bar{g}^{i} \tag{2.26}$$

or with respect to the deformed base vectors of the coordinate system $\xi^i$ as

$$\bar{F} = F^{i}\,\bar{G}_i = F_i\,\bar{G}^{i} \tag{2.27}$$

It should be noted that the stress tensors $S^{ij}$ and $\tau^{ij}$ are related to each other by

$$S^{ij} = \sqrt{\frac{G}{g}}\; \tau^{ij} \tag{2.28}$$

Also, from moment equilibrium it can be shown that $S^{ij}$ and $\tau^{ij}$ are symmetric stress tensors. Thus

$$S^{ij} = S^{ji} \quad , \quad \tau^{ij} = \tau^{ji} \tag{2.29}$$

### 2.2.3 Conservation of Mass

The conservation of mass may be expressed as (Ref. 11) to be

$$\iiint_{V_o} \rho_o \, d\, V_o = \iiint_{V} \rho \, d\, V \tag{2.30}$$

or using Eq. 2.21, one may write

$$\iiint_{V_o} \rho_o \sqrt{g}\; d\xi^1 d\xi^2 d\xi^3 = \iiint_{V} \rho \sqrt{G}\; d\xi^1 d\xi^2 d\xi^3 \tag{2.31}$$

where the integrals extend over the same particles. The quantity $\rho_o$ is the density in the original configuration and $\rho$ is the current density of the deformed body. Since this relation must hold for all bodies, one has

$$\rho_o \sqrt{g} = \rho \sqrt{G} \tag{2.32}$$

This gives the relation of densities in different configurations of the continuum to that of the original undeformed continuum.

### 2.2.4 The Principle of Virtual Work

In this subsection, the Principle of Virtual Work for the continuum will be presented and is employed to derive the equations of equilibrium and the boundary conditions.

Consider the deformed continuum in equilibrium, under the action of body forces, externally applied surface tractions, and with arbitrary deformation conditions consistent with the prescribed geometric boundary conditions. Let this equilibrium configuration be subjected to an arbitrary and independent set of infinitesimal virtual displacements without violating the prescribed geometric boundary conditions. The Principle of Virtual Work states that the virtual work done by the external forces (body forces and surface tractions) is equal to the virtual work of the internal stresses. By utilizing the undeformed metric of the coordinate system $\xi^i$, the Principle of Virtual Work may be stated mathematically as

$$\delta U - \delta W = 0 \tag{2.33}$$

where

$$\delta U = \iiint_{V_o} S^{ij} \delta \gamma_{ij} \, dV_o \quad = \text{variation of the work of the internal forces} \tag{2.33a}$$

$$\delta W = \iiint_{V_o} \rho_o \bar{F} \cdot \delta \bar{v} \, dV_o + \iint_{A_{o\sigma}} \bar{T}_o \cdot \delta \bar{v} \, dA_o =$$

variation of the work of: (1) the body force $\bar{F}$ per unit mass and (2) of the externally applied surface traction $\bar{T}_o$, measured per unit area of the undeformed state (2.33b)

where $S^{ij}$ is the Kirchhoff stress tensor

$\gamma_{ij}$ is the Lagrangian strain tensor

$\delta$ is the usual symbol denoting the variation of a function

$\delta\bar{v}$ is the variation of the displacement vector and may be expressed in terms of components with respect to the undeformed base vectors as

$$\delta \bar{v} = \delta ( v^i \bar{g}_i ) = ( \delta v^i ) \bar{g}_i$$

(because $\bar{g}_i$ does not depend upon displacement, $\delta\bar{g}_i = 0$) (2.34)

In Eqs. 2.33a and 2.33b, $V_o$ is the entire undeformed volume of the continuum which is bounded by the undeformed surface $A_o$. The boundary surface $A_o$ can be divided into two parts: (a) prescribed surface traction boundary $A_{o\sigma}$ and (b) prescribed displacement boundary $A_{ov}$. Then the variation in the Lagrangian strain tensor, $\delta\gamma_{ij}$ associated with the displacement variation $\delta\bar{v}$ about the deformed equilibrium configuration may be expressed as

$$\delta \gamma_{ij} = \frac{1}{2}\left( \bar{G}_i \cdot \frac{\partial \delta \bar{v}}{\partial \xi^j} + \frac{\partial \delta \bar{v}}{\partial \xi^i} \cdot \bar{G}_j \right)$$
$$= \frac{1}{2}\left[ (\delta^k_i + v^k_{,i})\, \delta v_{k,j} + (\delta^k_j + v^k_{,j})\, \delta v_{k,i} \right]$$

(2.35)

where $(\ )_{,n}$ signifies covariant differentiation with respect to the undeformed metric of the coordinate system $\xi^i$.

Substituting Eq. 2.35 into Eq. 2.33a one has

$$\delta U = \iiint_{V_o} S^{ij} \left[ (\delta^k_i + v^k_{,i})\, \delta v_{k,j} \right] d V_o \qquad (2.36)$$

where the symmetry of $S^{ij}$ has been used to combine terms. Upon integration by parts and using Green's theorem to convert volume integrals to surface integrals, Eq. 2.36 becomes

$$\delta U = \iint_{A_{o\sigma}} S^{ij} (\delta^k_i + v^k_{,i})\, \delta v_k \, n_{oj} \, d A_o$$
$$- \iiint_{V_o} \left[ S^{ij} (\delta^k_i + v^k_{,i}) \right]_{,j} \delta v_k \, d V_o$$

(2.37)

where $n_{oj}$ is the component of the unit normal vector, $\bar{n}_o$, to the undeformed boundary surface $A_o$, which is defined as

$$\bar{n}_o = n_{oj}\, \bar{g}^j \qquad (2.38)$$

Substituting Eqs. 2.26 and 2.34 into Eq. 2.33b results in

$$\delta W = \iiint_{V_o} \rho_o f^k \delta v_k \, d V_o + \iint_{A_{o\sigma}} T_o^k \, \delta v_k \, d A_o \qquad (2.39)$$

where $T_o^k$ is the component of $\bar{T}_o$ in the direction of the undeformed base vector.

Thus,

$$\bar{T}_o = T_o^k \bar{g}_k = T_{ok} \bar{g}^k \tag{2.40}$$

Substituting Eqs. 2.37 and 2.39 into the Principle of Virtual Work one obtains

$$\iiint_{V_o} \left\{ \left[ S^{ij} ( \delta_i^k + v^k_{,i} ) \right]_{,j} + \rho_o f^k \right\} \delta v_k \, dV_o + \iint_{A_{o\sigma}} \left[ - S^{ij} ( \delta_i^k + v^k_{,i} ) n_{oj} + T_o^k \right] \delta v_k \, dA_o = 0 \tag{2.41}$$

Since the variation $\delta v_k$ is independent and arbitrary, this leads to the following equation of equilibrium at any point in the continuum:

$$\left[ S^{ij} ( \delta_i^k + v^k_{,i} ) \right]_{,j} + \rho_o f^k = 0 \tag{2.42}$$

which is a bilinear function in $S^{ij}$ and $v^j$.

Also, on the boundary $A_{o\sigma}$ where the surface traction is prescribed, the following boundary condition relation must be satisfied:

$$S^{ij} ( \delta_i^k + v^k_{,i} ) n_{oj} = T_o^k \tag{2.43}$$

On the portion of the boundary $A_{ov}$ where the displacement is prescribed, the relation

$$v^i = \underset{\sim}{v}^i \tag{2.44}$$

should be satisfied.

It should be noted that all pertinent quantities appearing in $\delta U$ and $\delta W$ of Eq. 2.33 are defined consistently with respect to the (initial) undeformed metric of the coordinate system $\xi^i$. Also, the integrations are extended over the original (known) configuration of the continuum. This is usually called a "Lagrangian description".

Alternatively, by using the relations

$$\rho_o \sqrt{g} = \rho \sqrt{G} \, , \qquad S^{ij} = \sqrt{\frac{G}{g}} \, \tau^{ij} , \qquad \bar{T}_o dA_o = \bar{T} dA \tag{2.45}$$

the Principle of Virtual Work, Eq. 2.33, can be converted into the following equivalent form with reference to the present deformed state (designated as an Eulerian* description):

$$\iiint\limits_{V} \tau^{ij} \delta \gamma_{ij} \, dV = \iiint\limits_{V} \rho \bar{F} \cdot \delta \bar{V} \, dV + \iint\limits_{A_\sigma} \bar{T} \cdot \delta \bar{V} \, dA \tag{2.46}$$

It is worthy of special mention that this basic variational formulation, the Principle of Virtual Work, holds independent of the material stress-strain relation and the existence of potential functions of the external forces. Also, it embodies the equation of equilibrium of the continuum (overall and/or at any generic point). The variational technique has proved to be a very powerful and easily applied method for analyzing solid continuum problems. In the present study, the Principle of Virtual Work, together with the concept of D'Alembert's Principle is employed for analyzing the large-deflection elastic-plastic transient responses of structures which may be subjected to an initial impulse followed by a time-dependent externally-applied forcing function and geometric constraints.

The D'Alembert Principle states that the dynamic system can be considered to be in equilibrium under the externally-applied forces if the inertial forces are taken into account. The Principle of Virtual Work, Eq. 2.33, now with the virtual work done by the inertial forces specified explicitly may be written as

$$\delta U - \delta W + \delta I = 0 \tag{2.47}$$

where

$$\delta I = \iiint\limits_{V_0} \rho_0 \ddot{\bar{R}} \cdot \delta \bar{V} \, dV_0 = \iiint\limits_{V_0} \rho_0 \ddot{\bar{V}} \cdot \delta \bar{V} \, dV_0 \tag{2.47a}$$

= variation of the work done by the inertia forces

---

[*] It should be noted that, in fluid mechanics, the Eulerian description is concerned with the state of motion through a fixed grid or a fixed volume in space, in contrast with the above solid-mechanics terminology.

In Eq. 2.47a, $\ddot{\bar{R}} = \ddot{\bar{v}}$ since $\bar{R} = \bar{r} + \bar{v}$ and $\bar{r}$ is the position vector of the undeformed body. It is assumed that all body forces other than inertia forces are taken into account within $\delta W$.

Let Eq. 2.47 be integrated with respect to time between two time limits $t_1$ and $t_2$ to represent the conventional statement of Hamilton's Principle. Thus

$$\int_{t_1}^{t_2} [\delta U - \delta W + \delta I]\, dt = 0 \tag{2.48}$$

Integrating the last term which appears under the integral sign of Eq. 2.48 by parts, results in

$$\begin{aligned}\int_{t_1}^{t_2} \delta I\, dt &= \int_{t_1}^{t_2} [\iiint_{V_0} \rho_0\, \ddot{\bar{v}} \cdot \delta \bar{v}\, dV_0]\, dt \\ &= [\iiint_{V_0} \rho_0\, \dot{\bar{v}} \cdot \delta \bar{v}\, dV_0]\Big|_{t_1}^{t_2} - \int_{t_1}^{t_2} [\iiint_{V_0} \rho_0\, \dot{\bar{v}} \cdot \delta \dot{\bar{v}}\, dV_0]\, dt\end{aligned} \tag{2.49}$$

Since if the conditions of the dynamic system are prescribed (or are otherwise known) at the two time limits $t_1$ and $t_2$ and are not subjected to variation, one has

$$\delta \bar{v}\,(t = t_1) = 0 \quad , \quad \delta \bar{v}\,(t = t_2) = 0 \tag{2.50}$$

Then Eq. 2.49 reduces to

$$\int_{t_1}^{t_2} \delta I\, dt = -\int_{t_1}^{t_2} [\iiint_{V_0} \rho_0\, \dot{\bar{v}} \cdot \delta \dot{\bar{v}}\, dV_0]\, dt = -\int_{t_1}^{t_2} \delta K\, dt \tag{2.51}$$

where

$$K = \iiint_{V_0} \frac{1}{2} \rho_0\, \dot{\bar{v}} \cdot \dot{\bar{v}}\, dV_0$$ = the kinetic energy of the body (as usually seen in Hamilton's Principle).

Substituting Eq. 2.51 into Eq. 2.48, one has the Principle of Virtual Work of the dynamic system:

$$\int_{t_1}^{t_2} [\,\delta U - \delta W - \delta K\,]\, dt = 0 \tag{2.52}$$

It perhaps should be pointed out that either the Lagrangian form or the Eulerian form of Eq. 2.52 could be used in the exact or in an approximate analysis of structural responses. For convenient reference, these two forms are written out in full as follows:

$$\int_{t_1}^{t_2} \Big[ \iiint_{V_0} S^{ij}\,\delta\gamma_{ij}\, dV_0 - \iiint_{V_0} \rho_0 f^i\,\delta v_i\, dV_0 - \iint_{A_{0\sigma}} T_0^i\,\delta v_i\, dA_0$$

$$- \iiint_{V_0} \rho_0\, \dot{v}^i\,\delta\dot{v}_i\, dV_0 \Big]\, dt = 0$$

(Lagrangian form) (2.52a)

$$\int_{t_1}^{t_2} \Big[ \iiint_{V} \tau^{ij}\,\delta\gamma_{ij}\, dV - \iiint_{V} \rho F^i\,\delta V_i\, dV - \iint_{A_{\sigma}} T^i\,\delta V_i\, dA$$

$$- \iiint_{V} \rho\, \dot{\bar{v}}\cdot\delta\dot{\bar{v}}\, dV \Big]\, dt = 0$$

(Eulerian form) (2.52b)

It is seen that the Eulerian description is based on the current deformed volume, area, and metric tensor; these quantities are functions of the displacement vector, $\bar{v}$, which is to be determined as a function of time. On the other hand, the Lagrangian description is based on the original (known) volume, area, and metric tensors and, accordingly, is more convenient.

Because of the complexity in certain structural problems, numerical methods are of interest and include, for example, finite difference, finite element, forward integration, etc. In this study, however, the finite-element approach is used and is based on the variational formulation given by Eq. 2.52a. Since, in this Lagrangian point of view, the strain would take on its simple form and the mass matrix (as discussed later) would be constant throughout the calculation of the transient response (and hence need not be re-evaluated at each stage in the incremental time analysis as would be required by the Eulerian description), the use of the Lagrangian description would appear to result in some computational advantages and time saving in solving the problem over the use of the Eulerian description.

It perhaps should be noted that the Principle of Virtual Work, Eq. 2.52, can be applied either to conservative or to non-conservative dynamic systems. For conservative dynamic systems (that is, if the potential of the internal stress and externally-applied force exist), as well as for dynamic systems with both conservative and non-conservative forces, another very useful energy principle called Hamilton's Principle could also be used; this principle can be derived from the Principle of Virtual Work as employed here (i.e., Eq. 2.48 or Eq. 2.52).

Finally, it should be noted that one need not use the time integrated form of the Principle of Virtual Work (within which is imbedded D'Alembert's Principle) if one wishes simply to obtain the correct equations of motion and the correct boundary conditions -- the use of Eqs. 2.47 and 2.47a which hold at each instant in time will suffice for this purpose. However, if one wishes to formulate a finite-element analysis in both space and time (see Ref. 12), the "time integrated" variational statement represented by Eq. 2.48 or Eq. 2.52a, for example, is very useful.

### 2.2.5 Thermodynamic Equations

In this subsection, the thermodynamic equations which govern the large deflection (static or dynamic response) of the continuum in the presence of thermal and mechanical effects are presented since it is desired that the present general formulation include thermal effects for future use, although the illustrative example problems discussed herein do not include them. These thermodynamic equations will be used for the derivation of the material elastic and elastic-plastic constitutive relations presented in the next subsection.

Consider that the continuum initially in the undeformed state with volume $V_o$ and bounded by surface $A_o$ is subjected to mechanical and/or thermal loading. After deformation, its volume becomes V and is bounded by surface A.

The first law of thermodynamics or the law of conservation of energy may be written as:

For the Continuum as a Whole:

$$\iiint_{V_o} \rho_o \left( \bar{F} \cdot \dot{\bar{v}} + B \right) dV_o + \iint_{A_{o\sigma}} \bar{T}_o \cdot \dot{\bar{v}}\, dA_o - \iint_{A_{oh}} \bar{Q} \cdot \bar{n}_o\, dA_o = \iiint_{V_o} \rho_o \dot{U}\, dV_o \qquad (2.53)$$

At any Generic Point of the Continuum:

$$S^{ij} \dot{\gamma}_{ij} - Q^{i}_{,i} + \rho_o B = \rho_o \dot{U} \qquad (2.54)$$

where B is the rate of heat input per unit mass

$\bar{Q}$ is the rate of the heat flux vector across the body surface measured per unit undeformed area and $\bar{Q} = Q^j \bar{g}_j = Q_j \bar{g}^j$

$A_{oh}$ is the portion of the surface over which the heat flux proceeds

U is the internal energy per unit mass

$\rho_o$, $\bar{F}$, $\bar{T}_o$, $A_{o\sigma}$, $\bar{n}_o$, $S^{ij}$, and $\gamma_{ij}$ are defined as previously stated.

The second law of thermodynamics (or the increase of entropy principle) may be written as:

For the Continuum as a Whole:

$$\iiint_{V_o} \rho_o \dot{S}\, dV_o - \iiint_{V_o} \rho_o \frac{B}{T}\, dV_o + \iint_{A_{oh}} \frac{Q^i n_{oi}}{T}\, dA_o \geq 0 \qquad (2.55)$$

At any Generic Point of the Continuum

$$\rho_o \dot{S} - \rho_o \frac{B}{T} + \frac{1}{T^2} \left( T Q^{i}_{,i} - Q^{i} T_{,i} \right) \geq 0 \qquad (2.56)$$

where S is the entropy per unit mass

T is the absolute temperature

Let the Helmoltz function H be defined as

$$H = U - TS \tag{2.57}$$

Then, substituting for U of Eq. 2.57 into Eq. 2.54, results in

$$S^{ij}\dot{\gamma}_{ij} - Q^{i}_{,i} + \rho_0 B = \rho_0 (\dot{H} + \dot{T}S + S\dot{T}) \tag{2.58}$$

It is convenient to eliminate $\rho_o B$ from Eqs. 2.56 and 2.58 to obtain the inequality

$$S^{ij}\dot{\gamma}_{ij} - \rho_0 (\dot{H} + \dot{T}S) - \frac{1}{T} Q^{i} T_{,i} \geqslant 0 \tag{2.59}$$

Alternatively, the thermodynamic equations can be expressed in a form which refers to the deformed state of the continuum.

These thermodynamic equations, if desired, can be employed to deduce the equation of equilibrium, the continuity equation, and the boundary conditions.

It should be noted that all of the equations derived so far are exact for either finite strain or infinitesimal strain; that is, no restriction on the magnitude of strain has been made.

## 2.3 Constitutive Relations

This subsection is concerned with the elastic and elastic-plastic material behavior of the continuum; also, thermal effects and strain-rate effects will be discussed.

The elasticity theory (linear or nonlinear) postulates that a unique relation exists between the instantaneous states of stress and strain. When the material is deformed into the plastic range, a unique relation does not hold in general between stress and strain, but a functional relation exists: the strain depends not only on the current state of stress but also on the history of loading.

At finite strain and/or elevated temperatures, the coupling influences occurring through thermal effects, elastic deformation, and plastic flow may be significant in some cases, and an initially isotropic and homogeneous material may exhibit appreciably anisotropic and nonuniform behavior. The coupling influences include for example: (1) the elastic modulii of the material will change as functions of temperature and continued plastic straining; (2) heat, which is generated from the dissipation of plastic work can induce the redistribution of temperature; also, (3) the Bauschinger effect and hysteresis loop are observed which are believed to be due to differential hardening of the variously-oriented crystals. These complex coupling functional relations, and the limited available experimental data make it very difficult for one to carry out the finite strain and/or high temperature elastic-plastic analysis with confidence.

In classical thermal-elastic-plastic theory (Refs. 13, 14) which is restricted to infinitesimal strain, considerable simplification is attained by decoupling the effect of thermal elasticity, mechanical elastic deformation, and mechanical plastic flow. The total strain is assumed to be decomposed into elastic (thermodynamically reversible) strain, and plastic (thermodynamically irreversible) strain. The elastic strain can further be decomposed into thermal and mechanical parts. Each component has the same invariant properties as the total strain, but is not expressible in terms of the displacements. Only the total strain can be related to the displacements. The elastic strain is related to the stress through a linear-function relation, and the thermal-elastic strain is treated as an initial (or a prescribed) strain. The elastic modulus and heat capacity are considered to be invariant under plastic flow; that is, the influence of plastic flow on the thermal-elastic characteristics is neglected. Only very recently, some pertinent work has been extended to finite strain (Refs. 15, 16). However, these theories do not completely agree with each other, and further research is required.

In order to make the present study self-contained, the thermoelastic constitutive relation is presented in Subsection 2.3.1. Thermal-elastic-plastic material behavior is discussed in Subsection 2.3.2. Subsection 2.3.3 is concerned with the strain-rate effect. The general derivations are based on the thermodynamic equations and follow those of Refs. 14 and 15.

### 2.3.1 Thermoelastic Material Behavior

Consider an elastic continuum initially in a reference state with neither stress nor strain, and of uniform absolute temperature, $T_o$. This continuum is then subjected to a temperature distribution $T(\xi^i,t)$ as well as body forces and surface tractions which may vary both spatially and temporally. Now let it be assumed that the Helmholtz function H, entropy S, heat flux $Q_k$ and stress $S^{ij}$ are functions of strain $\gamma_{ij}$, temperature T, and/or temperature gradient $T_{,k}$ (Ref. 15). Thus,

$$\begin{aligned} H &= H\,(\gamma_{ij},\, T) \\ S &= S\,(\gamma_{ij},\, T) \\ S^{kl} &= S^{kl}(\gamma_{ij},\, T) \\ Q^k &= Q^k(\gamma_{ij},\, T,\, T_{,i}) \end{aligned} \tag{2.60}$$

where

$$H = S = S^{kl} = 0 \qquad \text{when} \quad \gamma_{ij} = 0 \text{ and } T = T_o \tag{2.60a}$$

Then the thermodynamic equation, Eq. 2.59, becomes

$$\left(S^{kl} - \rho_o \frac{\partial H}{\partial \gamma_{kl}}\right)\dot{\gamma}_{kl} - \rho_o\left(S + \frac{\partial H}{\partial T}\right)\dot{T} - \frac{Q^k T_{,k}}{T} \geqslant 0 \tag{2.61}$$

At a given state of $\gamma_{k\ell}$ and T, the quantities $\dot{\gamma}_{k\ell}$ and $\dot{T}$ can be chosen arbitrarily. Hence, it may be concluded that

$$S^{kl} = \rho_o \frac{\partial H}{\partial \gamma_{kl}}\,, \qquad S = -\frac{\partial H}{\partial T} \qquad \text{and} \qquad -Q^k T_{,k} \geqslant 0 \tag{2.62}$$

If the Helmholtz function, H, is specified (for example in terms of $\gamma_{k\ell}$ and T), the general thermal-elastic relation may be derived from Eq. 2.62.

For infinitesimal strain, the elastic relation between stress and strain may be assumed to be linear and is known as Hooke's law. Thus, the Helmholtz function H may be expressed as a quadratic function of $\gamma_{k\ell}$ (cubic and higher order terms are neglected):

$$H = \frac{1}{2} E_1^{ijkl} \gamma_{ij} \gamma_{kl} + E_2^{ij} \gamma_{ij} + E_3 + 0(\gamma_{ij})^3 \tag{2.63}$$

where $E_1^{ijkl}$, $E_2^{ij}$, $E_3$ are functions of T and

$$E_1^{ijkl} = E_1^{klij} = E_1^{jikl} = E_1^{ijlk} , \qquad E_2^{ij} = E_2^{ji} \tag{2.63a}$$

Then, from Eq. 2.62 one may obtain

$$S^{ij} = E_1^{ijkl} \gamma_{kl} + E_2^{ij} \tag{2.64}$$

Let the thermal strain be denoted by $\overset{T}{\gamma}_{ij}$; since it is required that $S^{ij} = 0$ when $\gamma_{ij} = \overset{T}{\gamma}_{ij}$, one has

$$E_2^{ij} = - E_1^{ijkl} \overset{T}{\gamma}_{kl} \tag{2.65}$$

and Eq. 2.64 becomes

$$S^{ij} = E_1^{ijkl} (\gamma_{kl} - \overset{T}{\gamma}_{kl}) \tag{2.66}$$

Equation 2.66 gives the linear thermoelastic stress-strain relation. The thermal strain is treated as an "initial strain" or a prescribed strain which produces no stress. When the material is isotropic both elastically and thermally, one may choose

$$\overset{T}{\gamma}_{kl} = \overset{T}{\gamma} \delta_{kl} \tag{2.67}$$

and (Ref. 17)

$$E_1^{ijkl} = \mu [G^{ik} G^{jl} + G^{il} G^{jk}] + \lambda G^{ij} G^{kl} \tag{2.68}$$

where $\mu$, $\lambda$ are temperature-dependent Lamé constants. Further, if the relation between the thermal strain and temperature is assumed to be

$$d\overset{T}{\gamma} = \alpha(T)\, dT \tag{2.69}$$

it follows that

$$\overset{T}{\gamma} = \int_{T_0}^{T} \alpha(T)\, dT \tag{2.69a}$$

where $\alpha$ is the temperature-dependent thermal expansion coefficient. Then, for an isotropic and homogeneous material, the linear thermoelastic stress-strain relation can be written in the form

$$S^i_j = \frac{E}{1+\nu}\left(\gamma^i_j + \frac{\nu}{1-2\nu}\gamma^m_m \delta^i_j\right) - \frac{E}{1-2\nu}\delta^i_j \int_{T_0}^{T} \alpha \, dT \tag{2.70}$$

where $\nu$ is Poisson's ratio, E is Young's modulus, and $\gamma^i_j$ is defined to be

$$\gamma^i_j = G^{mi}\gamma_{mj} \tag{2.70a}$$

It should be noted that the coupling between thermoelasticity and heat conduction is neglected in the above equations.

### 2.3.2 Thermoelastic-Plastic Material Behavior

There are two types of common plasticity theories, termed "flow" and "deformation". The deformation theory of plasticity assumes that, as in elasticity, there exists a one-to-one correspondence between stress and strain. The flow theory of plasticity states that there is a functional relation between the incremental stress and the incremental strain. Only for proportional loading where the stress ratio remains constant, and for a certain restricted range of loading paths other than proportional loading (Ref. 18) (through the assumption of the possibility of singularity in the yield surface) does the deformation theory agree with the flow theory. In order to include the capability to analyze general loading paths including loading, unloading, and cyclic loading, the "flow-type" theory will be incorporated into the present analysis.

The behavior of a general elastic-plastic material can be characterized by the following two ingredients. First, assume the existence of a boundary (yielding surface) in stress space which defines the elastic domain. Within the boundary the continuum deforms elastically. Only at the boundary, the onset of plastic flow (irreversible deformation in a thermodynamic sense) is possible and no meaning is associated with the region that is beyond the boundary. Second, one employs a flow rule which describes the behavior of the material after yielding has started; it gives the relation of plastic flow (strain increments) to the stress (or stress increment) and the loading history.

Another basic assumption in the theory of an elastic-plastic continuum is the introduction of a plastic strain tensor. The plastic strain tensor, $\gamma^p_{ij}$, is assumed to have the same invariance properties as does the Lagrangian strain tensor, $\gamma_{ij}$. The quantity $\gamma^p_{ij}$ is related to $\gamma_{ij}$ by an elastic strain tensor $\gamma^e_{ij}$, in the form (Ref. 15):

$$\gamma_{ij} = \gamma^p_{ij} + \gamma^e_{ij} \tag{2.71}$$

No kinematic meaning is given to $\gamma^e_{ij}$ and $\gamma^p_{ij}$, but only their sum, $\gamma_{ij}$ as defined by Eq. 2.8 is related to displacement by Eq. 2.9.

The yield surface, $\Phi$, is assumed to be expressible in terms of certain variables and may be expressed as

$$\Phi\left(S^{ij}, \gamma^p_{ij}, T, \kappa\right) = 0 \tag{2.72}$$

where $\kappa$ is a hardening parameter which depends on the strain history. Differentiating Eq. 2.72 with respect to time gives

$$\dot{\Phi} = \frac{\partial \Phi}{\partial S^{ij}}\dot{S}^{ij} + \frac{\partial \Phi}{\partial \gamma^p_{ij}}\dot{\gamma}^p_{ij} + \frac{\partial \Phi}{\partial T}\dot{T} + \frac{\partial \Phi}{\partial \kappa}\dot{\kappa} \tag{2.73}$$

If the conditions (a) $\dot{\Phi} \leq 0$ and $\Phi = 0$ or (b) $\Phi < 0$ are satisfied, the state change can only be elastic (reversible), any plastic deformation (which may have been incurred earlier) remains unchanged. Thus,

$$\begin{array}{llll}
\dot{\gamma}^p_{ij} = \dot{\kappa} = 0 \ \text{when} & \dfrac{\partial \Phi}{\partial S^{ij}}\dot{S}^{ij} + \dfrac{\partial \Phi}{\partial T}\dot{T} < 0 & \text{and} \ \Phi = 0 & \text{(unloading)} \\
\text{or} & \dfrac{\partial \Phi}{\partial S^{ij}}\dot{S}^{ij} + \dfrac{\partial \Phi}{\partial T}\dot{T} = 0 & \text{and} \ \Phi = 0 & \text{(neutral loading)} \\
\text{or} & \Phi < 0 & & \text{(elastic deformation)}
\end{array} \tag{2.74}$$

If it is postulated that the plastic strain rate $\dot{\gamma}^p_{ij}$ is linearly related to $\dot{S}^{ij}$ and $\dot{T}$ and with the consideration that $\dot{\gamma}^p_{ij}$ is zero for a neutral change of loading, the following linear relation may be chosen as a reasonable approximation:

$$\dot{\gamma}^{p}_{ij} = D_{ij}\left[\frac{\partial \Phi}{\partial S^{kl}}\,\dot{S}^{kl} + \frac{\partial \Phi}{\partial T}\,\dot{T}\right] \tag{2.75}$$

when

$$\frac{\partial \Phi}{\partial S^{kl}}\,\dot{S}^{kl} + \frac{\partial \Phi}{\partial T}\,\dot{T} \geq 0 \qquad \text{and} \qquad \Phi = 0 \qquad \text{(loading)}$$

where $D_{ij}$ is a symmetric function of $S^{k\ell}$, T, and the previous strain history, but not of $\dot{S}^{k\ell}$ and $\dot{T}$. This assumption, which is suggested by Ref. 14, is based on the consideration that in a crystal grain, when the stress state is such that the resolved shears along certain slip direction reach the critical value, the plastic-strain increment occurs. Hence, as a statistical average over all grains, a definite macroscopic stress is needed. The stress-increment only determines the magnitude of the plastic-strain increment. Further, the (thermodynamic) Helmholtz function H, entropy S, and heat flux $Q_k$, may be assumed to be functions of $\gamma^e_{k\ell}$, $\gamma^p_{k\ell}$, and T (Ref. 15). Thus,

$$\begin{aligned} H &= H(\gamma^e_{kl}, \gamma^p_{kl}, T) \\ S &= S(\gamma^e_{kl}, \gamma^p_{kl}, T) \\ Q^i &= Q^i(\gamma^e_{kl}, \gamma^p_{kl}, T, T_{,k}) \end{aligned} \tag{2.76}$$

Then, from the thermodynamic equation, Eq. 2.59, one may deduce that

$$\begin{aligned} S^{kl} &= \rho_0 \frac{\partial H}{\partial \gamma^e_{kl}} \\ S &= -\frac{\partial H}{\partial T} \end{aligned} \tag{2.77}$$

If the functions Φ, $D_{ij}$, and H are chosen, Eqs. 2.74 and 2.75 will permit the determination of the plastic strain increment corresponding to the stress increment and temperature increment, and Eq. 2.77 predicts the relation between elastic strain components and the stresses. It should be noted that no restriction is made on the magnitude of the strain and the symmetry of material properties in the above equations. But, for finite strain the assumption that the total strain can be linearly decomposed into elastic and plastic components and the postulate that plastic strain rate is linearly related to stress rate and/or temperature rate requires careful scrutiny, as claimed by Ref. 16, because of the non-Euclidean characteristic of the intermediate stress-free state associated with the plastic flow. However, for infinitesimal strain, these assumptions constitute a satisfactory approximation, since the deformation behavior exhibited by most engineering materials in infinitesimal strain is that the irreversible plastic flow causes no volume change and the reversible elastic strain is small. The specific considerations upon which the functions $\Phi$ and $D_{ij}$ are chosen will be discussed in the following.

In simple tension and/or compression tests of most engineering materials, the uniaxial stress-strain relation indicates the existence of a yield stress (elastic limit), $\sigma_o$, beyond which plastic (permanent) deformation takes place. However, under multiaxial stress (and strain) the behavior is much more complicated. Various yield criteria and flow rules have been proposed for the prediction of the onset of plastic flow and the relation among plastic flow, stress, and stress history. Among them is the Mises-Hencky yield criterion and its associated flow rule which usually fits experimental observations better than the Tresca criterion, for instance, for polycrystalline metals and yet is mathematically simple. The Mises-Hencky rules will be discussed and adopted in the present analysis.

The Mises-Hencky yield criterion may be physically interpreted as "yielding begins whenever the distortion energy equals the distortion energy at yield in simple tension". Thus, hydrostatic pressure, for an isotropic material, (tension or compression) does not affect the yielding, plastic flow, and resultant hardening. Stated otherwise, no plastic work is done by the hydrostatic component of the applied stress. This implies that there is no plastic (or irreversible) change in volume. Thus,

$$\dot{\gamma}^{p}_{ii} = 0 \qquad \text{or} \qquad \dot{\gamma}^{sp}_{ij} = 0 \tag{2.78}$$

where $\dot{\gamma}^{sp}_{ij}$ is the spherical plastic strain-rate tensor. For an initially isotropic material, the Mises-Hencky yield function can be written in the form

$$\Phi = \overset{D}{I}_2 - \frac{1}{3}\sigma_o^2(T) = 0 \tag{2.79}$$

where

$$\overset{D}{I}_2 = \frac{1}{2}\overset{D}{\tau}{}^{i}_{j}\,\overset{D}{\tau}{}^{j}_{i} = \frac{1}{2}\left[\tau^{i}_{j}\tau^{j}_{i} - \frac{1}{3}(\tau^{m}_{m})^2\right] \tag{2.79a}$$

$\overset{D}{\tau}{}^{i}_{j}$ is the deviatoric stress tensor of $\tau^{i}_{j}$ in mixed component form

$\sigma_o(T)$ is the temperature-dependent yield stress in simple tension.

Equation 2.79 represents a hypersurface in nine-dimensional stress space. Any point on this surface represents a point at which yield can begin. Also, it is assumed that the temperature effect changes only the size of the yield surface (through $\sigma_o(T)$) and that the surface will retain the same shape and orientation as in the initial reference temperature state. For moderate hydrostatic pressure and temperature, this is a very close approximation and is found to be in good agreement with experiment for common metals.

Then, from Eq. 2.78, the function $D_{ij}$ in Eq. 2.75 must satisfy the following two necessary conditions: (1) the restriction $D_{ii} = 0$ must be imposed to ensure zero plastic volume change and (2) the principal axes of the plastic strain increment and of $D_{ij}$ must coincide with the principal axes of stress, since the material is isotropic. These two conditions can be satisfied with sufficient generality by choosing

$$D_{ij} = \lambda \frac{\partial \tilde{D}}{\partial S^{ij}} \tag{2.80}$$

where $\lambda$ and $\tilde{D}$ are functions of the deviatoric stress invariant and possibly also of the stress history.

Next, the derivation of the function $\tilde{D}$ will be based on Drucker's postulate (Ref. 19). Drucker's postulate states that "the net work performed by an external agency over a cycle of loading and unloading is nonnegative, positive if the plastic flow has occurred, and zero if there is only change in elastic strain". This postulate leads to the following two requirements on the plastic behavior: (1) the convexity of the yield surface with respect to the origin of the stress space, and (2) the outward normality of the plastic strain increment vector to the yield surface. It is noted that the Mises-Hencky yield function given by Eq. 2.79 satisfies the convexity condition imposed on the yield surface. The second requirement suggests that the function $\widetilde{D}$ may take the same form as $\Phi$; thus,

$$\overset{Dp}{\dot{\gamma}}{}^i_j = \lambda \frac{\partial \Phi}{\partial S^j_i} \left[ \frac{\partial \Phi}{\partial S^{kl}} \dot{S}^{kl} + \frac{\partial \Phi}{\partial T} \dot{T} \right] = \lambda' \frac{\partial \Phi}{\partial S^j_i} \qquad (2.81)$$

where

$\lambda' = \lambda \left( \frac{\partial \Phi}{\partial S^{kl}} \dot{S}^{kl} + \frac{\partial \Phi}{\partial T} \dot{T} \right)$ is a nonnegative scalar quantity

and $\overset{Dp}{\dot{\gamma}}{}^i_j$ is the deviatoric plastic strain rate tensor.

Substituting the Mises-Hencky yield function, Eq. 2.79, into Eq. 2.81 and using Eq. 2.28, one obtains the following flow rule:

$$\overset{Dp}{\dot{\gamma}}{}^i_j = \lambda' \frac{\partial \Phi}{\partial S^j_i} = \lambda' \frac{\partial \Phi}{\partial \tau^k_l} \frac{\partial \tau^k_l}{\partial S^j_i} = \lambda' \frac{g}{G} \overset{D}{S}{}^i_j \qquad (2.82)$$

or

$$\overset{Dp}{\dot{\gamma}}{}^i_j = \widetilde{\lambda} \overset{D}{S}{}^i_j \qquad (2.82a)$$

where

$\widetilde{\lambda} = \lambda'(g/G)$

$\overset{D}{S}{}^i_j$ is the deviatoric stress tensor of $S^i_j$ in mixed component form and is defined to be

$\overset{D}{S}{}^i_j = S^i_j - \frac{1}{3} S^m_m \delta^i_j$

For certain materials, the yield surface will change in case of continued straining beyond the initial yield. The change of the yield surface (called subsequent yield function) that characterizes the work hardening (or strain hardening) behavior of the material depends on the loading history. There are several hardening rules available to describe the subsequent yield function. Among them, the popular ones are "isotropic hardening" and "kinematic hardening".

Isotropic hardening assumes that during subsequent yielding from a plastic state, the yield surface will expand uniformly with respect to the origin in the stress space but will retain the same shape and orientation as it had initially. It does not take into account the Bauschinger effect that is exhibited by many structural materials. Mathematically, the subsequent yield function for an isotropic hardening material can be put in the form:

$$\Phi = \overset{D}{I}_2 - \frac{1}{3}\bar{\sigma}^2 = 0$$

and

$$\bar{\sigma} = \bar{\sigma}\left(\int_0^{\gamma_{ij}^p} dW^p, T\right) \tag{2.83}$$

where $dW^p = s^{ij}\, d\gamma_{ij}^p > 0$ is the irreversible plastic work expended.

To account for the Bauschinger effect, Prager introduced the "kinematic hardening rule" which postulates that during subsequent plastic flow, the yield surface translates (as a rigid body) in the stress space and that it will retain the same size, shape, and orientation that it had initially. Mathematically, this can be expressed as

$$\Phi\,(\tau^{ij} - \alpha^{ij}) = 0 \tag{2.84}$$

where $\alpha^{ij} = \alpha^{ij}(\gamma_{ij}^p)$ which represents the translation of the referenced origin in the stress space of the yield surface and depends on the degree of hardening.

It should be noted that, in the present analysis, the strain-hardening behavior of the material will be accounted for by using the well-known "mechanical sublayer model" (Refs. 20, 21, 22). The feature of this model is the inclusion of kinematic hardening (see Appendix A). In this model, the material at any point is conceived of as consisting of "sublayers"; each sublayer behaves as an elastic, perfectly-plastic medium, having common strain and a common elastic modulus but appropriately different yield stresses. For a perfectly-plastic medium (nonhardening medium), the yield surface remains unchanged in the case of continued straining beyond initial yield.

### 2.3.3 Strain-Rate Effect

For some engineering materials, the uniaxial stress-strain curve of dynamic loading tests will usually be different from those of static tests. The yield stress frequently increases with the increase of strain rate. However, this strain-rate effect arises in a less understood fashion.

The most general form of the uniaxial stress-strain relation including the strain-rate effect may be expressed as (Ref. 23)

$$\dot{\varepsilon} = X\,(\sigma,\ \varepsilon,\ T)\,\dot{\sigma} + Y\,(\sigma,\ \varepsilon,\ T) \tag{2.85}$$

where

$\sigma$ and $\varepsilon$ are the uniaxial stress and strain, respectively

T is temperature

X and Y are functions of state

Under static loading tests, the rate-term may be neglected and one has the static uniaxial stress-strain relation

$$Y\,(\sigma,\ \varepsilon,\ T) = 0 \tag{2.86}$$

One of the simple methods for approximating the strain-rate effect and which is in good agreement with experiment on certain types of common metals and alloys is to assume that the uniaxial stress-strain curve is affected by strain-rate only by a quasi-steady increase in the yield stress above the "static" test yield stress and that the elastic deformation is independent of strain rate. The increase in the yield stress under strain rate may be expressed in the following simple form (Ref. 24):

$$\sigma_y = \sigma_o\ \left[\ 1 + \left|\frac{\dot{\varepsilon}}{D}\right|^{\frac{1}{p}}\ \right]. \tag{2.87}$$

where

$\sigma_o$ is the static yield stress

$\dot{\varepsilon}$ is the uniaxial (or equivalent) strain rate

D and p are empirically-determined constants for the material, which may be temperature dependent

$\sigma_y$ is the yield stress under $\dot{\varepsilon}$

Alternate approximations are discussed, for example, in Refs. 25 and 26. Equation 2.87, however, has been employed with satisfaction in recent years, and is adopted for the purposes of the present study.

## SECTION 3

## GENERAL OUTLINE OF METHOD OF ANALYSIS

### 3.1 Background and Survey of Pertinent Literature

In this investigation, attention is restricted to methods for analyzing dynamic structural response, with principal attention devoted to the transient responses of structures which are subjected to transient external loads such as those arising from gusts, blast, impact, etc.; simple-harmonic vibratory response is of secondary interest. Explicitly excluded from consideration is the "short time" or "early time" response which is often called "material response", and which pertains to the nature, propagation, and effects of intense stress waves in the material as a result of severe impact or impulsive loads (mechanical and/or thermomechanical) applied to the structure; roughly the time span of interest for this type of response is of the order of from 1 to 100 microseconds. Only the "late time" response which is usually termed "structural response" (in contrast with "material response") is discussed here; such responses involve times of interest extending from time zero to 1 millisecond or perhaps to several hundred milliseconds; this type of response pertains to the transient bending and/or stretching behavior of overall structures or of structural components such as beams, rings, plates, shell panels, etc. Furthermore, principal interest in this study centers upon transient structural responses involving both large deformations and elastic-plastic material behavior. Sought is information on both the peak transient responses (deflections, strains, and stresses at any selected point in the structure) together with the time of occurrence of that peak and the permanent deformation condition of the structure after subsidence of the externally-applied transient loading.

Accordingly, it is perhaps useful to review briefly the available analysis methods for various categories of transient structural response problems. Convenient categories are indicated in the following:

| | Deflections | | Material Behavior | |
|---|---|---|---|---|
| Category | Small | Large | Linear Elastic | Elastic-Plastic[+] |
| I | x | | x | |
| II | | x | x | |
| III | x | | | x |
| IV | | x | | x |

Further, it is useful to tabulate, as follows, the principal available transient response analysis methods[++] and to indicate which are applicable to each of the problem categories cited above.

| | Applicable Structural Response Category | | | |
|---|---|---|---|---|
| Transient Response Analysis Method[*] | I (SD-LE) | II (LD-LE) | III (SD-EP) | IV (LD-EP) |
| A. Normal Mode Method (NMM)<br>(Refs. 27-29, for example) | X | | X | |
| B. Assumed Mode Method (AMM) | | | | |
| 1. (Refs. 27, 28) | X | | | |
| 2. (Refs. 30,31) | | X | | |
| 3. (Ref. 31) | | | X | |
| 4. (Ref. 31) | | | | X |
| C. Conventional Lumped Parameter (CLP) | | | | |
| 1. (Refs. 27, 28, 32) | X | | | |
| 2. (Refs. 33, 34) | | X | | |
| 3. (Refs. 33-35) | | | X | |
| 4. (Refs. 33-35) | | | | X |

---

[+] This category includes strain hardening as well as strain-rate dependent and temperature-dependent material behavior.

[++] Some special-purpose less comprehensive methods are included in a separate brief discussion later.

[*] Only typical references in each category are cited; the citation of a complete bibliography is not intended. Also, note that there are many uncited references in each category, for which only static responses are discussed; selected such references are discussed at pertinent places later in the text.

| | Applicable Structural Response Category | | | |
|---|---|---|---|---|
| Transient Response Analysis Method | I<br>(SD-LE) | II<br>(LD-LE) | III<br>(SD-EP) | IV<br>(LD-EP) |
| D. Finite Difference in Space and Time (FD) | | | | |
| 1. (Refs. 2, 3, 36-41) | X | | | |
| 2. (Ref. 42) | | X | | |
| 3. (Same as under D.4) | | | X | |
| 4. (Refs. 3, 43-60) | | | | X |
| E. Forward Integration in Space with Finite Differences in Time | | | | |
| 1. (Refs. 4, 5, 61-62) | X | | | |
| 2. (Ref. 63[+]) | | X | | |
| 3. (No Refs.) | | | ** | |
| 4. (No Refs.) | | | | ** |
| F. Finite Element in Space with Finite Difference in Time (FES-FDT) | | | | |
| 1. (Refs. 64-73) | X | | | |
| 2. (Refs. 74-76) | | X | | |
| 3. (Same as under F.4) | | | X | |
| 4. (Refs. 77-78) | | | | X |
| G. Finite Element in both Space and Time (FES-FET) | | | | |
| 1. (Refs. 12, 79) | X | ** | ** | ** |

In addition one could have various combinations of the above. For example, one often hears speculation (Refs. 80 and 81, for example) concerning combining finite difference and finite element procedures in space to take maximum advantage of the special merits of each method for appropriate parts of the structure (that is, use finite differences for smoothly-varying regions of the structure, and finite elements in regions of structural irregularities such as irregular cutouts, etc.) -- in combination with an appropriate finite-difference

---

[**] Method applicable but not described explicitly in the literature.

[+] Only static problems are discussed.

operator in time. However, a concrete illustration of this approach in the open literature has not been found.

For small-displacement, linear-elastic structural behavior (Category I), the governing equations are linear and hence the use of the normal mode approach together with solution superposition is an applicable and efficient method of solution. Each of the other cited methods (B through G) may also be employed for this problem category but these are often more laborious and less attractive.

When large displacements are encountered but the material behavior is still linear-elastic (Category II), the governing equations become nonlinear. In this case the "normal modes" become amplitude-dependent; thus, the normal mode method of analysis becomes impractical even if one approximates the behavior as being piecewise linear. For such cases, methods B through G may be used.

On the other hand, for problems involving small-displacement, elastic-plastic behavior (Category III), one can legitimately regard the system as retaining its original small-displacement linear-elastic identity insofar as its normal modes are concerned (as identified by the mass and stiffness characteristics of the structure). Plasticity effects may be taken into account as equivalent plastic forces which are amplitude dependent. Hence, the NMM becomes unwieldy since "solution superposition" is destroyed by the essential nonlinear character of this type of problem. Accordingly, methods B, C, D, F, and G are better suited for this Category III type of problem, with methods D and F most widely employed.

Finally, Category IV poses the most severely nonlinear set of conditions -- both geometric nonlinearities and material nonlinearities are present. While methods B, C, D, F, and G are all applicable to this type of problem, only the finite-difference method (FD: method D) has been highly developed for analyzing this type of transient response problem (Refs. 3 and 43-60) -- only Refs. 77 and 78 have reported the use of the finite-element method (FE: method F) for this transient-response-problem category.

The finite-difference method is a very general and powerful method which has undergone more extensive development for each category (I, II, III, and IV) of problems than any of the other methods mentioned -- much literature, not cited here, exists for both static and transient response problems. In the past 15 years, however, the finite-element method has undergone much development for both static and transient response problems, especially those in Category I, with successively lesser developments in categories II, III, and IV.

For the finite-element analysis of static problems in Category II (large-deflection, linear-elastic), Turner et al. (Ref. 82) was the first to report, and many extensions have since been reported. Among these, four general schemes have emerged:

1. The first approach is based on establishing a linearized incremental formulation; the load is applied incrementally. This geometrically nonlinear problem is solved by carrying out a re-evaluation of the element-stiffness matrix at each load stage. This "incremental change" in the stiffness matrix is termed the "geometric stiffness matrix" (Refs. 83-88).
2. Schmit et al. (Ref. 89) has solved the geometrically nonlinear problem by seeking the minimum of the total potential energy function by a direct energy search procedure.
3. In the third approach, the governing equations are solved by an iteration procedure such as the Newton-Raphson technique (Refs. 90, 91).
4. Stricklin et al. (Refs. 92, 93) analyze this geometrically nonlinear problem by treating the large deflection terms as equivalent force terms which are derived from the pertinent energy expression in the variational formulation used; for those special terms, a restricted assumed displacement field is used for the finite-element analysis to avoid certain numerical difficulties. This approach has also been extended to transient problems (see Refs. 75-76); when an implicit finite-difference time operator is used, iterative and/or approximating extrapolative procedures are needed to take those terms into account.

For the finite-element analysis of static problems in category III (small-deflection, elastic-plastic), various investigations have been carried out (for example, Refs. 94-99). Two means for treating material elastic-plastic behavior were employed:

1. The method of initial strain (see Mendelson, Ref. 100). The idea is to modify the load-deflection equations of equilibrium so that the linear-elastic stiffness matrix is employed throughout the elastic-plastic load-deflection range of interest, and plastic effects are taken into account through the use of "effective plastic loading" (Refs. 94-97).

2. The tangent modulus method. This method is based upon the linearity of the incremental laws of plasticity, and deals with this behavior in a piecewise linear fashion (Refs. 98,99).

The relative merits of these two approaches have been discussed by Marcal (Ref. 101).

In Refs. 102 and 103, for example, the finite-element method is discussed for static problems in Category IV (both large-deflections and elastic-plastic behavior). Also in Ref. 104, the finite-element equations of dynamic equilibrium and an increment stiffness equation are derived; however, no transient response predictions are reported. Reference 102 utilizes the initial strain concept for including plastic behavior, while Refs. 103 and 104 employ the tangent modulus approach; in all of these cases, a linearized increment formulation results.

Recently, Salus, Ip, and VanDerlinden (Ref. 77) have described the formulation and application of a finite-element approach for predicting the large-deflection elastic-plastic transient response behavior of beam-type structures. The resulting predictions, for several examples reported, are in good agreement with pertinent finite-difference predictions and experimental results. This formulation is of the assumed displacement type but is not based upon variational principles. Emphasizing the plastic part of the behavior, only linear displacement fields are introduced for all of the displacements, and transverse shear deformation is included. While elastic, perfectly-plastic behavior is taken into account, the effect of transverse shear on yielding and flow appears to be accounted for only in an indirect fashion.

From the preceding brief review of the finite-element literature, it is apparent that only limited finite-element developments have been reported for Category IV transient response problems: involving both geometric nonlinearities (large deflections) and material nonlinearities (elastic-plastic behavior). Accordingly, the present study is devoted to developing, evaluating, and applying a finite-element variational method for analyzing the large-deflection elastic-plastic transient and permanent deformations of simple structures.

Finally, note should be made of a group of simpler but more restrictive methods for estimating transient responses and/or permanent deformations of structures; these include the "rigid-plastic" method and the "energy-absorption" method. In the rigid-plastic method (Refs. 105-116), the elastic deformation behavior is assumed to be negligibly small compared with that arising because of plasticity. Using the concept of plastic hinges, the equations of motion for a structure are derived for various levels of approximation for the kinematics of the system; the deflections may be small or large and the material may be rigid-plastic, rigid-visco-plastic, and/or strain-rate dependent rigid-plastic. Except for small displacements, the governing equations are nonlinear and numerical solution methods must be used. Often with this method one obtains reasonably good estimates of the permanent deformation; however, the transient response is always rather badly in error: the peak deformation is always under-estimated and the time to peak response is invariably too great. For "trends and/or parametric studies" wherein trends rather than accurate values are desired, the rigid-plastic approach is often useful. Various "bound theorems" have been developed (Refs. 117-122) to estimate upper bounds and lower bounds on the deformations of impulsively loaded rigid-plastic and elastic-plastic structures; these form useful supplements to the rigid-plastic analyses.

The "energy absorption" method (Refs. 123-127) is used only to estimate the permanent deformation of the structure; no transient response information is obtained. In the energy-absorption approach, it is assumed that the primary type or pattern of inelastic deformation is known for the structure being analyzed. Also, it is often assumed that the elastic energy stored in the deformed structure is negligible compared with that absorbed by plastic work. Accordingly, the permanent deformation is estimated by equating the plastic work absorbed by the structure in deforming in the prescribed deformation pattern to the total work done on the structure by the externally-applied loads. Thus, for example, if a structure were loaded impulsively, the structure would be given an initial kinetic energy which will, in general, would produce both rigid-body motion and structural deformations. The portion of this kinetic energy which is available to produce structural deformations is then equated to the plastic work absorbed by the structure -- thus providing an estimate of the permanent deformation state of the structure. The success of this method depends upon reasonable a priori estimates of the primary pattern of deformation occurring during the large-deformation response; for complex structures subjected to arbitrary transient external loading, this a priori knowledge is usually lacking. For certain structural configurations and external loadings, however, accumulated experimental evidence is available for making such deformation-pattern estimates. In such cases, very reasonable permanent deformation estimates result; Greenspon (Refs. 124-127) has made very effective use of this excellent and efficient special-purpose approach.

The deficiencies of the rigid-plastic method and the energy absorption method have been overcome by employing numerical methods such as the finite-difference (FDS-FDT) method and the finite-element (FES-FDT) method. The present investigation has as one of the main objectives, the extending of the FES-FDT approach to analyze in an accurate and rigorous manner the large-deformation elastic-plastic transient and permanent deformation of transiently loaded simple structures. The intent is that, if desirable, the techniques developed in this study for simple structures could be extended to analyze more complex structures.

## 3.2 Variational Derivation of the Equations of Motion Utilizing the Finite-Element Approximation

As noted earlier, the finite-element approach is utilized in conjunction with the Principle of Virtual Work and D'Alembert's Principle (in short:

PVW-DAP) integrated over time[+] between times $t_1$ and $t_2$ as in Hamilton's Principle to obtain the equations of motion for a continuum or structure which is permitted to undergo large-deflection elastic-plastic transient deformations. In the present investigation, the assumed displacement form of the finite-element method is employed; when this is applied via PVW-DAP and the usual reductions are carried out, the resulting equations of motion for an undamped system appear in the following conventional form (Refs. 93, 94, 96, 128):

$$[M]\{\ddot{q}^*\} + [K]\{q^*\} = \{F^*\} + \{F_q^{*NL}(q^{*2}, q^{*3})\} + \{F_p^{*L}\} + \{F_p^{*NL}(q^*)\} \tag{3.1}$$

where

| | |
|---|---|
| $q^*(\ddot{q}^*)$ | are the global generalized displacements (accelerations) |
| $[M]$ | is the mass matrix for the complete assembled discretized structure |
| $[K]$ | is the usual stiffness matrix (for linear elastic small displacement behavior) of the complete assembled discretized structure |
| $\{F^*\}$ | is the vector of externally-applied (global denoted by a superscript *) loading |
| $\{F_q^{*NL}(q^{*2}, q^{*3})\}$ | represents a "generalized loads" vector arising from large deflections and is a function of quadratic ($q^{*2}$) and cubic ($q^{*3}$) displacement terms -- a nonlinear force contribution |
| $\{F_p^{*L}\}$ | is a generalized loads vector arising from the presence of plastic and/or thermal strains, and is associated with the linear terms of the strain-displacement relations. |

---

[+] The use of the time integrated variational statement is optional; the use of the PVW-DAP directly is sufficient since it holds at every instant of time.

$\{F^{*NL}_{p}(q^*)\}$ is a generalized loads vector of origin similar to $\{F^{*L}_{p}\}$ but is associated with the nonlinear terms of the strain-displacement relations.

Alternatively, by employing the finite element assumed-displacement approach in conjunction with the PVW-DAP but by carrying out the reduction process differently, a computationally superior set of equations of motion is obtained. These "improved formulation" equations appear in the following form:

$$[M]\{\ddot{q}^*\} + \{P\} + [H]\{q^*\} = \{F^*\} \tag{3.2}$$

where the quantities [M], $\{\ddot{q}^*\}$, $\{q^*\}$, and $\{F^*\}$ retain the meanings given following Eq. 3.1. However, {P} can be shown to represent not only $[K]\{q^*\}$ of Eq. 3.1 but also some plastic behavior contributions. Also the term $[H]\{q^*\}$ represents "generalized loads" arising from both large deflections and plastic (and/or thermal) strains.

It is shown in Subsection 3.3.4 and in Section 5 that the improved formulation represented by Eq. 3.2 is much more efficient for a given solution accuracy than is the conventional (Eq. 3.1) formulation.

The improved formulation and the conventional formulation are developed in detail in Subsections 3.2.1 and 3.2.2, respectively in order to illustrate their similarities and differences.

### 3.2.1 Improved Formulation

In the finite-element-analysis method, the entire domain of the continuum is subdivided into a finite number of regions called "finite elements" or "discrete elements", each having a finite number of "nodes" as control points (see Fig. 3). These nodes are usually located at the boundary of each element but may also be in the interior region of the element. The behavior of the actual continuum which has an infinite number of degrees of freedom is thereby described approximately in terms of a finite number of degrees of freedom at each of the finite number of nodes since the generalized displacements within each finite element is expressed in terms of (a) such variables called "generalized degrees of freedom" which are defined at the node points in conjunction with (b) suitably-selected interpolation functions to describe the distribution of each quantity throughout the interior of each finite element. Applying this approach within the PVW-DAP framework results in a finite-sized system of second-order ordinary differential equations. The unknowns in these equations are the generalized degrees of freedom at each node of the complete assembled discretized structure (or continuum).

Although many different kinds of finite-element models exist (that is, displacement, equilibrium, hybrid, mixed, etc. -- see Ref. 7, for example), the assumed-displacement type of finite-element formulation or model has been chosen for development to analyze the present class of nonlinear transient response problems. A parallel study, of course, could be carried out by using perhaps each of the other types of finite-element models (see Appendix C) -- and the relative merits of each could be assessed; such an undertaking, however, is beyond the intended scope of this study.

In the assumed-displacement-type of finite-element analysis, the generalized displacements constitute the primary variables. Hence, one selects appropriate interpolation functions "anchored to" control-point values which are the nodal generalized displacements. In choosing appropriate interpolation functions for each finite element to be used in the assembled finite-element array, one may take into account the following "sufficient conditions" which will insure that the finite-element solution will converge to the exact solution as the continuum is more and more finely subdivided [129, 130]:

1. Rigid-body modes of an element must be included; otherwise, the equilibrium conditions of the element as a whole will be violated.
2. Uniform strain states must be included; otherwise, it cannot be assured that, as the mesh size is made finer, the strain will converge to the true state of deformation.
3. The admissible conditions of compatibility should be satisfied along the interelement boundaries as well as within the element.

Accordingly, these guidelines are followed in selecting interpolation functions to represent continuous generalized displacements in the interior of each finite element. A detailed description of this selection is given in Section 4 for an arbitrarily-curved beam element.

Let it be assumed that the continuum or structure being analyzed has been subdivided conceptually into N finite elements. Thus, one may write the Principle of Virtual Work combined with D'Alembert's Principle integrated over time from $t_1$ to $t_2$, Eq. 2.52a, as the sum of the contributions from finite elements 1, 2, ... , N as follows:

$$\int_{t_1}^{t_2} \left[ \sum_{n=1}^{N} ( \delta U_n - \delta W_n - \delta K_n ) \right] dt = 0 \qquad (3.3)$$

where variations $\delta$ are permitted only for the displacements, consistent with the displacement constraints for all times[+] except at $t_1$ and $t_2$ and where for any element n:

$$\delta U_n = \iiint_{V_n} S^{ij} \, \delta \gamma_{ij} \, dV_n \qquad (3.3a)$$

$$\delta W_n = \iiint_{V_n} \rho_0 f^{j} \, \delta v_j \, dV_n + \iint_{A_n} \underset{\sim}{T}^{j} \, \delta v_j \, dA_n \qquad (3.3b)$$

$$\delta K_n = \iiint_{V_n} \rho_0 \, \dot{v}^{j} \, \delta \dot{v}_j \, dV_n \qquad (3.3c)$$

---

[+] At times $t_1$ and $t_2$, the configuration of the system is regarded as being known and hence the displacements at times $t_1$ and $t_2$ are not subject to variation.

In Eqs. 3.3 through 3.3c, $V_n$ is the volume of the nth discrete element and $A_n$ is the portion of the surface or boundary area of element n on which the surface traction $T^j$ is prescribed. Both $V_n$ and $A_n$ pertain to the initial undeformed configuration. The summation, $\Sigma$, extends over the "N" elements of the continuum. The other quantities have been defined following Eq. 2.52a.

Let $\{v\}$ represent the displacement field which consists of the components of the displacement vector expressed with respect to the undeformed base vector system of the coordinates $\xi^j$ (see Fig. 1). One chooses for each element an assumed displacement field of the form:

$$\{v\} = [U(\xi^j)]\{\beta\} \tag{3.4}$$

where $[U(\xi^j)]$ is the matrix of appropriately assumed interpolation functions expressed in the coordinates $\xi^j$ of a generic point within the element, and $\{\beta\}$ represents a set of undetermined independent parameters which are functions of time only.

It follows that the nodal generalized degrees of freedom which are the nodal generalized displacements, $\{q\}$, are defined in terms of the local coordinate system of each element and can be obtained by substituting the coordinates of the nodal points into Eq. 3.4. Accordingly, one may obtain

$$\{q\} = [A]\{\beta\} \tag{3.5}$$

If one takes the same number of displacement parameters as the nodal generalized displacements, the transformation matrix [A] is a square matrix. By inverting Eq. 3.5, one has

$$\{\beta\} = [A]^{-1}\{q\} \tag{3.6}$$

and Eq. 3.4 becomes

$$\{v\} = [U(\xi^j)][A]^{-1}\{q\} = [N]\{q\} \tag{3.7}$$

where

$$[N] = [U(\xi^j)][A]^{-1}$$

Because $[U(\xi^j)]$ and $[A]^{-1}$ are a priori chosen functions expressed in the $\xi^j$ coordinate only, they are not subject to variation; hence,

$$\{\delta v\} = [N]\{\delta q\} \tag{3.8}$$

Also, the time derivative of Eq. 3.7 becomes

$$\{\dot{v}\} = [N]\{\dot{q}\} \tag{3.9}$$

By using Eqs. 2.9 and 3.7, one may obtain the corresponding strain $\gamma_{ij}$ at any point in the element as a function of position and the nodal generalized displacements, as follows:

$$\gamma_{ij} = \lfloor D_{ij} \rfloor \{q\} + \frac{1}{2} \lfloor q \rfloor \{D_{ai}\} \lfloor D^a_j \rfloor \{q\} \tag{3.10}$$

It follows that

$$\delta\gamma_{ij} = \lfloor D_{ij} \rfloor \{\delta q\} + \lfloor q \rfloor \{D_{ai}\} \lfloor D^a_j \rfloor \{\delta q\} \tag{3.11}$$

where $D_{ij}$, $D_{ai}$, and $D^a_j$ are the appropriate associated differential operators which include both small and large deflection effects and which may be expressed symbolically in the form*

$$\lfloor D_{ij} \rfloor = \frac{1}{2} \lfloor N_{i,j} + N_{j,i} \rfloor$$

$$\lfloor D_{ai} \rfloor = \lfloor N_{a,i} \rfloor$$

$$\lfloor D^a_j \rfloor = \lfloor N^a_{,j} \rfloor \tag{3.12}$$

Employing Eqs. 3.8 through 3.12, Eq. 3.3 becomes

---

*Explicit examples are given in Section 4.

$$\int_{t_1}^{t_2}\Big[\sum_{n=1}^{N}\lfloor\delta q\rfloor\Big(\iiint_{V_n}\{D_{ij}\}S^{ij}dV_n+\iiint_{V_n}\{D_{ai}\}\lfloor D^{a}_{j}\rfloor S^{ij}dV_n\{q\}$$
$$-\iiint_{V_n}[N]^{T}\rho_0\{\underset{\sim}{f}\}dV_n-\iint_{A_n}[N_B]^{T}\{\underset{\sim}{T}\}dA_n\Big)$$
$$-\sum_{n=1}^{N}\lfloor\delta\dot{q}\rfloor\iiint_{V_n}[N]^{T}\rho_0[N]dV_n\{\dot{q}\}\Big]dt=0$$

(3.13)

where subscript B is used to signify that the [N] are evaluated along the element boundaries.

In more compact form, Eq. 3.13 may be written as

$$\int_{t_1}^{t_2}\Big[\sum_{n=1}^{N}\lfloor\delta q\rfloor\left(\{p\}+[h]\{q\}-\{f\}\right)$$
$$-\sum_{n=1}^{N}\lfloor\delta\dot{q}\rfloor[m]\{\dot{q}\}\Big]dt=0$$

(3.14)

where the following quantities are evaluated for each finite element[+]:

$$\{p\}=\iiint_{V_n}\{D_{ij}\}S^{ij}dV_n \tag{3.14a}$$

$$[h]=\iiint_{V_n}\{D_{ai}\}\lfloor D^{a}_{j}\rfloor S^{ij}dV_n \tag{3.14b}$$

---

[+] The evaluation of $S^{ij}$ is discussed in Subsection 3.3.2.

$$\{f\} = \iiint\limits_{V_n} [N]^T \rho_0 \{\underset{\sim}{f}\}\, dV_n + \iint\limits_{A_n} [N_B]^T \{\underset{\sim}{I}\}\, dA_n \tag{3.14c}$$

$$[m] = \iiint\limits_{V_n} [N]^T \rho_0 [N]\, dV_n \tag{3.14d}$$

Since the element nodal generalized displacements {q} for different elements are not completely independent, hence, a transformation is required to relate the element nodal displacements to a column of independent global (master) displacements for the discrete-element assembly, as follows:

$$\{\underset{\sim}{q}_1, \underset{\sim}{q}_2, \underset{\sim}{q}_3, \cdots, \underset{\sim}{q}_N\} = [J]\{q^*\} \tag{3.15}$$

where $q_n$ are the element generalized coordinates in the local coordinate system, {q*} are the complete set of "master" generalized displacements including all node points of the complete assembled discretized structure, referred to the global coordinate system. The quantity [J] includes the effect of transferring from local coordinates for each individual element to global reference coordinates for the system as a whole. When the coordinate transformation is not required (that is, when the element generalized displacements are already in the same direction as the global generalized displacements), [J] is a simple Boolean matrix.

Performing the indicated transformation, Eq. 3.14 can be written as

$$\int_{t_1}^{t_2} \Big[ \lfloor \delta q^* \rfloor \left( \{P\} + [H]\{q^*\} - \{F^*\} \right) - \lfloor \delta \dot{q}^* \rfloor [M] \{\dot{q}^*\} \Big]\, dt = 0 \tag{3.16}$$

where

$$\{P\} = [J]^T \{\underset{\sim}{p}_1,\ \underset{\sim}{p}_2,\ ----,\ \underset{\sim}{p}_N\} \tag{3.16a}$$

$$[H] = [J]^T \begin{bmatrix} \underset{\sim}{h}_1 & & & \\ & \underset{\sim}{h}_2 & & \\ & & \ddots & \\ & & & \underset{\sim}{h}_n \end{bmatrix} [J] \tag{3.16b}$$

$$\{F^*\} = [J]^T \{\underset{\sim}{f}_1,\ \underset{\sim}{f}_2,\ ----,\ \underset{\sim}{f}_N\} \tag{3.16c}$$

$$[M] = [J]^T \begin{bmatrix} \underset{\sim}{m}_1 & & & \\ & \underset{\sim}{m}_2 & & \\ & & \ddots & \\ & & & \underset{\sim}{m}_N \end{bmatrix} [J] \tag{3.16d}$$

Integrating the last term which appears under the integral sign of Eq. 3.16 by parts and using the fact that the virtual generalized displacements vanish at the two time limits, one obtains:

$$\int_{t_1}^{t_2} \left[ \lfloor \delta q^* \rfloor \left( \{P\} + [H]\{q^*\} - \{F^*\} + [M]\{\ddot{q}^*\} \right) \right] dt = 0 \tag{3.17}$$

Since the virtual global (master) generalized displacements $\{\delta q^*\}$ are independent and arbitrary at each instant of time, the following equation of dynamic equilibrium results from Eq. 3.17:

$$[M]\{\ddot{q}^*\} + \{P\} + [H]\{q^*\} = \{F^*\} \tag{3.18}$$

Given a set of initial conditions $\{q^*\}$, $\{\mathring{q}^*\}$, and $\{F^*\}$ at $t = 0$, and the proper boundary conditions, the system of second-order differential equations represented by Eq. 3.18, may be solved in a step-by-step timewise fashion by using, for example, the finite-difference scheme. Further aspects of the solution process are noted in Subsection 3.3.

Equation 3.18 represents the "improved formulation" form of the equations of dynamic equilibrium.

### 3.2.2 Conventional Formulation

In order to make clear the source of the "apparent differences" between the improved formulation (Eqs. 3.2 or 3.18) and the conventional formulation represented by Eq. 3.1, a parallel derivation of the latter is presented in the following. In fact, the derivations are identical up to and including Eqs. 3.13 and 3.14 through 3.14e. For the conventional assumed-displacement formulation, one proceeds to express the stresses in terms of the displacements via the stress-strain relations and the strain-displacement relations. That is, only the terms represented by Eqs. 3.14a and 3.14b undergo a further reduction by using the following stress-strain relation:

$$S^{ij} = E^{ijkl} \left( \gamma_{kl} - \gamma_{kl}^{p} \right) \tag{3.19}$$

where $\gamma^{p}_{k\ell}$ represents the components of the total plastic strain. Next, expressing the total strain $\gamma_{k\ell}$ in terms of the generalized displacements $\{q\}$ via Eq. 3.10, Eqs. 3.14a and 3.14b may be rewritten as:

$$\begin{aligned} \{p\} &= \iiint\limits_{V_n} \{D_{ij}\} S^{ij} \, dV_n \\ &= \iiint\limits_{V_n} \{D_{ij}\} E^{ijkl} \left( \lfloor D_{kl} \rfloor \{q\} + \tfrac{1}{2} \lfloor q \rfloor \{D_{ak}\} \lfloor D^{a}_{l} \rfloor \{q\} - \gamma^{p}_{kl} \right) dV_n \\ &= [k]\{q\} - \{{}'f^{NL}_{q}\} - \{f^{L}_{p}\} \end{aligned} \tag{3.20a}$$

and (multiplying Eq. 3.14b by $\{q\}$):

$$\begin{aligned} [h]\{q\} &= \iiint\limits_{V_n} \{D_{ai}\} \lfloor D^{a}_{j} \rfloor S^{ij} \, dV_n \{q\} \\ &= \iiint\limits_{V_n} \{D_{ai}\} \lfloor D^{a}_{j} \rfloor E^{ijkl} \left( \lfloor D_{kl} \rfloor \{q\} + \tfrac{1}{2} \lfloor q \rfloor \{D_{ak}\} \lfloor D^{a}_{l} \rfloor \{q\} \right. \\ &\qquad \left. - \gamma^{p}_{kl} \right) dV_n \{q\} \\ &= -\{{}''f^{NL}_{q}\} - \{f^{NL}_{p}\} \end{aligned} \tag{3.20b}$$

where

$$[k] = \iiint\limits_{V_n} \{D_{ij}\} E^{ijkl} \lfloor D_{kl} \rfloor \, dV_n \tag{3.20c}$$

$$\{{}'f^{NL}_{q}\} = -\iiint\limits_{V_n} \{D_{ij}\} E^{ijkl} \left( \frac{1}{2} \lfloor q \rfloor \{D_{ak}\} \lfloor D^{a}_{l} \rfloor \{q\} \right) dV_n \tag{3.20d}$$

$$\{f^{L}_{p}\} = \iiint\limits_{V_n} \{D_{ij}\} E^{ijkl} \gamma^{p}_{kl} \, dV_n \tag{3.20e}$$

$$\{{}''f^{NL}_{q}\} = -\iiint\limits_{V_n} \{D_{ai}\} \lfloor D^{a}_{j} \rfloor E^{ijkl} \left( \lfloor D_{kl} \rfloor \{q\} + \frac{1}{2} \lfloor q \rfloor \{D_{ak}\} \lfloor D^{a}_{l} \rfloor \{q\} \right) dV_n \{q\} \tag{3.20f}$$

$$\{f^{NL}_{p}\} = \iiint\limits_{V_n} \{D_{ai}\} \lfloor D^{a}_{j} \rfloor E^{ijkl} \gamma^{p}_{kl} \, dV_n \{q\} \tag{3.20g}$$

and where superscripts L and NL refer to linear and nonlinear terms, respectively. Also note that the subscript "p" has been applied to $f^{L}_{p}$ and $f^{NL}_{p}$ to denote the presence especially of plastic strain but this can also refer to the presence of other "initial strains" such as thermal strains.

Substituting Eqs. 3.20a and 3.20b into Eq. 3.14, one obtains

$$\int_{t_1}^{t_2} \Big[ \sum_{n=1}^{N} \lfloor \delta q \rfloor \left( [k]\{q\} - \{f^{NL}_{q}\} - \{f^{L}_{p}\} - \{f^{NL}_{p}\} - \{f\} \right) - \sum_{n=1}^{N} \lfloor \delta \dot{q} \rfloor [m] \{\dot{q}\} \Big] dt = 0 \tag{3.21}$$

where {f} and [m] are defined as previously stated, and

$$\begin{aligned}\{f_q^{NL}\} &= \{{}'f_q^{NL}\} + \{{}''f_q^{NL}\} \\ &= -\iiint_{V_n} \{D_{ij}\} E^{ijkl}\left(\frac{1}{2}\lfloor q \rfloor \{D_{ak}\} \lfloor D_l^a \rfloor \{q\}\right) dV_n \\ &\quad -\iiint_{V_n} \{D_{ai}\} \lfloor D_j^a \rfloor E^{ijkl}\left(\lfloor D_{kl} \rfloor \{q\} + \frac{1}{2}\lfloor q \rfloor \{D_{ak}\} \lfloor D_l^a \rfloor \{q\}\right) dV_n \{q\}\end{aligned} \tag{3.22}$$

Then, transforming the element nodal displacements {q} to independent global displacements {q*} of the discrete-element assembly as described previously, Eq. 3.21 can be rewritten as

$$\int_{t_1}^{t_2} \lfloor \delta q^* \rfloor \left([K]\{q^*\} - \{F_q^{*NL}\} - \{F_p^{*L}\} - \{F_p^{*NL}\} - \{F^*\} + [M]\{\ddot{q}^*\}\right) dt = 0 \tag{3.23}$$

where

$$[K] = [J]^T \begin{bmatrix} \underset{\sim}{k}_1 & & & \\ & \underset{\sim}{k}_2 & & \\ & & \ddots & \\ & & & \underset{\sim}{k}_N \end{bmatrix} [J] \tag{3.23a}$$

$$\{F_q^{*NL}\} = [J]^T \{\underset{\sim}{f}_{q1}^{NL}, \underset{\sim}{f}_{q2}^{NL}, \cdots\cdots, \underset{\sim}{f}_{qN}^{NL}\} \tag{3.23b}$$

$$\{F_p^{*L}\} = [J]^T \{\underset{\sim}{f}_{p1}^{L}, \underset{\sim}{f}_{p2}^{L}, \cdots\cdots, \underset{\sim}{f}_{pN}^{L}\} \tag{3.23c}$$

$$\{F_p^{*NL}\} = [J]^T \{\underset{\sim}{f}_{p1}^{NL}, \underset{\sim}{f}_{p2}^{NL}, \cdots\cdots, \underset{\sim}{f}_{pN}^{NL}\} \tag{3.23d}$$

$$\{F^*\} = [J]^T \{\underset{\sim}{f}_1, \underset{\sim}{f}_2, \cdots\cdots, \underset{\sim}{f}_N\} \tag{3.23e}$$

$$[M] = [J]^T \begin{bmatrix} \underset{\sim}{m}_1 & & & \\ & \underset{\sim}{m}_2 & & \\ & & \ddots & \\ & & & \underset{\sim}{m}_N \end{bmatrix} [J] \tag{3.23f}$$

Since the variations $\lfloor \delta q^* \rfloor$ can be independent and arbitrary, the following conventional form of the equilibrium equations is obtained:

$$[M]\{\ddot{q}^*\}+[K]\{q^*\}=\{F^*\}+\{F_q^{*NL}\}+\{F_p^{*L}\}+\{F_p^{*NL}\} \tag{3.24}$$

## 3.3 Timewise Solution of the Governing Equations

In order to obtain the timewise solution of a set of equations of dynamic equilibrium such as Eq. 3.1 or Eq. 3.2, one may resort to analytical techniques or numerical techniques depending upon the mathematical (and/or physical) nature of the problem.

For small-deflection linear-elastic behavior, for example, one may recast these equations into normal mode form and solve the resulting equations of motion analytically, mode by mode if the forcing functions are modally uncoupled or are properly sequentially coupled. Superposition of the forced response of each mode then provides the total response of the system. Alternatively, if desired, one may solve these equations (Eq. 3.1 or 3.2 in their present generalized coordinate form) timewise by using a finite-difference numerical procedure whereby one obtains a recurrence equation which provides a solution step-by-step in finite-time increments.

Of these two methods, if the dynamic system is linear and is subjected to a transient forcing function which excites mainly the lower frequency modes of the system, it is frequently more convenient and efficient to use the normal mode approach. However, if the stiffness matrix (and/or the mass matrix) varies with time as in the present class of nonlinear problems, the normal modes also vary in time; hence, the normal mode approach becomes impractical. In such cases, the direct finite difference approach appears to be the only feasible method developed to date. Accordingly, the numerical finite-difference method is employed in the present study for solving equations of motion like Eq. 3.1 or Eq. 3.2.

In particular, the central-difference finite-difference time operator is employed for purposes of illustrating the solution process for the improved and for the conventional formulation in Subsections 3.3.1 and 3.3.2, respectively.

Then the comparative storage and computing requirements of these two formulations are discussed in Subsection 3.3.3. Next, since a wide variety of timewise finite-difference operators or methods has been developed, a brief discussion of the advantages and disadvantages of some of these methods is given in Subsection 3.3.4 -- leading to the selection of the central-difference method for principal use in the present study.

Finally, it should be noted that a somewhat different approach termed "the finite element method in space and time" has been developed (Refs. 12, 79). In this method, the initial value problem is handled as a boundary value problem with the given initial conditions treated as prescribed boundary conditions. By using a procedure similar to that used in the discretization of only the space domain (as described in previous subsections), the whole domain (both time and space) of interest is discretized into a finite number of discrete domains each having a finite number of nodes. At each node a finite number of degrees of freedom is permitted. Then, suitable interpolation functions, which are both time and space dependent, are selected throughout the interior of each discrete domain. By applying this approach within the framework of the time integrated PVW-D'Alembert variational statement results in a set of simultaneous algebraic equations in the space and time degrees of freedom. Depending upon the type of interpolation function used (especially for the time domain), one may obtain sets of equations corresponding to the use of many of the conventional finite-difference time operators, as well as a variety of other sets of simultaneous algebraic equations. In general, improved convergence and calculation stability will be observed as the entire space and/or time domain is more and more finely subdivided.

### 3.3.1 Solution Process

As indicated earlier, the equations of motion (Eqs. 3.1 or 3.18 and Eq. 3.2 or Eq. 3.24) are to be solved at a sequence of instants in time $\Delta t$ apart by employing the following central-difference finite-difference approximation for the acceleration $\ddot{q}_m$ at any instant $t_m$:

$$\ddot{q}_m = \frac{q_{m+1} - 2\,q_m + q_{m-1}}{(\Delta t)^2} + O(\Delta t)^2$$

(3.25a)

Also, one may approximate the velocity $\dot{q}_m$ at time $t_m$ by

$$\dot{q}_m = \frac{q_{m+1} - q_{m-1}}{2\,(\Delta t)} + O(\Delta t)^2$$

(3.25b)

Now note that at any time instant $t_m$, Eq. 3.24 for the conventional formulation may be written exactly as

$$[M]_m \{\ddot{q}^*\}_m + [K]_m \{q^*\}_m = \{F^*\}_m + \{F_q^{*NL}\}_m + \{F_p^{*L}\}_m + \{F_p^{*NL}\}_m \quad (3.26)$$

All quantities in Eq. 3.26 except [M] and [K] change with time (i.e., $[M] = [M]_1 = \ldots = [M]_m$; $[K] = [K]_1 = \ldots = [K]_m$). Assuming that all quantities in Eq. 3.26 except for $\{\ddot{q}^*\}_m$ are known at time $t_m$, one can solve Eq. 3.26 to obtain $\{\ddot{q}^*\}_m$. Since one has already obtained the solution for $\{q^*\}$ at all earlier time instants (that is, $\{q^*\}_m$, $\{q^*\}_{m-1}$, etc.), one can determine $\{q^*\}_{m+1}$ approximately from Eq. 3.25a as:

$$\{q^*\}_{m+1} \doteq \{\ddot{q}^*\}_m (\Delta t)^2 + 2\,\{q^*\}_m - \{q^*\}_{m-1} \quad (3.27)$$

where all quantities on the right-hand side of Eq. 3.27 are known. Thus, Eq. 3.27 gives an explicit evaluation for the generalized displacements at time $t_{m+1}$ in terms of known information at times $t_m$ and $t_{m-1}$. Accordingly, Eqs. 3.25a and 3.25b are known as explicit finite-difference operators.

Similarly, Eq. 3.24 for the improved formulation may be written at time $t_m$ as

$$[M]\{\ddot{q}^*\}_m + \{P\}_m + [H]_m\{q^*\}_m = \{F^*\}_m \tag{3.28}$$

In Eq. 3.28, all quantities except [M] change, in general, with time. If the solution has been obtained for earlier instants in time, one may compute $\{\ddot{q}^*\}_m$ from Eq. 3.28 and then use Eq. 3.27 to obtain $\{q^*\}_{m+1}$.

Assuming that at $t = 0$, the structure is at a known condition such as $\{q^*\}_o = \{0\}$ and $\{\dot{q}^*\}_o = \{a\}$, one can readily obtain $\{q^*\}_1$ from

$$\{q^*\}_1 = \{q^*\}_0 + \{\dot{q}^*\}_0 \Delta t + \{\ddot{q}^*\}_0 \frac{(\Delta t)^2}{2} + O(\Delta t)^3 \tag{3.29}$$

since $\{F^*\}_o$ is prescribed and all other quantities are known.

In the timewise step-by-step solution procedure involving large-deflection elastic-plastic transient responses via the spatial finite-element procedure described in Subsection 3.2 (from which Eqs. 3.18 and 3.24 resulted), certain quantities in the governing equations change with time and hence must be re-evaluated, in general, at each instant in time. For example, for the improved formulation, Eq. 3.18 or 3.28, it is necessary at time $t_m$ to evaluate $\{p\}_m$ and $[h]_m$ by using Eqs. 3.14a and 3.14b for each finite element -- the "assembly" of this information then provides $\{P\}_m$ and $[H]_m$ via Eqs. 3.16a and 3.16b, respectively. Similarly, for the conventional formulation, one must evaluate $\{f_q^{NL}\}_m$, $\{f_p^L\}_m$, and $\{f_p^{NL}\}_m$ from Eqs. 3.22, 3.20e, and 3.20g, respectively, for each finite element -- the assembly of this information then provides $\{F_q^{*NL}\}_m$, $\{F_p^{*L}\}_m$, and $\{F_p^{*NL}\}_m$ via Eqs. 3.23b, 3.23c, and 3.23d, respectively.

It is seen that the evaluation of $\{p\}_m$, $[h]_m$, $\{f_q^M\}_m$, $\{f_p^L\}_m$, and $\{f_p^{NL}\}_m$ involves volume integrals of certain quantities. For a structure undergoing large-deflection elastic-plastic behavior, it is impractical to evaluate these volume integrals analytically; instead, it is convenient and practical to perform this integration numerically. Among the various numerical integration (or quadrature) methods, Gaussian quadrature (Ref. 131) appears to be the most efficient for a given accuracy. Accordingly, Gaussian quadrature is employed herein -- this requires that the stresses and strains be evaluated at a selected finite number of Gaussian stations or points over the "spanwise" and depthwise region of each finite element.

Another ingredient which is common to both the improved formulation and the conventional formulation is the solution for $\{\ddot{q}^*\}_m$ at each instant of time $t_m$ via Eq. 3.28 and Eq. 3.26, respectively. These equations are of the form:

$$[M]\{x(t)\}_m = \{b(t)\}_m \qquad \text{for} \quad m=0,1,2,3,\cdots \tag{3.30}$$

where

| | |
|---|---|
| $[M]$ | is a known banded positive definite symmetric matrix (the mass matrix for the restrained or unrestrained structure, whichever case is being treated) |
| $\{x(t)\}_m$ | is a vector of unknowns which must be determined by solving Eq. 3.30 |
| $\{b(t)\}_m$ is | is a known vector (representing all terms except $[M]\{\ddot{q}^*\}_m$ in Eq. 3.26 or 3.28) |

In principle, one can always form the inverse matrix $[M]^{-1}$ and pre-multiply Eq. 3.30 by $[M]^{-1}$ to obtain

$$[M]^{-1}[M]\{x(t)\}_m = [M]^{-1}\{b(t)\}_m$$

which results in the solution:

$$\{x(t)\}_m = [M]^{-1}\{b(t)\}_m \tag{3.31}$$

since $[M]^{-1}[M] = [I]$ where $[I]$ is the unit diagonal matrix. However, it has been found that independent of the number of time instants at which one wishes to solve Eq. 3.30 such a procedure is not as efficient as is the Choleski method (Ref. 132).

Briefly, the Choleski method involves factoring the matrix $[M]$ to form a lower triangular matrix $[L]$ and an upper triangular matrix (which is the transpose of the former) such that $[M] = [L][L]^T$ where $[L]^T$ is the transpose of $[L]$. Thus, Eq. 3.30 may be rewritten as

$$[L][L]^T\{x(t)\}_m = \{b(t)\}_m \tag{3.32}$$

Next, form an intermediate matrix $\{y\}_m$ which is defined as

$$\{y\}_m = [L]^T \{x(t)\}_m \tag{3.33}$$

From Eqs. 3.32 and 3.33, it follows that

$$[L]\{y\}_m = \{b(t)\}_m \tag{3.34}$$

At each time instant, one solves Eq. 3.34 for $\{y\}_m$ very readily because [L] is a lower triangular matrix. One then solves Eq. 3.33 for $\{x\}_m$ very rapidly also by algebraic back-substitution.

In Subsections 3.3.1.1 and 3.3.1.2, the principal steps involved in the timewise solution of, respectively, (a) Eq. 3.28 for the improved formulation and (b) Eq. 3.26 for the conventional formulation through the use of the explicit central-difference finite-difference operator (Eqs. 3.25a, 3.25b, and/or 3.25c) are described briefly. This description is intended not only to point out the salient features of the solution but also to make clear the nature and extent of the similarities* and differences* between the improved and the conventional formulation.

#### 3.3.1.1 Improved Formulation

The structure is represented by an assemblage of a finite number of discrete elements (also called finite elements), and the geometric properties of each element are defined so as to approximate the actual geometry of the structure as closely as desired and/or feasible. The mechanical properties of the structural material are assumed to be known as a function of temperatures and strain rate. The structure is assumed to be subjected to externally-applied loads which are prescribed in both space (over the surface and/or throughout the volume of the structure) and time. The equations of motion, Eq. 3.18, to be solved according to the improved formulation are restated here for convenience:

$$[M]\{\ddot{q}^*\} + \{P\} + [H]\{q^*\} = \{F^*\} \tag{3.18}$$

---

*These aspects are then summarized in Subsection 3.3.3.

Starting from a set of given initial conditions at time $t = t_o = 0$ on the generalized displacements ($\{q^*\} = \{0\}$, for example) and the generalized velocities $\{\dot{q}\}_o$, one can solve Eq. 3.28 for $\{\ddot{q}^*\}_o$ at time $t_o$ and then employ Eq. 3.29 to compute $\{q^*\}_1$. A slightly different but similar procedure is then used to advance the solution in successive time increments $\Delta t$. The process involved in using the finite-element method and the present timewise solution procedure follows (see the information flow chart of Fig. 4a):

Step 1: Construct the mass matrix [m] for each finite element and then assemble these contributions according to Eq. 3.23f to form the mass matrix [M] for the complete assembled discretized structure. This [M] represents the "final" mass matrix if the structure has none of its generalized displacements constrained (that is, held equal to zero, for example); however, if such constraints exist, one forms a reduced or constrained mass matrix (and, in fact, a reduced set of the equations of motion) by deleting the rows and columns of [M] associated with those generalized displacements which are prescribed to be zero.

Next, this constrained mass matrix is factorized to consist of a lower triangular matrix [L] and an upper triangular matrix $[L]^T$ according to the Choleski scheme:

$$[M] = [L][L]^T \tag{3.35}$$

Since [M] does not change in value with time as the transient structural response proceeds, one needs to determine [L] and $[L]^T$ only once -- these quantities need not be re-evaluated at each time step of the calculation.

Step 2: The prescribed externally-applied transient forces can be employed to calculate the generalized applied forces {f} acting on each discrete element at each time instant $t_m$ of interest. These, in turn, can be assembled according to Eq. 3.16c to form the assembled applied-loads vector {F*} for the complete assembled discretized structure.

Step 3: Assuming that at zero time ($t = 0$), the generalized displacements $\{q^*\}_o = 0$, the generalized velocities are nonzero $\{\dot{q}^*\}_o = \{a\}$, and that nonzero external forces $\{F^*\}_o$ are present. In this case, Eq. 3.18 becomes

$$[M]\{\ddot{q}^*\}_0 = \{F^*\}_0 \tag{3.36}$$

or

$$[L][L]^T\{\ddot{q}^*\}_0 = \{F^*\}_0 \tag{3.36a}$$

from which one can calculate $\{\ddot{q}^*\}_0$ by using the earlier-described Choleski scheme. Then from Eq. 3.29 one obtains

$$\{\Delta q^*\}_1 = \frac{(\Delta t)^2}{2}\{\ddot{q}^*\}_0 + (\Delta t)\{\dot{q}^*\}_0 \tag{3.37}$$

where

$$\{\Delta q^*\}_1 \equiv \{q^*\}_1 - \{q^*\}_0 \tag{3.38}$$

$$\{\dot{q}^*\}_0 = \{a\}$$ = prescribed initial generalized velocities (3.38a)

Also,

$$\{q^*\}_1 = \{q^*\}_0 + \{\Delta q^*\}_1 \tag{3.39}$$

For this case, however, it has been assumed that $\{q^*\}_0 = \{0\}$. Thus the displacement configuration $\{q^*\}_1$ at time $t_1 = t_0 + \Delta t$ is known.

Step 4: Knowing the generalized nodal displacement increments $\{\Delta q^*\}_1 \equiv \{q^*\}_1 - \{q^*\}_0$ and the generalized nodal displacements $\{q^*\}_1$ at time $t_1$, one knows also the unstarred individual element quantities $\{\Delta q\}_1$ and $\{q\}_1$ via Eq. 3.15. Hence, one can calculate the strain increment $(\Delta\gamma_{ij})_1$ developed from time $t_0$ to $t_1$ at every Gaussian station (or point) required over and depthwise through each finite element from Eq. 3.10:

$$\begin{aligned}(\Delta\gamma_{ij})_1 &= (\gamma_{ij})_1 - (\gamma_{ij})_0 \\ &= \lfloor D_{ij} \rfloor \{\Delta q\}_1 + \lfloor q \rfloor_1 \{D_{ai}\} \lfloor D^a_j \rfloor \{\Delta q\}_1 - \frac{1}{2}\lfloor \Delta q \rfloor_1 \{D_{ai}\} \lfloor D^a_j \rfloor \{\Delta q\}_1\end{aligned} \tag{3.40}$$

With a knowledge of (a) the stresses at $t_o = t_1 - \Delta t$, and (b) the strain increment $(\Delta\gamma_{ij})_1$, one can determine the stress increments $(\Delta S^{ij})_1$ and the stresses $(S^{ij})_1$ at time $t_1$ at each Gaussian station by using the pertinent elastic-plastic stress-strain relations, including the yield condition and flow rule (this matter is discussed in detail in Subsection 3.3.2).

Step 5: Next, one can calculate $\{p\}_1$ and $[h]_1$ for each individual finite element by using Eqs. 3.14a and 3.14b, respectively. Assembly of this information according to Eqs. 3.16a and 3.16b, respectively, provides $\{P\}_1$ and $[H]_1$. Since the prescribed generalized force vector $\{F^*\}_1$ is available from known $\{f\}_1$ information, the equation of motion, Eq. 3.18, at time instant $t_1$ becomes:

$$[M]\{\ddot{q}^*\}_1 = \{F^*\}_1 - \{P\}_1 - [H]_1\{q^*\}_1 \tag{3.41}$$

In the interest of minimizing computer storage and the number of manipulations, one first forms for each individual element $\{b_n\}_1 \equiv (\{f\} - \{p\} - [h]\{q\})_1$. Then one forms the right-hand side vector of Eq. 3.41 by

$$[J]^T\{\underset{\sim}{b}_1, \underset{\sim}{b}_2, \cdots\cdots, \underset{\sim}{b}_N\}_1 \tag{3.42}$$

For clarity of discussion, however, the form of the equation represented by Eq. 3.41 is used here.

Step 6: Since the right-hand side of Eq. 3.41 is now known, one can use the Choleski scheme to solve the following equation for the acceleration $\{\ddot{q}^*\}_1$:

$$[L][L]^T\{\ddot{q}^*\}_1 = (\{F\} - \{P\} - [H]\{q^*\})_1 \tag{3.42a}$$

Step 7: With $\{\ddot{q}^*\}_1$ now known, one can calculate the generalized displacement increment $\{\Delta q^*\}_2$ from Eq. 3.25a as

$$\{\Delta q^*\}_2 = \{\Delta q^*\}_1 + (\Delta t)^2\{\ddot{q}^*\}_1 \tag{3.42b}$$

where

$$\{\Delta q^*\}_2 = \{q^*\}_2 - \{q^*\}_1 \tag{3.43a}$$

$$\{\Delta q^*\}_1 = \{q^*\}_1 - \{q^*\}_0 \tag{3.43b}$$

Thus, from Eq. 3.43a one has

$$\{q^*\}_2 = \{q^*\}_1 + \{\Delta q^*\}_2 \tag{3.44}$$

The process then proceeds cyclically from Step 4 onwards for as many time steps as desired.

For conciseness, the selection of a pertinent time increment size Δt is discussed in Subsection 5.3.

#### 3.3.1.2 Conventional Formulation

For convenience, the equations of motion which are to be solved in the conventional formulation (Eq. 3.24) are repeated here:

$$[M]\{\ddot{q}^*\}+[K]\{q^*\} = \{F^*\} + \{F_q^{*NL}\} + \{F_p^{*L}\} + \{F_p^{*NL}\} \tag{3.24}$$

The solution process for Eq. 3.24 (see Fig. 4b) is very similar to that just described for the improved formulation except for some modifications in Steps 1, 4, 5, and 6. To avoid needless repetition, only these modifications are described here.

Modifications to Step 1: In addition to forming and factoring [M], one must form the stiffness matrix [k] for each element and then assemble this information according to Eq. 3.23a to form [K] for the complete assembled discretized structure. Note that [M] and [K] need to be formed only once -- they do not change as the transient structural response proceeds in time. As in the case of [M], if displacement constraints are present in the problem being analyzed, one must form a "constrained" or "reduced" stiffness matrix for the entire assembled discretized structure.

Modifications to Step 4: In addition to requiring the determination and storage of stress increments and stresses at each Gaussian station, one is required now to determine and store also the plastic strain increments and plastic strains at each Gaussian station at each time instant.

Modifications to Step 5: Because of the presence of large deflections and elastic-plastic effects, one must calculate $\{f_q^{NL}\}_1$, $\{f_p^L\}_1$, and $\{f_p^{NL}\}_1$ for each finite element by performing numerically the volume integrals indicated by Eqs. 3.22, 3.20e, and 3.20g, respectively. The assembly of this information according to Eqs. 3.23b through 3.23d is then accomplished to form $\{F^{*NL}_q\}_1$, $\{F^{*L}_p\}_1$, and $\{F^{*NL}_p\}_1$. Here again the actual operations are done more compactly than this description implies.

Modifications to Step 6: Now at time $t_1$ all information needed to write Eq. 3.24 is available:

$$[L][L]^T\{\ddot{q}^*\}_1 = -[K]\{q^*\}_1 + \left(\{F^*\} + \{F^{*NL}_q\} + \{F^{*L}_p\} + \{F^{*NL}_p\}\right)_1 \tag{3.45}$$

Note that the forming of the right-hand side (RHS) of Eq. 3.45 requires the multiplication of [K] by $\{q^*\}_1$; then this "force vector" is added to the remaining terms of the RHS force vector. Thus one needs to have both [L] and [K] stored for use.

Otherwise the timewise solution process for the conventional formulation proceeds in the same fashion as that described for the improved formulation.

### 3.3.2 Evaluation of Stress Increments, Stresses, Plastic Strain Increments, and Plastic Strains[+]

In the present subsection, the calculation procedure for the determination of stress increments and stresses at any station (such as Gaussian, for example) in each element is described. Because the "mechanical sublayer model"

---

[+] This procedure applies for both the conventional and the improved formulation.

is adopted in the present analysis, the only constitutive relation considered is that for a homogeneous, initially isotropic, elastic, perfectly-plastic strain-rate dependent solid; strain hardening is automatically accommodated by the mechanical sublayer model.

A convenient way to compute the stress component increments and stress components at time $t_{m+1} = (m+1)\ \Delta t$, as discussed in Refs. 46 and 48 will be employed; it is assumed that all stresses and strains are known at time $t_m$. One begins by assuming that the strain increment $(\Delta\gamma_{ij})_{m+1}$, from time $t_m$ to time $t_{m+1}$ as calculated by Eq. 3.40, is entirely elastic, and a trial (overscript T) value of stress increment is calculated from the relation$^+$:

$$(\Delta \overset{T}{S}{}^i_j)_{m+1} = \frac{E}{1+\nu}\left[(\Delta\gamma^i_j)_{m+1} + \frac{\nu}{1-2\nu}(\Delta\gamma^k_k)_{m+1}\delta^i_j\right] \tag{3.46}$$

where

$$\Delta\gamma^i_j = G^{ik}(\Delta\gamma_{jk}) \tag{3.46a}$$

Hence, the trial stresses at time $t_{m+1}$ are given by

$$(\overset{T}{S}{}^i_j)_{m+1} = (S^i_j)_m + (\Delta\overset{T}{S}{}^i_j)_{m+1} \tag{3.47}$$

Then a check process is performed by substituting this trial value of the stress into the Mises-Hencky yield function, Eq. 2.79, to determine whether or not the trial stress state lies inside the yield surface; thus one may write

$$\overset{T}{\Phi}_{m+1} = \frac{g}{G}\left[(\overset{T}{S}{}^i_j)_{m+1}(\overset{T}{S}{}^j_i)_{m+1} - \frac{1}{3}(\overset{T}{S}{}^k_k)^2_{m+1}\right] - \frac{2}{3}\sigma_y^2 \tag{3.48}$$

where $\sigma_y$ is the appropriate known uniaxial yield stress. Also, it should be recalled that the Mises-Hencky yield function is expressed in Eq. 2.68 in terms of $\tau^i_j$ where $\tau^i_j = \sqrt{g/G}\ \ s^i_j$.

If $\overset{T}{\Phi}_{m+1} \leq 0$, the trial stress state lies within the elastic domain bounded by the yield surface. Therefore, for this time step there has been no plastic flow and the incremental deformation can only be elastic. Hence, the actual stress $(s^i_j)_{m+1}$ is equal to the trial stress; thus

$$(S^i_j)_{m+1} = (\overset{T}{S}{}^i_j)_{m+1} \tag{3.49}$$

---

$^+$Such calculations are carried out for each layer of the mechanical sublayer model.

and, the plastic strain state is

$$(\overset{p}{\gamma}{}^i_j)_{m+1} = (\overset{p}{\gamma}{}^i_j)_m \tag{3.50}$$

However, if $\Phi^T_{m+1} > 0$, the trial stress state lies outside the yield surface (i.e., in the undefined region). Therefore, the trial assumption that the entire strain increment in an elastic-strain increment is not valid. Plastic flow has occurred within this time step and the actual stress state must lie on the yield surface according to the theory of perfect plasticity. Then, the calculation proceeds as follows.

The total strain increment can be decomposed into elastic and plastic components

$$(\Delta\gamma^i_j)_{m+1} = (\Delta\overset{e}{\gamma}{}^i_j)_{m+1} + (\Delta\overset{p}{\gamma}{}^i_j)_{m+1} \tag{3.51}$$

The stress increment is related to the elastic component of the strain increment by the relation

$$(\Delta S^i_j)_{m+1} = \frac{E}{1+\nu}\left[\Delta\overset{e}{\gamma}{}^i_j + \frac{\nu}{1-2\nu}\,\Delta\overset{e}{\gamma}{}^k_k\,\delta^i_j\right]_{m+1} \tag{3.52}$$

and the actual stress is

$$(S^i_j)_{m+1} = (S^i_j)_m + (\Delta S^i_j)_{m+1} \tag{3.53}$$

Since the material is assumed to be incompressible with regard to plasticity, it follows that $\Delta\overset{p}{\gamma}{}^k_k = 0$ (or$\Delta\overset{Sp}{\gamma}{}^i_j = 0$: spherical component of the incremental plastic strain). Then from Eq. 3.51 one has

$$(\Delta\overset{e}{\gamma}{}^i_j)_{m+1} = (\Delta\gamma^i_j)_{m+1} - (\Delta\overset{p}{\gamma}{}^i_j)_{m+1} = (\Delta\gamma^i_j)_{m+1} - (\Delta\overset{Dp}{\gamma}{}^i_j)_{m+1} \tag{3.54}$$

and

$$(\Delta\overset{e}{\gamma}{}^k_k)_{m+1} = (\Delta\gamma^k_k)_{m+1} - (\Delta\overset{p}{\gamma}{}^k_k)_{m+1} = (\Delta\gamma^k_k)_{m+1} \tag{3.55}$$

Substituting Eqs. 3.54 and 3.55 into Eq. 3.52, results in

$$(\Delta S^i_j)_{m+1} = \frac{E}{1+\nu}\left[\Delta\gamma^i_j + \frac{\nu}{1-2\nu}\Delta\gamma^k_k\,\delta^i_j - \Delta\overset{Dp}{\gamma}{}^i_j\right]_{m+1} \tag{3.56}$$

where $\Delta\overset{Dp}{\gamma}{}^i_j$ is given, in general, by the plastic flow rule, Eq. 2.82, as

$$\Delta\overset{Dp}{\gamma}{}^i_j = \overset{D}{S}{}^i_j\,\tilde{\lambda} \tag{3.57}$$

where $\tilde{\lambda}$ is a real nonnegative constant which will be calculated later.

The stress $\overset{D}{S}{}^i_j$ determines the direction (or relative proportions) of the plastic strain increment. These directions will vary, over the time interval $\Delta t$ from $(\overset{D}{S}{}^i_j)_m$ to $(\overset{D}{S}{}^i_j)_{m+1}$ as a result of continually straining. However, for computational convenience, the deviatoric component of the trial stress $(\overset{DT}{S}{}^i_j)_{m+1}$ which lies between $(\overset{D}{S}{}^i_j)_m$ and $(\overset{D}{S}{}^i_j)_{m+1}$ will be used to approximate the correct direction.[+] Thus, Eq. 3.56 becomes

$$(\Delta S^i_j)_{m+1} = \frac{E}{1+\nu}\left[\Delta\gamma^i_j + \frac{\nu}{1-2\nu}\Delta\gamma^k_k\,\delta^i_j - \overset{DT}{S}{}^i_j\,\tilde{\lambda}\right]_{m+1} \tag{3.58}$$

Further, combining with Eq. 3.46, one has

$$(\Delta S^i_j)_{m+1} = (\Delta\overset{T}{S}{}^i_j)_{m+1} - (\overset{DT}{S}{}^i_j)_{m+1}\,\lambda^*_{m+1} \tag{3.59}$$

where

$$\lambda^*_{m+1} = \frac{E}{1+\nu}\,\tilde{\lambda}_{m+1}$$

Then, the actual stress at time $t_{m+1}$ is

$$(S^i_j)_{m+1} = (S^i_j)_m + (\Delta S^i_j)_{m+1} = (\overset{T}{S}{}^i_j)_{m+1} - (\overset{DT}{S}{}^i_j)_{m+1}\,\lambda^*_{m+1} \tag{3.60}$$

The plastic strain at time $t_{m+1}$ is given by

$$(\overset{p}{\gamma}{}^i_j)_{m+1} = (\overset{p}{\gamma}{}^i_j)_m + (\Delta\overset{Dp}{\gamma}{}^i_j)_{m+1} = (\overset{p}{\gamma}{}^i_j)_m + (\overset{D}{S}{}^i_j)_{m+1}\,\tilde{\lambda}_{m+1} \tag{3.61}$$

The quantities $\lambda^*_{m+1}$ and $\tilde{\lambda}_{m+1}$ in Eqs. 3.60 and 3.61 can be determined from the fact that $(S^i_j)_{m+1}$ must satisfy the yield condition:

---

[+] Alternate approximations could be used (see Refs. 133 and 134, for example).

$$\Phi_{m+1} = \frac{g}{G}\left[ (S^i_j)_{m+1} (S^j_i)_{m+1} - \frac{1}{3} (S^k_k)^2_{m+1} \right] - \frac{2}{3} \sigma_y^2 = 0 \tag{3.62}$$

Substituting Eq. 3.60 into Eq. 3.62 and solving for $\lambda^*_{m+1}$, one obtains the physically valid value:

$$\lambda^*_{m+1} = \frac{C}{B + \sqrt{B^2 - AC}} \tag{3.63}$$

where

$$A = ({}^{DT}S^i_j)_{m+1} ({}^{DT}S^j_i)_{m+1} - \frac{1}{3} ({}^{DT}S^k_k)^2_{m+1}$$

$$B = ({}^{T}S^i_j)_{m+1} ({}^{DT}S^j_i)_{m+1} - \frac{1}{3} ({}^{T}S^k_k)_{m+1} ({}^{DT}S^k_k)_{m+1}$$

$$C = {}^{T}\Phi_{m+1} \frac{G}{g} = ({}^{T}S^i_j)_{m+1} ({}^{T}S^j_i)_{m+1} - \frac{1}{3} ({}^{T}S^k_k)^2_{m+1} - \frac{2}{3} \frac{G}{g} \sigma_y^2 \tag{3.63a}$$

The preceding discussion has pertained to the use of elastic, perfectly-plastic rate-independent material whose yield stress is $\sigma_y \equiv \sigma_o$. However, if the yield stress is rate dependent, the same procedure applies except that the yield stress $\sigma_y$ in Eq. 3.48 is the strain-rate dependent yield stress which is given approximately by Eq. 2.87 as

$$\sigma_y = \sigma_o \left[ 1 + \left| \frac{\dot{\varepsilon}}{D} \right|^{\frac{1}{p}} \right] \tag{2.87}$$

where $\sigma_o$ is the static uniaxial yield stress, D and p are material constants, and $\dot{\varepsilon}$ is the uniaxial strain rate. For the three-dimensional problem, it is assumed that $\dot{\varepsilon}$ of Eq. 2.87 may be replaced by the second invariant of the deviatoric strain-rate tensor. Thus, this equivalent strain rate is given by

$$\dot{\varepsilon} = \sqrt{\frac{3}{2} \left[ \dot{\gamma}^i_j \dot{\gamma}^j_i - \frac{1}{3} (\dot{\gamma}^k_k)^2 \right]} \tag{3.64}$$

where the strain-rate components $\dot{\gamma}^i_j$ (and/or $\dot{\gamma}^j_i$) are given by $\dot{\gamma}^i_j = (\Delta\gamma^i_j)/(\Delta t)$. Other alternatives for $\dot{\varepsilon}$ have been proposed (see Refs. 46, 133, 134).

It should be noted that in the solution procedure for large-deflection elastic-plastic transient responses, the tracing of the stress history is required for both the conventional formulation, Eq. 3.1, and the improved formation, Eq. 3.2, because of the nature of the elastic-plastic theory used. However, in addition to the stress history, the tracing of the plastic strain history is also required for the conventional formulation but not for the improved formulation. This may result in the saving of computer storage, if the improved formulation is used. Further discussion of this will be given in the next subsection.

### 3.3.3 Comparison of Storage and Computing Requirements for the Improved versus the Conventional Formulation

From the solution process discussed in Subsections 3.3.1 and 3.3.2, it is clear that the storage/computing required are less for the improved formulation (I-method, for short) than for the conventional formulation (C-method). By comparing the conventional formulation, Eq. 3.1, with the improved formulation, Eq. 3.2, it is seen that the storage of both the assembled mass matrix and the assembled stiffness matrix are required by the C-method but only the assembled mass matrix is required by the I-method. Also at each time step, the matrix multiplication $[K]\{q^*\}$ is needed for the C-method but not for the I-method.

Further, as was mentioned before, because the structure undergoes large-deflection elastic-plastic behavior, Gaussian integration is employed to evaluate $\{p\}$ and $[h]$ in the I-method; hence, the storage of the stress history at every Gaussian station in each discrete element is required by the I-method. On the other hand, if the C-method is used and Gaussian integration is also employed to evaluate $\{f_q^{NL}\}$, $\{f_p^{L}\}$ and $\{f_p^{NL}\}$, then, in addition to the storage of the stress history, the storage of the plastic strain history at every Gaussian station in each discrete element is also required. As for the computer operations, at each time step, three matrices $\{f_q^{NL}\}$, and $\{f_p^{L}\}$, and $\{f_p^{NL}\}$ need to be evaluated for each discrete element, if the C-method is used. But only two matrices: $\{p\}$ and $[h]$ (or $\{p\}$ and $[h]\{q\}$) need to be evaluated for each discrete element, if the I-method is employed.

Based on the above storage and operation considerations, it may be concluded that the I-method is more efficient and simpler than the C-method. This conclusion is substantiated by the computing experience discussed in Section 5 for various illustrative examples.

### 3.3.4 Selection of a Temporal Finite-Difference Operator

For the timewise numerical solution of undamped linear dynamic structural problems, many finite-difference operators have been explored to assess their attributes and shortcomings. Some schemes are stable no matter how large the time increment $\Delta t$ is chosen to be -- and hence are termed "unconditionally stable"; others are unstable for $\Delta t$ larger than some critical value -- and thus are termed "conditionally stable". Some introduce (unintentionally) artificial or false damping whereas others do not exhibit this undesirable feature. All of these methods, however, usually* produce a phase-shift error in the predicted response, depending upon the size of the finite $\Delta t$ used -- some schemes exhibit more phase-shift error than others for a given $\Delta t$. A concise tabulation of some features of the more commonly-used varieties of this method is given on the next page (Refs. 132, 135-142) together with some examples of users of each method for linear and/or nonlinear transient response predictions.

The criteria for stability of each of these common methods have been established for linear transient response problems (Refs. 143-151). These studies have derived the $\Delta t$ conditions under which exponential round-off error growth will result. For smaller $\Delta t$ values, this type of error growth will not appear, and a "stable" calculation is said to result. O'Brien et al. [143], Leech et al. [146, 147, 148], Johnson [149], Nickell [150], and Krieg [151] have illustrated this type of analysis and behavior. Nickell's study [150] is especially extensive, treating the 3-point central-difference method, the Newmark $\beta$-method, the Wilson averaging method, and the Gurtin averaging method.

It should be noted (Ref. 48, for example) that one can readily construct m-point forward-difference, central-difference, or backward-difference operators by Taylor series representation of the accelerations $\ddot{x}$ and/or velocities $\dot{x}$

---

[*] An exception has been noted in Ref. 146 wherein the 3-point central-difference formula was used to solve the one-dimensional wave equation. When $\Delta t$ was chosen such that $(\Delta t)/(\Delta x) = 1$, a solution which was exact in both amplitude and phase was obtained.

### SUMMARY OF FINITE-DIFFERENCE OPERATOR FEATURES AS APPLIED TO UNDAMPED LINEAR DYNAMIC SYSTEMS

| Method | Conditionally Stable | Unconditionally Stable | False Damping | Phase Shift Error | Source* | Example Users |
|---|---|---|---|---|---|---|
| | | | IMPLICIT METHODS | | | |
| I1. Houbolt (4-point backward difference) | No | Yes | Yes | Yes | 135 | 36,37,60,76,92,93 |
| I2. Newmark β-Method | | | | | | |
| (a) $\gamma = \frac{1}{2},\ \beta = \frac{1}{4}$ | No | Yes | No | Yes | 136-138 | 71,153,154 |
| (b)$^{+}$ $\gamma = \frac{1}{2},\ 0 \leq \beta < \frac{1}{4}$ | Yes | No | Yes | Yes | 136-138 | 153 |
| I3. Gurtin Averaging | No | Yes | Yes | Yes | 139,140 | 139,140 |
| I4. Wilson Averaging | No | Yes | Yes | Yes | 66,141 | 66,72,141 |
| I5. de Vogelaere | No | Yes | ? | Yes | 142 | 155 |
| | | | EXPLICIT METHODS | | | |
| E1. Central Difference (3-point) | Yes | No | No | Yes | 132 | 43-52,54,55,58,59,<br>73,77, 78, 152 |

---

[*] Identified by references cited in the list of references.

[+] This method reduces to the explicit 3-point central difference method (E1) for $\beta = 0$.

in terms of displacement information at m instants in time; the truncation error of each approximation thus selected may be readily identified, and depends upon the number (m, such as 1, 2, 3, 4, etc.) of time instants used. Further by using the methods of Refs. 143, 145, 148, and/or 150, it can readily be shown that: (1) all forward-difference operators are unconditionally unstable, (2) all central difference operators are conditionally stable (a critical $\Delta t$ exists beyond which error blowup will occur), and (3) all backward-difference operators are unconditionally stable (i.e., stable for all $\Delta t$). The Houbolt method is a four-point implicit backward-difference method (that is, at time n, $\ddot{x}_n$ and $\dot{x}_n$ are expressed in terms of $x_n$, $x_{n-1}$, $x_{n-2}$, and $x_{n-3}$); this method accordingly is unconditionally stable [149]. Note that all of these implicit methods cited in the tabulation on page 70 are unconditionally stable except for type I2(b) -- a version of the Newmark $\beta$-method. Methods I2 through I5 were not constructed from the above-described Taylor's stress approximation -- somewhat different intuitive and/or rational procedures were used.

Note that all of the implicit methods except the $\beta = 1/4$ version of Newmark's $\beta$-method introduce false damping. The latter method and the 3-point central-difference method noted in the tabular summary do not introduce false damping. In Newmark's $\beta$-method, for example, the amount of false damping depends upon the value of $\beta$ used; Newmark suggests (a) choosing $\beta = 1/12$ if one seeks high prediction accuracy for an extended period of response for a structure with small actual damping or (b) choosing $\beta = 1/6$ if one is interested in only a few cycles of response -- the implication being that the error introduced by false damping would be acceptably small for many engineering purposes.

While round-off error instability is avoided by all of the unconditionally stable methods (permitting one to use as large a $\Delta t$ as one wishes), the forcing function in a given problem may have severe spatial and temporal variations such that one must use a fairly small $\Delta t$ in order to follow and identify the severe peaks, etc. in the structural response. Perhaps a $\Delta t$ of some chosen fraction of the period of the highest significantly-excited mode should be used -- provided that one can make a rational estimate of this situation. In such cases, the feature of unconditional stability may not be as much of an advantage over a conditionally stable method as one might think at first sight. However, for transient loadings which excite only the lowest few modes of the structure, the "larger $\Delta t$" permitted by the unconditionally stable methods compared with the "stringently small $\Delta t$" permitted by the 3-point central-difference conditionally stable method can be clearly advantageous.

Although one can construct finite-difference operators of the implicit type or of the explicit type having truncation errors as small as one wishes by using information at time stations (n,n-1, n-2, n-3, ... ) or (n+1, n, n-1, n-2, n-3, ... ), respectively, it is evident that one pays a price in the necessity of storing this information in order to march the solution ahead in time. Further, for large-deflection problems involving elastic-plastic behavior, the use of an explicit operator circumvents the iterative type of calculation (or extrapolation) for the equivalent generalized loads required when an implicit operator is used. These considerations indicate that one should choose an explicit operator whose accuracy vs. storage tradeoff is most beneficial. In view of its simplicity, accuracy, lack of false damping, and minimal storage required, the 3-point explicit central-difference operator has been chosen for principal use in this study; studies to define an "optimum" operator of this type have not been carried out.

Although the criteria for stability of each of these common methods have been established for linear transient response problems (Refs. 143-151), no similar assessment is known to have been made when these methods are applied to nonlinear structural response problems involving large deflections and inelastic material behavior. Various of these methods, however, have been applied to such problems -- with $\Delta t$ values chosen in conformity with the established stability and/or convergence criteria for their use on linear problems, or by numerical experimentation.

It has been demonstrated in the present study that the (a) Houbolt and (b) Newmark ($\beta = 1/4$) method both of which are unconditionally stable for linear structural response problems, now both become conditionally stable for large-deflection nonlinear responses whether the material behavior is linear elastic or elastic-plastic (see Subsection 5.3.2); also the 3-point central-difference method remains conditionally stable but the stability criterion becomes more severe (smaller $\Delta t$ is required) than for linear problems. These results confirm similar findings by Stricklin [75] and McLaughlin [156]. Further discussion of this matter is given in Subsection 5.3.2.

# SECTION 4

## FORMULATION FOR A CURVED BEAM

### 4.1 Introduction

In Section 2, the equations which govern the large-deflection, elastic-plastic dynamic responses of a general 3-dimensional continuum are described. Section 3 presents the overall method of analysis. Based on the Principle of Virtual Work and D'Alembert's Principle, the spatial finite-element approximation has been used to derive the equations of dynamic equilibrium. Then, a direct numerical integration scheme with an appropriate timewise finite-difference approximation is used to solve the resulting equations of motion.

In the present section, the application of this approach is demonstrated in detail for curved beamlike structures which undergo planar (two-dimensional) deformation with or without the inclusion of transverse shear deformation effects. In the structural finite-element context, such configurations are termed "one dimensional".

An arbitrarily-curved beam element is described here. Its specialization to represent simple circular ring and straight beam structural elements is given in Appendix B.

The geometry of a curved-beam element is described in Subsection 4.2. The formulation for a Bernoulli-Euler-type curved beam element is discussed in Subsection 4.3, while Subsection 4.4 is devoted to a corresponding development for a Timoshenko-type (shear deformable) curved beam element. Both small- and large-deflection behavior are included.

### 4.2 Geometry Description for a Curved Beam Element

The geometry and nomenclature of a typical undeformed curved beam element (Refs. 157 and 158) are shown in Fig. 5. The parametric equation of the beam's centroidal axis on the planar surface can be expressed as

$$\bar{r}_c = \bar{r}_c(\eta) = Y(\eta)\,\bar{j} + Z(\eta)\,\bar{k} \tag{4.1}$$

where η is the length coordinate measured from node i along the centroidal axis (meridian) and XYZ represent global reference Cartesian coordinates.

The unit tangent vector, $\bar{a}$, to the centroidal axis, and the unit normal vector, $\bar{n}$, are defined as

$$\bar{a}(\eta) = \frac{d\bar{r}_c}{d\eta} \quad , \quad \bar{n} = -\frac{1}{\mu}\frac{d\bar{a}}{d\eta} = -\frac{d^2\bar{r}_c}{\mu d\eta^2} \tag{4.2}$$

where μ is the magnitude of the curvature vector $d\bar{a}/d\eta$, and the reciprocal of μ is known as the radius of curvature, R, and is taken positive when the center of of curvature lies in the negative direction of $\bar{n}$.

It is assumed that the slope, ϕ, of the centroidal axis, which is the angle between the unit tangent vector and the y-axis of the local reference Cartesian coordinate system (x,y,z) may be approximated with sufficient accuracy by a second-order polynomial in η as follows:

$$\phi(\eta) = b_o + b_1\eta + b_2\eta^2 \tag{4.3}$$

The constants $b_o$, $b_1$, and $b_2$ can be determined from the known initial geometry of the curved-beam element by requiring (1) the slopes of the idealized approximated beam element and the actual beam element to have the same slopes at nodes i and i+1 and (2) the ends to lie on the y-axis (i.e., z = 0 at both ends). Thus

$$\phi(\eta = \eta_i = 0) = \phi_i \tag{4.4}$$

$$\phi(\eta = \eta_{i+1}) = \phi_{i+1} \tag{4.5}$$

$$\int_0^{\eta_{i+1}} \text{SIN}\,\phi\, d\eta = 0 \tag{4.6}$$

If ϕ is small, Eq. 4.6 may be approximated by

$$\int_0^{\eta_{i+1}} \phi\, d\eta = 0 \tag{4.7}$$

Using Eqs. 4.3, 4.4, 4.5, and 4.7, one obtains

$$
\begin{aligned}
b_0 &= \phi_i \\
b_1 &= \frac{-2\,(\phi_{i+1} + 2\,\phi_i)}{\eta_{i+1}} \\
b_2 &= \frac{3\,(\phi_{i+1} + \phi_i)}{\eta^2_{i+1}}
\end{aligned}
\tag{4.8}
$$

Accordingly, the radius of curvature, R, of the centroidal axis may be expressed as $R = \frac{1}{-\frac{d\phi}{d\eta}} = \frac{1}{-(b_1 + 2b_2\eta)}$ .

Consider the beam subjected to 2-dimensional deformation. A generic point p in the beam element is displaced to a new position P. Its new position vector, $\bar{R}$, is given by

$$
\bar{R} = \bar{r} + \bar{v}
\tag{4.9}
$$

where $\bar{r}$ is the position vector to point p, $\bar{v}$ is the displacement vector which is a function of $(\eta,\zeta)$ and $\zeta$ is the distance of point p from the centroidal axis along the unit outward normal, $\bar{n}$, direction. The displacement vector $\bar{v}$ may be written in terms of its components denoted by $\tilde{v}$ and $\tilde{w}$ in the direction of $\bar{a}$ and $\bar{n}$, respectively. Thus

$$
\bar{v} = \tilde{v}\,(\eta,\zeta)\,\bar{a} + \tilde{w}\,(\eta,\zeta)\,\bar{n}
\tag{4.10}
$$

and the displacement $\tilde{v}(\eta,\zeta)$ and $\tilde{w}(\eta,\zeta)$ may generally be expanded in power series of $\zeta$ by

$$
\begin{aligned}
\tilde{v}\,(\eta,\zeta) &= \tilde{v}\,(\eta,0) + \zeta\,\left(\frac{\partial \tilde{v}}{\partial \zeta}\right)_{\zeta=0} + \frac{1}{2}\zeta^2\left(\frac{\partial^2 \tilde{v}}{\partial \zeta^2}\right)_{\zeta=0} + O(\zeta^3) \\
\tilde{w}\,(\eta,\zeta) &= \tilde{w}\,(\eta,0) + \zeta\left(\frac{\partial \tilde{w}}{\partial \zeta}\right)_{\zeta=0} + \frac{1}{2}\zeta^2\left(\frac{\partial^2 \tilde{w}}{\partial \zeta^2}\right)_{\zeta=0} + O(\zeta^3)
\end{aligned}
\tag{4.10a}
$$

## 4.3 The Bernoulli-Euler-Type Curved Beam Element

### 4.3.1 Displacement Field

Let the Bernoulli-Euler hypothesis (Refs. 11 and 159, for example) that the beam cross section which is perpendicular to the centroidal axis prior to the deformation remains plane and perpendicular to the deformed centroidal locus after deformation, and also that it suffers no strain in the direction normal to the centroidal axis be employed. Hence, let the displacement field $\tilde{v},\tilde{w}$ of the beam, Eq. 4.10a, be approximated by the middle plane displacement v and w, and the rotation $\psi$ as follows:

$$\begin{aligned} \tilde{v}(\eta,\zeta) &= v(\eta) - \zeta\,\psi(\eta) \\ \tilde{w}(\eta,\zeta) &= w(\eta) \end{aligned} \tag{4.11}$$

where

$$\psi(\eta) = \frac{\partial w}{\partial \eta} - \frac{v}{R} \tag{4.11a}$$

The selection of a suitable interpolation function to represent each of those displacements throughout each element is one of the principal concerns in the construction of finite-element assemblage of the whole structure. It has been shown in Ref. 160 that the inclusion of rigid-body-displacement modes in the assumed displacement field of a cylindrical-shell element leads to a better coarse mesh solution than if the rigid-body modes are excluded from the assumed-displacement field for the linear-elastic static cylindrical shell problem. Also, it has been concluded in Ref. 161 that the use of a cubic polynomial to express both the axial displacement v and the normal displacement w in the circular ring element exhibits a marked improvement over the use of a linear expression for v and a cubic expression for w; also, the former converges very rapidly to the exact linear elastic static solution. Based on these considerations, two sets of assumed displacement functions for the present Bernoulli-Euler-type curved beam element will be formulated in the present analysis: (1) both v and w will be represented by cubic polynomials in $\eta$ with rigid-body modes included (the finite-element formulation from this expression will be denoted as a CC, or cubic cubic, element) and (2) a linear expression in $\eta$ for v and a cubic expression in $\eta$ for w, also with the rigid body modes taken into account (this is termed the LC, or linear cubic element).

Assuming that the element is subjected to small amplitude rigid-body translations $V_y$ and $V_z$, and rotation $\Omega_x$ with respect to the local reference Cartesian coordinate system (x,y,z), the rigid-body displacement expressed along the curvilinear directions $\bar{n}$, $\bar{a}$ of any point p(y,z) is given by

$$\begin{Bmatrix} v \\ w \end{Bmatrix}_{\text{rigid body}} = \begin{bmatrix} \cos\phi & \sin\phi & -z\cos\phi + y\sin\phi \\ -\sin\phi & \cos\phi & z\sin\phi + y\cos\phi \end{bmatrix} \begin{Bmatrix} V_y \\ V_z \\ \Omega_x \end{Bmatrix} \tag{4.12}$$

To account for the strain-inducing modes and the rigid-body modes, the assumed displacement field for the CC element takes the form (Ref. 160):

$$\begin{Bmatrix} v \\ w \end{Bmatrix} = \begin{bmatrix} \cos\phi & \sin\phi & -z\cos\phi + y\sin\phi & \eta & 0 & 0 & \eta^2 & \eta^3 \\ -\sin\phi & \cos\phi & z\sin\phi + y\cos\phi & 0 & \eta^2 & \eta^3 & 0 & 0 \end{bmatrix} \begin{Bmatrix} \beta_1 \\ \beta_2 \\ \vdots \\ \beta_8 \end{Bmatrix} \tag{4.13}$$

where $\beta_1$, $\beta_2$, ... , $\beta_8$ are parameters which will shortly be expressed in terms of the eight selected generalized displacements of the element. In more compact matrix form, Eq. 4.13 becomes

$$\underset{2\times 1}{\{\underset{\sim}{u}\}} = \underset{2\times 8}{[U(\eta)]} \underset{8\times 1}{\{\beta\}} \tag{4.13a}$$

The generalized displacements, termed {q}, are chosen to characterize the deformation state of the element, and are selected such that there are four degrees of freedom v, w, $\psi$, and $v,_\eta$ (= $\partial v/\partial\eta$) at each node of the element:

$$\{q\} = \lfloor v_i \quad w_i \quad \psi_i \quad v,_{\eta i} \quad v_{i+1} \quad w_{i+1} \quad \psi_{i+1} \quad v,_{\eta i+1} \rfloor^T \tag{4.14}$$

Corresponding to the assumed displacement field, Eq. 4.13, one finds

$$\psi = \frac{\partial w}{\partial\eta} - \frac{v}{R} = \lfloor 0 \quad 0 \quad 1 \quad -\eta/R \quad 2\eta \quad 3\eta^2 \quad -\eta^2/R \quad -\eta^3/R \rfloor \{\beta\} \equiv \lfloor G_\psi \rfloor \{\beta\} \tag{4.15}$$

$$\begin{aligned} v,_\eta = \frac{\partial v}{\partial\eta} &= \left\lfloor \frac{\sin\phi}{R} \quad -\frac{\cos\phi}{R} \quad \frac{\partial(-z\cos\phi + y\sin\phi)}{\partial\eta} \quad 1 \quad 0 \quad 0 \quad 2\eta \quad 3\eta^2 \right\rfloor \{\beta\} \\ &\equiv \lfloor G_{v,_\eta} \rfloor \{\beta\} \end{aligned} \tag{4.16}$$

The generalized nodal displacements, {q}, and the parameters, {β}, of the assumed displacement field are related by a transformation matrix [A] which may be obtained by substituting the coordinates of nodes i and i+1 into Eqs. 4.13, 4.15, and 4.16. Thus

$$\underset{8\times 1}{\{q\}} = \underset{8\times 8}{[A]} \underset{8\times 1}{\{\beta\}} \tag{4.17}$$

Because [A] is a square nonsingular matrix, one may write:

$$\underset{8\times 1}{\{\beta\}} = \underset{8\times 8}{[A]}^{-1}\underset{8\times 1}{\{q\}} \tag{4.18}$$

Substituting Eq. 4.18 into Eq. 4.13, one obtains

$$\underset{2\times 1}{\{u\}} = \underset{2\times 8}{[U(\eta)]}\,\underset{8\times 8}{[A]}^{-1}\underset{8\times 1}{\{q\}} \tag{4.19}$$

Turning now to the LC formulation, the assumed displacement field takes the form

$$\begin{Bmatrix} v \\ w \end{Bmatrix} = \begin{bmatrix} \cos\phi & \sin\phi & -z\cos\phi + y\sin\phi & \eta & 0 & 0 \\ -\sin\phi & \cos\phi & z\sin\phi + y\cos\phi & 0 & \eta^2 & \eta^3 \end{bmatrix} \begin{Bmatrix} \beta_1 \\ \beta_2 \\ \vdots \\ \beta_6 \end{Bmatrix} \tag{4.20}$$

and the generalized nodal displacements now chosen to characterize the deformation state of this LC element are defined to be v, w, and ψ at each end of the element. Thus

$$\underset{6\times 1}{\{q\}} = \lfloor v_i \quad w_i \quad \psi_i \quad v_{i+1} \quad w_{i+1} \quad \psi_{i+1} \rfloor^T = \underset{6\times 6}{[A]}\,\underset{6\times 1}{\{\beta\}} \tag{4.21}$$

It should be noted that by the nature of the assumed displacement finite-element variational principle used, the internal equilibrium equation as well as the force boundary conditions are generally not satisfied everywhere exactly by its solution, although the displacements obtained by this method are usually a very good approximation. The effect of using more displacement modes is to improve the satisfaction of the equilibrium condition in the interior of each individual element and hence also the accuracy of the approximate solution. However, the compatibility of the additional displacement mode, such as $v,_{\eta}$ in Eq. 4.14, with neighboring elements is not necessarily required from the point of view of defining and evaluating the variational argument in Eq. 3.3 because the strain depends only on the first derivative of v with respect to η, as will be seen in the next subsection . For a static problem, the two generalized coordinates $v,_{\eta i}$ and $v,_{\eta i+1}$ of each element may be condensed out through the use of the static condensation process (Ref. 7), but a rational condensation process has not yet been devised for the corresponding dynamic problem. In the present CC-type element, the $v,_{\eta}$ will be treated as an independent generalized coordinate at each node of the finite-element assemblage, and the compatibility of $v,_{\eta}$ between neighboring elements is retained.

In the following, the CC-type assumed displacement field is employed in conjunction with the strain-displacement relations to obtain the equations of dynamic equilibrium from the pertinent variation statement, Eq. 3.3. The finite-element properties and the governing equations for the LC-type assumed displacement field may be derived in a similar manner, except that the corresponding $[U]_{2x6}[A]^{-1}_{6x6}$ matrix should be used. The various matrices which are used symbolically in this section of the text are documented in Appendix B.

### 4.3.2 Strain-Displacement Relations

Under the Bernoulli-Euler hypothesis, the only nonvanishing stress component and corresponding strain component which need be introduced into the appropriate beam theory are the axial stress $\sigma$ and axial strain, $\varepsilon$. Also, let the ratio of thickness to radius of curvature be negligible in comparison with unity. The appropriate nonlinear strain-displacement relation may be expressed as (Refs. 9 and 159):

$$\varepsilon = \varepsilon_o + \zeta \kappa \tag{4.22}$$

where

$$\varepsilon_o = \frac{\partial v}{\partial \eta} + \frac{w}{R} + \frac{1}{2}\left(\frac{\partial w}{\partial \eta} - \frac{v}{R}\right)^2$$

$$\kappa = -\frac{\partial \psi}{\partial \eta} = -\frac{\partial}{\partial \eta}\left(\frac{\partial w}{\partial \eta} - \frac{v}{R}\right) \tag{4.23}$$

or in matrix form:

$$\varepsilon_o = \lfloor \frac{\partial}{\partial \eta} \quad \frac{1}{R} \rfloor \begin{Bmatrix} v \\ w \end{Bmatrix} + \frac{1}{2} \lfloor v \quad w \rfloor \begin{Bmatrix} -\frac{1}{R} \\ \frac{\partial}{\partial \eta} \end{Bmatrix} \lfloor -\frac{1}{R} \quad \frac{\partial}{\partial \eta} \rfloor \begin{Bmatrix} v \\ w \end{Bmatrix}$$

$$\equiv \lfloor B_1 \rfloor \{\underset{\sim}{u}\} + \frac{1}{2} \lfloor \underset{\sim}{u} \rfloor \{B_2\} \lfloor B_2 \rfloor \{\underset{\sim}{u}\}$$

$$\kappa = \lfloor \left(\frac{1}{R}\frac{\partial}{\partial \eta} - \frac{\partial^2 \phi}{\partial \eta^2}\right) \quad -\frac{\partial^2}{\partial \eta^2} \rfloor \begin{Bmatrix} v \\ w \end{Bmatrix} \equiv \lfloor B_3 \rfloor \{\underset{\sim}{u}\} \tag{4.23a}$$

Combining Eq. 4.19 with Eq. 4.23a, one obtains

$$\varepsilon_o = \lfloor D_1 \rfloor \{q\} + \frac{1}{2} \lfloor q \rfloor \{D_2\} \lfloor D_2 \rfloor \{q\}$$
$$K = \lfloor D_3 \rfloor \{q\} \qquad (4.24)$$

where

$$\lfloor D_i \rfloor = \lfloor B_i \rfloor [U(\eta)][A]^{-1} \qquad i = 1, 2, 3$$

In the process of solution, it is necessary to evaluate the strain increment, $\Delta\varepsilon_i$, from time $t_{i-1}$ to time $t_i$. Using Eqs. 3.40 and 4.24, the strain increment is related to both the displacement and the displacement increment by

$$\Delta \varepsilon_i = \Delta \varepsilon_{oi} + \zeta \Delta K_i \qquad (4.25)$$

where

$$\Delta \varepsilon_{oi} = \lfloor D_1 \rfloor \{\Delta q\}_i + \lfloor q \rfloor_i \{D_2\} \lfloor D_2 \rfloor \{\Delta q\}_i - \frac{1}{2} \lfloor \Delta q \rfloor_i \{D_2\} \lfloor D_2 \rfloor \{\Delta q\}_i \qquad (4.25a)$$

$$\Delta K_i = \lfloor D_3 \rfloor \{\Delta q\}_i \qquad (4.25b)$$

In Eq. 4.25a, $\{\Delta q\}_i$ is the generalized nodal displacement increment from time $t_{i-1}$ to $t_i$, which is computed directly from the equation of dynamic equilibrium of the system, $\{q\}_i$ is the generalized nodal displacement at time $t_i$ and is $\{q\}_i = \{q\}_{i-1} + \{\Delta q\}_i$. The last term in Eq. 4.25a is of higher order compared with the other two terms, if the time increment step, $\Delta t$, is small. However, this term can become significant for the case of a sufficiently large time increment step. Its effect will be discussed later in Section 5 in the context of numerical examples.

It should be noted that the only nonlinear term retained in the strain-displacement relations, Eq. 4.23, is due to the rotation of the centroidal axis. This expression for the strain is suitable for the cases where the deflection is large compared with the thickness of the beam, but it is still small compared with the spanwise (longitudinal) dimension of the beam. Otherwise, the following more accurate displacement and strain-displacement relations should be used (Ref. 9):

$$\begin{aligned} \hat{v}(\eta,\zeta) &= v(\eta) - \zeta\,\psi(\eta) \\ \tilde{w}(\eta,\zeta) &= w(\eta) + \zeta\,\chi(\eta) \end{aligned} \tag{4.26}$$

and

$$\varepsilon = \varepsilon_o + \zeta\,\kappa \tag{4.27}$$

where

$$\psi = \frac{\partial w}{\partial \eta} - \frac{v}{R} \quad , \quad \chi = \frac{\partial v}{\partial \eta} + \frac{w}{R}$$

$$\varepsilon_o = \left(\frac{\partial v}{\partial \eta} + \frac{w}{R}\right) + \frac{1}{2}\left(\frac{\partial w}{\partial \eta} - \frac{v}{R}\right)^2 + \frac{1}{2}\left(\frac{\partial v}{\partial \eta} + \frac{w}{R}\right)^2$$

$$\kappa = \left(1 + \frac{\partial v}{\partial \eta} + \frac{w}{R}\right)\left(-\frac{\partial \psi}{\partial \eta} + \frac{\chi}{R}\right) + \left(\frac{\partial w}{\partial \eta} - \frac{v}{R}\right)\left(\frac{\partial \chi}{\partial \eta} + \frac{\psi}{R}\right) \tag{4.27a}$$

However, in the numerical examples carried out in the present analysis, only Eqs. 4.11 and 4.23 are used.

Also, it should be noted that the rigid-body displacements given by Eq. 4.12 are only approximate because of the assumption that the amplitude of the rigid-body rotation $\Omega_x$ is small; this displacement field yields zero strain when applied in the strain-displacement relation given by Eq. 4.23 (or Eq. 4.27) only for small deflections. If the element is subjected to large amplitude rigid-body translations $V_y$, and $V_z$, and rotation $\Omega_x$ with respect to the (x,y,z) coordinate system, then the correct rigid-body displacements expressed along the curvilinear direction $\bar{a},\bar{n}$ of any point p(y,z) would be

$$\begin{Bmatrix} v \\ w \end{Bmatrix} = \begin{bmatrix} \cos\phi & \sin\phi \\ -\sin\phi & \cos\phi \end{bmatrix} \begin{Bmatrix} V_y \\ V_z \end{Bmatrix} + \begin{Bmatrix} A\cos\phi + B\sin\phi \\ -A\sin\phi + B\cos\phi \end{Bmatrix} \tag{4.28}$$

where

$$\begin{aligned} A &= y\cos\Omega_x - z\sin\Omega_x - y \\ B &= y\sin\Omega_x + z\cos\Omega_x - z \end{aligned} \tag{4.28a}$$

These large amplitude rigid-body displacements expressed by Eq. 4.28, will result in the prediction of zero strain when the more accurate strain-displacement relation Eq. 4.27 is used, but not when the approximate strain-displacement relation represented by Eq. 4.23 is applied. However, in the present analysis, the "simplified" strain-displacement relation Eq. 4.23 together with the small amplitude rigid-body displacement modes represented by Eq. 4.12 are employed principally because of the unwieldy nature of the expressions resulting from using Eq. 4.27 together with an assumed displacement field which includes both the proper deformations and the exact rigid-body displacements given by Eq. 4.28.

### 4.3.3 The Discrete-Element Property Matrices

Under the Bernoulli-Euler assumption, the consistent mass matrix of the discrete element including both rotatory and translational inertia effects may be obtained from the expression for the kinetic energy, $K_E$, as follows:

$$\begin{aligned} K_E &= \frac{1}{2} \iiint_{V_n} \rho_o \left( \dot{\tilde{v}}^2 + \dot{\tilde{w}}^2 \right) d V_n \\ &= \frac{1}{2} \iiint_{V_n} \rho_o \left[ \left( \dot{v} - \zeta \dot{\psi} \right)^2 + \dot{w}^2 \right] d V_n \end{aligned} \tag{4.29}$$

or

$$K_E = \frac{1}{2} \int_{\eta_i}^{\eta_{i+1}} \lfloor \dot{v} \quad \dot{w} \quad \dot{\psi} \rfloor [B] \begin{Bmatrix} \dot{v} \\ \dot{w} \\ \dot{\psi} \end{Bmatrix} d\eta \tag{4.29a}$$

where

$$[B] = \begin{bmatrix} \rho_o b h & 0 & 0 \\ 0 & \rho_o b h & 0 \\ 0 & 0 & \frac{\rho_o b h^3}{12} \end{bmatrix} \tag{4.29b}$$

and, b is the width, h is the thickness of the beam, and $\rho_o$ is the mass density per unit volume of the undeformed body.

With the assumption that the velocity field is of a form which is consistent with the displacement function, Eqs. 4.13 and 4.15, one has

$$\begin{Bmatrix} \dot{v} \\ \dot{w} \\ \dot{\psi} \end{Bmatrix} = \begin{bmatrix} U(\eta)_{2\times 8} \\ \hline G_\psi(\eta)_{1\times 8} \end{bmatrix} \{\dot{\beta}\}_{8\times 1} = [N(\eta)]_{3\times 8} \{\dot{q}\}_{8\times 1} \tag{4.30}$$

where

$$\underset{3\times 8}{[N(\eta)]} = \begin{bmatrix} \underset{2\times 8}{U(\eta)} \\ \hline \underset{1\times 8}{G_\psi(\eta)} \end{bmatrix} \underset{8\times 8}{[A]}^{-1} \tag{4.30a}$$

is consistent with Eqs. 4.13, 4.15, and 4.18.

Substituting Eq. 4.30 into Eq. 4.29a, one obtains:

$$K_E = \frac{1}{2} \lfloor \dot{q} \rfloor \int_{\eta_i}^{\eta_{i+1}} [N(\eta)]^T [B] \, [N(\eta)] d\eta \; \{\dot{q}\} \tag{4.31}$$

or

$$K_E = \frac{1}{2} \lfloor \dot{q} \rfloor \; [m] \; \{\dot{q}\} \tag{4.31a}$$

where the consistent mass matrix [m] of the element is

$$[m] = \int_{\eta_i}^{\eta_{i+1}} [N(\eta)]^T [B] [N(\eta)] \; d\eta \tag{4.31b}$$

The element's consistent mass matrix defined by Eq. 4.31b is symmetric and positive definite, and is consistent (in the variational sense) with the assumed displacement field. The resulting equations of motion obtained by using the consistent mass matrix will be a system of simultaneous (coupled) second-order ordinary differential equations. In order to take advantage of potential storage and computing efficiencies, another mass matrix called the lumped (diagonal) mass matrix (Refs. 68, 73, 153, 162, 163) is often used in dynamic analyses; the resulting equations of motion will be a system of de-coupled second-order ordinary differential equations. The lumped element mass matrix of the present beam element can be written as

$$\underset{\text{lumped}}{[m]} = \rho_0 b h \begin{bmatrix} \alpha s & & & & & & & \\ & \alpha s & & & & & 0 & \\ & & \delta s^3 & & & & & \\ & & & \delta s^3 & & & & \\ & & & & \alpha s & & & \\ & 0 & & & & \alpha s & & \\ & & & & & & \delta s^3 & \\ & & & & & & & \delta s^3 \end{bmatrix} \tag{4.32}$$

where $s = \eta_{i+1} - \eta_i$ = element size, $\alpha$ and $\delta$ are constants, and taken to be $\alpha = 1/2$, $\delta = 1/24$ (Ref. 162); other values also have been chosen for the constants $\alpha$ and $\delta$, Ref. 73.However, further studies are needed to develop appropriate lumping for each of the various types of selected criteria such as (a) by frequency matching in which the lumped mass properties are chosen such that the lumped-mass system and the consistent-mass system have the same highest natural frequency (Ref. 73); (b) by statically-equivalent considerations wherein the lumped mass properties are chosen to be statically equivalent to the actual mass distribution (Refs. 68, 153, 162, and 163), etc. Also, some very useful information for this type of analysis is described in Ref. 190 in which the rates of convergence of the mode shapes and frequencies by the finite-element method using consistent- and lumped-mass formulations are established.

The equivalent generalized nodal forces which correspond to or represent the externally-applied loading can be obtained by placing the assumed displacement field into the expression for the variation of the work of the externally-applied loading:

$$\delta W = \int_{\eta_i}^{\eta_{i+1}} \left( F_v(t)\,\delta v + F_w(t)\,\delta w + \underset{\sim}{M}(t)\,\delta \Psi \right) d\eta \tag{4.33}$$

where

$\bar{F}(t) = F_v(t)\bar{a} + F_w(t)\bar{n}$ is the applied time varying force per unit length

$\bar{M}(t) = \underset{\sim}{M}(t)\bar{i}$ is the applied time-varying moment per unit length.

Substituting the assumed displacement function, Eqs. 4.13, 4.15, and 4.18 into Eq. 4.33

$$\begin{aligned} \delta W &= \lfloor \delta q \rfloor \int_{\eta_i}^{\eta_{i+1}} [N(\eta)]^T \begin{Bmatrix} F_v \\ F_w \\ \underset{\sim}{M} \end{Bmatrix} d\eta \\ &\equiv \lfloor \delta q \rfloor \; \{f\} \end{aligned} \tag{4.34}$$

where

$$\{f\} = \int_{\eta_i}^{\eta_{i+1}} [N(\eta)]^T \begin{Bmatrix} F_v \\ F_w \\ \underset{\sim}{M} \end{Bmatrix} d\eta = \text{generalized nodal force matrix for the element} \tag{4.34a}$$

The equivalent nodal force which corresponds to the internal axial stress, $\sigma$, also can be obtained by placing the assumed displacement field into the expression of the variation of the work of the axial stress:

$$\delta U = \iiint_{V_n} \sigma \delta \varepsilon \, d V = \iiint_{V_n} \sigma ( \delta \varepsilon_0 + \zeta \delta \kappa ) \, d V_n \tag{4.35}$$

Substituting Eq. 4.24 into Eq. 4.35 and introducing the stress resultants for the beam cross section

$$L = \iint_A \sigma \, d A \quad , \quad M = \iint_A \sigma \zeta \, d A \tag{4.36}$$

where the integrations being taken over the cross section, A, of the beam element, L, is the internal force, and M is the internal bending moment of the cross section, results in

$$\begin{aligned} \delta U &= \lfloor \delta q \rfloor \Big[ \int_{\eta_i}^{\eta_{i+1}} ( \{D_1\} L + \{D_3\} M ) d\eta + \int_{\eta_i}^{\eta_{i+1}} ( \{D_2\} \lfloor D_2 \rfloor L \, d\eta \, \{q\} \Big] \\ &\equiv \lfloor \delta q \rfloor ( \{p\} + [h] \{q\} ) \end{aligned} \tag{4.37}$$

where

$$\begin{aligned} \{p\} &= \int_{\eta_i}^{\eta_{i+1}} ( \{D_1\} L + \{D_3\} M ) \, d\eta \\ [h] &= \int_{\eta_i}^{\eta_{i+1}} ( \{D_2\} \lfloor D_2 \rfloor L ) \, d\eta \end{aligned} \tag{4.37a}$$

The integrations along the centroidal axis length of the beam element which appear in {p} and [h] of Eq. 4.37a may be performed numerically, for example, by using the Gaussian quadrature scheme (see Ref. 131). The axial force L and moment M at those spanwise integration stations will be described and evaluated in the next subsection. Note that {p} and [h] are quantities pertinent to the improved formulation.

In the conventional formulation, the variation of the work of the axial stress, δU, is expressed in terms of displacements, and the plasticity effects are taken into account through the use of "effective plastic loading". This formulation will be described in the following:

By substituting the relation

$$\sigma = E(\varepsilon - \varepsilon^{p}) = E(\varepsilon_0 + \zeta \kappa - \varepsilon^{p}) \tag{4.38}$$

into Eq. 4.35 one has

$$\delta U = \iiint_{V_n} E(\varepsilon_0 + \zeta \kappa - \varepsilon^{p})(\delta \varepsilon_0 + \zeta \delta \kappa)\, dV_n \tag{4.39}$$

Employing the strain-displacement relation, Eq. 4.24, Eq. 4.39 becomes

$$\begin{aligned}
\delta U = {} & \lfloor \delta q \rfloor \int_{\eta_i}^{\eta_{i+1}} \left( \{D_1\} E b h \lfloor D_1 \rfloor + \{D_3\} \frac{E b h^3}{12} \lfloor D_3 \rfloor \right) d\eta \, \{q\} \\
& + \lfloor \delta q \rfloor \left\langle \iint_A \int_{\eta_i}^{\eta_{i+1}} - E \varepsilon^{p} (\{D_1\} + \zeta \{D_3\})\, dV_n + \iint_A \int_{\eta_i}^{\eta_{i+1}} - E \varepsilon^{p} \{D_2\} \lfloor D_2 \rfloor \, dV_n \{q\} \right\rangle \\
& + \lfloor \delta q \rfloor \left\langle \int_{\eta_i}^{\eta_{i+1}} E b h \left( \tfrac{1}{2} \lfloor q \rfloor \{D_2\} \lfloor D_2 \rfloor \{q\} \right) \{D_1\}\, d\eta \right. \\
& \qquad \left. + \int_{\eta_i}^{\eta_{i+1}} E b h \left( \lfloor D_1 \rfloor \{q\} + \tfrac{1}{2} \lfloor q \rfloor \{D_2\} \lfloor D_2 \rfloor \{q\} \right) \{D_2\} \lfloor D_2 \rfloor \, d\eta \{q\} \right\rangle \\
\equiv {} & \lfloor \delta q \rfloor \left( [k]\{q\} - \{f_p^{L}\} - \{f_p^{NL}\} - \{f_q^{NL}\} \right)
\end{aligned} \tag{4.40}$$

where

$$[k] = \int_{\eta_i}^{\eta_{i+1}} \left( \{D_1\} E b h \lfloor D_1 \rfloor + \{D_3\} \frac{E b h^3}{12} \lfloor D_3 \rfloor \right) d\eta \tag{4.40a}$$

$$\{f_p^{L}\} = \iint_A \int_{\eta_i}^{\eta_{i+1}} \left( E \varepsilon^{p} \{D_1\} + \zeta E \varepsilon^{p} \{D_3\} \right) dV_n \tag{4.40b}$$

$$\{f_p^{NL}\} = \iint_A \int_{\eta_i}^{\eta_{i+1}} E \varepsilon^{p} \{D_2\} \lfloor D_2 \rfloor \, dV_n \{q\} \tag{4.40c}$$

$$\{f_q^{NL}\} = -\Big\langle \int_{\eta_i}^{\eta_{i+1}} E\,b\,h\,\left(\tfrac{1}{2}\lfloor q\rfloor\{D_2\}\lfloor D_2\rfloor\{q\}\right)\{D_1\}\,d\eta + \int_{\eta_i}^{\eta_{i+1}} E\,b\,h\left(\lfloor D_1\rfloor\{q\} + \tfrac{1}{2}\lfloor q\rfloor\{D_2\}\lfloor D_2\rfloor\{q\}\right)\{D_2\}\lfloor D_2\rfloor\,d\eta\,\{q\}\Big\rangle \qquad (4.40d)$$

In Eqs. 4.40b and 4.40c, $\varepsilon^P$ is the total plastic strain at the end of the ith time step. Thus

$$\varepsilon_i^p = \sum_{m=1}^{i-1} \Delta\varepsilon_m^p + \Delta\varepsilon_i^p \qquad (4.41)$$

and the integrations along the length of the beam element are also performed numerically. The plastic strain increment, $\Delta\,\varepsilon_i^P$, and the integration of the total plastic strain $\varepsilon_i^P$ over the cross section, A, of the beam at those spanwise integration stations will be described next.

### 4.3.4 Stress-Strain Relations

Because of nonlinear material behavior, although the strain variation through the beam thickness, by the Bernoulli-Euler hypothesis, is linear, the variation of stress across the thickness may be nonlinear. For computational convenience, the stresses are evaluated at selected Gaussian points across the thickness, and the corresponding weighting factors are used in evaluating the pertinent integrals by Gaussian quadrature. The strain-hardening behavior of the material may be accounted for by using the mechanical sublayer model in which the material at each Gaussian station is treated as consisting of equally-strained sublayers of elastic, perfectly-plastic material, with each sublayer having the same elastic modulus but an appropriately different yield stress, as described in Appendix A.

It should be noted that within the framework of the Bernoulli-Euler beam theory, although the transverse shear strain $\gamma$ is zero, the transverse shear stress $\tau$, is nonzero. With the presence of both axial stress $\sigma$, and transverse shear stress $\tau$, the Mises-Hencky yield function may be written as

$$\Phi = \sigma^2 + 3\tau^2 - \sigma_{ok}^2 = 0 \qquad (4.42)$$

where $\sigma_{ok}$ is the yield stress of the idealized elastic, perfectly-plastic kth sublayer in the uniaxial-tension engineering stress-strain diagram (see

Appendix A). The process presented in Subsection 3.3.2 of calculating stresses and plastic strains will not function properly, if the yield function (Eq. 4.42) is used. (Because in that process, the transverse shear stress $\tau$, should be evaluated from a trial value of $\tau$ by assuming that the $\Delta\tau$ arises from wholly-elastic behavior of $\Delta\gamma$, but $\Delta\gamma$ is always zero and hence $\tau$ is also zero). To avoid an unduly complicated analysis, and still achieve good accuracy, and also because the transverse shear stress, $\tau$, often may be small compared with the axial stress $\sigma$, (Ref. 20), the following yield function is adopted for the present Bernoulli-Euler-type beam

$$\Phi = \sigma^2 - \sigma_{ok}^2 = 0 \tag{4.43}$$

However, the yield function (Eq. 4.42) is used for the Timoshenko-type beam where both the axial and transverse shear stresses and strains are taken into account; this will be described in the next subsection.

An illustration of the method of computing the axial stress and/or plastic strain increment is presented as follows. One begins by knowing the sublayer stress $\sigma_{jk,i-1}$ at time $t_{i-1}$ for the kth sublayer of the jth depthwise Gaussian station, and the strain increment $\Delta\varepsilon_{j,i}$ at station j at time $t_i$ (that is, the strain increment from time $t_{i-1}$ to time $t_i$). One then takes a trial value (superscript T) of $\sigma_{jk,i}$ which is computed by assuming an elastic path[+]:

$$\sigma_{jk,i}^{T} = \sigma_{jk,i-1} + E\,\Delta\varepsilon_{j,i} \tag{4.44}$$

A check is then performed to see what the correct value of $\sigma_{jk,i}$ must be.

$$\begin{array}{llllll}
\text{If} & -\sigma_{ok} \leq \sigma_{jk,i}^{T} \leq \sigma_{ok} & \text{then} & \sigma_{jk,i} = \sigma_{jk,i}^{T} & \text{and} & \Delta\varepsilon_{jk,i}^{p} = 0 \\
\text{If} & \sigma_{jk,i}^{T} > \sigma_{ok} & \text{then} & \sigma_{jk,i} = \sigma_{ok} & \text{and} & \Delta\varepsilon_{jk,i}^{p} = \dfrac{\sigma_{jk,i}^{T} - \sigma_{ok}}{E} \\
\text{If} & \sigma_{jk,i}^{T} < -\sigma_{ok} & \text{then} & \sigma_{jk,i} = -\sigma_{ok} & \text{and} & \Delta\varepsilon_{jk,i}^{p} = \dfrac{\sigma_{jk,i}^{T} + \sigma_{ok}}{E}
\end{array} \tag{4.45}$$

where E is Young's modulus.

This procedure is applied to all sublayers of each Gaussian station j;

---

[+] It should be noted that the subscripts in quantities such as $\sigma_{jk,i-1}$, for example, represent only identifying labels, not tensor notation as used heretofore.

having done this, the axial force and moment of the beam cross section can be determined by

$$\begin{aligned} L &= \iint_A \sigma \, dA \doteq b \frac{h}{2} \sum_j \Big( \sum_k \sigma_{jk} A_{jk} \Big) \\ M &= \iint_A \sigma \zeta \, dA \doteq b \frac{h}{2} \sum_j \zeta_j \Big( \sum_k \sigma_{jk} A_{jk} \Big) \end{aligned} \tag{4.46}$$

In a similar manner the integration of the plastic strain over the cross section of the beam element can be determined by

$$\begin{aligned} &\iint_A \varepsilon^p \, dA \doteq b \frac{h}{2} \sum_j \Big( \sum_k \varepsilon^p_{jk} A_{jk} \Big) \\ &\iint_A \zeta \varepsilon^p \, dA \doteq b \frac{h}{2} \sum_j \zeta_j \Big( \sum_k \varepsilon^p_{jk} A_{jk} \Big) \end{aligned} \tag{4.47}$$

where b is the width and h is the thickness of the beam and $A_{jk}$ is a combination of the mechanical sublayer weighting factor and the Gaussian weighting factor $W_j$, which is defined by

$$A_{jk} = \frac{W_j}{E} \left( E_k - E_{k+1} \right) \tag{4.48}$$

In Eq. 4.48, $W_j$ is the Gaussian weighting factor (Ref. 131) and

$$E_k = \frac{\sigma_k - \sigma_{k-1}}{\varepsilon_k - \varepsilon_{k-1}} \tag{4.49}$$

is the kth slope of the polygonal approximate stress-strain diagram. It can be verified that the relations

$$\Big( \sum_k A_{jk} \Big) / W_j = 1 \qquad \text{and} \qquad W_j \sigma_j = \sum_k A_{jk} \sigma_{jk}$$

are satisfied.

If desired, the sublayer yield stresses may be treated as strain-rate dependent. Since the strain increment at the jth Gaussian station and hence the strain rate is known at this stage of computation, then the rate-dependent yield stress $\sigma_{yk}$ of this kth sublayer at station j is

$$\sigma_{yk} = \sigma_{ok} \left[ 1 + \left| \frac{\Delta\varepsilon / \Delta t}{D} \right|^{\frac{1}{p}} \right] \tag{4.50}$$

where D and p are empirically-determined constants for the material and may, in general, be different for each sublayer.

$\sigma_{ok}$ is the static uniaxial yield stress of the kth sublayer at any jth Gaussian station

## 4.4 The Timoshenko-Type Curved Beam Element

### 4.4.1 Displacement Field

In the previous subsection, the derivation of the beam element properties is based on the Bernoulli-Euler hypothesis in which the transverse shear deformation is assumed to be zero. In the present subsection, the formulation for a general curved beam element with nonzero transverse shear deformation taken into account (termed a Timoshenko-type beam element) will be presented. However, the following assumptions (Ref. 159) are used: plane cross sections perpendicular to the undeformed centroidal axis remain plane and suffer no strain in their plane, although they no longer remain perpendicular to the deformed centroidal axis.

With these assumptions, the displacement field, including transverse shear deformation of the beam may be specified by the middle plane displacements and cross-section rotation, as follows:

$$\tilde{v}(\eta,\zeta) = v(\eta) + \zeta\,\theta(\eta)$$
$$\tilde{w}(\eta,\zeta) = w(\eta) \tag{4.51}$$

where $v(\eta)$ = axial displacement of the middle plane
$w(\eta)$ = transverse displacement
$\theta(\eta)$ = rotation of the plane cross section about the x axis
$\zeta$ = normal distance from the centroidal axis (middle plane)

### 4.4.2 Strain-Displacement Relations

Neglecting the variation of the transverse shear strain across the thickness of the beam, the expression for the engineering components of the strain distribution may be written as

$$\varepsilon(\eta,\zeta) = \varepsilon_o(\eta) + \zeta\,\kappa(\eta)$$
$$\gamma(\eta,\zeta) = \gamma_o(\eta) \tag{4.52}$$

where $\varepsilon_o$ is the middle-plane axial strain
$\kappa$ is the curvature change
$\gamma_o$ is the transverse shear strain

The strain-displacement relations of the curved-beam element may be expressed as

$$\begin{aligned}
\varepsilon_o &= \frac{\partial v}{\partial \eta} + \frac{w}{R} + \frac{1}{2}\left(\frac{\partial w}{\partial \eta} - \frac{v}{R}\right)^2 \\
K &= \frac{\partial \theta}{\partial \eta} \\
\gamma_o &= \left(\frac{\partial w}{\partial \eta} - \frac{v}{R}\right) + \theta
\end{aligned} \tag{4.53}$$

In this equation also, the only nonlinear term retained is due to the rotation of the centroidal axis about the x axis. Equation 4.53 may be expressed in matrix form as

$$\begin{aligned}
\varepsilon_o &= \lfloor \tfrac{\partial}{\partial \eta} \quad \tfrac{1}{R} \quad 0 \rfloor \begin{Bmatrix} v \\ w \\ \theta \end{Bmatrix} + \frac{1}{2} \lfloor v \quad w \quad \theta \rfloor \begin{Bmatrix} -\frac{1}{R} \\ \frac{\partial}{\partial \eta} \\ 0 \end{Bmatrix} \lfloor -\tfrac{1}{R} \quad \tfrac{\partial}{\partial \eta} \quad 0 \rfloor \begin{Bmatrix} v \\ w \\ \theta \end{Bmatrix} \\
&\equiv \lfloor B_1 \rfloor \{ \underset{\sim}{u} \} + \frac{1}{2} \lfloor \underset{\sim}{u} \rfloor \{ B_2 \} \lfloor B_2 \rfloor \{ \underset{\sim}{u} \} \\
K &= \lfloor 0 \quad 0 \quad \tfrac{\partial}{\partial \eta} \rfloor \begin{Bmatrix} v \\ w \\ \theta \end{Bmatrix} \equiv \lfloor B_3 \rfloor \{ \underset{\sim}{u} \} \\
\gamma_o &= \lfloor -\tfrac{1}{R} \quad \tfrac{\partial}{\partial \eta} \quad 1 \rfloor \begin{Bmatrix} v \\ w \\ \theta \end{Bmatrix} \equiv \lfloor B_4 \rfloor \{ \underset{\sim}{u} \}
\end{aligned} \tag{4.53a}$$

It should be noted that in the previous Bernoulli-Euler-type beam element, the highest derivatives upon which the strain depends are the second derivative of the transverse displacement, w, and the first derivative of in-plane axial displacement, v. In order that the assumed displacement interpolation function be admissible in the variational argument of Eq. 3.3, it is required that the assumed displacement function of w at least possess a second derivative and v possess a first derivative; this means that the assumed displacement field must generate continuous displacements and continuous normal slopes at the interelement nodes. However, the inclusion of transverse shear deformation reduces the order of the derivative requirement and hence also the the stringency of the compatibility imposed on the assumed displacement field, because the strains depend only on the first derivative of displacements v,w and the rotation $\theta$. For the variational argument of Eq. 3.3 to be defined, it is required that the assumed displacement field have at least a first derivative and provide continuous displacements and rotations at the interelement nodes. Consequently, the simplest assumed displacement field for this Timoshenko-type beam element with the rigid-body displacement modes included is

$$\begin{Bmatrix} v \\ w \\ \theta \end{Bmatrix} = \begin{bmatrix} \cos\phi & \sin\phi & -z\cos\phi + y\sin\phi & \eta & 0 & 0 \\ -\sin\phi & \cos\phi & z\sin\phi + y\cos\phi & 0 & 0 & 0 \\ 0 & 0 & 0 & 0 & 1 & \eta \end{bmatrix} \begin{Bmatrix} \beta_1 \\ \beta_2 \\ \vdots \\ \beta_6 \end{Bmatrix} \equiv [U(\eta)]\{\beta\} \tag{4.54}$$

The generalized nodal displacements {q} are defined to be the three degrees of freedom v, w, and θ at each node of the element as follows:

$$\{q\} = \lfloor v_i \quad w_i \quad \theta_i \quad v_{i+1} \quad w_{i+1} \quad \theta_{i+1} \rfloor^T \tag{4.55}$$

In a manner similar to that described in the previous subsection, one may write

$$\{q\} = [A]\{\beta\} \tag{4.56}$$

and

$$\{\underset{\sim}{u}\} = \begin{Bmatrix} v \\ w \\ \theta \end{Bmatrix} = [U(\eta)][A]^{-1}\{q\} \equiv [N(\eta)]\{q\} \tag{4.57}$$

It perhaps should be mentioned that by this linear interpolation function (Eq. 4.54) of the displacement, the strain and moment representation will be very crude unless the element size is kept small enough, since as can be seen in this formulation, the bending strain is constant over each individual element. In order to improve the strain representation, higher order displacement interpolation functions and hence more degree of freedom (or internal nodes) should be used (see Ref. 164). Further discussion of this matter is given in Subsection 5.2.2. However, for the purpose of illustrating the calculation procedure, the linear interpolation function is discussed here.

Combining Eq. 4.57 with Eq. 4.53a results in

$$\begin{aligned} \varepsilon_o &= \lfloor D_1 \rfloor \{q\} + \frac{1}{2} \lfloor q \rfloor \{D_2\} \lfloor D_2 \rfloor \{q\} \\ \kappa &= \lfloor D_3 \rfloor \{q\} \\ \gamma_o &= \lfloor D_4 \rfloor \{q\} \end{aligned} \tag{4.58}$$

where

$$\lfloor D_i \rfloor = \lfloor B_i \rfloor [N(\eta)] \qquad i = 1, 2, 3, 4 \tag{4.58a}$$

Also, the strain increments from time $t_{i-1}$ to time $t_i$ are given by

$$\begin{aligned} \Delta \varepsilon_i &= \Delta \varepsilon_{oi} + \zeta \Delta \kappa_i \\ \Delta \gamma_i &= \Delta \gamma_{oi} \end{aligned} \tag{4.59}$$

where

$$\begin{aligned} \Delta \varepsilon_{oi} &= \lfloor D_1 \rfloor \{\Delta q\}_i + \lfloor q \rfloor_i \{D_2\} \lfloor D_2 \rfloor \{\Delta q\}_i \\ &\quad - \frac{1}{2} \lfloor \Delta q \rfloor_i \{D_2\} \lfloor D_2 \rfloor \{\Delta q\}_i \\ \Delta \kappa_i &= \lfloor D_3 \rfloor \{\Delta q\}_i \\ \Delta \gamma_{oi} &= \lfloor D_4 \rfloor \{\Delta q\}_i \end{aligned} \tag{4.59a}$$

### 4.4.3 The Discrete-Element Property Matrices

The element mass matrix and the element generalized nodal forces can be obtained following the same argument as in the previous subsection. Also, in addition to L and M, the transverse shear force, S, of the cross section, A, is given by

$$S = \iint_A \tau \, dA \tag{4.60}$$

where $\tau$ is the transverse shear stress.

Then, from the Principle of Virtual Displacements equation, Eq. 3.14, one may obtain for the improved formulation:

$$\sum_{n=1}^{N} \lfloor \delta q \rfloor \left( [m]\{\ddot{q}\} + \{p\} + [h]\{q\} - \{f\} \right) = 0 \tag{4.61}$$

where

$$[m] = \int_{\eta_i}^{\eta_{i+1}} [N(\eta)]^T \begin{bmatrix} \rho_o b h & & 0 \\ & \rho_o b h & \\ 0 & & \frac{\rho_o b h^3}{12} \end{bmatrix} [N(\eta)] \, d\eta$$

$$\{f\} = \int_{\eta_i}^{\eta_{i+1}} [N(\eta)]^T \begin{Bmatrix} F_v \\ F_w \\ \underset{\sim}{M} \end{Bmatrix} d\eta$$

$$\{p\} = \int_{\eta_i}^{\eta_{i+1}} ( \{D_1\} L + \{D_3\} M + \{D_4\} S ) \, d\eta$$

$$[h] = \int_{\eta_i}^{\eta_{i+1}} \{D_2\} \lfloor D_2 \rfloor L \, d\eta \qquad (4.61a)$$

Also, for the conventional formulation:

$$\sum_{n=1}^{N} \lfloor \delta q \rfloor ( [m]\{\ddot{q}\} + [k]\{q\} - \{f\} - \{f_p^L\} - \{f_p^{NL}\} - \{f_q^{NL}\} ) = 0 \qquad (4.62)$$

where

$$[k] = \int_{\eta_i}^{\eta_{i+1}} ( \{D_1\} E b h \lfloor D_1 \rfloor + \{D_3\} \frac{E b h^3}{12} \lfloor D_3 \rfloor + \{D_4\} G b h \lfloor D_4 \rfloor ) \, d\eta$$

$$\{f_p^L\} = \iint_A \int_{\eta_i}^{\eta_{i+1}} ( E \varepsilon^p \{D_1\} + \zeta E \varepsilon^p \{D_3\} + G \gamma^p \{D_4\} ) \, dV_n$$

$$\{f_p^{NL}\} = \iint_A \int_{\eta_i}^{\eta_{i+1}} E \varepsilon^p \{D_2\} \lfloor D_2 \rfloor \, dV_n \{q\}$$

$$\{f_q^{NL}\} = -\langle \int_{\eta_i}^{\eta_{i+1}} E b h ( \tfrac{1}{2} \lfloor q \rfloor \{D_2\} \lfloor D_2 \rfloor \{q\} ) \{D_1\} \, d\eta$$
$$+ \int_{\eta_i}^{\eta_{i+1}} E b h ( \lfloor D_1 \rfloor \{q\} + \tfrac{1}{2} \lfloor q \rfloor \{D_2\} \lfloor D_2 \rfloor \{q\} ) \{D_2\} \lfloor D_2 \rfloor \, d\eta \{q\} \rangle \qquad (4.62a)$$

Finally, one can recast Eqs. 4.61 and 4.62 in terms of global generalized displacements {q*} to obtain the corresponding equations of motion as described in Subsection 3.2.

### 4.4.4 Stress-Strain Relations

For this Timoshenko-type beam element with transverse shear deformation included, the calculation of stresses and stress resultants for both normal and transverse shear components is illustrated as follows.

One begins by knowing the sublayer normal stress $\sigma_{jk,i-1}$ and transverse shear stress $\tau_{jk,i-1}$ at time $t_{i-1}$ for the kth sublayer of the jth depthwise Gaussian station (layer) and the jth layer normal and transverse shear strain increments $\Delta\varepsilon_{j,i}$ and $\Delta\gamma_{j,i}$, respectively, at time $t_i$. The trial stresses are calculated from the relations

$$\begin{aligned} \sigma^T_{jk,i} &= \sigma_{jk,i-1} + E\,\Delta\varepsilon_{j,i} \\ \tau^T_{jk,i} &= \tau_{jk,i-1} + G\,\Delta\gamma_{j,i} \end{aligned} \tag{4.63}$$

Then, the trial stresses are introduced into the Mises-Hencky yield function

$$\Phi^T_i = \left[ (\sigma^T_{jk,i})^2 + 3(\tau^T_{jk,i})^2 - \sigma^2_{ok} \right] \tag{4.64}$$

where E is Young's modulus of elasticity

G is shear modulus of elasticity

and $\sigma_{ok}$ is the yield stress of the idealized elastic perfectly-plastic kth sublayer.

If $\Phi^T_i \leq 0$, the stress state lies within the yield surface, no plastic flow occurs within this time step, and the actual stress increments arise from wholly elastic behavior, then

$$\sigma_{jk,i} = \sigma^T_{jk,i} \quad , \quad \tau_{jk,i} = \tau^T_{jk,i} \tag{4.65}$$

and

$$\varepsilon^p_{jk,i} = \varepsilon^p_{jk,i-1} \quad , \quad \gamma^p_{jk,i} = \gamma^p_{jk,i-1} \tag{4.66}$$

If, on the other hand $\Phi^T_i > 0$, plastic yielding has occurred. Then, the flow rule, Eq. 2.82a gives the plastic strain increments as

$$\Delta \varepsilon^{p}_{jk,i} = 2\tilde{\lambda}\,\sigma^{T}_{jk,i}$$

$$\Delta \gamma^{p}_{jk,i} = 6\tilde{\lambda}\,\tau^{T}_{jk,i} \qquad (4.67)$$

and the actual stresses are

$$\sigma_{jk,i} = (1-\lambda^{*}E)\,\sigma^{T}_{jk,i} \quad , \quad \tau_{jk,i} = (1-3\lambda^{*}G)\,\tau^{T}_{jk,i} \qquad (4.68)$$

where $\lambda^{*} = 2\tilde{\lambda}$ and can be solved from the requirement that the actual stress state must be on the yield surface. Thus, the following condition must be satisfied:

$$\Phi = \left[(\sigma_{jk,i})^{2} + 3(\tau_{jk,i})^{2} - \sigma_{0k}^{2}\right] = 0 \qquad (4.69)$$

Substituting Eq. 4.68 into Eq. 4.69, one may solve for $\lambda^{*}$ as follows:

$$\lambda^{*} = \frac{C}{B+\sqrt{B^{2}-AC}} \qquad (4.70)$$

where

$$A = \left[E^{2}(\sigma^{T}_{jk,i})^{2} + 27\,G^{2}(\tau^{T}_{jk,i})^{2}\right]$$

$$B = \left[E\,(\sigma^{T}_{jk,i})^{2} + 9\,G\,(\tau^{T}_{jk,i})^{2}\right]$$

$$C = \Phi^{T}_{i} \qquad (4.70a)$$

With $\lambda^{*}$ obtained, the stress state at time $t_i$ and the plastic strain increment from time $t_{i-1}$ to $t_i$ are known. This process must be carried out for each layer (i.e., depthwise Gaussian station and sublayer). Once the stresses in each layer and sublayer have been determined, the axial force, moment, and transverse shear force of the cross section can be obtained by

$$
\begin{aligned}
L &\doteq b\frac{h}{2} \sum_{j} \Big( \sum_{k} \sigma_{jk} \, A_{jk} \Big) \\
M &\doteq b\frac{h}{2} \sum_{j} \zeta_{j} \Big( \sum_{k} \sigma_{jk} \, A_{jk} \Big) \\
S &\doteq b\frac{h}{2} \sum_{j} \Big( \sum_{k} \tau_{jk} \, A_{jk} \Big)
\end{aligned}
\tag{4.71}
$$

and the integration of the plastic strain over the cross section can be obtained by

$$
\begin{aligned}
\iint_{A} \varepsilon^{p} \, dA &\doteq b\frac{h}{2} \sum_{j} \Big( \sum_{k} \varepsilon^{p}_{jk} \, A_{jk} \Big) \\
\iint_{A} \zeta \, \varepsilon^{p} dA &\doteq b\frac{h}{2} \sum_{j} \zeta_{j} \Big( \sum_{k} \varepsilon^{p}_{jk} \, A_{jk} \Big) \\
\iint_{A} \gamma^{p} \, dA &\doteq b\frac{h}{2} \sum_{j} \Big( \sum_{k} \gamma^{p}_{jk} \, A_{jk} \Big)
\end{aligned}
\tag{4.72}
$$

Then the equilibrium equation, Eq. 4.61 or Eq. 4.62, must be used next in the calculation cycle to find the displacement or displacement increment of the next time cycle, as discussed in Subsection 3.3.1.

# SECTION 5

# EVALUATION AND DISCUSSION

## 5.1 Introduction

In Section 4, the curved beam element, which may undergo large deflections and elastic-plastic strains, as well as deforming such as either to include or omit transverse shear deformation, has been developed for the displacement variational model. The timewise numerical 3-point central-difference finite-difference procedure is employed to solve the resulting system of coupled second-order ordinary differential equations.

In order to evaluate the accuracy and versatility of the present finite-element formulation and solution scheme, this analysis has been implemented in a computer program and several numerical examples have been carried out. First, in Subsection 5.2, comparisons are made between the present finite-element solutions and known analytical solutions for small-deflection linear-elastic transient responses of mechanically-loaded beams. Next, in Subsection 5.3, the present predictions are compared with those from available finite-difference (both spatial and temporal) predictions and with experimental observations for large-deflection, elastic-plastic transient responses of impulsively-loaded beam and ring structures, and various features of the present method are assessed.

## 5.2 Small-Deflection Linear-Elastic Transient Responses of Mechanically Loaded Beams

In order to check on the proper functioning and correctness of the present analysis and computer program, the small-deflection linear-elastic transient responses of beams have been analyzed first; the finite-element predictions have been compared with available analytical solutions. Two beam problems have been studied: one pertains to Bernoulli-Euler (or Kirchhoff) deformation behavior while the other includes a significant amount of transverse shear deformation. These examples are discussed in the following.

### 5.2.1 Small-Deflection Linear-Elastic Responses of a Beam with Bernoulli-Euler-Type Deformation Behavior

A simply-supported beam is subjected to a uniform lateral transient loading over the whole span. The geometry, dimensions, material properties, and transient-loading history are depicted in Fig. 6. The Bernoulli-Euler-type small-deflection elastic beam element with a linear interpolation function for the axial displacement v and a cubic interpolation function for the transverse displacement, w, was employed; this element has been termed an LC element in Section 4. Because of symmetry, only one-half of the span of the beam was modeled; five equal-length discrete elements were used in the attendant finite-element analysis. The solution was obtained by using the 3-point central-difference timewise integration method with a time increment size of $\Delta t = 4$ μsec which satisfies the stability criterion, $\Delta t \leq (2/\omega_{max})$, for this method (see Ref. 148) where $\omega_{max}$ represents the largest natural frequency contained in the mathematical model, $[M]\{\ddot{q}^*\} + [K]\{q^*\} = 0$ which approximates the actual linear elastic small deflection structure.

A comparison of the mid-span transverse deflection response predicted by using the present finite-element scheme with the exact normal-mode solution is shown in Fig. 6. It is seen that very good agreement between these solutions is observed. It should be noted that for this small-deflection linear-elastic straight beam with Bernoulli-Euler deformation behavior: (1) the inplane (axial) displacement is zero and (2) the selected assumed cubic displacement function for the transverse displacement w is, in fact, identical with the exact displacement field. Hence, the finite-element calculation which utilizes the central-difference time integration method gives very accurate amplitude and phase predictions for small-deflection linear-elastic behavior as long as the time increment size used is small enough to satisfy the stability criterion.

### 5.2.2 Small-Deflection Linear-Elastic Transient Responses of a Beam with Timoshenko-Type Deformation Behavior

The second example is selected to test the convergence of predictions utilizing the various assumed displacement functions for the Timoshenko-type beam element when it is applied to a small-deflection linear-elastic dynamic system. Transverse shear deformation and rotatory inertia effects are included in the formulation. A free-free beam is subjected to an applied loading concentrated at the mid-span with a triangular pulse time history (this problem has been analyzed in Ref. 165). Figure 7 gives the geometry and the dimensionless parameters for this problem.

Because of symmetry, only a half-span of the beam was treated in the finite-element solution. The Newmark constant average acceleration timewise integration scheme[+] ($\gamma = 1/2$, $\beta = 1/4$) with a dimensionless time increment size $\Delta\tau = 0.0025$ was used, where $\Delta\tau = \Delta t\sqrt{EI/\rho bh}/\ell^2$. It should be recalled that this integration operator is unconditionally stable for linear (small-deflection) elastic dynamic systems; however, too large a $\Delta\tau$ may cause some phase shift from the correct behavior.

For this beam problem with a significant amount of transverse shear deformation, the following four types of assumed displacement fields (designated as T1 through T4) have been tested (note that zero inplane displacements v are involved -- v is ignored):

(T1) Linear functions in $\xi$ for both transverse displacement w, and rotation $\theta$:

$$\begin{aligned} w &= a_1 + a_2\,\xi \\ \theta &= a_3 + a_4\,\xi \end{aligned} \tag{5.1a}$$

The generalized coordinates $\{q\}$ are selected such that there are two degrees of freedom (w, $\theta$) at each end node i and i+1 of the element:

$$\{q\} = \lfloor\, w_i \quad \theta_i \quad w_{i+1} \quad \theta_{i+1} \,\rfloor^T \tag{5.1b}$$

(T2) Cubic variation of w and linear variation of transverse shear strain $\gamma_{\xi\zeta}$:

$$\begin{aligned} w &= a_1 + a_2\,\xi + a_3\,\xi^2 + a_4\,\xi^3 \\ \gamma_{\xi\zeta} &= \frac{\partial w}{\partial \xi} + \theta = a_5 + a_6\,\xi \end{aligned} \tag{5.2a}$$

---

[+] This operator rather than the 3-point central-difference operator was employed in an attempt to use a larger $\Delta\tau$ than the latter permits, and thus reduce the computing time.

Three degrees of freedom ($w$, $w_{,\xi}$, $\theta$) are selected at each end node of the element and the generalized coordinates are:

$$\{q\} = \lfloor w_i \quad w_{,\xi i} \quad \theta_i \quad w_{i+1} \quad w_{,\xi\, i+1} \quad \theta_{i+1} \rfloor^T \tag{5.2b}$$

The reason for choosing the linear function for the transverse shearing strain (i.e., quadratic function of the rotations) is that the bending effect dominates the transverse shearing effect when the element size is large, and the bending strains are derivatives of the rotation. Accordingly, this function could represent the strain energy of the element more accurately for a large mesh size (Ref. 164).

(T3) The same assumed displacement functions as for T2 (i.e., with a cubic variation of $w$ and a linear variation of $\gamma_{\xi\zeta}$) except that the generalized coordinates are selected such that there are two degrees of freedom ($w$, $\theta$) at the two end nodes and at a midpoint node of the element. Thus,

$$\begin{aligned} w &= a_1 + a_2 \xi + a_3 \xi^2 + a_4 \xi^3 \\ \gamma_{\xi\zeta} &= a_5 + a_6 \xi \end{aligned} \tag{5.3a}$$

and

$$\{q\} = \lfloor w_i \quad \theta_i \quad w_m \quad \theta_m \quad w_{i+1} \quad \theta_{i+1} \rfloor^T \tag{5.3b}$$

(T4) Quadratic variation of $w$ and linear variation of $\gamma_{\xi\zeta}$:

$$\begin{aligned} w &= a_1 + a_2 \xi + a_3 \xi^2 \\ \gamma_{\xi\zeta} &= a_4 + a_5 \xi \end{aligned} \tag{5.4a}$$

Two degrees of freedom ($w$, $\theta$) at the two end nodes and one degree of freedom, $w$, at the midpoint node of the element are selected. The generalized coordinates are

$$\{q\} = \lfloor w_i \quad \theta_i \quad w_m \quad w_{i+1} \quad \theta_{i+1} \rfloor^T \tag{5.4b}$$

Shown in Fig. 8 are the corresponding dimensionless transverse shear force responses predicted at the quarter-span station by using the four different sets of assumed displacement functions (T1 through T4) with various numbers of discrete elements for the half span. Shown also are the "exact" modal solutions of Ref. 165 based on the Timoshenko assumption for convenient comparison. It is seen that the use of linear interpolation functions for both w and $\theta$ (T1) gives very crude coarse-mesh transverse shear force responses compared with that from the modal solution. Whereas, predictions obtained by using the higher-order interpolation function (T2, T3, and T4) with a coarse-mesh finite-element array show better agreement with the modal solution than the predictions by using linear interpolation function (T1). However, as the number of finite elements employed increases (the element size decreases), all four of these interpolation-function predictions converge to the modal solution both in phase and in amplitude. If one bases the comparison on the total number of degrees of freedom (unknowns) which were used in the finite-element solutions, it is seen that, for a given number of unknowns, the predictions obtained by using T2 or T4 type interpolation-function elements leads to a solution which is closer to the modal solution than is the case if T1 or T3 type interpolation function elements are employed. The reason for this comparative behavior is that in the T1 type (linear) interpolation function, the strain and moment representation over each element are very crude; whereas in T2, T3, and T4 type interpolation function elements, the strain and moment representation is much improved over that with the T1 type element. Also, by using T3 type elements, the mesh size is relatively larger compared with that from using T2 or T4 type elements if they have the same number of degrees of freedom for the half-span of the beam. Finally, it should be noted that the size of the finite elements which provide good shear response agreement with the exact solution are such that their (equal) length is less than the depth of the beam (see Fig. 8) --- such a required modeling pertains to problems which include transverse shear and rotary inertia.

It perhaps should be noted that under various loading conditions, slope discontinuities along interelement boundaries are permitted when considering the presence of transverse shear deformations; thus, the T2 type element over-constrains the continuity of slope at the interelement nodes. Based on this consideration, it may be concluded that the T4 type assumed-displacement function is the most efficient one and the T2 type assumed displacement function comes next, when they are applied to beams with transverse shear deformation behavior.

The finite-element predictions for the quarter-span moment responses and the midspan deflection responses are shown in Figs. 9 and 10, respectively. The above-mentioned convergence behavior of the shear-force responses obtained by employing the four types of assumed displacement functions are also observed in both of these latter two figures for the moment and displacement responses.

This example illustrates that the linearly-varying (T1) assumed displacement Timoshenko-type beam finite element can provide accurate transient response predictions only if the element size is kept small enough. However, in order to obtain more accurate coarse-mesh solutions, one would need (a) to employ higher-order assumed displacement functions (T2, T3, T4) or (b) to use an assumed stress hybrid finite-element model (Ref. 166).

## 5.3 Large-Deflection Elastic-Plastic Transient Responses of Impulsively-Loaded Simple Structures

In order to evaluate the reliability and accuracy of the present finite-element method for predicting large-deflection elastic-plastic transient responses of simple structures, the various features and options of the present prediction method are examined in this subsection. Also, comparisons of the present predictions with other available finite-difference (both spatial and temporal) predictions (Ref. 44) and with experimental observations (Refs. 44, 167 and 168) are made.

### 5.3.1 Example Problems Analyzed

As examples with which the various features of the present finite-element prediction method can best be illustrated, the following three types of problems have been analyzed; the geometries and the types of finite elements employed are presented in Fig. 11 for reference convenience.

(1) A straight beam of 6061-T6 aluminum alloy is clamped at each end and has dimensions: 1/8-in. thickness, 1.2-in. width and 10-in. span between supports. The beam is loaded impulsively over a spanwise segment centered at the midspan and covering a length of 2 inches, as depicted in Fig. 11a.

(2) A 6061-T6 aluminum alloy ring sector with a subtended angle of 315° is clamped at each end and has dimensions: 2.935 in. mean radius, 0.123-in. thickness, 1.197-in. width. The clamped ring is loaded explosively over a peripheral sector of 120° of its exterior, as shown in Fig. 11b.

(3) A free circular 6061-T6 aluminum alloy ring, 0.124-in. thick, 1.195-in. wide, and 2.937 in. mean radius is subjected to severe explosive loading over a peripheral sector of 120° of its exterior, as shown in Fig. 11c.

As a matter of convenience for reducing the computer time and storage required by the solution of these problems, these three examples were treated as symmetrical problems. Taking account of the symmetry of the impulsive loading, geometry, and boundary conditions, only half of each configuration was modeled in all of the attendent discrete-element analyses.

### 5.3.2 Effects of Using Various Timewise Integration Operators: Central-Difference Method, Houbolt's Method, and Newmark's β-Method

In this subsection, the numerical stability behavior of the timewise integration operators: central-difference method, Houbolt's method and Newmark's β-method ($\gamma = 1/2$, $\beta = 1/4$) when employed for the solution of large-deflection elastic-plastic transient responses of the impulsively loaded clamped beam will be studied. The conventional finite-element formulation of the equilibrium equations is used, where the large-deflection and elastic-plastic effects are accounted for through the use of "equivalent generalized forces" which are given automatically from the variational formulations.

To minimize the computer time for the structural response calculations, one should use the largest permissible time increment which will avoid numerical instability (for example, roundoff error blowup or truncation error accumulation) and still provide a reliable prediction. Unfortunately, for the present nonlinear dynamic system, a reliable and validated criterion by which the proper time-step size can be chosen a priori is not readily available for any of these methods.

If the 3-point central-difference (timewise) method is used, as was pointed out in Subsection 3.3.4, the judicious selection of the proper time increment $\Delta t$ can be guided by the stability criterion of a corresponding linear dynamic system, $\Delta t_{c\ell} \leq 2/\omega_{max}$, as an initial selection; numerical experimentation then subsequently can provide the suitably smaller $\Delta t$ to insure stability where $\omega_{max}$ represents the largest natural frequency in the mathematical model, $[M]\{\ddot{q}^*\} + [K]\{q^*\} = 0$, which approximates the actual (linear-elastic small-deflection) structure. Thus, it would be very valuable to know $\omega_{max}$, such that the "suitable initial $\Delta t$" can be chosen immediately and hence reduce the amount of subsequent numerical experimentation. Figure 12a presents $\omega_{max}$ of the clamped beam as a function of the number of elements per half span; the Bernoulli-Euler-type LC beam element with a consistent mass matrix is used to model the structure. The maximum $\omega$ was obtained by an iteration process in double precision applied to (see Art. 4.5 of Ref. 27):

$$\omega^2\{q^*\} = [M]^{-1}[K]\{q^*\} \tag{5.5}$$

Also shown in Fig. 12a are the maximum frequencies of pure membrane behavior and pure bending behavior (with or without including the rotatory inertia effect). It is seen that the maximum frequencies of combined membrane and bending behavior are equal to the pure membrane maximum frequencies when the mesh size $\varepsilon$, to thickness, h, ratio is large ($\varepsilon/h \geq 4$), and are equal to the pure bending maximum frequencies when the mesh size to thickness ratio is small ($\varepsilon/h \leq 4$). This is to be expected for the linear Bernoulli-Kirchhoff beam system, because membrane and bending effects are decoupled. It is also noticed that the rotatory inertia effect arising from the consistent mass matrix can be significant when the mesh size is small, and the neglect of rotatory inertia by deleting those terms from the consistent mass matrix leads to a maximum frequency higher than that obtained by including this rotatory inertia effect (as seen in Fig. 12a).

It should be noted that simple analytical methods to estimate the upper bound and the lower bound of $\omega_{max}$ have been presented, for example in Ref. 162, in terms of the maximum eigenvalue of all the individual element matrices and its associated eigenvector:

$$\frac{max(\nu_n^2) + \Sigma' \lfloor x^* \rfloor [k_n] \{x^*\}}{1 + \Sigma' \lfloor x^* \rfloor [m_n] \{x^*\}} \leqslant \omega_{max}^2 \leqslant max(\nu_n^2) \tag{5.6}$$

where $max(\nu_n^2)$ denotes the largest $\nu_n^2$ of all the finite element and $\nu_n^2$ is the maximum eigenvalue of the equation

$$\nu_n^2 [m_n] \{x\} = [k_n] \{x\} \tag{5.6a}$$

$\{x^*\}$ is the eigenvector of Eq. 5.6a for the element j, which has max $(\nu_n^2)$,

and $\Sigma'$ indicates summation over only the neighboring elements of element j.

The element matrices $[m_n]$ and $[k_n]$ involve fewer degrees of freedom than the assembled matrix [M] and [K], so it is relatively much easier to find the element's maximum eigenvalue than the $\omega_{max}$ of the assembled matrix representing the complete structure. However, the bounds may not be very sharp; also the boundary conditions (which the cited "bound method" does not take into account) and the nature of the problem will affect the $\omega_{max}$ as shown in Fig. 12b where the upper and lower bounds of the maximum frequencies of pure beam bending behavior (by using consistent mass matrices from which are deleted the rotatory inertia effect) are given by[+] (Ref. 162):

$$1900 \frac{EI}{\rho \varepsilon^4} \leqslant \omega_{max}^2 \leqslant 8400 \frac{EI}{\rho \varepsilon^4} \tag{5.6b}$$

where $\rho$ is the mass per unit length and $\varepsilon$ is the element length. In view of

---

[+] Similar bounds could be developed when one uses lumped mass matrices such as those discussed in Subsection 4.3.3.

the wide bounds given by these results and in order to reduce the effort involved in subsequent numerical experimentation to determine a maximum permissible $\Delta t$, the exact $\omega_{max}$ has been evaluated in the present analysis; fortunately, for the beam (or ring) problem, the total degrees of freedom are not too many to be handled by the scheme represented by Eq. 5.5. However, for problems with an enormous number of degrees of freedom, one would perhaps need to resort to the simple analytical bound methods to estimate the upper and lower bounds of $\omega_{max}$; for such cases, the "bound scheme" may be more economical and efficient.

Now, turning to the large-deflection elastic-plastic transient response predictions, the half-span of the beam is modeled by 10 elements and the timewise 3-point central-difference operator is used. The critical $\Delta t$, if based on the stability criterion of a corresponding linear system would be $\Delta t_{c\ell} = 2/\omega_{max} = 1.47$ μsec. Computational experiments have been carried out using various time step sizes as shown in Fig. 13a to predict the midspan deflection responses. This clearly demonstrates the immediate divergence of the predictions if $\Delta t$ is only slightly greater than $\Delta t_{c\ell}$ ($\Delta t = 1.5$ μsec $= 1.02 \times \Delta t_{c\ell}$); reliable predictions are obtained if $\Delta t \leq 0.99 \times \Delta t_{c\ell} = 1.45$ μsec. Calculations also have been carried out by using Houbolt's method and Newmark's method as shown in Fig. 13b and 13c, respectively; it is observed for both of these methods that for $\Delta t$ values which are too large, the predicted response degrades gradually but badly from the correct behavior. The critical $\Delta t$ for reliable predictions was found to lie between 6 and 8 μsec for Houbolt's method and between 3 and 4 μsec for Newmark's method.

In view of these results and those of Refs. 55, 75, and 156, it is conceivable that the following situation may generally be considered to be true. The introduction of material nonlinearity often decreases the highest natural frequency of the system because the plastic pulse travels at a velocity which is less than the elastic pulse velocity, but elastic response contributions are still present and govern the allowable $\Delta t$. However, the geometric nonlinearity effect (large deflections) renders Houbolt's method and Newmark's method no longer to be "unconditionally stable".

It should be remembered that for this beam problem the calculation of strain increments from displacement increments and displacements, Eq. 4.25, at any time $t_m$ is given by

$$(\Delta \varepsilon)_m = (\Delta \varepsilon_0)_m + \zeta (\Delta K)_m$$

where

$$(\Delta \varepsilon_0)_m = \left(\frac{\partial \Delta V}{\partial \eta}\right)_m + \left(\frac{\partial W}{\partial \eta}\right)_m \left(\frac{\partial \Delta W}{\partial \eta}\right)_m - \frac{1}{2}\left(\frac{\partial \Delta W}{\partial \eta}\right)_m^2$$

$$(\Delta K)_m = -\left(\frac{\partial^2 \Delta W}{\partial \eta^2}\right)_m \tag{5.7}$$

The higher-order term $1/2(\partial \Delta w/\partial \eta)_m^2$ has been included in the above calculations. The predictions made by neglecting this term in the calculation of the strain increment are shown in Figs. 14a, 14b, and 14c for the central-difference method, Houbolt's method, and Newmark's method, respectively. Comparing Fig. 14 with Fig. 13, it is seen that the neglecting of this higher-order term may degrade the long-time responses due to the accumulation of "errors of approximation" introduced at each time step, especially for larger Δt as can be seen more prominently in the predictions obtained by Houbolt's method and Newmark's method. Accordingly, it is recommended that the exact strain-increment equation (Eq. 4.25) including all the linear and nonlinear terms in the displacements and the displacement increments should be used; fortunately the computer time and storage increase is insignificant.

It should be noted that Houbolt's method and Newmark's method are implicit in nature; that is, the generalized nodal forces (which may be due to large-deflections and elastic-plastic effects) at each time step depend on the displacements (or stress, strain) at that time step, which remain to be determined; thus, iteration or extrapolation is needed at each time step. Linear extrapolation (see Ref. 75, for example) by using the generalized nodal forces at two previous time steps is employed in the present calculations. The central-difference method on the other hand is explicit in nature and thus no iteration or extrapolation is required at each time step. The storage of the displacements at three previous time steps is required by Houbolt's method but information only at two previous time steps is needed when the 3-point central-difference method or Newmark's method is used. Also, for $\Delta t$ values which are too large, the very gradual degradation of the responses predicted by using Houbolt's method or Newmark's method gives no warning to the analyst that this degradation may be happening. However, the central-difference method usually exhibits a violent degradation of response when $\Delta t$ is too large, thus warning the analyst of this state of affairs.

Based on these considerations[+], only the timewise central-difference method is employed in the following example calculations. However, it should be mentioned that based on the present information, it is still far from conclusive as to whether any one timewise operator is superior to the others for analyzing nonlinear transient response problems of the present type.

### 5.3.3 Comparison of the Conventional Formulation Versus the Improved Formulation for the Dynamic Equilibrium Equations

By using the timewise 3-point central-difference method, comparisons have been made of the responses of the impulsively-loaded clamped beam obtained by employing the conventional finite-element formulation with those obtained by using the improved finite element formulation of dynamic equilibrium. Complete agreement of these predictions is observed in Fig. 15 for both the large-deflection elastic-plastic transient responses and the small deflection linear-elastic transient responses. However, as was discussed in Subsection 3.3, the improved formulation shows significant simplification in form over the conventional formulation for solving large-deflection elastic-plastic dynamic equilibrium behavior. Also, the computer storage and manipulations required for the improved formulation are less than those required for the conventional formulation. For this problem, it has been found that when using the conventional formulation, the computer time is about 24% more than that required when the

---

[+] Also in order to make convenient comparisons, because in the available independent finite-difference (both spatial and temporal) predictions involving large-deflection elastic-plastic behavior (Ref. 44), the timewise central-difference method is used.

improved formulation is used. Based on these considerations, only the improved formulation will be used in the following further example calculations of large-deflection elastic-plastic structural transient responses.

### 5.3.4 Comparison of LC Versus CC Assumed Displacement Functions for the Bernoulli-Euler-Type of Ring Element

The free ring has been analyzed by using the Bernoulli-Euler type of ring element with either CC or LC assumed-displacement functions. Shown in Fig. 16a is the maximum natural frequency $\omega_{max}$ for the linear behavior of the finite-element representation of the ring as a function of the number of elements per half ring. It is seen that for the same mesh size, the use of CC assumed-displacement elements has a larger $\omega_{max}$ (hence requires a small critical time step $\Delta t_{c\ell} = 2/\omega_{max}$) than that occurring when the LC assumed displacement elements are used. The ring centerline separation time histories predicted by using CC assumed-displacement elements compared with that predicted by using LC assumed displacement elements are shown in Fig. 16b, where the ring material is considered to be elastic linear-strain hardening (EL-SH). The experimentally observed response is also shown for convenient comparison. It is seen that as the structure is modeled as more and more finely subdivided, the LC element solutions converge and provide a somewhat stiffer response compared with experiment, while the solutions obtained from using the CC element converge more rapidly but tend to be "too flexible". However, the strain-time histories as shown in Fig. 16c indicate that the strain responses predicted by the CC element are very close to measured values, while the LC element under-predicts the strain.

It should be noted that for this free ring subjected to severe impulse loading (see Fig. 11c), one may expect the strain-rate effect to become rather important. The central line separation and strain time histories predicted from the elastic linear strain-hardening and strain rate (EL-SH-SR) calculations are shown in Fig. 17a and Fig. 17b, respectively. Far better (in fact, excellent) agreement with experiment of the CC element predictions than those of the LC element predictions are observed. It should be mentioned that for this free ring involving a rather severe degree of response, computational experiments have indicated that reliable deflection and strain predictions are obtained if the time steps are $\Delta t \leq 0.8 \times \Delta t_{c\ell} \cong 0.8(2/\omega_{max})$. Comparing with $\Delta t \leq 0.99(2/\omega_{max})$ for the clamped beam, it is believed that the critical time step is affected by the severity of the structural responses. That is, large deflections play the key role in effectively stiffening the structure and thus requiring a smaller $\Delta t$ to avoid round-off error instability.

The above-mentioned comparable behavior of the CC element predictions versus LC element predictions are also observed in the clamped ring calculations; see for example, the central deflection responses presented in Fig. 18.

In view of the present results and those of (Ref. 161), it can be concluded that the CC-type assumed displacement function exhibits significantly improved predictions, especially for the strains, over the LC assumed-displacement elements. Also, the former converges very rapidly but at the expense of a smaller allowable time-increment step compared with the latter.

It should be noted that in the above example, the converged solution obtained by using a finer mesh size is caused not only by the better approximation of the original continuum, but also by the better representation of the abrupt change of the initial impulse loading imparted to the system at the edge of the high explosive. This matter is discussed further in Subsection 5.3.6.1.

### 5.3.5 Comparison of the Use of a Consistent Mass Matrix Versus a Lumped Mass Matrix

If the lumped mass matrix is used ($\alpha = 1/2$, $\delta = 1/24$, see Eq. 4.32) for the analysis of the clamped beam example, it is observed in Fig. 19a that, for the same mesh size, the maximum frequency represented by the lumped mass matrix system (linear-elastic, small deflection) is smaller than that obtained by the use of a consistent mass matrix system. Hence, a larger time increment size (to avoid numerical instability) can be used for the lumped-mass-matrix system than for the consistent-mass-matrix system.

Figure 19b shows the midspan deflection responses for large-deflection elastic-plastic strain-rate dependent behavior. The responses predicted by both types of mass-matrix systems are quite close to each other, where the half-span of the beam is modeled by 10 elements and the time increment size used for a stable solution is $\Delta t \leq 0.99\ \Delta t_{c\ell} = 0.99(2/\omega_{max})$. That is, 1.45 μsec for the consistent mass matrix system and 2.45 μsec for the lumped mass matrix system. A violent degradation of the responses occurs when $\Delta t$ is only a trifle larger than $\Delta t_{c\ell}$. Comparisons of lumped mass model ($\alpha = 1/2$, $\delta = 1/24$, see Eq. 4.32) predictions versus consistent mass model predictions for the free ring example using Bernoulli-Euler CC-type ring elements are presented in Figs. 20a, 20b, and 20c for the maximum natural frequencies, the central-line separation, and the strain responses, respectively. Again, by using the lumped mass matrix, a smaller maximum natural frequency and good accuracy of the predicted nonlinear responses compared with the use of the consistent mass matrix are observed.

It should be noted that the use of the lumped mass matrix (with $\alpha = 1/2$, $\delta = 1/24$) not only decreases the maximum natural frequency (hence enables one to employ a larger time increment step for the response calculation than the consistent mass matrix system), but also reduces the storage and computer time required for the solution of the transient response problem. Because the lumped mass matrix is a diagonal matrix, $[M] = [m_i \delta_{ij}]$, its inverse is just $[M]^{-1} = [1/m_i (\delta_{ij})]$. However, it should be noted that further studies need to be conducted to develop mass matrix lumping rules which are appropriate for various user-selected criteria.

### 5.3.6 Assessment of Some Features of the Method

Among the various features of the present finite-element analysis which are examined and discussed in the following are:

(a) the effects of various initial velocities, specified at the nodal points of the finite-element assembled structure, to approximate the impulse loading which is produced by the detonation of a sheet of finite-span high explosive;

(b) effects of the number of spanwise Gaussian points used to evaluate the properties of each discrete element {p} and [h], and the number of depthwise Gaussian points used to evaluate stress resultants (axial force, moment and/or shear force) at each spanwise Gaussian station;

(c) the effect on the predicted transient response of including strain-rate sensitivity;

(d) the effect on the predicted transient response of including transverse shear deformation.

Each of these matters is discussed as follows.

### 5.3.6.1 Effects of Using Various Initial Nodal Velocities to Approximate the Impulse Loading

Experimentally, the impulsive loading may be produced by the detonation of a sheet of high explosive (HE). Between the HE and the test specimen is a thin layer of a suitable buffer material to prevent intense stress-wave-induced spall fracture of the test specimen. Experiment indicates that a nearly uniform initial normal impulse is imparted to those portions of the specimen immediately underneath the HE layer. However, for the region of the beam near the spanwise edges of the HE layer, a very steep gradient of imparted impulse is observed. A typical normalized distribution (Ref. 44) of the imparted impulse, is shown in Fig. 21a for the clamped beam covered by 0.015-in. thick HE layer (DuPont EL 506D) over a 2-in. span. The finite-span HE edge effect persists to a distance of about 0.5 to 1.0 inch.

In theoretical analyses the impulsive loading can conveniently be approximated by assuming an initial velocity distribution. Corresponding to the present finite-element approach, the initial conditions to be specified are those nodal generalized initial velocities $\{\dot{q}^*\}_{t=0}$. From the spanwise experimental impulse distribution data shown in Fig. 21a, a uniform initial transverse nodal velocity is assumed to occur at those nodes of the beam elements which are entirely covered by the HE layer. However, for nodes within the HE edge-effect zone, the specification of initial velocities poses some uncertainty. Because the compatibility conditions required by the Bernoulli-Euler finite-element displacement model are that at boundary nodes of each element, the compatibility of $w$ and $\psi(=\partial w/\partial \eta - v/R)$ with neighboring elements is required, the initial velocities of node n (if it is located at the middle of the HE edge zone) may be specified by either (1) $\dot{w} = a$, $\dot{\psi} = 0$ or (2) $\dot{w} = a/2$, $\dot{\psi} = 0$, or (3) $\dot{w} = a/2$, $\dot{\psi} = a/\ell$, where "a" is the uniform initial normal velocity assigned to the nodes covered by the HE layer but not in the HE edge zone of span "$\ell$". These three initial velocity simulations of the effect of a finite span of the HE layer on the distribution of imparted impulse (as depicted in Fig. 21b and designated as IV1, IV2, and IV3) have been tested in the present analysis.

The clamped-beam midspan deflection responses resulting from using these three different initial conditions are compared with each other and with experiment in Fig. 22. As shown in Fig. 22, it can be seen that the use of IV1 initial velocity representation gives a response with higher amplitude than both that of experiment and those responses predicted by using IV2 and IV3, whereas the responses obtained by employing IV2 and IV3 initial velocity representations are close to each other and are in good agreement with experiment. Hence, it may be concluded that the IV1 initial velocity representation gives a higher amount of impulse than the actual impulse imparted to the beam, whereas the IV2 and IV3 initial condition representations tend to simulate the experimentally-imparted impulse better than the first one does. In this example, 10 uniform elements are used to model the half-span of the beam. But, when a coarser mesh is used, as shown in Fig. 23 for the free-ring central-plane separation responses, the IV2 and the IV3 initial condition simulations can give very different responses. However, both predictions approach each other when the mesh sizes become finer. From the above examples, it may be concluded that a finer space mesh would be required, especially near the edge of the HE layer, before a reasonably accurate representation of the initial impulse loading conditions can be obtained by the present computational method, as correlated with experiment.

#### 5.3.6.2 Effects of the Number of Spanwise and Depthwise Gaussian Integration Points

Concerning the numerical evaluation of the integrals for determining the element properties $\{p\}$ and $[h]$ of Eq. 4.37, Gaussian quadrature has been employed to carry out the spanwise integrations over the length of the element and depthwise at each spanwise Gaussian point. Gaussian quadrature has been used also to evaluate the stress resultants (axial force, moment, and/or shear force).

As illustrated by the clamped-beam example, the midspan-deflection responses obtained by using various numbers of spanwise Gaussian points are shown in Fig. 24; in each case, 4 depthwise Gaussian stations have been employed to evaluate the stress resultants at each spanwise Gaussian point. It is seen that the prediction obtained by using only one spanwise Gaussian point tends to deviate appreciably from the behavior predicted by using 2, 3, or 4 spanwise Gaussian points; the 2-spanwise-Gaussian-point result tends to be somewhat too stiff; while the 3- and 4-spanwise-Gaussian-point results are very close to each other. Also shown in Fig. 24 are the results obtained by assuming that the stress resultants may be approximated over the length of the element by their values at the center of the element; this prediction is seen to be better than that for the 1-spanwise-Gaussian-point case, but the "structure" tends to be too stiff.

As for the effects of varying the number of depthwise Gaussian points to evaluate the stress resultants, shown in Fig. 25 are the midspan-deflection responses of the clamped-beam obtained by using 2, 3, 4, and 5 depthwise Gaussian points. In each case, 3 spanwise Gaussian points are used. It is seen that there is not very much difference among the deflection responses, as the number of depthwise Gaussian points is increased from 2 to 5. This is probably because the stretching behavior is predominant for the present clamped-beam example. The responses of the 2- and of the 4-point case differ somewhat, while the use of more than 4 depthwise Gaussian points affected the predicted response only very little.[+] In view of the above results and those of Refs. 44 and 48, it appears reasonable to conclude that the use of 3 spanwise Gaussian points (or stations) and 4 depthwise Gaussian points at each spanwise Gaussian station suffices for (a) representing the internal stress distributions across the elements thickness and (b) the spanwise integration over the element length.

#### 5.3.6.3 The Effect of Strain-Rate Sensitivity

In order to illustrate the effect on the transient response of using material strain-rate sensitivity in the present analysis, the impulsively-loaded

---

[+] Similar calculations for the free ring (Fig. 11c) using 3 spanwise Gaussian stations and either 4 or 6 depthwise Gaussian stations exhibited very little difference in the predicted responses.

clamped beam has been analyzed with the material property approximated either by EL-PP (elastic-perfectly plastic) or by EL-PP-SR (elastic perfectly-plastic and strain-rate sensitive). The midspan deflection responses are compared in Fig. 26. The EL-PP-SR solution gives an 8% reduction in peak deflection compared with the EL-PP results and this peak occurs about 40 μsec earlier than in the EL-PP solution.

For the impulsively-loaded free ring with CC Bernoulli-Euler-type ring elements, the predicted centerline midplane separation responses obtained by using the EL-SH-SR (elastic, linear-strain-hardening, and strain-rate sensitive) approximation for the material behavior leads to a 29% smaller peak amplitude and this peak occurs about 400 μsec earlier than in the EL-SH solution, as shown in Fig. 27. Shown also are the responses predicted by using LC Bernoulli-Euler-type ring elements with or without including the strain-rate effect.

Figure 28 shows the strain-rate effect on the central deflection responses of the impulsively-loaded clamped ring which was modeled by using either the LC Bernoulli-Euler-type element or the Timoshenko-type element. It is seen that including the strain-rate effect produces a "stiffer response"; i.e., small peak deformation response and earlier time-to-peak compared with the corresponding strain-rate independent predictions.

The above-mentioned peak deformation response reductions and earlier peak responses caused by assuming the material to be strain-rate sensitive (and to follow Eq. 2.75) is also observed in the finite-difference calculations of Ref. 44.

#### 5.3.6.4 The Effects of Including Transverse Shear Deformation

In order to examine the influence on the predicted response by using the present Timoshenko-type element as developed in Subsection 4.4 (which takes the transverse shear deformation into account) as compared with that obtained by using the LC and CC Bernoulli-Euler elements, the impulsively-loaded ring problems were analyzed with only the linear assumed displacement functions for $v$, $w$, and $\theta$ for the Timoshenko-type element.

The maximum natural frequency (linear system) as computed by employing the Timoshenko-type elements is compared with that obtained by using

Bernoulli-Euler-type elements, in Fig. 29 and Fig. 30 for the clamped beam and the free ring, respectively, as a function of the number of elements per half-span. It is observed for both the beam and the ring that the use of Timoshenko-type elements gives a larger maximum natural frequency, and hence a small critical $\Delta t$, than that obtained by the use of Bernoulli-Euler-type elements.

For the clamped beam, shown in Fig. 31 are the Timoshenko-type prediction and the Bernoulli-Euler-type prediction of the midspan deflection responses. Good agreement between these solutions is observed.

Turning to the clamped ring results, the predicted central deflection responses for the Timoshenko-type element are compared with those obtained by using (1) LC Bernoulli-Euler-type elements and (2) CC Bernoulli-Euler-type elements in Fig. 32. The observations are that the agreement of the Timoshenko-type element prediction with the CC Bernoulli-Euler-type prediction is far better than with the LC Bernoulli-Euler-type element prediction.

It should be noted that, for the present beam and ring examples, the transverse shear deformation effect essentially can be neglected, because of the thinness of the beam (thickness/span = 0.0125) and ring (thickness/radius = 0.042). Hence, these examples permit confirming: (1) that the present Timoshenko-type element provides accurate large-deflection elastic-plastic transient response predictions of Bernoulli-Euler-type deformation and (2) the deficiency in the LC-type element, but do not provide a critical evaluation of the present Timoshenko-type element to predict large-deflection elastic-plastic responses with significant transverse shear deformation effects. An appropriate such example having a reliable solution (or test result) has not been located.

### 5.3.7 Comparison of Accuracy and Efficiency of Finite-Element Solutions Versus Finite-Difference Solutions

#### 5.3.7.1 Scope of Comparisons

In Ref. 44, experimental measurements of transient deformations and strains for impulsively-loaded clamped beams, clamped rings, and free rings which undergo large-deflection, elastic-plastic responses are compared with finite-difference (FD) predictions -- wherein finite differencing is employed for both spatially- and time-varying quantities. Good theoretical-experimental agreement has been demonstrated.

Since the free-ring example (Fig. 11c) embodies the most reliably defined boundary conditions of the above-cited three cases, only this example is used (see Subsection 5.3.7.2) to compare the present finite-element (FE) predictions with FD predictions, and with experiment. Similar comparisons, carried out for the other two examples of Fig. 11, show similar comparative results.

This free-ring example is also used in Subsection 5.3.7.3 to illustrate and assess the comparative efficiency of the FD and the present FE prediction method(s) -- in terms of the amount of computer central processing unit (CPU) time required to carry out calculations for a given time of actual structural response and at the same time to provide peak deformation (and/or peak strain) predictions within a given percentage of the converged value (displacement or strain). This comparison is believed to provide a reasonably good, although tentative, assessment of the comparative cost for providing predictions of a "given accuracy" by the FE and the FD approach.

### 5.3.7.2 Comparison of Experiment with FE and FD Predictions

The geometry, material properties, and loading conditions (represented here as initial velocity conditions) are shown in Fig. 11c for the free ring. It has been demonstrated both in Ref. 44 and in Subsection 5.3.6.3 that the neglect of strain-rate effects in representing the mechanical properties of this 6061-T6 aluminum alloy material leads to a vast overprediction of the structural response. Accordingly, for convenience, the only material property representation employed in the present comparison is EL-SH-SR (elastic, linear strain hardening, and strain-rate dependent), with $D = 6500 \text{ sec}^{-1}$ and $p = 4$ (see Eq. 4.50). Also, the free ring is assumed to undergo Bernoulli-Euler-type deformation.

In both the FE and the FD predictions being discussed, the temporal 3-point central-difference operator is used. In view of the FE results discussed in the previous subsections, only the improved formulation type of FE predictions is included here; also, the following features are used as being appropriate and "adequate":

(a) in each element, three spanwise Gaussian stations are used to evaluate {p} and [h].

(b) four depthwise Gaussian stations are used to evaluate the inplane stress resultants and the moment resultants at each spanwise Gaussian station.

(c) Bernoulli-Euler finite-elements having the CC type of assumed displacement function are employed.

For the FD predictions, the method of Ref. 44 as subsequently improved and embodied in the JET 2 computer program of Ref. 169 has been used. In this method, the stress and moment resultants are evaluated only at each "finite-difference mass-point" station; at each such station, four depthwise Gaussian stations are used to carry out these evaluations in order to provide appropriate correspondence to the evaluations used in the present FE calculations. It should be noted that in the finite-difference calculations for the present type of structure, there are only two degrees of freedom (axial displacement and lateral displacement) at each space-mesh intersection (also called "mass point station"). Also, the mass matrix in the FD method is obtained by (automatic) lumping.

If one were to take advantage of symmetry, one could model the half ring by a number $N_E$ of finite elements of the CC-type assumed-displacement function or by $N_D$ finite-difference space-mesh stations. Accordingly, the associated number of degrees of freedom for each would be as follows:

| Number | Degrees of Freedom Unrestrained ($dof_u$) | Retained Number of Degrees of Freedom with Symmetry Restraints Applied ($dof_s$) |
|---|---|---|
| FE: $N_E$ | $4N_E + 4$<br>(for CC elements) | $4N_E$ |
| FD: $N_D$ | $2N_D$ | $2N_D$ |

In order to illustrate typical comparisons of the FE vs FD predictions, calculations which utilize a roughly comparable number of degrees of freedom are selected for presentation here. Accordingly, predictions for $N_E^+ = 18$ (or $dof_u = 76$ and $dof_s = 72$) and $N_D^+ = 40$ (or $dof_u = dof_s = 80$) are compared in Fig. 33a for the centerline midplane separation history and in Fig. 33b for the deformation profiles at 1140 μsec and 2580 μsec. It is seen that there is very good agreement between the FE and the FD prediction shown here; also, both predictions are in reasonably good agreement with experiment. Note that the experimental deformed-ring profiles exhibit some asymmetry, possibly from initial out-of-roundness and/or some unintentional and undefined asymmetry in the applied impulsive loading. Whereas, in both the FE and FD predictions, symmetry was imposed by choice -- nonsymmetric cases could be analyzed, however.

For the improved-formulation FE analysis of this ring which was modeled by 18 CC elements, transient response calculations were carried out by using (a) the consistent mass matrix and (b) the lumped mass matrix. In each case, the $\Delta t$ used was approximately $0.8\ \Delta t_{c\ell} = 0.8\ [2/\omega_{max}]$ as numerical experiments had previously verified to be acceptable; accordingly, the $\Delta t$'s were, 0.6 and 1.8 μsec, respectively. Since to the scale of the present plots these two transient response predictions were nearly alike, only the "more efficient" lumped-mass FE prediction is shown in Fig. 33. For the FD calculation, the $\Delta t$ employed was 9/8 μsec which is 99% of $\Delta t_{critical} = (\Delta s)/(E/\rho)^{1/2}$ where $\Delta s$ is the finite-difference mesh length.

An examination of a more sensitive quantity is provided by the dynamic strain responses. Predicted and experimentally-measured strain-time histories at 6 locations on the ring are compared in Figs. 33c and 33d. Again, both the FE and the FD predictions are in reasonably good amplitude and phase agreement with experiment, with the FE results being somewhat better.

Strain profiles predicted and measured at the 3,000 μsec instant are compared in Fig. 33e. Fairly good agreement among the FE prediction, the FD prediction, and experiment is observed. Also, note in Fig. 33e that abrupt reversal of the strain occurs at $\theta = 60°$ which is the location of the edge of the high explosive layer, and that the ring undergoes essentially pure bending for $\theta$ greater than about 70°. Considerable compression strain plus bending

---

[+] Uniform element lengths and uniform mesh lengths were used.

strain is seen to exist for small-θ locations.

### 5.3.7.3 Convergence and Efficiency Comparisons

It was noted in Subsection 5.3.3 that the conventional finite-element formulation requires more computer storage and running time to analyze a given problem than does the improved finite-element formulation. For example, for 1000 cycles of computing for the clamped-beam example of Fig. 11a, the conventional formulation required 1.85 minutes while the improved formulation required 1.41 minutes of CPU time (a saving of about 24%) where the same number of LC elements was used for both computations; the predictions from these two calculations were almost indistinguishable. Since it is clear that the improved formulation provides more efficient predictions, only the improved formulation is used in subsequent comparisons in this subsection.

For assessing the comparative efficiencies of the FE approaches (a) consistent mass and (b) lumped mass versus the finite-difference calculation, the free-ring example of Fig. 11c is used for both convenience and the fact that large deformations and elastic-plastic transient responses are involved.

By increasing the number of equal-length finite elements (of the CC type) to model the half ring (taking advantage of symmetry), transient response predictions have been carried out. The following two useful indices of the response were monitored, and are discussed herein, in obtaining a useful measure of convergence:

(1) the peak relative displacement of the ring at the symmetry plane (or ℄ ).

(2) the peak circumferential strain at several locations on the outer surface of the ring.

By plotting these results as a function of $(1/N_E)^2$, and extrapolating to $(1/N_E)^2 = 0$, "converged" results were estimated. The peak responses predicted were then ratioed to the appropriate "converged" result. Accordingly, shown in Fig. 34a is the ratio to the converged result of the predicted peak centerline relative displacement as a function of the number of unrestrained degrees of freedom $dof_u$ $(= 4N_E + 4)$. Shown in Fig. 34b is the average at θ = 87°, 92.5°, and 177° of the peak circumferential strain ratioed to the respective converged value as a function of $dof_u$; a mean dashed line is shown as well as a speckled band to indicate that such results show scatter depending upon the $\theta$-location chosen and the number of $\theta$-locations which one could use to construct this "average". It should be noted that, as discussed in Subsection 5.3.6.1, the specification of initial nodal velocity at the node of the finite element which is located at the spanwise edge of the high-explosive layer poses some uncertainty; that is, the use of different initial nodal velocities (IV2 or IV3) will yield very different coarse-mesh deformation responses because of the nature of the initial-velocity distribution. Improvements can be made by using finer meshes near the edge of the high-explosive layer. However, pending a more rational way of representing the finite span impulsive loading can be devised, the results presented in Figs. 34a and 34b are based on a uniform-mesh size and the IV3 type of initial-velocity representation.

Similar calculations and reductions were carried out for the finite difference method using the JET2 computer program. Shown in Fig. 35a is the ratio to the converged value of the predicted peak centerline relative displacement as a function of the number of degrees of freedom (i.e., $2N_D$). Similarly, Fig. 35b shows the average at $\theta = 27°, 45°, 63°, 81°, 99°$ and 171° of the peak circumferential strain ratioed to the respective converged value as a function of the number of degrees of freedom in the finite-difference model; for these $\theta$-locations, the peak strain ranged from about 2 to 4 percent. In Fig. 35b a dashed "average" curve through a speckled band is shown to indicate that such results show scatter which depends upon the $\theta$-location studied.

With respect to computing time, the amount of computer central processing unit time is believed to provide a reasonable basis for comparing the "time consumption" of the FE and the FD calculations. For the improved formulation version of the finite-element method when applied to large-deformation elastic-plastic transient response problems, it has been found that the maximum allowable time-increment size $\Delta t$ is about $0.8(2/\omega_{max})$ where $\omega_{max}$ is the largest natural frequency contained in the finite-element model of the structure for small vibrations, where the 3-point central-difference finite-difference time operator is used. When the present CC type of finite element is used together with (a) the consistent mass (C) matrix or (b) the lumped mass (L) matrix, the $\omega_{max}$ is found to be (see Fig. 16a):

$$(\omega_C)_{max} = [-0.1445 + 0.03578(dof_u)]10^6 \text{ radians/sec} \tag{5.8a}$$

$$(\omega_L)_{max} = [-0.0927 + 0.0127(dof_u)]10^6 \text{ radians/sec} \tag{5.8b}$$

where $dof_u = 4N_E + 4$ for the half ring; note that $(\omega_L)_{max} << (\omega_C)_{max}$. Further, it has been found that the amount of central processing unit time (CPUT) in minutes, for the improved FE method, is given approximately by:

$$CPUT = [42 \times 10^{-6}][dof_u] \frac{t}{\Delta t} \quad \text{(minutes)} \tag{5.9}$$

where t is the number of seconds of actual structural response to be computed and $\Delta t$ is also in seconds. Since the allowable $\Delta t = 0.8\ (2/\omega_{max})$, it follows that:

$$(CPUT)_C = [-3.794(dof_u) + 0.9393(dof_u)^2]t \tag{5.10a}$$

$$(CPUT)_L = [-2.433(dof_u) + 0.3325(dof_u)^2]t \tag{5.10b}$$

Similarly for the JET 2 program which uses the finite-difference method, it has been found that

$$(CPUT)_{FD} = [23 \times 10^{-6}][dof_u] \frac{t}{\Delta t} \quad \text{(minutes)} \tag{5.11}$$

where $dof_u = 2N_D$. Also since the largest allowable $\Delta t$ is given by $(\Delta s)/(E/\rho)^{1/2}$, it follows for the half ring with R = 3 in. and $\Delta t$ for conservatism taken as $0.99(\Delta s)/(E/\rho)^{1/2}$ that

$$(CPUT)_{FD} = 0.2513(dof_u)^2\ t \tag{5.12}$$

With the "convergence" results of Figs. 34a through 35b and with the above central processing unit time for computing, one may estimate the comparative CPUT values for the $FE_C$, $FE_L$, and FD computer programs used here in order to predict the peak centerline relative deformation or the peak circumferential strain to within selected percentages of the converged value for each type of calculation. An example of such estimates is tabulated as follows for computing 1500 μsec of transient response of the free ring, wherein it has been assumed that the "convergence rate" for the lumped mass version of the finite-element method is essentially the same as that shown in Figs. 34a and 34b for the consistent mass version of the finite-element method.

CENTRAL PROCESSING UNIT COMPUTING TIME ON IBM 370/155
AT MIT (MINUTES) FOR 1500 MICROSECONDS OF ACTUAL
STRUCTURAL RESPONSE

| | Finite-Element Improved Formulation | | Finite Difference |
|---|---|---|---|
| | CC and Consistent Mass | CC and Lumped Mass | |
| Percent of "Converged" Peak Ring ℄ Relative Displacement | | | |
| 3 | 2.03 | .65 | 1.36 |
| 2 | 3.24 | 1.06 | 1.64 |
| 1 | 6.89 | 2.32 | 2.01 |
| Percent of "Converged" Peak Strain on the Average | | | |
| 10 | 2.48 | .82 | 1.85 |
| 5 | 5.58 | 1.87 | 2.47 |
| 3 | 7.50 | 2.53 | 2.92 |

Comparing the two types of finite element calculations (consistent mass and lumped mass), it is evident that it is substantially more efficient to use the lumped-mass version of the finite element method. Further, since the transient responses of the consistent mass and of the lumped mass FE calculations differ only slightly, it is recommended that the lumped mass version of the FE method be selected as being more efficient and adequate for engineering prediction purposes.

Note also that this example comparison indicates that the $FE_L$ calculation is often more efficient than the FD prediction method. However, the conclusion that the $FE_L$ calculation will usually be more efficient than the FD method is not warranted on the basis of this limited comparison. Many more examples and much more thorough comparisons would be required before any judgment of this type could be made -- it would not be unexpected to find that one method would be superior for certain types of examples and the other method would be superior for certain other types of structural transient response problems.

Finally, in comparing $FE_L$ calculations with FD calculations wherein each employs the same number of degrees of freedom $dof_u$, for the free ring, it is seen that the ratio $(CPUT)_{FD}/(CPUT)_L$ for $dof_u$ = 10, 50, and 100 is 2.815, 0.884, and 0.816, respectively, and asymptotically approaches 0.755 as $dof_u$ is increased indefinitely if it is presumed that Eqs. 5.10b and 5.12 would apply -- these equations would, of course, cease to be valid where $dof_u$ becomes so large that resort to auxiliary storage and retrieval would be needed. The reasons for this relative computing time consumption involve the facts that:

(a) For the same number of degrees of freedom, the total number of spanwise Gaussian points employed in the FE method is 1.5 times as large as the total number of space-mesh intersections used in the FD method; Gaussian evaluations in the latter are performed only at the space-mesh intersection stations. At each spanwise Gaussian station, inplane stress resultants and moment resultants are evaluated.

(b) In the FD method, the strain is computed from the strain-displacement relations by finite-difference approximations in terms of displacements at two or three neighboring space-mesh stations. On the other hand, in the FE evaluation of strains, one computes the strains from the strain-displacement relations directly by using the assumed-displacement field of the finite element involved; this involves a time-consuming matrix multiplication. Of course, one could circumvent this in part in the FE method by resorting to the use of finite-difference approximations for each spanwise Gaussian station in terms of nearby nodal generalized displacements.

Also, several recent papers (Refs. 187, 188, and 189) in which various aspects of the finite-difference method versus the finite-element method are discussed have just appeared; these documents are recommended reading -- covering some of the present aspects as well as others. It perhaps should be mentioned that the finite-difference equations formulated in Refs. 39, 188, and 189 are based upon the variational-energy principle; the derivatives of the field variables in the variational functional are replaced by appropriate finite-difference quotients which involve only the values of the variables at the space-mesh stations. This finite-difference formulation is, hence, somewhat different from that described in Section 3, wherein the derivatives in the governing differential equations and boundary conditions are replaced by appropriate finite-difference expressions.

# SECTION 6

## APPLICATION: CONTAINMENT/DEFLECTION RING RESPONSES TO ENGINE ROTOR BLADE FRAGMENT IMPACT

### 6.1 Introduction and Problem Definition

Since the advent of the turbojet engine, there have been, from time to time, failures of turbine and/or compressor rotor blades and/or disks on engines of both military and civilian aircraft (Refs. 1, 170-173). Fragments which are uncontained (that is, penetrate the engine casing) might injure personnel occupying the aircraft and might cause additional damage to fuel lines and tanks, control systems, and other vital components. Although strenuous efforts have been and continue to be made to avoid blade/disk failures through improved materials, design, fabrication, and inspection, a not-insignificant number of such failures persist. It is desirable, therefore, to provide protection (a) for on-board personnel of aircraft in flight and (b) for vital components.

Similar but perhaps less severe fragment containment/control problems may be encountered where turbines and/or energy-storing flywheels are used in stationary power plants, aboard ships, and/or in land vehicles such as buses, trucks, automobiles, and train locomotives. In these cases, there would usually be less concern about the "weight penalty" for insuring fragment containment than for aircraft.

Two distinct avenues for providing this protection are evident. First, the structure surrounding the "failure-prone" rotor region could be designed to contain (that is, prevent the escape of) the rotor-burst fragments completely. Second, the structure surrounding this rotor could be designed so as to prevent fragment penetration in, and to deflect fragments away from, certain critical regions or directions but to permit fragment escape readily in other "harmless" regions or directions. One or both of these schemes could, in principle, be employed in a given design. In any event, this desired protection is sought for the least weight and/or cost penalty. If only one of these two schemes were to be adopted, one might expect that the second would be most cost and/or weight effective. However, the present (1) knowledge of the fragment-structure interaction phenomena and (2) analysis/design tools are inadequate to permit making a definitive comparative assessment at this time, although much progress has been made in both of these areas in the past few years.

As pointed out in Ref. 1, NASA has been sponsoring a research program which is designed to meet the objective of providing the necessary protection to aircraft without imposing large weight penalties. Starting about 1964, the Naval Air Propulsion Test Center (NAPTC) under NASA sponsorship has constructed and employed a spin-chamber test facility wherein rotors of various sizes can be operated at high rpm, failed, and very importantly the interactions of the resulting fragments with various types of containment and/or deflection structures can be studied with high-speed photography, in addition to post-mortem studies of the containment/deflection structure and the fragments. Many such tests involving single fragments or many complex fragments impinging upon containment structures of various types and materials have been conducted (Refs. 170-174) and have substantially increased the body of knowledge of the attendant phenomena. For the past several years NASA has sponsored a research effort at the MIT Aeroelastic and Structures Research Laboratory (ASRL) to develop methods for predicting theoretically the interaction behavior between fragments and containment/deflection structures, as well as the transient deformations and responses of containment/deflection structures -- the principal objective being to devise reliable prediction/design procedures and containment/deflection techniques. Important cross-fertilization has occurred between the NAPTC experimental and the MIT-ASRL theoretical studies, with special supportive-diagnostic experiments and detailed measurements being designed jointly by NASA, NAPTC, and MIT personnel and conducted at the NAPTC. Subsequent analysis and theoretical-experimental correlation work has been increasing both the understanding of the phenomena involved and the ability to predict these interaction/structural-response phenomena quantitatively.

Because of the multiple complexities involved in the very general case wherein the failure of one blade leads to impact against the engine casing, rebound, interaction with other blades and subsequent cascading rotor-failures and multiple-impact interactions of the various fragments with the casing and with each other, it is necessary to focus attention initially upon a much simpler situation in order to develop an adequate understanding of these collision-interaction processes. Accordingly, rather than considering the general three-dimensional large deformations of actual engine casings under multiple rotor-fragment attack, the simpler problem of planar structural response of containment structures has been scrutinized. That is, the containment structure is regarded simply as a structural ring lying in a plane; the ring may undergo large deformations but these deformations are confined essentially to that plane. For such a case, a numerical method of analysis to predict the transient large-deformation responses of such structures to known impulsive and/or transient external loading has been developed at the MIT-ASRL and has been verified (Refs. 44 and 45) by evaluative comparison with high-quality experimental data, to provide reliable predictions. This prediction method is sufficiently simple that one can feasibly carry out certain types of parametric structural response calculations, provided that known or prescribed externally-applied forces or impulses are employed; limited such studies are reported in Refs. 175 and 176.

In the present context, therefore, the crucial information which needs to be determined (if the structural response of a containment ring is to be predicted reliably) concerns the magnitude, distribution, and time history of the loading which the ring experiences because of fragment impact and interaction with the ring. Two means for supplying this information have been considered:

(1) The TEJ concept (Refs. 169, 176, 177) which utilizes measured experimental ring position-time data during the ring-fragment interaction process in order to deduce the external forces experienced by the ring. This concept has been pursued. An important merit of this approach is that it can be applied with equal facility to ring problems involving simple single fragments such as one blade, or to cases involving a complex multi-bladed-disk fragment. The central idea here is that if the TEJ type analysis were applied to typical cases of, for example, (a) single-blade impact, (b) disk-segment impact, and/or (c) multi-bladed disk fragment impact (see Figs. 36

and 37), one could determine the distribution and time history of the forces applied to the containment ring for each case. Such forces could then be applied tentatively in computer code response-prediction-and-screening studies for similar types of ring-fragment interaction problems involving various other materials, where guidance in the proper application of these forces or their modification could be furnished by dimensional-analysis considerations and selected spot-check experiments.

On the other hand, this approach suffers from the fact that experimental transient structural deformation data must be available; the forcing function is not determined from basic material property, geometry, and initial impact information.

(2) The second approach, however, utilizes basic material property, geometry, and initial impact information in an approximate analysis which employs the basic principles of energy and momentum conservation as well as material property constitutive data. If the problem involves only a single fragment, this method can be carried out and implemented without undue difficulty, but can become very complicated and time consuming if complex fragments and/or multiple fragments must be taken into account.

Approach 1 is explained in detail in Refs. 169, 176, and 177. The present report deals with approach 2 and confines attention to problems involving only a single simple fragment; problems involving more complicated fragments are left for future consideration.

Various levels of sophistication may be employed in approach 2. One could, for example, employ finite-difference methods wherein both the containment ring and the fragment are represented by a suitably fine three-dimensional spatial mesh and the conservation equations are solved in time for simple configurations by digital computer codes such as HEMP (Ref. 178), STRIDE (Ref. 179), and/or HELP (Ref. 180), which take into account elastic, plastic, strain hardening, and strain-rate behavior of the material. Such computations, while vital for certain types of problems, are very lengthy and expensive, and are not well suited for the type of engineering analysis/design purposes needed in the present problem; for complicated or multiple fragments, such calculations would be prohibitively complicated, lengthy, and expensive. A simpler, less complicated, engineering-analysis attack within this general framework is needed.

Two categories of such an engineering analysis may be identified and are termed: (a) the collision-imparted velocity method (CIVM) and (b) the collision-force method (CFM). The essence of each method follows:

### (a) Collision-Imparted Velocity Method (CIVM)

In this approach the local deformations of the fragment or of the ring at the collision interface do not enter explicitly, but the containment ring can deform in an elastic-plastic fashion by membrane and bending action as a result of having imparted to it a collision-induced velocity at the contact region via (a) perfectly-elastic or (b) perfectly-inelastic behavior. In fact, any type of material behavior may be accommodated readily. Since the collision analysis provides only collision imparted *velocity information* for the ring and the fragment (*not* the collision-induced interaction forces themselves), this procedure is called the collision-imparted velocity method.

### (b) Collision-Force Method (CFM)

In this method the primary information predicted in the collision analysis consists of the collision-induced interaction *forces themselves*; the associated and subsequent ring and fragment responses are also predicted.

Since the CIVM is much simpler to implement than the CFM approach, the CIVM scheme has been studied and is discussed (later) in some detail in Subsections 6.2, 6.3, and 6.4 of this report. The CFM approach, described briefly in Subsection 6.2.2, is currently under study, development, and feasibility evaluation; these findings will appear in a future report.

In Subsection 6.2 approximate collision analyses are discussed in detail. Some applications and evaluation of the CIVM approach are documented in Subsection 6.3. Finally, some comments on potential extensions of the CIVM scheme to more complex problems are given in Subsection 6.4.

## 6.2 Approximate Collision Analyses

Under consideration in this subsection are approximate methods for predicting the "immediate consequences" of the impact of a fragment against another physical body. One may regard the fragment as being (a) rigid, (b) perfectly elastic, (c) perfectly inelastic, or (d) deformable elastic-plastic with EL-SH-SR behavior; similar behavior may be attributed to the body which is struck by the fragment. When both bodies are treated as behaving according to (d), the modeled constitutive behavior of each most closely simulates the true physical behavior, but the associated impact-interaction is the most complex of the various options. For engineering applications purposes, one desires to employ the simplest and least expensive procedure which will give adequate engineering accuracy. Accordingly, various convenient and plausible assumptions are invoked to predict the "immediate impact-interaction" behavior of a fragment which collides with a containment/deflection structure.

For present purposes, the subject collision-interaction problem is simplified by restricting the motion to lie in one plane; the extension of the analysis to the more general three-dimensional motion-and-deformation behavior can be carried out, if desired, in a future investigation. Also, only a single simple fragment is considered, as depicted schematically in Fig. 36a. As noted earlier, principal attention is given in this report to the approximate analysis which is termed the collision-imparted velocity method (CIVM); only limited discussion is devoted to the collision-force method (CFM) in Subsection 6.2.2.

### 6.2.1 Collision-Imparted Velocity Method (CIVM)

For the CIVM approach, the following additional simplifying assumptions are invoked:

(1) In an overall sense, the fragment is treated as being rigid. It does not undergo bending or extensional deformation, but

at the "immediate contact region" between the fragment and the struck object (termed the "target" for convenience), the collision process is regarded as being instantaneous with a perfectly-elastic or a perfectly-inelastic interaction.

(2) The colliding surfaces of both the fragment and the target are perfectly smooth; hence, no forces and/or velocities (or momentum) are either transmitted or imparted in the tangential direction.

(3) During the collision, the contact forces are the only ones considered to act on the fragment and (in an antiparallel fashion) on the ring. The internal forces are approximated as being zero because the duration of the impact is so short as to preclude their "effective development".

(4) The collision process is instantaneous and involves only the fragment and the containment-ring segment which encompasses the ring-fragment collision point, as indicated schematically in Fig. 38. The word "instantaneous" implies that the internal forces can be neglected because stress waves have not had time to traverse the area near the collision from regions reasonably remote from the impact point in the ring. It is this instantaneity which permits one to omit the internal forces from the CIVM model.

(5) To avoid unduly complicating the analysis and because of the smallness of the arc length of the target-ring element, the ring element is treated as a straight beam in the derivation of the impact equations.

Two different approximation models are evident for the collision-interaction calculation for the fragment with the ring; namely, the consistent mass model and the lumped mass model. The former scheme treats each ring element as having a distributed mass; the latter scheme, employed in Ref. 181, considers the mass of each ring element to be concentrated at its two end nodes.

Accordingly, there are two sets of impact equations corresponding to these two approximate interaction models, which are described, respectively, in Subsections 6.2.1.1 and 6.2.1.2.

#### 6.2.1.1 Consistent-Mass Collision Model

In this collision model, the affected ring segment is idealized as a straight beam of length s having a nonuniform distribution of mass. Since perfectly smooth[+] surfaces for both the ring segment and the fragment are assumed to exist at the impact location, the instantaneous collision process results in an equal and opposite impulse applied to the ring (beam) segment and to the fragment in the direction normal to the axis of the ring segment; accordingly, tangential-component velocities are unaffected -- only the normal-direction components of the velocities of these two bodies undergo change because of the collision. Hence, only these components are employed in the following conservation relations.

Referring to the schematic and notation of Fig. 39a and to the idealized "line" geometry depicted in Fig. 40a, the impulse-momentum law and the kinetic energy conservation law may be written to characterize the "instantaneous impact behavior" of this system, as follows:

Translational Impulse-Momentum Law

$$m_r \left[ ( U_r' - U_r ) + a ( \omega_r' - \omega_r ) \right] = p_n \qquad \text{(ring segment)} \qquad (6.1)$$

$$m_f \left[ U_f' - U_f \right] = - p_n \qquad \text{(fragment)} \qquad (6.2)$$

Rotational Impulse-Momentum Law

$$I_{rg} \left[ \omega_r' - \omega_r \right] = - p_n \, ( d - \gamma ) s \qquad \text{(ring segment)} \qquad (6.3)$$

$$I_f \left[ \omega_f' - \omega_f \right] = p_n \, ( \ell \sin \theta ) \qquad \text{(fragment)} \qquad (6.4)$$

---

[+] The smooth surface assumption is invoked, for convenience, in the present analysis, but could be relaxed, if desired, in future work.

Conservation of Kinetic Energy

$$\begin{aligned}\frac{1}{2} m_r [U_r' + a\,\omega_r']^2 + \frac{1}{2} I_{rg} [\omega_r']^2 + \frac{1}{2} m_f [U_f']^2 + \frac{1}{2} I_f [\omega_f']^2 \\ = \frac{1}{2} m_r [U_r + a\,\omega_r]^2 + \frac{1}{2} I_{rg} [\omega_r]^2 \\ + \frac{1}{2} m_f U_f^2 + \frac{1}{2} I_f \omega_f^2\end{aligned} \tag{6.5}$$

where

$m_r$ = mass of the ring element which has a length s

$m_f$ = mass of the fragment whose length is $\ell_{f1} + \ell_{f2}$ (Fig. 39a)

$\ell$ in Eq. 6.4 = fragment length from the impact point to the c.g. of the fragment

$I_{rg}$ = mass moment of inertia of the ring element about its center of gravity (c.g.)

$$= \int_0^{\gamma s} m(\xi)\,\xi^2\,d\xi + \int_0^{\delta s} m(\eta)\,\eta^2\,d\eta \qquad \text{(see Fig. 39a)}$$

$m(\xi)$ or $m(\eta)$ denotes mass per unit length of the ring element

$I_f$ = mass moment of inertia of the fragment about its c.g.

$p_n$ = normal impulse

$a = (\frac{1}{2} - \gamma)s$

$U_r = \dfrac{U_1 + U_2}{2}$

$\omega_r = \dfrac{U_1 - U_2}{s}$ = angular velocity of the ring element

$U_1, U_2$ = normal velocities at ring-element nodes 1 and 2, respectively, immediately before impact

$U_f, \omega_f$ = fragment c.g. normal-direction velocity and angular velocity immediately before impact

$U'_r$, $\omega'_r$, $U'_1$, $U'_2$, $U'_f$, $\omega'_f$ = translational normal-direction velocities and angular velocities immediately after impact (primes indicate these after-impact quantities).

Equations 6.1 through 6.5 represent five equations expressed in terms of the five unknowns $U'_r$, $\omega'_r$, $U'_f$, $\omega'_f$, and $p_n$.

Next, it is convenient to eliminate $p_n$ by using the Eq. 6.1-value for $p_n$ to replace $p_n$ in Eqs. 6.2, 6.3, and 6.4 to obtain, after dividing each equation by $m_f$:

$$U'_f - U_f = -m\left[ (U'_r + a\,\omega'_r) - (U_r + a\,\omega_r) \right] \tag{6.2a}$$

$$I_1 \left[ \omega'_r - \omega_r \right] = -y\,m\left[ (U'_r + a\,\omega'_r) - (U_r + a\,\omega_r) \right] \tag{6.3a}$$

$$I_2 \left[ \omega'_f - \omega_f \right] = z\,m\left[ (U'_r + a\,\omega'_r) - (U_r + a\,\omega_r) \right] \tag{6.4a}$$

where

$$m = \frac{m_r}{m_f} \quad , \qquad I_1 = \frac{I_{rg}}{m_f} \quad , \qquad I_2 = \frac{I_f}{m_f}$$

$$y = (\alpha - \gamma)\,S \quad , \qquad z = \ell \sin\theta \tag{6.6}$$

Rewriting and dividing Eq. 6.5 (the kinetic energy equation) by $m_f$ one obtains, with the use of Eq. 6.6:

$$\frac{1}{2}\,m\left[ (U'_r + a\,\omega'_r)^2 - (U_r + a\,\omega_r)^2 \right] + \frac{1}{2}\,I_1\left[ (\omega'_r)^2 - (\omega_r)^2 \right]$$
$$+ \frac{1}{2}\left[ (U'_f)^2 - (U_f)^2 \right] + \frac{1}{2}\,I_2\left[ (\omega'_f)^2 - (\omega_f)^2 \right] = 0 \tag{6.5a}$$

If to the second, third, and fourth terms of Eq. 6.5a, one applies, respectively, Eqs. 6.3a, 6.2a, and 6.4a, one obtains:

$$\frac{1}{2} m \left\{ (U_r' + a\,\omega_r')^2 - (U_r + a\,\omega_r)^2 \right\}$$

$$+ \frac{1}{2} I_1 \left\{ \omega_r' + \omega_r \right\} \left\{ \frac{-y\,m}{I_1} \left[ (U_r' + a\,\omega_r') - (U_r + a\,\omega_r) \right] \right\}$$

$$+ \frac{1}{2} \left\{ U_f' + U_f \right\} \left\{ -m \left[ (U_r' + a\,\omega_r') - (U_r + a\,\omega_r) \right] \right\}$$

$$+ \frac{1}{2} I_2 \left\{ \omega_f' + \omega_f \right\} \left\{ \frac{z\,m}{I_2} \left[ (U_r' + a\,\omega_r') - (U_r + a\,\omega_r) \right] \right\} = 0 \tag{6.7}$$

Next, dividing Eq. 6.7 by $\frac{m}{2}[(U_r' + a\omega_r') - (U_r + a\omega_r)]$,

one obtains

$$\left\{ \left[ U_r' + (\tfrac{1}{2} - \alpha) S\,\omega_r' \right] - \left[ U_f' - z\,\omega_f' \right] \right\} = -\left\{ \left[ U_r + (\tfrac{1}{2} - \alpha) S\,\omega_r \right] - \left[ U_f - z\,\omega_f \right] \right\} \tag{6.8}$$

Equation 6.8 states that the velocity at the ring-impact point (C) relative to the velocity at the fragment impact point (A) is simply reversed by perfectly-elastic impact, since one may readily verify, for example, that

$$U_A = U_f - (\ell \sin\theta)\,\omega_f \tag{6.9a}$$

$$U_C = U_r + (\tfrac{1}{2} - \alpha) S\,\omega_r \equiv U_1 + (U_2 - U_1)\,\alpha \tag{6.9b}$$

Thus, if desired, one may express Eq. 6.8 by the self-evident notation

$$\left\{ U_C' - U_A' \right\} = -\left\{ U_C - U_A \right\} \tag{6.8a}$$

As pointed out in Ref. 182 (pg. 4-37), experiments on direct central impact of spherical bodies have shown that the relative velocities of spheres after impact are always less than before impact, and that these relative velocities are opposite in direction. The ratio of the relative velocity after impact to that before impact is called the "coefficient of restitution" and is generally denoted as e. It is found that $0 \leq e \leq 1$, where e = 1 represents a perfectly-elastic impact and e = 0 denotes a perfectly-inelastic impact. Typically, for glass e is 15/16, for ivory 8/9, steel and cork 5/9, wood about

1/2, and clay and putty 0.* Further, it should be recalled that during imperfect impact of two colliding bodies of masses $m_1$ and $m_2$, with initial velocities $V_1$ and $V_2$, there is a kinetic energy loss given by

$$\text{K.E.Loss} = \frac{m_1 m_2}{2(m_1 + m_2)} (V_1 - V_2)^2 (1 - e^2) \tag{6.10}$$

For the perfectly-elastic case of $e = 1$, no kinetic energy loss occurs. For $e \neq 1$, there is a loss of kinetic energy; however, since the total energy must be conserved, the "lost kinetic energy" is simply converted to other forms such as thermal or heat energy, etc. A proper accounting of all of the energy could be done in a complete thermo-mechanical analysis. For the present approximate analysis, however, one need not keep account of this kinetic energy loss.

Applying the concept of the coefficient of restitution, e, to Eq. 6.8, one may "generalize" this equation to read:

$$\left\{ [U_r' + (a-y)\omega_r'] - [U_f' - z\,\omega_f'] \right\} = -e \left\{ [U_r + (a-y)\omega_r] - [U_f - z\,\omega_f] \right\} \tag{6.11}$$

where $(1/2 - \alpha)s \equiv (a - y)$ has been used.

Finally, one can solve Eqs. 6.2a, 6.3a, 6.4a, and 6.11 to obtain expressions for $U_r'$, $\omega_r'$, $U_f'$, and $\omega_f'$, the "unknown" after-impact quantities. First, solving Eq. 6.3a for $\omega_r'$ in terms of $U_r'$

$$\omega_r' = \omega_r - \frac{y m}{I_1 + y a m} (U_r' - U_r) \tag{6.3b}$$

Next, applying Eq. 6.3b to Eq. 6.2a and solving for $U_f'$ in terms of $U_r'$:

$$U_f' = U_f - \frac{I_1 m}{I_1 + y a m} (U_r' - U_r) \tag{6.2b}$$

Also, applying Eq. 6.3b to Eq. 6.4a and solving for $\omega_f'$ in terms of $U_r'$:

$$\omega_f' = \omega_f + \frac{I_1 m z}{I_2 (I_1 + y a m)} (U_r' - U_r) \tag{6.4b}$$

---

*It will be shown subsequently that predicted containment ring structural responses to fragment impact are insensitive to the value of e employed for $0 \leq e \leq 1$.

Finally, applying Eqs. 6.2b, 6.3b, and 6.4b to Eq. 6.11, the following expression for $U_r'$ is obtained:

$$U_r' = U_r - \left(\frac{1+e}{K_c}\right) U_R \tag{6.12}$$

Thus, using Eq. 6.12, Eqs. 6.2b, 6.3b, and 6.4b yield, respectively,

$$U_f' = U_f + \frac{I_1\, m}{I_1 + yam}\left(\frac{1+e}{K_c}\right) U_R \tag{6.13}$$

$$\omega_r' = \omega_r + \frac{ym}{I_1 + yam}\left(\frac{1+e}{K_c}\right) U_R \tag{6.14}$$

$$\omega_f' = \omega_f - \frac{I_1\, m\, z}{I_2(I_1 + yam)}\left(\frac{1+e}{K_c}\right) U_R \tag{6.15}$$

Since $U_r' = (U_1' + U_2')/2$ and $\omega_r' = (U_1' - U_2')/s$, and similarly for the unprimed preimpact quantities, it follows that

$$U_1' = U_1 - \left\{1 - \frac{ym}{I_1 + yam}\,\frac{s}{2}\right\}\left(\frac{1+e}{K_c}\right) U_R \tag{6.16}$$

$$U_2' = U_2 - \left\{1 + \frac{ym}{I_1 + yam}\,\frac{s}{2}\right\}\left(\frac{1+e}{K_c}\right) U_R \tag{6.17}$$

where

$$K_C = 1 + \frac{m}{I_1 + yam}\left[I_1 - (a-y)y + \frac{I_1}{I_2} z^2\right] \tag{6.18a}$$

$$\begin{aligned} U_R &= [U_r + (a-y)\omega_r] - [U_f - z\,\omega_f] \\ &\equiv [\beta U_1 + \alpha U_2] - [U_f - z\,\omega_f] \end{aligned} \tag{6.18b}$$

$\equiv U_C - U_A$ = relative velocity of the impact points: C and A.

Note that subscript C of $K_C$ denotes that this quantity is associated with the consistent-mass collision model.

#### 6.2.1.2 Lumped-Mass Collision Model

For this collision calculation, the ring segment is treated as having only point masses $m_1$ and $m_2$ at nodes 1 and 2, respectively, rather than a distributed mass, as indicated schematically in Figs. 39b and 40b. The impulse-momentum law and the kinetic energy conservation law can be applied to this model also to obtain:

Translational Impulse-Momentum Law

$$(m_1 + m_2)\left[ (U_r' - U_r) + b\,(\omega_r' - \omega_r)\right] = p_n \qquad \text{(6.19a)}$$

or

$$m_1 [ U_1' - U_1 ] + m_2 [ U_2' - U_2 ] = p_n \qquad \text{(ring segment)} \qquad \text{(6.19b)}$$

$$m_f \; [ U_f' - U_f ] = - p_n \qquad \text{(fragment)} \qquad \text{(6.20)}$$

Rotational Impulse-Momentum Law

$$\begin{aligned} m_1 [ U_1' - U_1 ] \gamma_L s - m_2 [ U_2' - U ] (1 - \gamma_L) s \\ = - p_n [\alpha - \gamma_L ] s \end{aligned} \qquad \text{(ring segment)} \qquad \text{(6.21)}$$

$$I_f \; [ \omega_f' - \omega_f ] = p_n \; [ \ell \sin \theta ] \qquad \text{(fragment)} \qquad \text{(6.22)}$$

Kinetic Energy Conservation Law

$$\begin{aligned} \frac{1}{2} m_1 (U_1')^2 + \frac{1}{2} m_2 (U_2')^2 + \frac{1}{2} m_f (U_f')^2 + \frac{1}{2} I_f (\omega_f')^2 \\ = \frac{1}{2} m_1 (U_1)^2 + \frac{1}{2} m_2 (U_2)^2 + \frac{1}{2} m_f (U_f)^2 + \frac{1}{2} I_f (\omega_f)^2 \end{aligned} \qquad \text{(6.23)}$$

where

$$b = \left( \frac{1}{2} - \gamma_L \right) s$$

$$\gamma_L = \frac{m_2}{m_1 + m_2} \qquad \text{(see Fig. 40b)} \qquad \text{(6.24)}$$

and other quantities retain their previous meanings.

By using a reduction procedure similar to that described previously and introducing the coefficient of restitution, e, the following equation which is analogous to Eq. 6.11 is obtained:

$$\left\{ [\beta U_1' + \alpha U_2'] - [U_f' - z\,\omega_f'] \right\} = -e \left\{ [\beta U_1 + \alpha U_2] - [U_f - z\,\omega_f] \right\} \quad (6.25)$$

By following a solution procedure similar to that described previously, one obtains

$$U_1' = U_1 - m_2 \beta \left( \frac{1+e}{K_L} \right) U_R \quad (6.26)$$

$$U_2' = U_2 - m_1 \alpha \left( \frac{1+e}{K_L} \right) U_R \quad (6.27)$$

$$U_f' = U_f + \frac{m_1 m_2}{m_f} \left( \frac{1+e}{K_L} \right) U_R \quad (6.28)$$

$$\omega_f' = \omega_f - \frac{m_1 m_2 z}{I_f} \left( \frac{1+e}{K_L} \right) U_R \quad (6.29)$$

where

$$K_L = \frac{m_1 m_2}{m_f} + m_1 \alpha^2 + m_2 \beta^2 + \frac{m_1 m_2}{I_f} z^2 \quad (6.30)$$

and where all other quantities retain their previous definitions.

### 6.2.1.3 Governing Equations

Summarized here, for convenience, are the governing equations of motion for both the ring (target) structure and the rotor blade (fragment).

#### Ring-Structure Motion

As described in Subsection 3.2, the governing equations of motion[+] for either a complete ring or a partial-ring structure may be written as follows

---

[+] Note that Eq. 6.31 represents one of the two forms of the equations of motion discussed in Subsection 3.2; the second form, Eq. 3.1, could be discussed in a similar fashion if desired.

for the spatial finite-element representation of the complete assembled discretized structure (CADS):

$$[M]\{\ddot{q}^*\} + \{P\} + [H]\{q^*\} = \{F^*\} \tag{6.31}$$

| | |
|---|---|
| where $\{q^*\}$, $\{\ddot{q}^*\}$ | represent the generalized displacements and generalized accelerations, respectively |
| $[M]$ | is the mass matrix for the CADS |
| $\{P\}$ | is an "internal force matrix" which replaces the conventional stiffness terms $[K]\{q\}$ for small displacements but also now includes some plastic behavior contributions |
| $[H]$ | represents a "new" stiffness matrix which arises because of large deflections and also plastic behavior |
| $\{F^*\}$ | denotes the externally applied generalized forces acting on the CADS |

It should be noted that all quantities in Eq. 6.31 refer to the global Y,Z inertial reference system indicated in Figs. 41 and 42. For the case in which the structure is subjected to distributed linear restoring springs as depicted, for example, in Figs. 41 and 42, Eq. 6.31 becomes

$$[M]\{\ddot{q}^*\} + \{P\} + [H]\{q^*\} = \{F^*\} - [K_s]\{q^*\} \tag{6.32}$$

where $[K_s]$ represents the global effective stiffness supplied by the elastic foundation and/or other "restraining springs". Further, it is presumed that Eq. 6.32 has already incorporated within it all pertinent boundary conditions and restraints as depicted, for example, in Figs. 42a through 42d.

As discussed in Subsection 3.3, the timewise solution of Eq. 6.32 may be accomplished by employing an appropriate timewise finite-difference scheme such as the central difference method. Accordingly, for the cases of CIVM fragment impact or of prescribed externally-applied forces, Eq. 6.32 at time instant j may be written in the following form:

$$[M]\{\ddot{q}^*\}_j = (\{F^*\} - [K_s]\{q^*\} - \{P\} - [H]\{q^*\})_j \tag{6.33}$$

Let it be assumed that all quantities are known at any given time instant $t_j$. Then one may determine the generalized displacement solution at time $t_{j+1}$ (i.e., $\{q^*\}_{j+1}$) by the following procedure. First, one employs the timewise central-difference expression for the acceleration $\{\ddot{q}^*\}_j$:

$$\{\ddot{q}^*\}_j = \frac{1}{(\Delta t)^2}\left(\{q^*\}_{j+1} - 2\{q^*\}_j + \{q^*\}_{j-1}\right) \tag{6.33a}$$

It follows that one can solve for $\{q^*\}_{j+1}$ since $\{\ddot{q}^*\}_j$ is already known from Eq. 6.33 and all other quantities in Eq. 6.33a are known. However, a fragment-ring collision may occur between time instants $t_j$ and $t_{j+1}$; this would require a "correction" to the $\{q^*\}_{j+1}$ found from Eq. 6.33a. Thus, one uses and rewrites Eq. 6.33a to form a trial value (overscript T):

$$\{\Delta \overset{T}{q}{}^*\}_{j+1} = \{\Delta q^*\}_j + (\Delta t)^2 \{\ddot{q}^*\}_j \tag{6.33b}$$

where

$$\{\Delta q^*\}_j = \{q^*\}_j - \{q^*\}_{j-1}$$

$$\{\Delta \overset{T}{q}{}^*\}_{j+1} = \{\overset{T}{q}{}^*\}_{j+1} - \{q^*\}_j \quad = \text{trial increment} \tag{6.33c}$$

$$\{q^*\}_j = \{q^*\}_0 + \{\Delta q^*\}_1 + \cdots + \{\Delta q^*\}_j$$

$\Delta t$ = time increment step

Note that $t_j = j(\Delta t)$ where $j = 0, 1, 2, \ldots,$ and $\{\Delta q^*\}_0 \equiv 0$. Also, no such trial value is needed if only prescribed external forces were applied to the containment/deflection ring.

Let it be assumed that one prescribes at $t = t_0 = 0$ ($j=0$) values for the initial velocities $\{\dot{q}^*\}_0$ and external forces $\{F^*\}_0$, and that the initial stresses and strains are zero. The increment of displacement between time $t_0$ and time $t_1$ is then given by:

$$\{\Delta q^*\}_1 \doteq \{\dot{q}^*\}_0 (\Delta t) + \{\ddot{q}^*\}_0 \frac{(\Delta t)^2}{2} \tag{6.34}$$

where $\{\ddot{q}^*\}_0$ can be calculated from

$$[M]\{\ddot{q}^*\}_0 = \{F^*\}_0 \tag{6.34a}$$

wherein it is assumed that no ring-fragment collision occurs between $t_0$ and $t_1$ (accordingly, overscript T is not used on $\{\Delta q^*\}_1$ in Eq. 6.34).

### Fragment Motion

In the present analysis, the fragment is assumed to be undeformable and, for analysis convenience to have semi-circular ends; hence, its equations of motion are:

$$m_f \ddot{Y}_f = 0 \tag{6.35}$$

$$m_f \ddot{Z}_f = 0 \tag{6.36}$$

$$I_f \ddot{\theta} = 0 \tag{6.37}$$

where $(Y_f, Z_f)$ and $(\ddot{Y}_f, \ddot{Z}_f)$ denote, respectively, the global coordinates and acceleration components of the center of gravity of the fragment (see Fig. 43)

$\theta$ represents the angular displacement of the fragment.

In timewise finite-difference form, Eqs. 6.35 through 6.37 become

$$(\Delta \overset{T}{Y}_f)_{j+1} = (\Delta Y_f)_j \tag{6.38}$$

$$(\Delta \overset{T}{Z}_f)_{j+1} = (\Delta Z_f)_j \tag{6.39}$$

$$(\Delta \overset{T}{\theta})_{j+1} = (\Delta \theta)_j \tag{6.40}$$

where overscript "T" signifies a trial value which requires modification, as explained later, if ring-fragment collision occurs between $t_j$ and $t_{j+1}$.

By an inspection procedure to be described shortly, the instant of ring-fragment collision is determined, and the resulting collision-induced velocities which are imparted to the fragment and to the affected ring segment are determined in accordance with the analysis of Subsection 6.2.1.1 or 6.2.1.2.

#### 6.2.1.4 Solution Procedure

The following procedure indicated in the flow diagram of Fig. 44 (and described also in Ref. 181), may be employed to predict the motions of the ring and the rigid fragment, their possible collision, the resulting collision-imparted velocities experienced by each, and the subsequent motion of each body:

Step 1: Let it be assumed at instant $t_j$ that the coordinates $\{q_j^*\}$, $Y_{f_j}$, and $Z_{f_j}$, and coordinate increments $\{\Delta q^*\}_j$, $\Delta Y_{f_j}$, and $\Delta Z_{f_j}$ are known. One can then calculate the strain increments $\Delta\varepsilon_j$ at all Gauss stations j along and through the thickness of the ring from Eq. 4.25.

Step 2: Using a suitable constitutive relation for the ring material, the stress increments $\Delta\sigma_j$ at corresponding Gaussian stations can be determined from the now-known strain increments $\Delta\varepsilon_j$ (see Subsections 2.3 and 4.3.4). Since the $\sigma_{j-1}$ are known at time instant $t_{j-1}$, the stresses at $t_j$ are given by $\sigma_j = \sigma_{j-1} + \Delta\sigma_j$. This information permits determining all quantities on the right-hand side of Eq. 6.33, where for the present CIVM problem $\{F^*\}_j$ is regarded as being zero.

Step 3: Solve Eq. 6.33 for the trial ring displacement increments $\{\Delta \overset{T}{q}{}^*\}_{j+1}$. Also, use Eqs. 6.38, 6.39, and 6.40 for the trial fragment displacement increments $(\Delta \overset{T}{Y}_f)_{j+1}$, $(\Delta \overset{T}{Z}_f)_{j+1}$, and $(\Delta \overset{T}{\theta})_{j+1}$.

Step 4: Since a ring-fragment collision may have occurred between $t_j$ and $t_{j+1}$, the following sequence of substeps may be employed to determine whether or not a collision occurred and, if so, to effect a correction of the coordinate increments of the affected ring segment and of the fragment.

Step 4a: To check the possibility of a collision between the fragment in the vicinity of point A of the fragment with ring element i (approximated as a straight beam) as depicted in Fig. 43, compute the trial projection $(\overset{T}{p}_i)_{j+1}$ of the line from ring node i to point A of the fragment, upon the straight line connecting ring nodes i and i-1, as follows, at time instant $t_{j+1}$:

$$(\overset{T}{p}_i)_{j+1} = [\overset{T}{Y}_i - \overset{T}{Y}_A]_{j+1} \cos(\overset{T}{\alpha}_i)_{j+1} + [\overset{T}{Z}_i - \overset{T}{Z}_A]_{j+1} \sin(\overset{T}{\alpha}_i)_{j+1} \qquad (6.41)$$

where the Y,Z are inertial Cartesian coordinates. Now, examine $(\overset{T}{p}_i)_{j+1}$; three cases are illustrated in Fig. 43a.

**Step 4b**: If $(\overset{T}{p}_i)_{j+1} < 0$ or if $(\overset{T}{p}_i)_{j+1} > s_i$ where $s_i > 0$, a collision between the fragment near point A and ring element i is impossible. Proceed to check ring element i+1, etc. for the possibility of a collision of fragment end A with other ring elements.

**Step 4c**: If $0 \leq (\overset{T}{p}_i)_{j+1} \leq s_i$, a collision with ring element i is possible, and further checking is pursued. Next, calculate the fictitious "penetration distance" $(\overset{T}{a}_i)_{j+1}$ of the fragment at end A into ring element i by (see Fig. 43b):

$$(\overset{T}{a}_i)_{j+1} = \frac{1}{2}[h_{1i} + \alpha(h_{2i} - h_{1i}) + h_f]_{j+1} - [\overset{T}{d}_i]_{j+1} \qquad (6.42)$$

where

$\frac{1}{2}[h_{1i} + \alpha(h_{2i} - h_{1i})]$ = local semi-thickness of the ring element which is approximated as a straight beam in this "collision calculation"

$\frac{h_f}{2}$ = tip radius of the fragment at the impact end A

$\alpha_{j+1} = (\frac{\overset{T}{p}_i}{s_i})_{j+1}$ = fractional distance of $s_i$ from node i to where the collision occurs (recall: $\alpha + \beta = 1$, and $\alpha_{j+1}$ should not be confused with the angle $(\overset{T}{\alpha}_i)_{j+1}$).

$$(\overset{T}{d}_i)_{j+1} = -[\overset{T}{Y}_i - \overset{T}{Y}_A]_{j+1} \sin(\overset{T}{\alpha}_i)_{j+1} + [\overset{T}{Z}_i - \overset{T}{Z}_A]_{j+1} \cos(\overset{T}{\alpha}_i)_{j+1} \qquad (6.43)$$

= the projection of the line connecting node i with point A upon a line perpendicular to the line joining nodes i and i-1.

Next, examine $(\overset{T}{a}_i)_{j+1}$ which is indicated schematically in Fig. 43b and is given by Eq. 6.42.

Step 4d: If $(\overset{T}{a}_i)_{j+1} \leq 0$, no collision of the fragment near point A upon element i has occurred during the time interval from $t_j$ to $t_{j+1}$. Hence, one can proceed to check element i+1, etc. for the possibility of a collision of fragment end A with other ring elements.

Step 4e: If $(\overset{T}{a}_i)_{j+1} > 0$, a collision has occurred; corrected coordinate increments (overscript "C") may be determined approximately by (see Fig. 43b):

$$(\Delta \overset{C}{V}_f)_{j+1} = (\Delta \overset{T}{V}_f)_{j+1} + (\Delta t^*)[U_f' - U_f] \sin(\overset{T}{\alpha}_i)_{j+1} \tag{6.44a}$$

$$(\Delta \overset{C}{W}_f)_{j+1} = (\Delta \overset{T}{W}_f)_{j+1} - (\Delta t^*)[U_f' - U_f] \cos(\overset{T}{\alpha}_i)_{j+1} \tag{6.44b}$$

$$(\Delta \overset{C}{\theta})_{j+1} = (\Delta \overset{T}{\theta})_{j+1} + (\Delta t^*)[\omega_f' - \omega_f] \tag{6.44c}$$

$$(\Delta \overset{C}{V}_{i-1})_{j+1} = (\Delta \overset{T}{V}_{i-1})_{j+1} - (\Delta t^*)[U_2' - U_2] \sin(\overset{T}{\alpha}_i)_{j+1} \tag{6.44d}$$

$$(\Delta \overset{C}{W}_{i-1})_{j+1} = (\Delta \overset{T}{W}_{i-1})_{j+1} + (\Delta t^*)[U_2' - U_2] \cos(\overset{T}{\alpha}_i)_{j+1} \tag{6.44e}$$

$$(\Delta \overset{C}{V}_i)_{j+1} = (\Delta \overset{T}{V}_i)_{j+1} - (\Delta t^*)[U_1' - U_1] \sin(\overset{T}{\alpha}_i)_{j+1} \tag{6.44f}$$

$$(\Delta \overset{C}{W}_i)_{j+1} = (\Delta \overset{T}{W}_i)_{j+1} + (\Delta t^*)[U_1' - U_1] \cos(\overset{T}{\alpha}_i)_{j+1} \tag{6.44g}$$

where the after-impact quantities $U_1'$, $U_2'$, $U_f'$, and $\omega_f'$ may be found, respectively, from (Eqs. 6.16, 6.17, 6.13, and 6.15) or from (Eqs. 6.26, 6.27, 6.28, and 6.29), whichever collision model one wishes to use, and where

$$\Delta t^* = \frac{(\overset{T}{a}_i)_{j+1}}{(U_{Ri})_j} = \text{time interval from actual impact on ring element i until } t_{j+1} \tag{6.45a}$$

$$(U_{Ri})_j = [\beta_{j+1}(U_1)_j + \alpha_{j+1}(U_2)_j] - [(U_f)_j - z(\omega_f)_j]$$

= preimpact relative velocity of points A and C (6.45b)

The terms, in Eqs. 6.44a through 6.44g, which are multiplied by ($\Delta t^*$) represent corrections to the trial incremental quantities for the ($\Delta t^*$) time interval. Also, since $\Delta t$ is small, one may use either angle $(\alpha_i^T)_{j+1}$ or angle $(\alpha_i)_j$ in Eqs. 6.44a through 6.44g.

Step 5: Having determined the corrected coordinate increments[+] for the impacted ring element, this time cycle of calculation is now complete. One then proceeds to calculate the ring nodal coordinate increments and the fragment coordinates for the time step from $t_{j+1}$ to $t_{j+2}$, starting with Step 1. The process proceeds cyclically thereafter for as many time increments as desired.

If, however, one finds no collision of fragment end A with any of the ring segments, the checking process should be repeated for any other possible fragment points of impact (such as end B, for example) with the ring.

This solution procedure may be carried out for as many time steps as desired or may be terminated by invoking the use of a termination criterion such as, for example, the reaching of a critical value of the strain at the inner surface or the outer surface of the ring. Appropriate modifications of this approximate analysis could be made, if desired, to follow the behavior of the ring and the fragment after the initiation and/or completion of local fracturing of the ring has occurred.

---

[+] It should be noted that in this approximate calculation, only the coordinate increments of the fragment and of the impacted ring segment are corrected. Those for all other ring segments are regarded as already being correct. The time increment $\Delta t$ is regarded as being sufficiently small to make these approximations acceptable.

### 6.2.2 Outline of the Collision-Force Method (CFM)

Although the collision-force method will be described in detail in Ref. 183, it is perhaps useful to outline briefly the essence of this approach. In this method, the primary information predicted in the collision analysis consists of the collision-induced interaction forces themselves. One may readily identify the following three versions of the method (where the accompanying sketches indicate the associated qualitative behavior):

(a) The deformation of the fragment and the ring may be neglected in the collision-interface region.

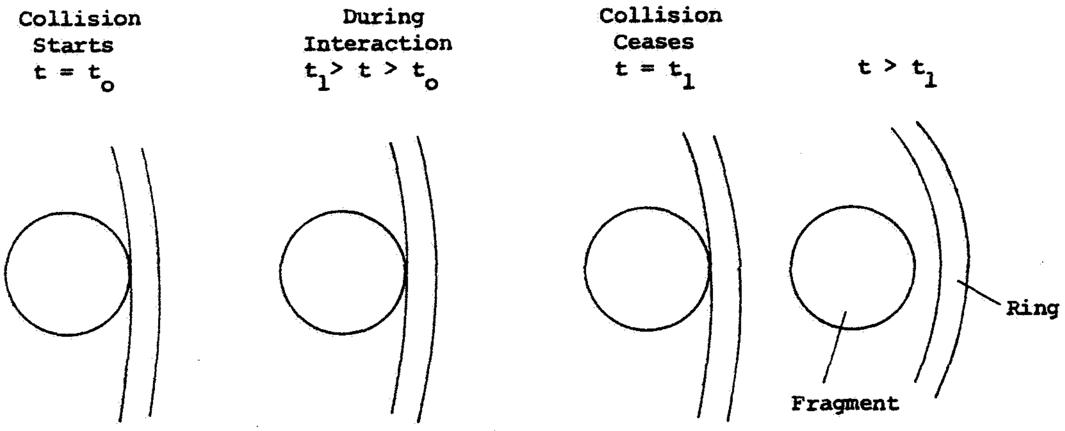
Collision Starts $t = t_o$
During Interaction $t_1 > t > t_o$
Collision Ceases $t = t_1$
$t > t_1$
Ring
Fragment

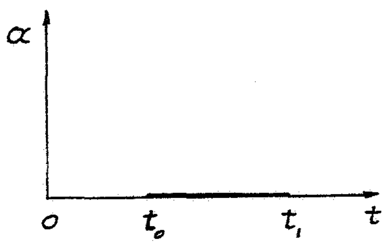

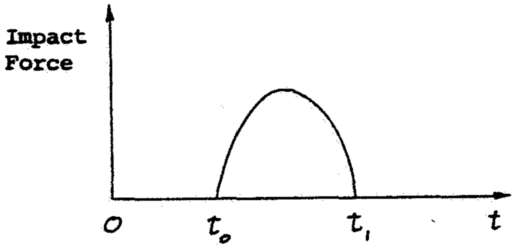

where $\alpha$ denotes the total local deformation of the ring and fragment at the center of the impact region (for this case $\alpha \equiv 0$).

(b) The fragment and the ring deform in a reversible elastic manner in the collision-interface region.

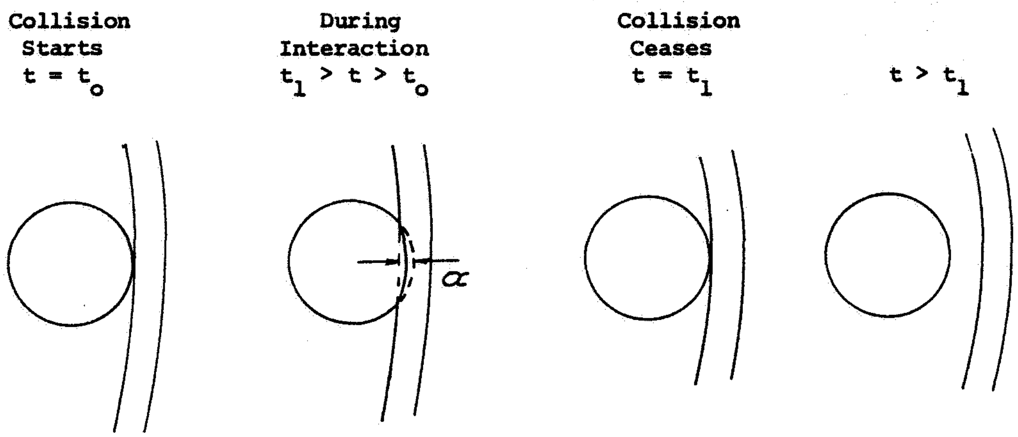
Collision Starts
$t = t_o$
During Interaction
$t_1 > t > t_o$
Collision Ceases
$t = t_1$
$t > t_1$
$\alpha$

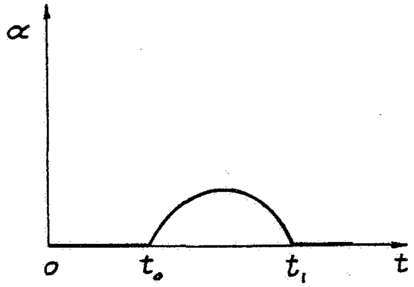

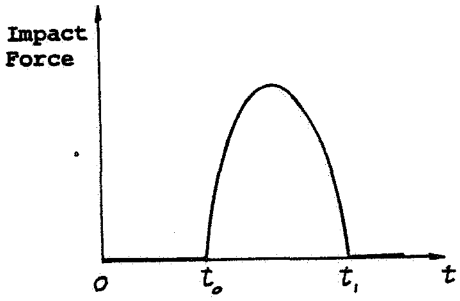

This reversible elastic local indentation $\alpha$ is related to the impact force F by the Hertz Law: $F = k\alpha^{3/2}$ where k is a constant found from the elastic properties of the colliding materials.

(c) The fragment and the ring may deform in a general elastic-plastic fashion in the collision-interface region.

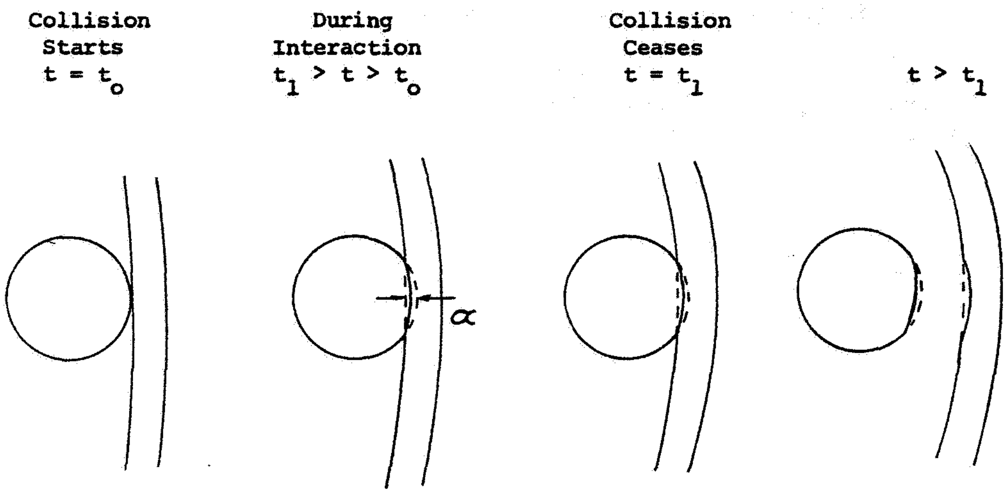
Collision Starts
$t = t_o$
During Interaction
$t_1 > t > t_o$
$\alpha$
Collision Ceases
$t = t_1$
$t > t_1$

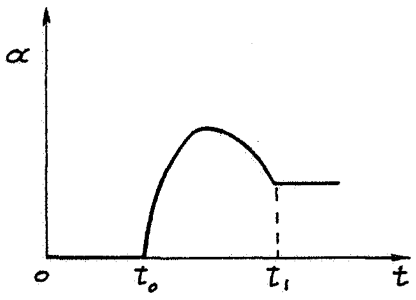

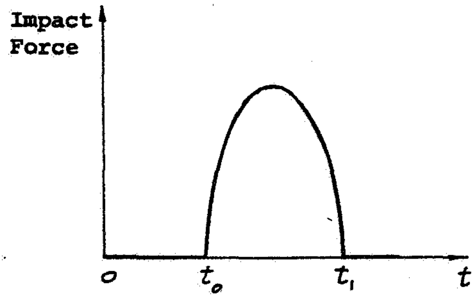

Here both the ring and the fragment exhibit permanent deformation in the "collision zone"; for this situation the impact force may be expressed approximately by $F = N\alpha^n$ where N and n are constants depending upon the properties of the colliding materials.

For all of the CIVM cases and CFM cases (a), (b), and (c), the containment rings may undergo elastic-plastic membrane and bending behavior.

## 6.3 Application and Evaluation of the CIVM Approach

Described in this subsection is a set of very limited calculations in which the CIVM approach has been employed. The calculations have involved the impact of a single rotor blade (fragment) against: (a) a complete free circular containment ring and (b) a "fragment-deflection" ring quadrant which is supported at a selected station in one of several ways. These brief calculations serve to illustrate minimally (1) the effect of the type of collision model (consistent mass, CM, or lumped mass, LM), (2) the effect of the coefficient of restitution e, (3) the effect of plausible ring material strain-rate behavior, (4) calculation convergence with an increasing number of ring elements, and (5) preliminary comparisons with experimental response data for a complete free ring subjected to impact by a single-blade fragment. These studies are described in the following.

### 6.3.1 Definition of Example Problems and Calculations

To illustrate the CIVM approach, the two categories of example problems depicted schematically in Fig. 45 were analyzed: (a) a free complete circular ring subjected to impact from a single-blade fragment, as represented by the conditions pertaining to experiment in NAPTC Ring Tests 88 and/or 91 (Ref. 177) and (b) a ring quadrant chosen to represent an example deflection device and also subjected to single-blade impact. For the complete-ring example, preliminary experimental ring response and blade motion data (from NAPTC Ring Tests 88 and 91, with the latter being the more reliable) are available for comparison with predictions. However, experimental data are not available for the ring-quadrant cases.

Summarized in Table 1 are the pertinent geometric and test-condition data for NAPTC Ring Tests 88 and 91. The (complete) free containment ring consisted of 2024-T4 aluminum; for analysis, its uniaxial static stress-strain behavior was approximated (closely) as being elastic, perfectly-plastic (EL-PP) with a yield stress $\sigma_o$ of 50,000 psi and an elastic modulus of $10^7$ psi. A single T-58 rotor blade which was fabricated from material designated as SEL-15 by General Electric was the fragment employed; for the present analysis, this "fragment" is treated as being rigid. For the ring-quadrant examples, the same geometric, material property, and test conditions were employed as for the Test 88 complete-ring example.

Shown in Tables 2 and 3 are the characterizing data for the sequence of CIVM calculations carried out for, respectively, (1) the complete ring -- Runs CR-1B through CR-11B, and (2) the ring quadrant examples -- Runs RQ-1B through RQ-9B. For all cases except CR-8B through CR-11B, the conditions pertinent to NAPTC Test 88 were used; NAPTC Test 91 conditions were used for calculation Runs CR-8B through CR-11B.

Shown in Table 2 for the complete-ring problem are (a) the number of segments into which each quadrant of the ring was discretized for analysis, (b) the interpolation function used to represent the displacement field throughout each ring element (the linear distribution of the inplane displacement together with a cubic distribution of the transverse displacement is termed LC; the cubic distribution of both the inplane and transverse displacement along each ring finite element is termed CC for cubic cubic), (c) the type of mass matrix used for each ring element (the mass matrix which is variationally consistent with the assumed displacement field is termed C and the lumped-mass matrix is termed L), (d) the ring material property representation (elastic, perfectly plastic EL-PP, or EL-PP-SR, where SR denotes strain-rate sensitive behavior), (e) the type of collision model employed (consistent mass, CM, or lumped mass, LM), and (f) the coefficient of impact restitution e, where e = 1 represents a perfectly-elastic impact and e = 0 denotes a perfectly-inelastic impact.

For the partial-ring or ring-quadrant cases, Table 3 identifies: (a) the number of equal-length segments into which the ring quadrant was idealized for analysis, (b) the type of mass matrix used for each ring finite element (L or C), (c) the type of support (ideally clamped IC, or smoothly hinged), and (d) the type of collision model (CM or LM) used. For all cases, the LC type assumed-displacement function over each ring finite element, EL-PP-SR, and e = 1 conditions were used in these calculations.

The various matters examined in these studies are described in the following.

### 6.3.2 Effect of Type of Idealized Collision Model

The two types of idealized collision models, consistent-mass CM and lumped-mass LM, discussed in Subsections 6.2.1.1 and 6.2.1.2, respectively, have been employed in example calculations to examine their behavior and relative merits.

First, consider the CM collision model. A comparison of ring quadrant calculations RQ-1B vs RQ-2B (see Table 3) have illustrated dramatically the undesirably sensitive nature of the CM collision model. For case RQ-1B, the ring quadrant was modeled by 9 equal-length segments while for case RQ-2B, 10 equal-length segments were employed; in all other respects the conditions were the same: the same fragment properties and initial conditions, the ring material properties EL-PP-SR, and e = 1 for the coefficient of restitution were employed. Dispite this slight change in the modeling of the ring (from 9 to 10 equal-length elements), the resulting responses of the ring quadrant and of the blade fragment were dramatically different (see Fig. 46) when the CM model was employed. Increasing the number of segments to 15 to model the ring quadrant in case RQ-3B resulted in ring quadrant and blade responses that also differed significantly from the 9-element case but very little from the 10-element case. These results illustrate the sensitive nature of the CM collision model.

On the other hand, the use of the LM collision model for identical ring-quadrant modelings: 9, 10, and 15 elements for cases RQ-4B, RQ-5B, and RQ-6B, respectively, demonstrated improved convergence and much less sensitivity to the number of segments (elements) used to model the ring quadrant. These results are illustrated in Fig. 47. Note that the 9-element result differs somewhat from the 10-element result, but the 10-element result and the 15-element result are nearly the same; this suggests that the 10-element calculation provides a "converged" solution. Because of the greater consistency of the LM collision model in comparison with the CM collision model, the LM collision model has been selected for principal use, although additional CM collision calculations have also been carried out.

Similar predicted ring response and blade response behavior for single-blade impact upon a free complete ring is illustrated in Fig. 48. CM collision model cases CR-1B and CR-3B for ring discretizations 5-5-5-5 and 9-6-6-6, respectively, are compared with LM collision model case CR-5B which utilizes ring discretization 10-6-6-6 (see Table 2); the latter calculation is assumed to provide a converged result. Here again the CM results appear to exhibit somewhat "erratic" behavior.

An approximate collision model which leads to very different results when only a slight change in modeling of the ring is employed is undesirable and unacceptable. A trustworthy approximate collision model should not exhibit such extreme sensitivity to a slight change in the discretization modeling of a containment ring or of a "deflector" ring structure. Accordingly, the CM collision model has been set aside and the LM collision model has been adopted for future calculations until a better model has been devised.

The reasons for the erratic CM collision model behavior versus the more satisfactory LM collision model features may be seen most conveniently perhaps by examining the collision-imparted velocity behavior of the blade and the affected ring element. It should be recalled that the ring element was idealized by a straight-line beam element (for the impact-collision calculation only). Consider the case in which the uniform beam element with length s, mass $m_r$, is struck by the blade tip at a point very near one end of the beam element (for example, near node 1, see Fig. 40), in which case $\alpha = 0$ and $\beta = 1$; assuming that the normal impulse resulting from the collision is $p_n$, the blade c.g. normal-direction velocity change and angular velocity change due to impact are given by Eqs. 6.2 and 6.4 (also Eqs. 6.20 and 6.22) as

$$U_f' - U_f = -\frac{p_n}{m_f} \tag{6.46a}$$

$$\omega_f' - \omega_f = \frac{p_n \, \ell \sin\theta}{I_f} \tag{6.46b}$$

where the angle $\theta$ is the inclination of the blade to the normal of the beam element.

The beam nodal velocity and the angular velocity changes predicted by the CM collision model (Eqs. 6.14, 6.16, and 6.17) for a collision occurring at node 1($\alpha = 0$ and $\beta = 1$) are

$$(U_1' - U_1)_{CM} = \left\{ 1 - \frac{ym}{I_1 + yam} \frac{S}{2} \right\} \frac{p_n}{m_r} = 4 \frac{p_n}{m_r} \tag{6.47a}$$

$$(U_2' - U_2)_{CM} = \left\{ 1 + \frac{ym}{I_1 + yam} \frac{S}{2} \right\} \frac{p_n}{m_r} = -2 \frac{p_n}{m_r} \tag{6.47b}$$

$$(\omega_r' - \omega_r)_{CM} = \frac{ym}{I_1 + yam} \frac{p_n}{m_r} = \frac{6}{S} \frac{p_n}{m_r} \tag{6.47c}$$

On the other hand, the LM collision model predicts the beam nodal velocity and angular velocity changes (Eqs. 6.26, 6.27) to be

$$(U_1' - U_1)_{LM} = \beta \frac{p_n}{m_r} = \frac{p_n}{m_r} \tag{6.48a}$$

$$(U_2' - U_2)_{LM} = \alpha \frac{p_n}{m_r} = 0 \tag{6.48b}$$

$$(\omega_r' - \omega_r)_{LM} = \frac{1}{S} \frac{p_n}{m_r} \tag{6.48c}$$

Comparing Eq. 6.47c with Eq. 6.48c, it is seen that, for a certain normal impulse $p_n$, the angular velocity change predicted by the CM model would be six times larger than that predicted by the LM model. This larger consequent change of the orientation of the beam segment for the CM model compared with that for the LM model may subsequently lead to the larger change of the angle $\theta$, and hence, the angular velocity change of the blade (see Eq. 6.46b) for the subsequent impact(s) of the blade with the beam element will also be more seriously altered. As observed in Fig. 46, the use of the CM collision model with 10-element and 15-element modeling of the ring quadrant, after a certain time stage, predicts that the angular velocity of the blade becomes negative (the direction of rotation is reversed). No such reversal of the direction of blade rotation is predicted when the LM collision model is used in corresponding 10-element and 15-element calculations for the quadrant ring.

The above example case may serve to illustrate (a) the relative insensitivity of the LM vs the CM idealized collision analysis and (b) associated sources of the differences in predicted collision behavior.

Finally, it should be noted that at initial impact: (a) the angle θ between the blade and the normal to the impacted ring segment and (b) the location of the impact point on that impacted straight-line collision-model ring segment (as reflected by the associated values of α and β) will be different when one uses different numbers of ring segments to represent the ring. As the number of ring segments increases, θ will approach the true value for the ring itself, but α and β will continue to "fluctuate". These factors together with the sensitivity of the CM collision model are responsible for the significant difference in predicted blade motion between the 9-element CM case RQ-1B and the 10-element CM case RQ-2B.

### 6.3.3 Effect of Coefficient of Restitution

As noted in Subsection 6.2.1.1, the coefficient of restitution e is a useful quantity for discussing "local impact" of two colliding bodies, since this quantity represents the ratio of the relative velocity of the two bodies after impact to that before impact. Perfectly elastic impact is represented by $e = 1$ whereas $e = 0$ denotes perfectly-inelastic impact (i.e., zero relative velocity after impact). However, the importance of the value of e upon the transient structural deformations of a fragment-impacted structure such as the containment ring depicted in Fig. 45a is not obvious.

To examine this matter, CIVM calculation examples have been carried out by using $e = 1$ and $e = 0$ in (1) cases CR-1B and CR-2B, respectively, (2) cases CR-5B and CR-6B, respectively, and (3) cases CR-10B and CR-11B, respectively. Although these three categories of comparisons involved somewhat different modelings, as can be seen from Table 2, it was found that to the scale of the plots shown on Fig. 48, the differences in ring structural responses for $e = 1$ vs $e = 0$ in each category are almost imperceptible. A more critical comparison, however, is afforded by examining the predicted strains at given locations; shown in Fig. 49 are strains predicted on both the outer surface and the inner surface of the ring at two interesting θ-locations (θ = 13.5° and θ = 49.5°) for case CR-10B (e = 1) and for case CR-11B (e = 0) -- these cases involve the best combination of modeling conditions of all cases listed in Table 2. It is seen that generally the circumferential strains predicted for e = 1 are slightly larger than when e = 0 is employed. It should be noted that initial impact occurs at θ = 44.5°; in regions or quadrants well removed from the impact zone or quadrant, the predicted strains are very small. For example, at θ = 233°, the peak outer surface strain is only about $3.35 \times 10^{-3}$ in/in.

Another interesting effect of the coefficient of restitution is that the number of ring-fragment collisions which has occurred up to a given instant in time after initial impact is much larger for perfectly inelastic impact (e = 0) than for perfectly elastic impact (e = 1). This is illustrated in Fig. 50 where the accumulated number of impacts (ANI) is shown as a function of time after initial impact for cases CR-10B and CR-11B. For perfectly-elastic impact, e = 1 (case CR-10B), the ANI reached 73 by 370 microseconds after initial impact; no further ring-fragment impacts occurred thereafter (at least during the period to 818 μsec after initial impact, during which the response was examined in these calculations). On the other hand, for perfectly-inelastic impact, e = 0 (case CR-11B), the ANI reached 377 by 392 microseconds after initial impact, with no further impacts occurring to at least 818 μsec after initial impact.

The large ANI for the perfectly-inelastic case (e = 0) as compared with the perfectly-elastic collision calculation (e = 1) may be readily appreciated by recalling that for e = 0, the relative velocity of the contact points of the blade and the impacted ring segment are zero. For the next time increment, Δt, of the prediction process, the ring and the blade are treated in a trial incremental calculation as moving independently of each other. Thus, the motion of the impacted ring segment is "retarded" by the action of the internal forces applied to it by its neighboring ring elements, while the fragment proceeds with "uninhibited" motion. The subsequent collision inspection, therefore, frequently reports that during this Δt another collision has taken place -- and the process continues. But for e = 1, a nonzero relative velocity of the impact points of these two objects occurs; subsequent collisions, hence, are less frequent.

It is interesting also to note in the following tabulation that after the impacts have ceased, the blade has somewhat different cg-translational and rotational velocities for the e = 1 case as compared with the e = 0 calculation:

| Blade Motion Quantities | Pre-Impact Conditions of Blade | After Impacts have Ceased<br>e = 1<br>Case CR-10B | <br>e = 0<br>Case CR-11B |
|---|---|---|---|
| $V_y$ (in/sec) | - 7884 | - 2826.8 | - 2138.4 |
| $V_z$ (in/sec) | 0 | - 3038.2 | - 3015.4 |
| $\omega_f$ (rad/sec) | + 1638.3 | + 3137.5 | + 3015.4 |
| $\alpha_f$ (deg) | 0 | + 111.4* | + 105.9** |
| $\alpha_f$ (deg) at TAII = 818 μsec | - | + 192.0 | + 170.3 |

It is seen that after all impacts have ceased, the blade has larger cg-translational ($V_y$ and $V_z$) and rotational ($\omega_f$) velocities for the e = 1 case than for the e = 0 case. Finally, had these calculations been carried out for longer times, it is clear from the fragment and ring motions that further blade-ring collisions would have been seen.

### 6.3.4 Strain Rate Effect

In the present analysis the fragment (blade) is treated as being rigid, but the containment ring is deformable. Thus strain-rate dependent mechanical behavior of the ring can be taken into account, and is expected to influence primarily the response of the ring and secondarily the motion of the fragment.

As described in Subsection 2.3.3, it is assumed herein that strain rate $\dot{\epsilon}$ raises the uniaxial yield point of the material, approximately as follows:

---

*At time after initial impact (TAII) = 370 μsec, or time = 552 + 370 = 922 μsec

**At TAII ≐ 392 μsec

$$\sigma_y = \sigma_o \left[ 1 + \left| \frac{\dot{\varepsilon}}{D} \right|^{\frac{1}{p}} \right]$$

where

$\sigma_y$ = strain-rate dependent uniaxial yield stress

$\sigma_o$ = static uniaxial yield stress

and D and p are constants which depend upon the material involved. For 6061-T6 aluminum, D = 6500 $\sec^{-1}$ and p = 4 are commonly used; these values have been employed in the cases denoted by SR (in EL-PP-SR) in Tables 2 and 3. It is also assumed that the elastic modulus of the material at room temperature conditions is not affected by $\dot{\varepsilon}$.

The effect of $\dot{\varepsilon}$ in the ring-blade problem can be seen by comparing the predicted ring and blade responses for case CR-5B (EL-PP) versus case CR-7B (EL-PP-SR); these cases are identical except for the inclusion of the strain-rate effect in case CR-7B. Let it suffice for present purposes to note that the inclusion of the $\dot{\varepsilon}$ effect in case CR-7B manifests itself in making the ring "stiffer" than in case CR-5B (EL-PP); the peak deformations of the ring were reduced slightly by including the $\dot{\varepsilon}$ effect. The result is in accord with the more detailed $\dot{\varepsilon}$-affected structural responses described in detail in Subsection 5.3.6.3.

Finally, some blade-motion data (which is of secondary interest) for cases CR-5B and CR-7B are compared in Table 4; these include the fragment cg-velocity components $V_y$ and $V_z$ and the angular velocity $\dot{\omega}_f$ of the fragment (blade). From Table 4 it is seen that the predicted velocity histories of the blade for the EL-PP and the EL-PP-SR calculations are very similar. In fact, the "residual" velocities of the blade after no further impacts occur (up to at least TAII = 818 μsec) differ only slightly are are as follows:

| Case | TAII for Last Impact (μsec) | ANI | $V_y$(in/sec) | $V_z$(in/sec) | $\omega_f$(rad/sec) |
|---|---|---|---|---|---|
| CR-5B<br>EL-PP<br>e = 1 | 348 | 89 | - 2791.0 | - 2999.4 | + 2611.7 |
| CR-7B<br>EL-PP-SR<br>e = 1 | 327 | 47 | - 2912.0 | - 2991.3 | + 2621.5 |

The most interesting difference in these results is that the accumulated number of impacts to "impact cutoff" is 89 and 47 for the EL-PP case and the EL-PP-SR case, respectively. That is, the inclusion of "strain-rate stiffening" of the ring reduced the predicted number of impacts (up to at least TAII = 818 μsec); this, incidentally, reduces the computational effort and time.

### 6.3.5 Comparison of Predictions with Experiment for a Complete Free Ring Subjected to Rotor Blade Impact

Having examined the effects of various features in the CIVM approach and various modelings of a free complete circular "containment ring" subjected to impact by a "nondeformable" single rotor blade, it is now perhaps of interest to compare predictions with measurements from NAPTC Tests 88 and 91 (see Table 1). These comparisons are regarded as tentative because of the facts that:

(a) the time from the instant of initial impact until the "time instant" of each photograph in each experiment is uncertain by as much as, perhaps, about 200 to 300 microseconds* (that is, initial impact may have occurred earlier than reported in Ref. 184 by about 200 to 300 μsec) and

(b) the present CIVM analysis contains some simplifying assumptions which expedite the present study but which do not accommodate some aspects of the anticipated and observed behavior (these deficiencies could be remedied in future work).

---

*This uncertainty will be essentially eliminated in planned forthcoming tests of this type through the use of improved techniques.

The predictions discussed in this subsection are limited to only the best two calculation cases for each experiment, Tests 88 and 91. Accordingly, shown in Fig. 51 are deformed-ring profiles and blade locations at a sequence of times for: experiment (NAPTC Test 88), case CR-5B (EL-PP, e = 1), and case CR-7B (EL-PP-SR, e = 1). The plotted points represent the locations of the node points or ends of the finite elements or segments into which the ring has been discretized for analysis. For comparing predictions with experiment, the initial impact location was matched to that observed experimentally. It is seen that there is reasonably good agreement between predictions and experiment, with calculation case CR-7B providing the better comparison. In Fig. 51, the time interval between the "instant of impact" and the photograph for which the deformed-ring data were measured is as reported in Ref. 184.

Figure 52 shows a similar comparison between predictions and experimental results measured for NAPTC Test 91; the predictions are for case CR-10B (EL-PP-SR, e = 1) and case CR-11B (EL-PP-SR, e = 0). Hence, seen again are the effects of perfectly-elastic impacts (e = 1) versus perfectly-inelastic impacts (e = 0); on the scale of Fig. 52, this coefficient-of-restitution effect is minor. Here also (1) it is seen that the predictions agree favorably with experiment, and (2) the "experimental instant of impact" used is as reported in Ref. 184.

A preliminary assessment in Ref. 185 of the Ref. 184 data for NAPTC Tests 88 and 91 suggests that the actual instant of impact in each case may have been significantly earlier than reported in Ref. 184. For NAPTC Test 91, for example, it was estimated in Ref. 185 that the actual instant of impact was perhaps about 200 to 300 microseconds earlier than implied in the experimental data of Fig. 52 and Ref. 184. Hence, as a matter of curiosity, an "impact time correction" of 240 μsec has been applied to the NAPTC Test 91 data and the resulting comparisons with the case CR-10B predictions are shown in Fig. 53. It is seen that the predicted ring responses are somewhat larger than the Test 91 data show when a revised instant of initial impact is used. As mentioned in the beginning of this subsection, this discrepancy may possibly be due to the uncertainty of the time elapsed from the instant of actual initial impact to the "test-recorded" initial impact instant, and may also be due to the simplifying assumptions employed in the present approximate predictions. Further experimental and theoretical studies of this situation are required.

With reference to the results shown in Figs. 51-53, it is seen that the predicted ring responses agree fairly well with experiment, but the observed blade motion (which is of secondary interest in the present context, but of considerable interest in other situations) is not in satisfactory agreement with experimental observations. As for the ring itself, the method of large deflection, elastic-plastic transient response analysis has been evaluated and its accuracy verified by comparison with reliable experimental data in Subsection 5.3 and, hence, is not a source of significant error. However, one source of error is readily apparent: in the experiments, the rotor blade undergoes a significant amount of deformation over a portion of its length at and near the "impact tip" during a brief period following initial impact; little further blade deformation is observed at later times. The blade, hence, becomes a shortened fragment with a smooth curved portion at one end while the other end essentially retains its pre-impact configuration. Accordingly, the "new" fragment which continues the blade-ring interaction process often has the same mass as before but has a reduced moment of inertia -- this factor probably accounts for much of the discrepancy between the observed and the predicted blade motion. Other neglected factors which may contribute to the experimental-theoretical discrepancies include: (a) the neglect of the true material properties of the blade in the collision calculation itself (but this should be minor as results from the $e = 1$ and $e = 0$ extremes show) and (b) forces arising with and energy loss by gouging the ring by the blade.

### 6.3.6 Responses of a Variously-Supported Ring Quadrant to Rotor Blade Impact

As noted in Subsection 6.3.1 and in Figs. 36b and 45b, partial rings are of interest as possible fragment deflection devices. Accordingly, illustrative calculations have been carried out for certain ring quadrant configurations (see Fig. 45b) subjected to impact by a single rotor blade. These ring-quadrant configurations are supported in one of the three following ways: (1) ideally clamped (IC) at $\theta = 0°$, (2) smoothly hinged (H) at $\theta = 0°$, or (3) smoothly hinged (H) at $\theta = 27°$. The pertinent CIVM calculation features are summarized in Table 3, and include cases RQ-1B through RQ-9B; identical "blade release" conditions at t = 0 are used for all cases. The Test 88 conditions reported in Table 1 were used for these calculations. No experimental data, however, are available for comparison with these predictions.

For the ideally-clamped quadrant ring, the predicted ring quadrant and blade responses have already been noted for cases RQ-1B through RQ-3B and cases RQ-4B through RQ-6B in Figs. 46 and 47, respectively. The results from case RQ-7B differ little from those of case RQ-6B and hence are not shown here.

Compared in Fig. 54 are the responses of quadrant rings with an ideally-clamped end (case RQ-5B) and a smoothly-hinged end (case RQ-8B). These responses exhibit the expected qualitative differences. The "blade diversion angle" ($\phi$, see Fig. 36b) is predicted to be approximately 42.6° for both the IC case RQ-5B and the hinged-end case RQ-8B.

The influence of locating the smoothly-supported hinge at $\theta = 27°$ (case RQ-9B) rather than at the end, $\theta = 0°$, of the quadrant ring is depicted in Fig. 55 by the sequence of deformed ring quadrant configurations for case RQ-9B. For this case, the rotor blade cg-trajectory diversion angle $\phi$ is 43.3°.

These examples, RQ-1B through RQ-9B, illustrate only a few of the many possible situations (various ring boundary conditions, various fragments, etc.) and configurations (variable thickness ring, etc.) which may be worthy of study for fragment deflection purposes, and to which the CIVM analysis can readily be applied.

### 6.4 Comments on Potential Extensions of the CIVM Approach to More Complex Problems

In this report the CIVM approach has been illustrated and applied to only a few (see Fig. 45) of the many situations of interest; also, some simplifying approximations have been employed. One fragment having a simple shape has been used, rather than (a) many fragments (Fig. 37c) or (b) a fragment of complex geometry (Fig. 37b); the useful but drastic simplifying assumption that the fragment acts as a nondeformable body was employed. At this point it is useful perhaps to comment briefly on steps which might be taken within the CIVM context to perform a more physically-realistic analysis and/or to analyze containment/deflection devices which are subjected to more complicated fragments and/or conditions.

It is convenient for discussion to consider two categories of problems: (1) those in which various kinds and numbers of fragments are involved but in which the fragments are all nondeformable and (2) a category analogous to (1) except that all of the fragments are treated as deformable. There could also be analyses in which for a certain period of time in the impact-interaction-response behavior, the fragment(s) is regarded as deformable, and in another appropriately-selected time period as nondeformable. In addition to considering problems in which all motion and deformations occur in one plane (planar problems) as is the case throughout this report, more general motion and deformation conditions could be analyzed. However, discussion herein shall be restricted to planar problems.

First, let attention be directed to cases involving only nondeformable fragments. Beyond the simple single-fragment problems depicted in Fig. 36, one could apply the CIVM approach readily to analyze the interaction with containment-deflection rings of complex single fragments such as those shown in Fig. 37b or multiple fragments such as shown in Fig. 37c. Only the bookkeeping becomes more complicated and lengthy than for the Fig. 36 category of problems; no conceptual or analytical difficulties are anticipated. If in addition to interacting with the ring (and/or with each other) the fragment(s) collide with one or more blades of the "remaining" rotating rotor and hence receive a new kick, the bookkeeping becomes still more lengthy and complex, but no basic difficulty is anticipated. However, as noted earlier, treating the fragment(s) as nondeformable will lead to progressively less accurate blade-fragment motion and accordingly to less reliable predictions of subsequent blade-rotor collisions, blade-ring collisions, and ring structural response. How important this effect will be upon the predicted containment/deflection capability of a given system cannot be ascertained at present. However, it is believed that some modification of the analysis should be made to provide more accurate blade-motion predictions for the time period following the initial collision-interaction of the fragment with the containment/deflection ring than is currently afforded by the present rigid-fragment analysis.

Next, therefore, it is appropriate to consider modifying the analysis to account for deformable fragments. Starting with the simple single-fragment configurations of Fig. 36, one could proceed logically to treat the blade as deformable by modeling it as consisting of an appropriate number of finite elements (or segments). While somewhat more complex inspection procedures would need to be devised to determine when and where ring-fragment collisions would occur, the same basic collision-interaction calculation as now employed could be used; as done for the ring itself at present, the blade could be treated as behaving in an EL-SH-SR manner. In this scheme finite-element modeling of both the ring and the blade could be employed throughout the analysis from initial impact until all impact/interaction behavior of interest had occurred; more degrees of freedom and more computing time than currently needed in the present rigid-blade analysis would be involved. Some economies could perhaps be effected by treating the blade as deformable in the initial impact stage and at other critical collision-interaction stages, and by treating the blade as nondeformable for the "in-between" periods.

Another useful variant of this analysis extension might be to treat the ring always and the fragments (always or "intermittently") as deformable but to treat the still-spinning rotor disk and the remaining attached rotor blades as nondeformable. Further study is needed to determine an optimum analysis mix for both accuracy and computational efficiency.

Finally, cognizance should be taken of one aspect of the immediate collision analysis which should be improved -- the seriousness of this defect with respect to predicting efficient, assured containment is not entirely clear. In the present study, the fragment-ring collision has been idealized as a process in which the applied and reactive forces could occur only in a direction perpendicular to the surface of the impacted ring segment. For certain cases, this may be a very good approximation; for other cases (where gouging of the ring by the blade is imminent or present, for example), there would be also both applied and reactive force components in a direction parallel to the surface of the ring. Hence, a modification of the collision analysis to predict and to take into account such "shearing forces" -- as in machining and tool-wear studies -- would be a useful step toward a more realistic simulation of the actual physical situation for certain cases.

# SECTION 7

# SUMMARY AND CONCLUSIONS

## 7.1 Summary

The present study is devoted principally to developing and validating a spatial finite-element (FE) variational method for analyzing the large-deflection elastic-plastic transient deformations of simple structures. As a result, accurate FE predictions of transient strains and large transient deformations of simple structures subjected to known forcing functions have been demonstrated (see Section 5 and Subsection 7.2). A practical problem to which the present method of analysis has been applied is that of containment/deflection structural ring responses to engine rotor-blade fragment impact.

The equations which govern the large deflection dynamic and/or static responses of a solid continuum are discussed in tensor form for convenience and generality. Elastic, elastic-plastic, and strain-rate dependent material behavior are considered. Under the restriction that the strain is small, considerable simplification is attained by assuming that the strain can be decomposed into an elastic (thermodynamically reversible) part and a plastic (thermodynamically irreversible) part. The Mises-Hencky yield criterion and its associated flow rule are adopted to describe the elastic-plastic behavior of an initially homogeneous isotropic material. The strain-hardening behavior is taken into account by using the mechanical sublayer model. The strain-rate effect is approximated by assuming that the uniaxial stress-strain relation is affected by strain rate, only by a quasi-steady increase in the yield stress above the static-test yield stress.

The spatial assumed-displacement finite-element (FE) approach is used to approximate the true infinite degree-of-freedom description of the actual continuum by one which involves a finite number of degrees of freedom. The finite-element concept is used in conjunction with the Principle of Virtual Work and D'Alembert's Principle to obtain the equations of motion of a general solid continuum which is permitted to undergo large-deflection elastic-plastic transient deformations. The resulting equations of motion are developed in two forms: (a) the conventional form, and (b) an improved form; the latter represents a new development. In both forms, the Lagrangian description for displacements, strains, and stresses is employed; that is, the initial undeformed configuration of the continuum is used as a reference for the subsequent motion of the continuum. The resulting equations of motion consist of a finite-size system of second order ordinary (coupled) nonlinear differential equations with the unknowns to be determined being the values of the degrees of freedom (generalized displacements) at the nodes of the finite-element assemblage which represents the continuum. This set of equations is solved timewise by using a direct numerical integration scheme with an appropriate temporal finite-difference approximation operator.

The formulation is developed in detail for a curved beamlike structure which undergoes planar deformations with: (a) zero transverse shear deformation (Bernoulli-Euler-type of deformation behavior) or (b) nonzero transverse shear deformation (Timoshenko-type of deformation behavior). The nonlinearities resulting from both large-deflections and elastic-plastic material behavior are included.

For the Bernoulli-Euler-type of curved beam element, two sets of assumed displacement functions have been employed: (1) both the axial and the transverse displacements are represented by cubic order polynomials with small-amplitude rigid-body modes included (this is termed a CC element) and (2) the axial displacement is represented by a first-order polynomial while the transverse displacement is represented by a cubic-order polynomial, with small-amplitude rigid-body modes included (this is termed an LC element).

As for the Timoshenko-type of curved beam elements, four sets of assumed displacement functions each with various orders of polynomials to approximate the transverse displacement have been studied.

An assessment of this method of analysis is made by means of a sequence of problems for beam and ring example structures which are subjected to transient mechanical loading or to initial impulsive loading; the present predictions are compared with reliable experimental data and/or independent predictions (finite-difference and/or analytical). The temporal central-difference finite-difference operator is used for most of the calculations; however, the use of Houbolt's method and Newmark's method is also explored for the present nonlinear problems.

The structural response predictions and evaluations were carried out in the following categories:

(a) Small-Deflection Linear-Elastic Transient Response

(1) An impulsively-loaded simply-supported beam was analyzed by the present FE method with the Bernoulli-Euler type of LC element and the predicted responses were in excellent agreement with the exact normal mode solution. This comparison served principally to verify the correctness of the computer program.

(2) A free-free "thick" beam loaded by a transient concentrated load at midspan was analyzed by using the several types of Timoshenko-type finite elements developed in this study. The present predictions were compared with the available exact modal solution.

(b) Large-Deflection Elastic-Plastic Transient Response

Included in this category were the following impulsively-loaded structures: (1) a clamped-clamped beam, (2) a ring sector with clamped ends, and (3) a free ring. Transient response predictions carried out by using the present finite-element approach were compared with experimental measurements (of transient strains and large transient deformations) and finite difference predictions.

The problem of engine rotor fragments interacting with either a complete (containment) or a partial (deflection) structural ring is discussed as an example application of the present analysis to a problem of current practical interest. Energy and momentum considerations are employed to predict the collision-induced velocities which are imparted to the colliding fragment and to the affected ring segment; the associated analysis method is termed the collision-imparted velocity method, CIVM. This collision analysis is combined with the FE analysis developed in this study to permit one to predict the resulting large deformation responses of containment/deflection rings. Comparisons with limited experimental data are also given.

## 7.2 Conclusions

A spatial assumed-displacement finite-element variational formulation and solution scheme for the prediction of large-deflection elastic-plastic transient responses of curved beamlike structures has been developed and has been implemented in a computer program; both the older conventional FE formulation and a new improved FE formulation for analyzing this class of problems have been developed and discussed. The accuracy and versatility of these FE methods of analysis have been demonstrated on problems for beam and ring example structures which are subjected to transient mechanical loading or to initial impulsive loading. The present finite-element-predicted responses are found to be in reasonably good agreement with experimental measurements and/or with independent predictions (finite-difference and/or analytical). Also, the present finite-element analysis combined with the impact analysis has been applied to the prediction of containment/deflection structural ring responses to engine rotor fragment impact; the predicted ring responses agree favorably with experiment.

On the basis of the present study, the following conclusions may be stated:

(1) The improved finite-element formulation is more efficient and economical for computing the large-deflection elastic-plastic transient responses of simple structures than the conventional finite-element formulation.

(2) The 3-point central-difference time integration method gives very accurate amplitude and phase transient predictions as long as the time increment size used is small enough. The largest permissible time increment size $\Delta t$ which will avoid calculation instability is affected by the severity of the structural responses; that is, large-deflections play the key role in stiffening the structure and thus requiring a smaller $\Delta t$ than that required for small deflection transient response problems to avoid numerical instability. Also, the large-deflection effects render Houbolt's method and Newmark's method no longer "unconditionally stable" as they are for

small-deflection problems. This is consistent with the observations in Ref. 75.

(3) The Bernoulli-Euler-type of curved beam element with CC assumed-displacement functions exhibits significantly improved predictions, especially for the strain, over the Bernoulli-Euler-type of curved beam element with LC assumed-displacement functions for a given number of degrees of freedom. Also, the former converges very rapidly, but at the expense of a smaller allowable time increment step size compared with the latter.

(4) The Timoshenko-type of beam element with linearly-varying assumed-displacement functions (T1) can provide accurate small-displacement linear-elastic transient response predictions only if the element size is kept small enough. However, in order to obtain more accurate coarse-mesh solutions, one would need to employ assumed displacement polynomial functions of higher order. Better and more efficient solutions, however, are obtained by using T2, T3, or T4 elements, with the T4 type of element being the best. Unfortunately, however, pertinent experimental and/or predicted results for large-deflection, elastic-plastic transient responses with important transverse shear deformation behavior against which to compare predictions which could be readily accomplished with the present FE analysis have not been located.

(5) It is substantially more efficient to use the lumped-mass matrix version (L) rather than the consistent-mass matrix version (C) of the finite-element method for typical transient response problems of the present class; the allowable $\Delta t$ is larger for the former than for the latter. Further, since the transient responses predicted by using the C and the L finite-element calculation are quite close to each other, it is recommended that the lumped-mass (L) version of the finite-element method be selected as being more

efficient (and adequate) for engineering prediction purposes.

(6) For the present planar structures, it has been demonstrated that the present FE method provides accurate predictions of transient structural responses, both deformations and strains, for strains at least as large as about 5 per cent. (It is reasonable to hope that reasonably accurate strain predictions will be provided by this method for strains as large perhaps as 20 per cent which approaches fracture levels of strain for many common aerospace structural materials.)

(7) Based upon the limited comparative studies reported in Subsection 5.3.7.3 between the finite element and the finite difference method, the lumped-mass improved-formulation finite-element method is competitive with the finite difference method with respect to efficiency (computing time and cost) and accuracy for predicting large-deflection elastic-plastic transient responses of simple structures.

(8) The use of the present approximate CIVM approach (Section 6), in conjunction with either the present finite-element procedure or the finite-difference method provides reasonable estimates of the fragment and ring responses arising from single-blade-fragment impact upon a structural ring. Several deficiencies in the present "first-cut" CIVM analysis could be remedied readily by further work, and would clearly lead to improved qualitative and quantitative predictions.

## 7.3 Suggestions for Further Study

Possible areas of interesting and useful further research along the lines of the present investigation are described in the following.

Although one can always resort to numerical experimentation to provide a suitable time increment step size to insure stability, it would be desirable to develop criteria for the maximum allowable time increment step for the large-deflection nonlinear structural transient response problems of the present type; a useful beginning for this type of analysis is described in Chapter 3 of

Ref. 186. Also, before more definite conclusions can be drawn as to whether any one timewise operator is superior to the others, more extensive studies than could be carried out here are required.

Pertinent theoretical and/or experimental results for large-deflection elastic-plastic transient responses of beamlike structure having significantly large transverse-shear deformations have not been found for checking the present Timoshenko-type of finite element; the evaluation of the present Timoshenko-type element for this kind of problem, therefore, remains to be accomplished.

The present-developed finite-element analysis method for predicting large-deflection elastic-plastic transient structural responses is quite general and pertains to any type of loaded body. However, in this report, its application is demonstrated only for simple (curved and/or straight) beamlike structures whose significant deformations are confined to one plane. An extension and application of the present method to analyze plate and shell structures or to structures with complicated geometric shape, material properties, and boundary conditions would be of considerable interest and value, and would provide useful versatility to permit analyzing this group of nonlinear three-dimensional-deformation transient-response problems -- which comprises the largest group of practical-interest problems of this type. Although there are many ways of constructing a lumped-mass matrix (from finite-difference equations, for example) there needs to be developed for these general dynamic systems, better rational ways of constructing the lumped mass matrix.

More definite conclusions need to be drawn as to which of the two general methods the finite-difference or the finite-element method will prove to be superior for particular types of problems in this nonlinear transient response category.

Further, the combining of the finite-difference and the finite-element procedures in space to take maximum advantage of the special merits of each method for appropriate parts of the structure (that is, one might use the finite-difference procedure for smoothly-varying regions of the structure and the finite-element procedure in regions of structural irregularities) is also suggested for further research.

Finally, as noted in Subsection 6.4, the extension of the present collision-imparted velocity method to perform a more physically-realistic analysis (for example, to account for the roughness of the ring-fragment impact surfaces, the deformations of the fragment, etc., and to analyze containment/deflection devices which are subjected to more complicated fragment impact and/or conditions) would be a useful variant of this collision-imparted-velocity method of analysis.

## REFERENCES

1. Chiarito, P.T., "Status of Engine Rotor Burst Protection Program for Aircraft." NASA Aircraft Safety and Operating Problems Conference, Volume I. Langley Research Center, NASA SP-270, May 4-6, 1971, pp. 75-88.

2. Budiansky, B., and Radkowski, P.P., "Numerical Analysis of Unsymmetrical Bending of Shells of Revolution." AIAA Journal, Vol. 1, No. 8, August 1963, pp. 1833-1842.

3. Witmer, E.A., Balmer, H.A., Leech, J.W., and Pian, T.H.H., "Large Dynamic Deformations of Beams, Rings, Plates, and Shells." AIAA Journal, Vol. 1, No. 8, August 1963, pp. 1848-1857.

4. Kalnins, A., "Static, Free Vibrations, and Stability Analysis of Thin Elastic Shells of Revolution." Air Force Flight Dynamic Laboratory Report, AFFDL-TR-68-144, March 1969.

5. Cohen, G.A., "Computer Analysis of Asymmetrical Buckling of Ring-Stiffened Orthotropic Shells of Revolution." AIAA Journal, Vol. 6, No. 1, January 1968, pp. 141-169.

6. Svalbonas, V. and Agrisano, N., "Numerical Analysis of Shells - Vol. II: User's Manual for Stars II - Shell Theory Automated for Rotational Structures." Grumman Aircraft Engineering Corp., Report No. FSR-AD2-01-68.5, August 1968.

7. Pian, T.H.H. and Tong P., "Basis of Finite Element Methods for Solid Continua." International Journal for Numerical Methods in Engineering, Vol. 1, 1969, pp. 3-28.

8. Green, A.E. and Adkins, J.E., Large Elastic Deformations. Oxford, 1960.

9. Novozhilov, V.V., Foundations of the Nonlinear Theory of Elasticity. Graylock Press, 1963.

10. Biot, M.A., Mechanics of Incremental Deformations. John Wiley and Sons, 1965.

11. Fung, Y.C., Foundations of Solid Mechanics. Prentice-Hall, 1965.

12. Fried, I., "Finite Element Analysis of Time-Dependent Phenomena." AIAA Journal, Vol. 7, No. 6, June 1969, pp. 1170-1173.

13. Naghdi, P.M., "Stress-Strain Relations in Plasticity and Thermoplasticity." Proceedings of 2nd Symposium on Naval Structural Mechanics, Pergamon Press, 1960.

14. Hill, R., Mathematical Theory of Plasticity. Oxford, 1950.

15. Green, A.E., and Naghdi, P.M., "A General Theory of an Elastic-Plastic Continuum." Arch. Rational Mech. Anal., Vol. 18, 1965, pp. 251-281.

16. Lee, E.H., "Elastic-Pastic Deformation at Finite Strains." J. Applied Mechanics, Vol. 36, No. 7, March 1969.

17. Chen, W.H., "Necking in a Bar." Technical Report No. ARPA-40, Division of Engineering and Applied Physics. Harvard University, March 1970.

18. Budiansky, B., "A Reassessment of Deformation Theories of Plasticity." J. Appl. Mech., Vol. 26, June 1959, pp. 259-264.

19. Drucker, D.C., "A More Fundamental Approach to Plastic Stress-Strain Relations." Proc. 1st U.S. Natl. Congr. Appl. Mech., ASME, New York, 1952, pp. 487 -491.

20. Prager, W. and Hodge, P.G., Jr., Theory of Perfectly Plastic Solids Dover, New York, 1951.

21. White, G.N., Jr., "Application of the Theory of Perfectly Plastic Solids to Stress Analysis of Strain Hardening Solid." Graduate Div. of Applied Math., Brown University, Tech. Report 51, August 1950.

22. Besseling, J.F., "A Theory of Plastic Flow for Anisotropic Hardening in Plastic Deformation of an Initially Isotropic Material." Rept. S410, National Aeronautical Research Institute, Amsterdam, The Netherlands, 1953.

23. Lee, E.H., "Constitutive Relation for Dynamic Stressing." Technical Report No. 196, Stanford University, June 1969.

24. Ting, T.C.T., "The Plastic Deformation of a Cantilever Beam with Strain Rate Sensitivity under Impulsive Loading." Brown University, TR 70, ONR Contract 562(10), July 1961.

25. McLellan, D.L., "Prediction of Stress-Strain Behavior at Various Strain Rates and Temperatures." 7th International Symposium on High Speed Testing; The Rheology of Solids, Boston, Massachusetts, March 17-18, 1969.

26. Malvern, L.E., "The Propagation of Longitudinal Waves of Plastic Deformation in a Bar of Material Exhibiting a Strain-Rate Effect." J. of Applied Mechanics, V. 18, 1951, pp. 203.

27. Bisplinghoff, R.L., Ashley, H., and Halfman, R.L., Aeroelasticity. Addison-Wesley, Massachusetts, 1957.

28. Hurty, W.R. and Rubenstein, M., Dynamics of Structures, Prentice-Hall, New Jersey, 1964.

29. Meirovitch, L., Analytical Methods in Vibrations. Macmillan Co., 1967.

30. Bolotin, V.V., Dynamic Stability of Elastic Systems. Holden-Day Inc., 1964.

31. Hobbs, N.P., "The Prediction of Lethality Envelopes for Aircraft in Flight", Part 5 - Simplified Prediction Methods (U)", Massachusetts Institute of Technology, WADC TR 56-150 (Part 5), AD 155603, June 1958 (Confidential).

32. Hobbs, N.P., Frazsinelli, G., Wetmore, K.R., and Brown, C.H., Jr., "The Effects of Atomic Explosion Aircraft -- Vo. III: Structural and Aeroelastic Effects (U)", WADC TR 52-244, Vol. III, 1 Jan. 1953 (S-RD).

33. Criscione, E.S., Hobbs, N.P., and Witmer, E.A., "Outline of a Method of Calculating the Elastic and the Post-Buckling Responses of an F-80 Horizontal Stabilizer to Blast." Massachusetts Institute of Technology, WADC TN 56-137, May 1956.

34. Criscione, E.S. and Hobbs, N.P., "The Prediction of Lethality Envelopes for Aircraft in Flight, Part 2 - Detailed Theoretical Analysis (U)." Massachusetts Institute of Technology, WADC TR 56-150 (Part 2), AD 302202, October 1958 (Confidential)

35. Criscione, E.S.,and Hobbs, N.P., and Witmer, E.A., "The Prediction of Lethality Envelopes for Aircraft in Flight, Part 3 - Correlation of Predictions with Field-Test Results on F-80 Drone Aircraft (U)", WADC TR 56-150, Part 3, January 1959 (S-FRD).

36. Roth, R.S., Muskat, R., and Grady, P.J., "Unsymmetrical Bending of Shells of Revolution -- A Digital Computer Program." Avco Corp., Wilmington, Mass., Report KHDR-6, Feb. 1965.

37. Parisse, R.F. and Rossettos, J.N., "SAMS 8, Dynamic Analysis of Multi-region Cone-Cylinders User's Manual." Avco Corp., Report S301-T-4, September 1968.

38. Stern, P. "SADISTIC IV-Stresses and Displacements in Layered Orthotropic Shells of Revolution with Temperature Dependent Properties." Lockheed Missiles and Space Co., Sunneyvale, Calif., Report L-41-66-7, Hardening Technology Studies II, September 1966.

39. Bushnell, D., "Stress, Stability, and Vibration of Complex Shells of Revolution: Analysis and User's Manual for BOSOR 3." Lockheed Missiles and Space Co., SAMSO TR 69-375, September 1969.

40. Cappelli, A.P., Nishimoto, T.S., and Radkowski, P.R., "Analysis of Shells of Revolution Having Arbitrary Stiffness Distributions." AIAA J. Vol. 7, No. 10, Oct. 1969, p. 1909-1915.

41. Schaeffer, H.G., "Computer Programs for Finite-Difference Solutions of Shells of Revolution under Asymmetric Loads." NASA TN D-3926, 1967.

42. Liepins, A.A., "Asymmetric Nonlinear Dynamic Response and Buckling of Shallow Spherical Shells." NASA CR-1376, June 1969.

43. Leech, J.W., Pian, T.H.H., Witmer, E.A., and Herrmann, W., "Dynamic Response of Shells to Externally-Applied Dynamic Loads." Massachusetts Institute of Technology, ASD-TDR-62-610, 1962.

44. Balmer, H.A. and Witmer, E.A., "Theoretical-Experimental Correlation of Large Dynamic and Permanent Deformations of Impulsively-Loaded Simple Structures." Massachusetts Institute of Technology, AFFDL-TDR-64-108, July 1964.

45. Balmer, H.A., "Improved Computer Programs -- DEPROSS 1, 2, and 3 -- to Calculate the Dynamic Elastic-Plastic Two-Dimensional Responses of Impulsively-Loaded Beams, Rings, Plates, and Shells of Revolution." Massachusetts Institute of Technology, ASRL TR 128-3, August 1965.

46. Leech, J.W., "Finite Difference Calculation Method for Large Elastic-Plastic Dynamically-Induced Deformations of General Thin Shells." Massachusetts Institute of Technology, AFFDL-TR-66-171, December 1966.

47. Leech, J.W., Witmer, E.A., and Pian, T.H.H., "Numerical Calculation Technique for Large Elastic-Plastic Transient Deformations of Thin Shells." AIAA Journal, Vol. 6, No. 12, Dec. 1968, pp. 2352-2359.

48. Morino, L., Leech, J.W., and Witmer, E.A., "PETROS 2: A New Finite-Difference Method and Program for the Calculation of Large Elastic-Plastic Dynamically-Induced Deformations of General Thin Shells." Massachusetts Institute of Technology, ASRL TR 152-1 (BRL CR 12) December 1969.

49. Morino, L., Leech, J.W., and Witmer, E.A., "An Improved Numerical Calculation Technique for Large Elastic-Plastic Transient Deformations of Thin Shells." Journal of Applied Mechanics, Vol. 38, No. 2, June 1971, pp. 423-436.

50. Atluri, S., Witmer, E.A., Leech, J.W., and Morino, L., "PETROS 3: A Finite-Difference Method and Program for the Calculation of Large Elastic-Plastic Dynamically-Induced Deformations of Multilayer Variable-Thickness Shells." Massachusetts Institute of Technology, ASRL TR 152-2, (BRL CR 60), November 1971.

51. Pirotin, S.D., Morino, L., Witmer, E.A., and Leech, J.W., "Finite-Difference Analysis for Predicting Large Elastic-Plastic Transient Deformations of Variable-Thickness Soft-Bonded Thin Shells." Massachusetts Institute of Technology, ASRL TR 152-3, Dec. 1971.

52. Huffington, N.J.,Jr., "Blast Response of Panels." BRL TN 1702, August 1968.

53. Massard, J.M., "General Inelastic Response of Layered Shells." Lockheed Missiles and Space Co., (GIRLS I and IA, Report L-H-66-12), (GIRLS II, Report L-41-66-6), September 1966.

54. Krieg, R.D., and Duffey, T.A., "UNIVALVE II: A Code to Calculate the Large Deflection Dynamic Response of Beams, Rings, Plates, and Cylinders." Sandia Corporation, Report SC-RR-68-303, October 1968.

55. Krieg, R.D., Duffey, T.A., and Key, S.W., "The Large Deflection Elastic-Plastic Response of Impulsively-Loaded Beams -- A Comparison between UNIVALVE Computations and Experiment." Sandia Laboratory, SC-RR-68-226, July 1968.

56. Wrenn, B.G., Sobel, L.H., and Silsby, W., "Nonsymmetrical and Nonlinear Response of Thin Shells." Lockheed Missiles and Space Co., Report LMSC-B-72-67-3, Dec. 1967.

57. Silsby, W., Sobel, L.H., and Wrenn, B.G., "Nonsymmetrical and Nonlinear Dynamic Response of Thin Shells, Vol. 1, User's Manual for STAR (Shell Transient Asymmetric Response)." Lockheed Missiles and Space Co., Report LMSC-B-70-68-19, Dec. 1968.

58. Hubka, W.F., "A Calculation Method for the Finite Deflection, Elastic-Plastic Dynamic Response of Shells of Revolution." Kaman Nuclear Report No. KN-69-26(M), January 1969.

59. Fromme, J.A., "Anelastic Three-Dimensional Dynamic Response of Structures of Revolution." Kaman Nuclear, KN-68-447A(R), Dec. 18, 1968.

60. Ball, R.E. "A Program for the Nonlinear Static and Dynamic Analysis of Arbitrarily-Loaded Shells of Revolution." Conference on Computer-Oriented Analysis of Shell Structures, Palo Alto, Calif., August 1970.

61. Kalnins, A., "Free Vibration of Rotationally Symmetric Shells." J. Acoustical Soc. Am., Vol. 36, No. 7, July 1964, pp. 1355-1365.

62. Svalbonas, V. and Angrisano, N., "Numerical Analysis of Shells, Volume I: Unsymmetric Analysis of Orthotropic Reinforced Shells of Revolution." NASA CR-61299, Sept. 1969.

63. Cohen, G.A., "Computer Program for Analysis of Imperfection Sensitivity of Ring-Stiffened Shells of Revolution." NASA CR-1801, October 1971.

64. Archer, J., "Consistent Matrix Formulations for Structural Analysis Using Finite-Element Techniques." AIAA Journal, Vol. 3, October 1965, pp. 1910-1918.

65. Argyris, J.H. "Continua and Discontinua -- An Apercu of Recent Developments of the Matrix Displacement Methods." Proceedings of the First AFFDL Conference on Matrix Methods in Structural Mechanics, AFFDL-TR-66-80, December 1965, pp. 11-190.

66. Wilson, E.L., "A Computer Program for the Dynamic Stress Analysis of Underground Structures." University of California, Berkeley, Report SEL-68-1, January 1968.

67. Greene, B.E., Herness, E.D., Ice, M.W., Salus, W.L., and Strome, D.R., ASTRA: Boeing's Advanced Structural Analyzer." Proceedings, International Symposium on Structures Technology for Large Radio and Radar Telescope Systems, Massachusetts Institute of Technology, Cambridge, Mass. Oct. 1967.

68. Greene, B.E., Jones, R.E., McLay, R.W., and Strome, D.R., "Dynamic Analysis of Shells Using Doubly-Curved Finite Elements." Proc. 2nd AFFDL Conference on Matrix Methods in Structural Mechanics, AFFDL-TR-68-150, October 1968, pp. 185-212.

69. MacNeal, R.H. (Editor), "NASTRAN; Theoretical Manual; User's Manual; Programmer's Manual; and Demonstration Problem Manual." NASA documents, respectively, SP-221, SP-222, SP-223, SP-224, 1969.

70. Klein, S. and Sylvester, R.J., "The Linear Elastic Dynamic Analysis of Shells of Revolution by the Matrix Displacement Method." Proceedings of the First AFFDL Conference in Matrix Methods in Structural Mechanics, AFFDL-TR-66-80, December 1968, pp. 299-328.

71. Kotanchik, J.J., Yeghiayan, R.P., Witmer, E.A., and Berg, B.A., "The Transient Linear Elastic Response Analysis of Complex Thin Shells of Revolution Subjected to Arbitrary External Loadings, by the Finite Element Program SABOR5/DRASTIC." SAMSO TR 70-206 (MIT-ASRL TR 146-10) AD 709189, April 1970.

72. Clough, R.W. and Wilson, E.L., "Dynamic Finite Element Analysis of Arbitrary Thin Shells." Conference on Computer-Oriented Analysis of Shell Structures at Lockheed Palo Alto Research Laboratory, August 1970.

73. Key, S.W. and Beisinger, Z.E., "The Transient Dynamic Analysis of Thin Shells by the Finite Element Method." Third AFFDL Conference on Matrix Methods in Structural Mechanics, October 1971.

74. Stephens, W.B. and Fulton, R.E., "Axisymmetric Static and Dynamic Buckling of Spherical Caps due to Centrally Distributed Pressures." AIAA Journal, Vol. 7, No. 11, Nov. 1969, pp. 2120-2126.

75. Stricklin, J.A., Martinez, J.E., Tillerson, J.R., Hong, J.H., and Haisler, W.E., "Nonlinear Dynamic Analysis of Shells of Revolution by the Matrix Displacement Method." Dept. of Aerospace Eng., Texas A & M University, Report 69-77, Feb. 1970.

76. Stricklin, J.A., Martinez, J.E., Tillerson, J.R., Hong, J.H., and Haisler, W.E., "Nonlinear Dynamic Analysis of Shells of Revolution by the Matrix Displacement Method." AIAA Journal, Vol. 9, No. 4, April 1971, pp. 629-636.

77. Salus, W.L., Ip,C., and VanDerlinden, J.W., "Design Considerations of Elastic-Plastic Structures Subjected to Dynamic Loads." Bound Volume of Technical Papers on Materials and Structural Dynamics, AIAA/ASME 11th Structures, Structural Dynamics, and Materials Conference, Denver, Colorado, April 22-24, 1970, pp. 145-153.

78. Wu, R. W-H., and Witmer, E.A., "Finite-Element Analysis of Large Elastic-Plastic Transient Deformations of Simple Structures." AIAA Journal, Vol. 9, No. 9, Sept. 1971, pp. 1719-1724.

79. Zienkiewicz, O.C., and Parekh, C.J., "Transient Field Problems: Two-Dimensional and Three-Dimensional Analysis by Isoparametric Finite Elements." Intl. Journal for Numerical Methods in Engineering, Vol. 2, 1970, pp. 61-71.

80. Private communication, Prof. L. Sanders, Harvard University 1968.

81. Private communication, W. Broding, Avco Corp. 1968.

82. Turner, M.J., Dill, E.H., Martin, H.C., and Melosh, R.J., "Large Deflection Analysis of Complex Structures Subjected to Heating and External Loads." J. Aero Space Sciences, Vol. 27, Feb. 1960, pp. 97-106.

83. Gallagher, R.H., Gellatly, R.A., Padlog, J., and Mallett, R.H., "Discrete Element Procedure for Thin-Shell Instability Analysis." AIAA Journal, Vol. 5, No. 1, 1967, pp. 138-145.

84. Argyris, J.H., "Matrix Analysis of Shells - Small and Large Displacements." AFFDL TR-67-197, November 1968.

85. Martin, H.C.,, "Derivation of Stiffness Matrices for the Analysis of Large Deflection and Stability Problems." Proc. 1st Conf. on Matrix Methods in Structural Mech., AFFDL-66-80, 1966.

86. Navaratna, D.R., Pian, T.H.H., and Witmer, E.A., "Stability Analysis of Shells of Revolution by the Finite-Element Method." AIAA Journal, Vol. 6, No. 2, February 1968, pp. 355-361.

87. Pian, T.H.H., Tong, P., "Variational Formulation of Finite-Displacement Analysis." A Colloquium of the Internal Union of Theoretical and Applied Mechanics (IUTAM) on High Speed Computing of Elastic Structures, Univ. of Liege, Belgium, August 1970.

88. Pirotin, S.D., "Incremental Large Deflection Analysis of Elastic Structures." Ph.D. Thesis, Department of Aeronautics and Astronautics, Massachusetts Institute of Technology, February 1971.

89. Schmit, L.A., Bogner, F.D., and Fox, R.L., "Finite Deflection Structural Analysis Using Plate and Shell Discrete Elements." AIAA Journal, Vol. 6, No. 5, May 1968, pp.781-791.

90. Oden, J.T., "Numerical Formulation of Nonlinear Elasticity Problems." J. of the Struct. Division, ASCE, Vol. 93, No. ST3, June 1967.

91. Wissman, J.W., "Nonlinear Structural Analysis: Tensor Formulation." Proc. of 1st Conf. on Matrix Methods in Struct. Mech. AFFDL-TR-66-80, pp.679-696.

92. Stricklin, J.A., Haisler, W.E., MacDougall, H.R., and Stebbins, F.J., "Nonlinear Analysis of Shells of Revolution by the Matrix Displacement Method." AIAA Journal, Vol. 6, No. 12, December 1968.

93. Stricklin, J.A., DeAndrade, J.C., Stebbins, F.J., and Cwertny, A.J., Jr., "Linear and Nonlinear Analysis of Shells of Revolution with Asymmetrical Stiffness Properties." Proc. of 2nd Conf. on Matrix Methods in Struct. Mech., AFFDL-TR-68-150, October 1968, pp. 1231-1252.

94. Fowler, J.N., "Elastic-Plastic Discrete-Element Analysis of Asymmetrically Loaded Shells of Revolution." Massachusetts Institute of Technology, ASRL TR 146-3, July 1967.

95. Khojasteh-Bakht, M., and Popov, E.P., "Analysis of Elastic-Plastic Shells of Revolution under Axisymmetric Loading by the Finite Element Method." Univ. of California, Berkeley, Report SESM 67-8, April 1967.

96. Argyris, J.H., Kelsey, S., and Kamel, W.H., "Matrix Methods of Structural Analysis." Proc. 14th Meeting of Structures and Materials Panel, AGARD 1963.

97. Jensen, W.R., Falby, W.E., and Prince, N., "Matrix Analysis Methods for Anisotropic Inelastic Structures." AFFDL-TR-65-220, 1966.

98. Pope, G., "A Discrete Element Method for Analysis of Plane Elastic-Plastic Stress Problems." Royal Aeronautical Establishment, TR 65028 1968.

99. Marcal, P.V., and King, I.P., "Elastic-Plastic Analysis of Two-Dimensional Stress Systems by the Finite-Element Method." Int. J. Mech., Vol. 9, No. 3, 1967, pp. 143-155.

100. Mendelson, A., and Manson, S.S., "Practical Solution of Plastic Deformation Problems in the Elastic-Plastic Range." NASA TR R28, 1959.

101. Marcal, P.V., "A Comparative Study of Numerical Methods of Elastic-Plastic Analysis." AIAA Journal, Vol. 6, No. 1, January 1968, pp. 157-158.

102. Armen, H., Jr., Levine, H.S., and Pifko, A., "Elastic-Plastic Behavior of Plates Under Combined Bending and Stretching." Bound Volume of Technical Papers on Structures, AIAA/ASME 11th Structures, Structural Dynamics and Materials Conference, Denver, Colorado, April 22-24, 1970, pp. 224-238.

103. Yaghmai, S., "Incremental Analysis of Large Deformations with Applications to Axisymmetric Shells of Revolution." NASA CR-1350, June 1969.

104. Hibbitt, H.D., Marcal, P.V., and Rice, J.R., "A Finite Element Formulation for Problems of Large Strain and Large Displacements." Division of Engineering, Brown University, Report N00014-0007/2, June 1969.

105. Lee, E.H., and Symonds, P.S., "Large Plastic Deformations of Beams Under Transverse Impact." Journal of Applied Mechanics, Vol. 19, No. 3, Trans. ASME, Vol. 74, Sept. 1952, pp. 308-314.

106. Pian, T.H.H., "A Note on Large Plastic Deformations of Beams Under Transverse Impact." Massachusetts Institute of Technology ASRL TR 25-11, May 1952.

107. Owen, R.H., and Symonds, P.S., "Plastic Deformations of a Free Ring Under Concentrated Dynamic Loading." Journal of Applied Mechanics, Vol. 22, No. 4, Trans. ASME, Vol. 77, December 1955, pp. 523-529.

108. Wang, A.J., "The Permanent Deflection of a Plastic Plate Under Blast Loading." Journal of Applied Mechanics, Vol. 22, 1955, pp. 375-376.

109. Symonds, P.S., and Mentel, T.J., "Impulsive Loading of Plastic Beams with Axial Constraints." Journal of the Mechanics and Physics of Solids, Vol. 6, 1958, pp. 186-202.

110. Florence, A.L., and Firth, R.D., "Rigid-Plastic Beams Under Uniformly Distributed Impulses." Journal of Applied Mechanics, Vol. 32, No. 3, Trans. ASME, Vol. 87, Series E, Sept. 1965, pp. 481-488.

111. Florence, A.L., "Circular Plate Under a Uniformly Distributed Impulse." International Journal of Solids and Structures, Vol. 2, No. 1, 1966, pp. 37-47.

112. Symonds, P.S., "Survey of Methods of Analysis for Plastic Deformation of Structures Under Dynamic Loading." Final Report BU/NSRDC/1-67, Office of Naval Research Contract Nonr 3248 (01)(X), Division of Engineering, Brown University, June 1967.

113. Jones, N., "Finite Deflection of a Rigid Viscoplastic Strain-Hardening Annular Plate Loaded Impulsively." Journal of Applied Mechanics, Vol. 35, No. 2, Trans. ASME, Vol. 90, Series E, June 1968, pp. 349-356.

114. Jones, N., "The Influence of Large Deflections on the Behavior of Rigid-Plastic Cylindrical Shells Loaded Impulsively." Report No. 68-21, Department of Naval Architecture and Marine Engineering, Massachusetts Institute of Technology, Cambridge, Mass., Nov. 1968.

115. Jones, N., "A Theoretical Study of the Dynamic Plastic Behavior of Beams and Plates with Finite Deflections." Int. J. Solid Structures, Vol. 7, 1971, pp. 1007-1029.

116. Walters, R.M. and Jones, N., "An Approximate Theoretical Study of the Dynamic Plastic Behavior of Shells." Massachusetts Institute of Technology, Dept. of Ocean Engineering, Report No. 71-12, August 1971.

117. Martin, J.B., "A Displacement Bound Principle for Inelastic Continua Subjected to Certain Classes of Dynamic Loading." J. of Appl. Mech., Vol. 32, No. 1, 1965, pp. 1-6.

118. Martin, J.B., and Symonds, P.S., "Mode Approximations for Impulsively Loaded Rigid-Plastic Structures." Proceedings, ASCE, Journal of Engineering Mechanics Division, Vol. 92, 1966, pp. 43-66.

119. Martin, J.B., "The Determination of Upper Bounds on Displacements Resulting From Static and Dynamic Loading by the Application of Energy Methods." Proceedings of the 5th U.S. National Congress of Applied Mechanics, ASME, 1966, pp. 221-236.

120. Martin, J.B., "Time and Displacement Bound Theorems for Viscous and Rigid-Visco-Plastic Continua Subjected to Impulsive Loading." Proc. 3rd Southeastern Conference on Developments in Th. and Appl. Mech., Vol. 3, 1968, pp. 1-22.

121. Morales, W. and Nevill, G.E., "Lower Bounds on Deformations of Dynamically-Loaded Rigid-Plastic Continua." AIAA Journal, Vol. 8, No. 11, Nov. 1970, pp. 2043-2046.

122. Robinson, D.N., "A Displacement Bound Principle for Elastic-Plastic Structures Subjected to Blast Loading." J. Mech. and Physics of Solids, Vol. 18, No. 1, Jan. 1970, pp. 65-80.

123. Witmer, E.A., et al., "Responses of Plates and Shells to Intense Loads of Short Duration." Massachusetts Institute of Technology, WADD TR-60-433, April 1960.

124. Greenspon, J.E., "Elastic and Plastic Behavior of Cylindrical Shells Under Dynamic Loads Based on Energy Criteria." Technical Report 3, J.G. Engineering Research Associates, Baltimore, Md., Feb. 1963.

125. Greenspon, J.E., "Post-Failure Deflections of Cylindrical Shells Under Dynamic Lateral Loads." J.G. Engineering Research Associates, Baltimore, Md., August 1964.

126. Greenspon, J.E., "Collapse, Buckling, and Postfailure Behavior of Cylindrical Shells Under Elevated Temperature and Dynamic Loads." Technical Report 6, J.G. Engineering Research Associates, Baltimore, Md., Nov. 1965.

127. Greenspon, J.E.,, "Elastic-Plastic Response of Structures to Blast and Impulse Loads." Technical Report 7, J.G. Engineering Research Associates, Baltimore, Md., Mar. 1967.

128. Witmer, E.A., and Kotanchik, J.J.,"Progress Report on Discrete-Element Elastic and Elastic-Plastic Analysis of Shells of Revolution Subjected to Axisymmetric and Asymmetric Loading." Proceeding of 2nd AFFDL Conference on Matrix Methods in Structural Mechanics, AFFDL-TR-68-150, Oct. 1968, pp. 1341-1453.

129. Irons, B.M., and Draper, K.J., "Inadequacy of Nodal Connections in a Stiffness Solution of Plate Bending." AIAA Journal, Vol. 3, No. 5, May 1965, pg . 961.

130. Tong, P., and Pian, T.H.H., "The Convergence of Finite Element Method in Solving Linear Elastic Problems." Intl. Jnl. Solids and Structures, 3, 1967, pp. 865-879.

131. Kopal, Z., Numerical Analysis. Chapman and Hall Ltd., London, 1961.

132. Hildebrand, F.B., Introduction to Numerical Analysis, McGraw-Hill Book Co., New York 1956.

133. Huffington, N.J., Jr., "Numerical Analysis of Elastoplastic Stress." U.S. Army Ballistic Research Laboratory, Memorandum Report No. 2006, September 1969.

134. Barr, G.W. and Young, E.G., "MAT2D: A Plane-Stress Material Model for an Elastic-Plastic Anisotropic Strain-Hardening Material." Sandia Laboratories, Report SC-RR-69-656, January 1970.

135. Houbolt, J.C., "A Recurrence Matrix Solution for the Dynamic Response of Elastic Aircraft." Journal of the Aero. Sciences, Vol. 17, 1950, pp. 540-550.

136. Newmark, N.M. and Chan, S.P., "A Comparison of Numerical Methods for Analyzing Dynamic Response of Structures." Univ. of Illinois, Civil Engineering Structural Research Series 36, October 1952.

137. Newmark, N.M., "A Method of Computation for Structural Dynamics." Journal of the Engineering Mechanics, Div., Proceedings of the Am. Soc. of Civil Eng., Vol. 85, July 1959, pp. 67-94.

138. Chan, S.P., Cox, H.L., and Benfield, W.A., "Transient Analysis of Forced Vibrations of Complex Structural-Mechanical Systems." J. Royal Aero. Soc., Vol. 66, No. 619, July 1962, pp. 457-460.

139. Gurtin, M.E., "Variational Principles for Linear Elastodynamics." Arch. Rat. Mech. Ancl., Vol. 16, 1964, pp. 34-50.

140. Becker, E.B. and Nickell, R.E., "Stress Wave Propagation Using the Extended Ritz Method.", Proc. 10th ASME/AIAA Structures, Structural Dynamics, and Materials Conference, 1969.

141. Wilson, E.L., "Elastic Dynamic Response of Axisymmetric Structures." Univ. of Calif., Berkeley, Report 69-2, 1969.

142. de Vogelaere, R., "A Method for the Numerical Integration of Differential Equations of Second Order Without Explicit First Derivatives." Journal of Research, National Bureau of Standards, Vol. 54, No. 3, 1955.

143. O'Brien, G.G., Hyman, M.A., and Kaplan, S., "A Study of the Numerical Solution of Partial Differential Equations." J. Math and Phys., Vol. 29, 1951, pp. 223-251.

144. Levy, S. and Kroll, W.D., "Errors Introduced by Finite Space and Time Increments in Dynamic Response Computation." Journal of Research, National Bureau of Standards, Vol. 51, 1953, pp. 57-68.

145. Lax, P.D., and Richtmyer, R.D., "Survey of the Stability of Finite Difference Equations." Comm. on Pure and Appl. Math., Vol. 9, 1956, No. 267-293.

146. Leech, J.W., "Some Experiments with the Wave Equation." Term Project in 2.092, MIT, May 1964.

147. Leech, J.W., "Stability of Finite-Difference Equations for the Transient Response of a Flat Plate." AIAA Journal, Vol. 3, No. 9, Sept. 1965, pp. 1772-1773.

148. Leech, J.W., Hsu, P.T., and Mack, E.W., "Stability of a Finite-Difference Method for Solving Matrix Equations." AIAA Journal, Vol. 3, No. 11, November 1965, pp. 2172-2173.

149. Johnson, D.E., "A Proof of the Stability of the Houbolt Method." AIAA Journal, Vol. 4, 1966, pp. 1450-1451.

150. Nickell, R.E., "On the Stability of Approximation Operators in Problems of Structural Dynamics." Bell Telephone Laboratories, Tech. Memo 69-4116-14, Nov. 1969 (also Int'l J. Solids and Structures, Vol. 7, 1971, pp. 301-319).

151. Krieg, R.D., "Unconditional Stability in Numerical Time Integration Methods." Sandia Laboratories, Report SC-DR-70-400, 1970.

152. Krieg, R.D. and Monteith, H.C., "A Large Deflection Transient Analysis of Arbitrary Shells Using Finite Differences." LMSC/AFFDL Conference on Computer Oriented Analysis of Shell Structures, Palo Alto, Calif., August 1970.

153. Wilson, E.L. and Clough, R.W., "Dynamic Response by Step-by-Step Matrix Analysis." Symposium on the Use of Computers in Civil Engineering, Lisbon, Portugal, October 1962.

154. Sylvester, R.J., "DRASTIC II." Aerospace Corp. TR-0158(S3816-71)-2 (also SAMSO TR 68-226), May 1968.

155. Fu, C.C., "A Method for the Numerical Integration of the Equations of Motion Arising from a Finite Element Analysis." Journal of Applied Mechanics, Vol. 37, September 1970, pp. 599-605.

156. McLaughlin, D.K., "Solution to the Nonlinear Vibrating String Equation Using the Finite Difference Technique." Term Project in 2.092, MIT, May 1965.

157. Stricklin, J.A., Navaratna, D.R., and Pian, T.H.H., "Improvements on the Analysis of Shells of Revolution by the Matrix Displacement Method." AIAA Journal Vol. 4, No. 11, November 1966, pp. 2069-2071.

158. Jones, R.E., Strome, D.R., "Direct Stiffness Method Analysis of Shells of Revolution Utilizing Curved Elements." AIAA Journal, Vol. 4, No. 9, September 1966, pp. 145-153.

159. Washizu, K., Variational Methods in Elasticity and Plasticity. Permagon Press Ltd., 1968.

160. Cantin, G. and Clough, R.W., "A Curved, Cylindrical Shell Discrete Element." AIAA Journal, Vol. 6, No. 6, June 1968, pp. 1057-1062.

161. Coco, R.H., "Stiffness Matrix for Curved-Tapered and Straight-Tapered Shell Stiffeners." SAMSO TR 69-135 (also MIT ASRL TR 146-6), March 1969.

162. Tong, P., "On the Numerical Problems of the Finite Element Methods." The SMD Symposium on Computer Aided Engineering, The University of Waterloo, Waterloo, Ontario, Canada, May 1971.

163. Clough, R.W., and Felippa, C.A., "A Refined Quadrilater Element for Analysis of Plate Bending." Proceeding of 2nd AFFDL Conference on Matrix Methods in Struct. Mechanics, AFFDL-TR-68-150, October 1968, pp. 399-440.

164. Wu, R. W-H., "Discrete Element Analysis of Beams, Plates, and Cylindrical Shells including Transverse Shear Deformation", M.S. Thesis, Department of Aeronautics and Astronautics, Massachusetts Institute of Technology, June 1969.

165. Leonard, R.W., "On Solution of the Transient Response of Beams." NASA TR R-21, 1959.

166. Pian, T.H.H. and Tong, P., "Rationalization in Deriving Element Stiffness Matrix by Assumed Stress Approach." Proc. 2nd AFFDL Conference on Matrix Methods in Structural Mechanics, AFFDL-TR-68-150, October 1968, pp. 441-470.

167. Clark, E.N., Schmitt, F.H., Ellington, D.G., Engle, I.A., and Nicolaides,S., "Plastic Deformation of Structures.I: Plastic Deformation of Beams," Picatinny Arsenal, FDL-TDR-64-64, Vol. I, May 1965.

168. Clark, E.N., Schmitt, F.H., and Nicolaides, S., "Plastic Deformation of Structures.II: Plastic Deformation of Rings." Picatinny Arsenal, FDL-TDR-64-64, Vol. II, March 1968.

169. Yeghiayan, R.P., Witmer, E.A., and Leech, J.W., "Theoretical and Experimental Studies of the Interaction Forces and Responses of Structural Rings Subjected to Engine Rotor Fragment Impact." ASRL TR 154-5, Aeroelastic and Structures Research Laboratory, Massachusetts Institute of Technology (in preparation).

170. Martino, A.A., and Mangano, G.J., "Turbine Disk Burst Protection Study. Phase I -- Final Report on Problem Assignment NASA DPR R-105. NAEC-AEL-1793, U.S. Navy, March 1965. (Available as NASA CR-80962.)

171. Martino, A.A., and Mangano, G.J., "Turbine Disk Burst Protection Study. Phases II and III -- Final Report on Problem Assignment NASA DPR R-105. NAEC-AEL-1848, U.S. Navy, February 1967. (Available as NASA CR-84967.)

172. Martino, A.A., and Mangano, G.J., "Rotor Burst Protection Program Initial Test Results. Phase IV - Final Report [on Problem Assignment] NASA DPR R-105. NAPTC-AED-1869, U.S. Navy, April 1968. (Available as NASA CR-95967.)

173. Martino, A.A., and Mangano, G.J., "Rotor Burst Protection Program. Phase V -- Final Report [on] Problem Assignment NASA DPR R-105. NAPTC-AED-1901, May 1969. (Available as NASA CR-106801.)

174. -- "Rotor Burst Protection Program." (Study for NASA Lewis Research Center on NASA DPR R-105 and NASA Interagency Order C-41581-B), Naval Air Propulsion Test Center, Phila., Pa., Monthly Progress Reports, September 1969 to December 1971.

175. Loden, W.A,and Witmer, E.A., "A Limited Parametric Study of Large Elastic-Plastic Dynamic Response of Single-Layer Circular Rings to Sequential External Forces." Picatinny Arsenal Tech. Memo. No. 1604 (also ASRL TR 122-3 Aeroelastic and Structures Research Laboratory, M.I.T.), February 1965.

176. McCallum, R.B., Leech, J.W., and Witmer, E.A., "Progress in the Analysis of Jet Engine Burst-Rotor Containment Devices. ASRL TR 154-1, Aeroelastic and Structures Research Laboratory, MIT, August 1969. (Available as NASA CR-107900.)

177. McCallum, R.B., Leech, J.W., and Witmer, E.A., "On the Interaction Forces and Responses of Structural Rings Subjected to Fragment Impact. ASRL TR 154-2, Aeroelastic and Structures Research Laboratory, MIT, Sept. 1970. (Available as NASA CR-72801.)

178. Wilkins, M.L., "Calculation of Elastic-Plastic Flow." Lawrence Radiation Laboratory, Livermore, UCRL-7322, Rev. I, Jan. 1969.

179. Kreyenhagen, K.N., Read, H.E., Rosenblatt, M., and Moore, W.C.,,"Hardening Technology Studies - III, STRIDE Code Solutions and Extension to Multi-material Systems." SAMSO-TR-69-16, December 1968.

180. Hageman, L.J. and Walsh, J.M., "HELP: A Multimaterial Eulerian Program for Compressible Fluid and Elastic-Plastic Flows in Two Space Dimensions and Time." (Vol. I - Formulation; Vol. II - Fortran Listing of HELP), BRL CR No. 39, Systems, Science, and Software, La Jolla, Calif., May 1971.

181. Balmer, H.A. and Witmer, E.A., "Theoretical-Experimental Correlation of Large Dynamic and Permanent Deformations of Impulsively-Loaded Unbonded Concentric Rings." AFFDL-TR-65-143, Aeroelastic and Structures Research Laboratory, Massachusetts Institute of Technology, Nov. 1965.

182. Eshbach, O.W. (Editor), Handbook of Engineering Fundamentals. John Wiley and Sons, New York, 1936.

183. Zirin, R., "Examination of the Collision Force Method for Analyzing the Response of Simple Containment/Deflection Structures to Engine Rotor Fragment Impact." ASRL TR 154-6, Aeroelastic and Structures Research Laboratory, Massachusetts Institute of Technology (in preparation).

184. Private communications from A.A. Martino, Naval Air Propulsion Test Center, Phila., Pa., April 1970.

185. Private communications from R.P. Yeghiayan, Aeroelastic and Structures Research Laboratory, Massachusetts Institute of Technology, 1971.

186. Lapidus, L., and Seinfeld, J.H., Numerical Solution of Ordinary Differential Equations. Academic Press, N.Y., 1971.

187. Key, S.W., Krieg, R.D., "Comparison of Finite Element and Finite Difference Methods," Sandia Corporation, SC-DC-713890, International Symposium on Numerical and Computer Methods in Structural Mechanics, Urbana, Illinois, September 8-10, 1971.

188. Bushnell, D., "Energy Approaches to Finite Difference and Finite Element Methods," International Symposium on Numerical and Computer Methods in Structural Mechanics, Urbana, Illinois, September 8-10, 1971.

189. Pian, T.H.H., "Variational Formulations of Numerical Methods in Solid Continua," The SMD Symposium on Computer Aided Engineering, The University of Waterloo, Waterloo, Ontario, Canada, May 1971.

190. Tong, P., Pian, T.H.H., and Bucciarelli, L.L., "Mode Shapes and Frequencies by Finite Element Method Using Consistent and Lumped Masses", International Journal of Computers and Structures, Vol. 1, 1971, pp. 623-638.

## TABLE 1

## DATA CHARACTERIZING NAPTC RING TESTS 88 and 91

### Ring Data

| | Test 88 | Test 91 |
|---|---|---|
| Outside Diameter (in) | 17.619 | 17.619 |
| Radial Thickness (in) | 0.153 | 0.152 |
| Axial Length (in) | 1.506 | 1.506 |
| Material | 2024-T4 Aluminum | 2024-T4 |
| Elastic Modulus E (psi) | $10^7$ | $10^7$ |
| PP Yield Stress $\sigma_o$ (psi) | 50,000 | 50,000 |

### Fragment Data

| | | |
|---|---|---|
| Type | T-58 Single Blade | T-58 Single Blade |
| Material | SEL-15 | SEL-15 |
| Outer Radius (in) | 7.0 | 7.0 |
| Fragment Centroid from Center of Rotation (in) | 4.812 | 4.812 |
| Fragment Tip Clearance from Ring (in) | 1.657 | 1.658 |
| Fragment Length (in) | 3.5 | 3.5 |
| Fragment Length from CG to Tip (in) | 2.188 | 2.188 |
| Fragment Weight (lbs) | 0.084 | 0.084 |
| Fragment Moment of Inertia about its CG (in lb $sec^2$) | $2.163 \times 10^{-4}$ | $2.163 \times 10^{-4}$ |
| Failure Speed (RPM) | 15,374.3 | 15,644.4 |
| Fragment Tip Velocity (ips) | 11,270. | 11,467. |
| Fragment Centroidal Velocity (ips) | 7,748. | 7,884. |
| Fragment Initial Angular Velocity (rad/sec) | 1,610. | 1,638.3 |
| Fragment Translation KE (in lb) | 6,525. | 6,756. |
| Fragment Rotational KE (in lb) | 280.4 | 290.3 |

TABLE 2

SUMMARY OF CIVM CALCULATION CASES FOR SINGLE-BLADE FRAGMENT IMPACT AGAINST A FREE COMPLETE CIRCULAR RING

| Run | Ring Finite Element Data |  |  |  |  |  | Material Properties of Ring | Collision Features |  | Time Increment Δt(μsec) | Time of Initial Impact (μsec) |
|---|---|---|---|---|---|---|---|---|---|---|---|
|  | Breakdown by Quadrant |  |  |  | Element Type (LC or CC) | Mass Matrix (C or L) |  | Collision Model (CM or LM) | Coef. of Restitution e |  |  |
|  | Q1 | Q2 | Q3 | Q4 |  |  |  |  |  |  |  |
| Test 88 Conditions |  |  |  |  |  |  |  |  |  |  |  |
| CR-1B | 5 | 5 | 5 | 5 | LC | C | EL-PP | CM | 1.0 | 1.0 | 542 |
| CR-2B | 5 | 5 | 5 | 5 | LC | C | EL-PP | CM | 0 | " | 542 |
| CR-3B | 9 | 6 | 6 | 6 | LC | C | EL-PP | CM | 1.0 | " | 556 |
| CR-4B | 9 | 6 | 6 | 6 | LC | C | EL-PP-SR | CM | 1.0 | " | 556 |
| CR-5B | 10 | 6 | 6 | 6 | LC | L | EL-PP | LM | 1.0 | " | 562 |
| CR-6B | 10 | 6 | 6 | 6 | LC | L | EL-PP | LM | 0 | " | 562 |
| CR-7B | 10 | 6 | 6 | 6 | LC | L | EL-PP-SR | LM | 1.0 | " | 562 |
| Test 91 Conditions |  |  |  |  |  |  |  |  |  |  |  |
| CR-8B | 10 | 6 | 6 | 6 | LC | L | EL-PP-SR | LM | 1.0 | " | 552 |
| CR-9B | 10 | 6 | 6 | 6 | CC | L | EL-PP-SR | LM | 1.0 | " | 552 |
| CR-10B | 10 | 6 | 6 | 6 | CC | C | EL-PP-SR | LM | 1.0 | " | 552 |
| CR-11B | 10 | 6 | 6 | 6 | CC | C | EL-PP-SR | LM | 0 | " | 552 |

## TABLE 3

## SUMMARY OF CIVM CALCULATION CASES FOR SINGLE-BLADE FRAGMENT IMPACT UPON A SUPPORTED PARTIAL RING*

| Run | Ring Quadrant Finite Element Data | | | Supported End | Material Properties of Ring | Collision Features | | Time Increment Δt (μsec) | Time of Initial Impact (μsec) |
|---|---|---|---|---|---|---|---|---|---|
| | No. | Element Type (LC or CC) | Mass Matrix (C or L) | | | Collision Model (CM or LM) | Coef. of Restitution e | | |
| RQ-1B | 9 | LC | C | IC | EL-PP-SR | CM | 1.0 | 1.0 | 556 |
| RQ-2B | 10 | LC | C | IC | EL-PP-SR | CM | " | " | 562 |
| RQ-3B | 15 | LC | C | IC | EL-PP-SR | CM | " | " | 561 |
| RQ-4B | 9 | LC | L | IC | EL-PP-SR | LM | " | " | 556 |
| RQ-5B | 10 | LC | L | IC | EL-PP-SR | LM | " | " | 562 |
| RQ-6B | 15 | LC | L | IC | EL-PP-SR | LM | " | " | 561 |
| RQ-7B | 15 | LC | C | IC | EL-PP-SR | LM | " | " | 561 |
| RQ-8B | 10 | LC | L | Hinged End | EL-PP-SR | LM | " | " | 562 |
| RQ-9B | 10 | LC | L | Hinged at 27° | EL-PP-SR | LM | " | " | 562 |

*The Test 88 conditions of Table 1 were used for these calculations.

## TABLE 4

### BLADE MOTION AND IMPACT DATA FOR CASE CR-5B(EL-PP) VS. CASE CR-7B(EL-PP-SR)

| | Case CR-5B (EL-PP) | | | | Case CR-7B (EL-PP-SR) | | | |
|---|---|---|---|---|---|---|---|---|
| TAII (μsec) | ANI | $V_y$ (in/sec) | $V_z$ (in/sec) | $\omega_f$ (rad/sec) | ANI | $V_y$ (in/sec) | $V_z$ (in/sec) | $\omega_f$ (rad/sec) |
| Pre-Impact | 0 | -7748. | 0 | +1610.0 | 0 | -7748.0 | 0 | +1610.0 |
| 0 | 1 | -6786.9 | -1125.3 | +2249.9 | 1 | -6786.9 | -1125.3 | +2249.9 |
| 16 | 2 | -6604.2 | -1267.7 | +2266.5 | 2 | -6523.8 | -1330.4 | +2273.9 |
| 23 | 5 | -6332.4 | -1476.1 | +2289.4 | 6 | -6231.8 | -1551.7 | +2297.3 |
| 27 | 7 | -6216.2 | -1561.6 | +2297.3 | 7 | -6099.5 | -1647.6 | +2305.8 |
| 35 | 10 | -6018.5 | -1702.0 | +2308.1 | 11 | -5893.0 | -1792.2 | +2316.9 |
| 36 | 11 | -5871.2 | -1802.6 | +2314.3 | 12 | -5877.9 | -1802.6 | +2317.6 |
| 44 | -- | -- | -- | -- | 15 | -5599.2 | -1989.5 | +2330.3 |
| 45 | 14 | -5614.4 | -1970.0 | +2322.0 | -- | --- | -- | -- |
| 50 | 15 | -5457.2 | -2068.6 | +2325.7 | 17 | -5452.6 | -2084.6 | +2336.9 |
| 61 | 17 | -5300.2 | -2164.0 | +2329.4 | 21 | -5132.4 | -2285.5 | +2354.6 |
| 71 | 19 | -4934.2 | -2377.3 | +2343.9 | -- | -- | -- | -- |
| 72 | -- | -- | -- | -- | 24 | -4933.6 | -2406.7 | +2373.7 |
| 79 | -- | -- | -- | -- | 25 | -4894.9 | -2430.2 | +2380.0 |
| 85 | 21 | -4781.7 | -2463.1 | +2360.5 | -- | -- | -- | -- |
| 141 | -- | -- | -- | -- | 26 | -3967.9 | -2765.6 | +2406.8 |
| 144 | 22 | -4449.1 | -2581.8 | +2370.7 | -- | -- | -- | -- |
| 168 | 25 | -3827.3 | -2786.4 | +2391.7 | -- | -- | -- | -- |
| 178 | 28 | -3724.7 | -2815.7 | +2396.5 | -- | -- | -- | -- |
| 188 | -- | -- | -- | -- | 28 | -3477.0 | -2895.3 | +2447.0 |
| 189 | 32 | -3569.7 | -2857.8 | +2405.6 | -- | -- | -- | -- |
| 198 | 35 | -3459.5 | -2886.0 | +2414.6 | -- | -- | -- | -- |
| 210 | 42 | -3353.0 | -2911.6 | +2426.9 | -- | -- | -- | -- |
| 215 | -- | -- | -- | -- | 29 | -3453.0 | -2901.0 | +2451.3 |
| 222 | 45 | -3305.6 | -2922.4 | +2434.5 | -- | -- | -- | -- |
| 246 | 53 | -3233.8 | -2937.9 | +2450.2 | 31 | -3287.9 | -2939.5 | +2488.1 |
| 255 | 58 | -3213.0 | -2942.2 | +2456.3 | -- | -- | -- | -- |

TABLE 4 (CONCLUDED)

| | Case CR-5B (EL-PP) | | | | Case CR-7B (EL-PP-SR) | | | |
|---|---|---|---|---|---|---|---|---|
| TAII (μsec) | ANI | $V_y$ (in/sec) | $V_z$ (in/sec) | $\omega_f$ (rad/sec) | ANI ANI | $V_y$ (in/sec) | $V_z$ (in/sec) | $\omega_f$ (rad/sec) |
| 264 | 61 | -3199.8 | -2944.8 | +2460.8 | -- | -- | -- | -- |
| 273 | 63 | -3032.1 | -2971.7 | +2513.3 | -- | -- | -- | -- |
| 274 | -- | -- | -- | -- | 32 | -3110.8 | -2966.9 | +2544.9 |
| 298 | 65 | -2951.6 | -2982.0 | +2543.2 | 39 | -2996.9 | -2982.2 | +2587.6 |
| 307 | 71 | -2888.0 | -2989.6 | +2567.9 | -- | -- | -- | -- |
| 310 | -- | -- | -- | -- | 42 | -2941.6 | -2988.9 | +2611.1 |
| 316 | 76 | -2841.8 | -2994.6 | +2587.4 | 43 | -2939.2 | -2989.2 | +2612.2 |
| 326 | 80 | -2816.8 | -2997.1 | +2598.7 | 46 | -2922.5 | -2991.0 | +2620.2 |
| 327 | 81 | -2812.7 | -2997.5 | +2600.6 | 47 | -2912.0 | -2991.3 | +2621.5 |
| 335 | 84 | -2802.0 | -2998.5 | +2605.8 | " | " | " | " |
| 345 | 87 | -2794.9 | -2999.1 | +2609.5 | " | " | " | " |
| 347 | 88 | -2794.5 | -2999.1 | +2609.8 | " | " | " | " |
| 348 | 89 | -2791.0 | -2999.4 | +2611.7 | " | " | " | " |
| . | " | " | " | " | " | " | " | " |
| . | " | " | " | " | " | " | " | " |
| . | " | " | " | " | " | " | " | " |
| 818 | 89 | -2791.0 | -2999.4 | +2611.7 | 47 | -2912.0 | -2991.3 | +2621.5 |

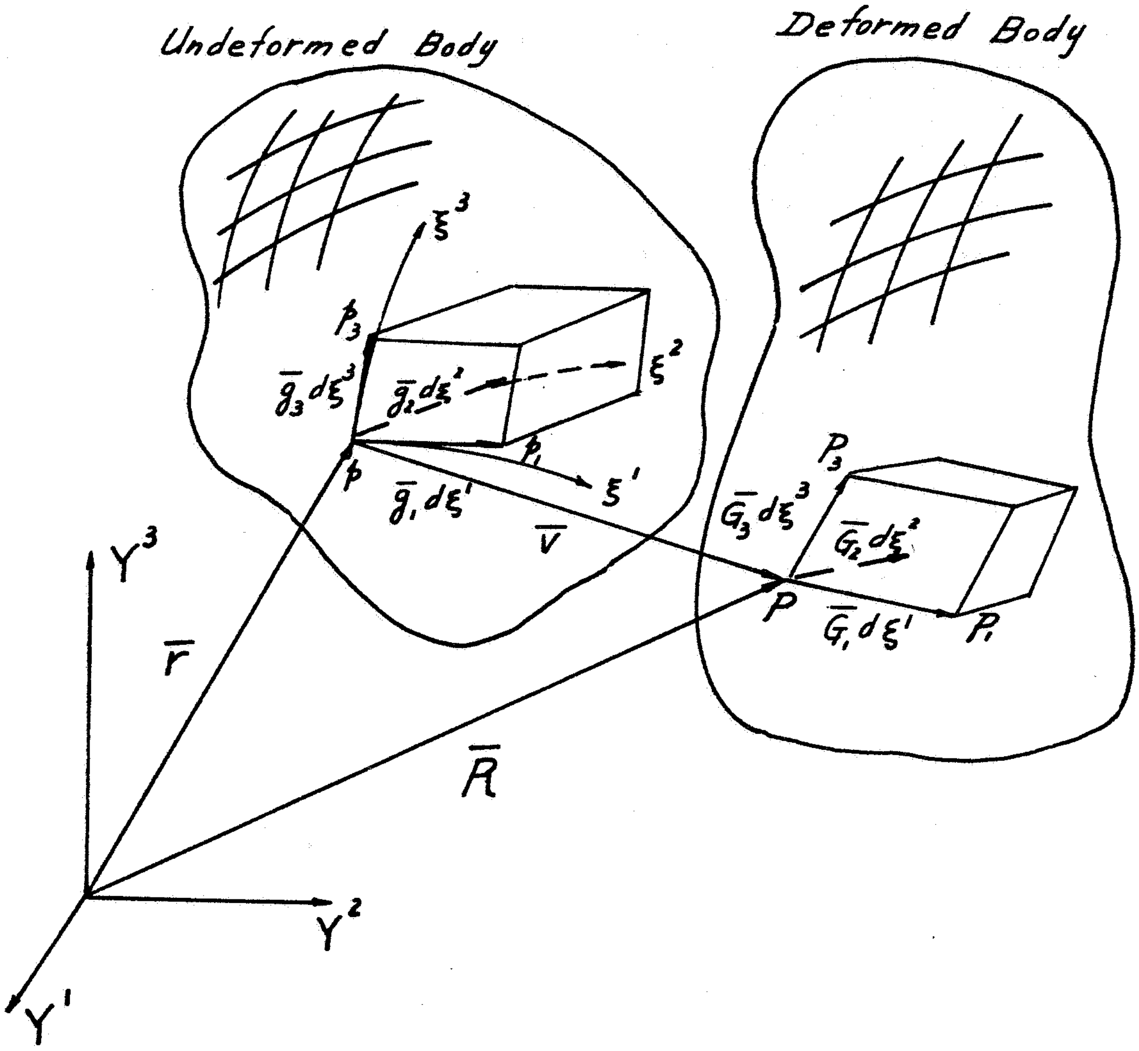

Undeformed Body
Deformed Body
$\xi^3$
$p_3$
$\bar{g}_3 d\xi^3$
$\bar{g}_2 d\xi^2$
$\xi^2$
$p_1$
$\xi^1$
$p$
$\bar{g}_1 d\xi^1$
$\bar{V}$
$P_3$
$\bar{G}_3 d\xi^3$
$\bar{G}_2 d\xi^2$
$P$
$\bar{G}_1 d\xi^1$
$P_1$
$Y^3$
$\bar{r}$
$\bar{R}$
$Y^2$
$Y^1$

FIG.1 NOMENCLATURE FOR SPACE COORDINATES AND DEFORMATION

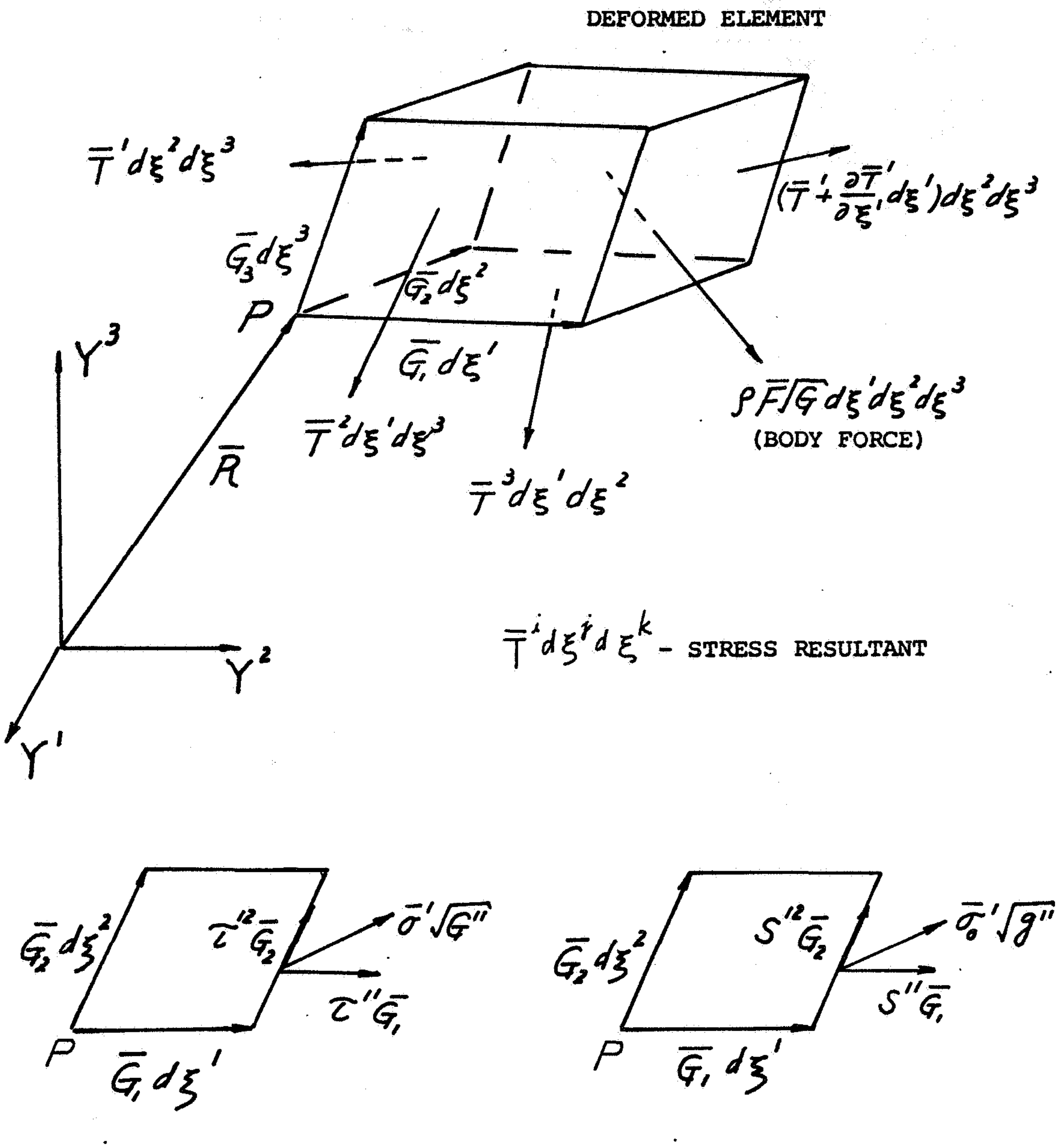
DEFORMED ELEMENT
$\bar{T}^1 d\xi^2 d\xi^3$
$(\bar{T}^1 + \frac{\partial \bar{T}^1}{\partial \xi^1} d\xi^1) d\xi^2 d\xi^3$
$\bar{G}_3 d\xi^3$
$\bar{G}_2 d\xi^2$
$P$
$Y^3$
$\bar{G}_1 d\xi^1$
$\rho \bar{F} \sqrt{G}\, d\xi^1 d\xi^2 d\xi^3$
(BODY FORCE)
$\bar{T}^2 d\xi^1 d\xi^3$
$\bar{R}$
$\bar{T}^3 d\xi^1 d\xi^2$
$\bar{T}^i d\xi^j d\xi^k$ - STRESS RESULTANT
$Y^2$
$Y^1$
$\bar{G}_2 d\xi^2$
$\tau^{12} \bar{G}_2$
$\bar{\sigma}^1 \sqrt{G^{11}}$
$\tau^{11} \bar{G}_1$
$P$
$\bar{G}_1 d\xi^1$
$\bar{G}_2 d\xi^2$
$S^{12} \bar{G}_2$
$\bar{\sigma}_0^1 \sqrt{g^{11}}$
$S^{11} \bar{G}_1$
$P$
$\bar{G}_1 d\xi^1$

$\tau^{ij}$ - EULERIAN STRESS TENSOR

$S^{ij}$ -KIRCHHOFF STRESS TENSOR

FIG. 2 NOMENCLATURE FOR STRESS TENSORS

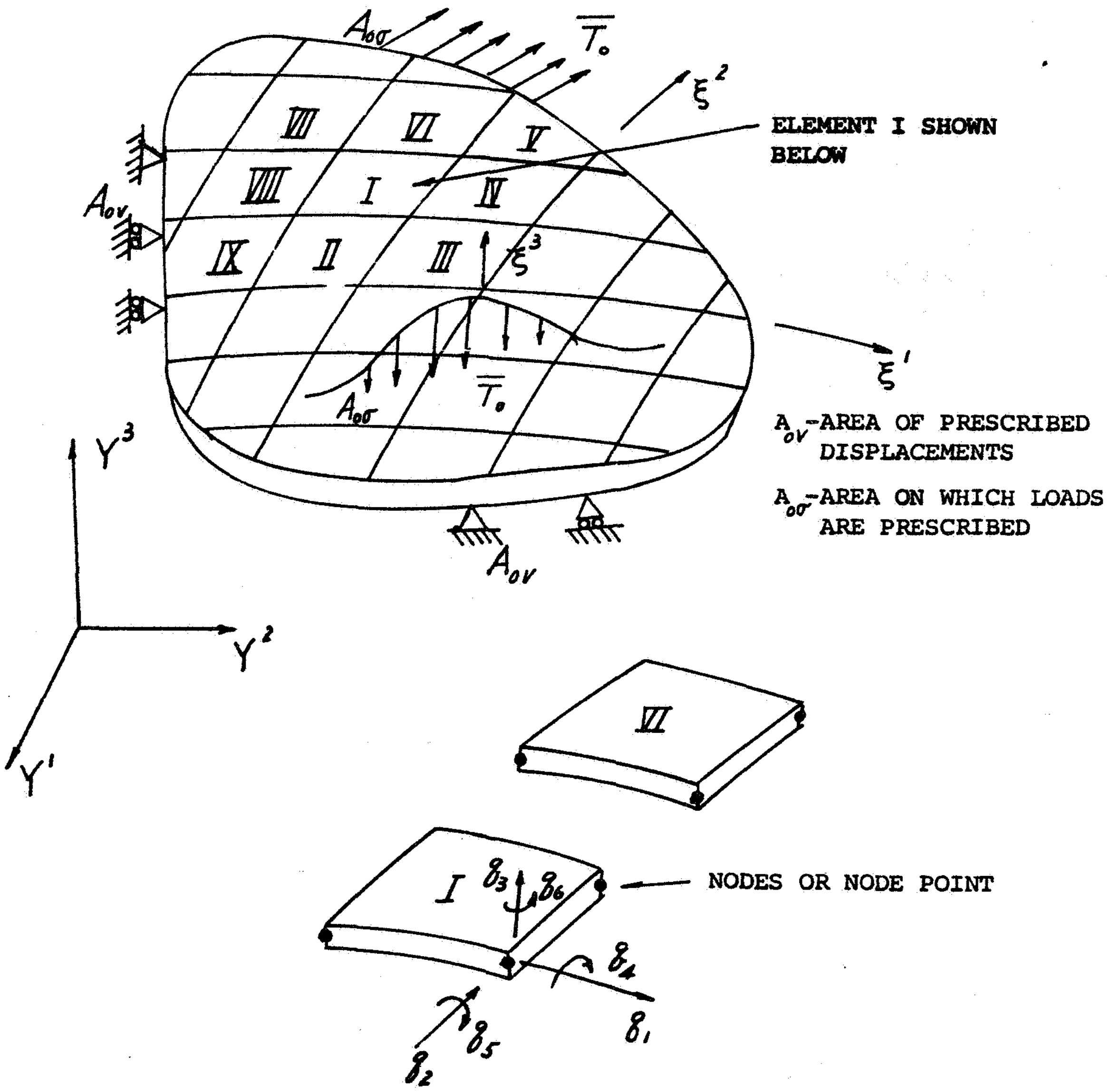
$A_{0\sigma}$
$\overline{T}_0$
$\xi^2$
ELEMENT I SHOWN BELOW
VII
VI
V
VIII
I
IV
IX
II
III
$\xi^3$
$A_{0V}$
$\xi^1$
$A_{0\sigma}$
$\overline{T}_0$
$A_{0V}$-AREA OF PRESCRIBED DISPLACEMENTS
$A_{0\sigma}$-AREA ON WHICH LOADS ARE PRESCRIBED
$A_{0V}$
$Y^3$
$Y^2$
$Y^1$
VI
I
$q_3$
$q_6$
NODES OR NODE POINT
$q_4$
$q_1$
$q_5$
$q_2$

FIG.3 NOMENCLATURE FOR A POSSIBLE FINITE ELEMENT REPRESENTATION OF A GENERAL TWO-DIMENSIONAL STRUCTURE

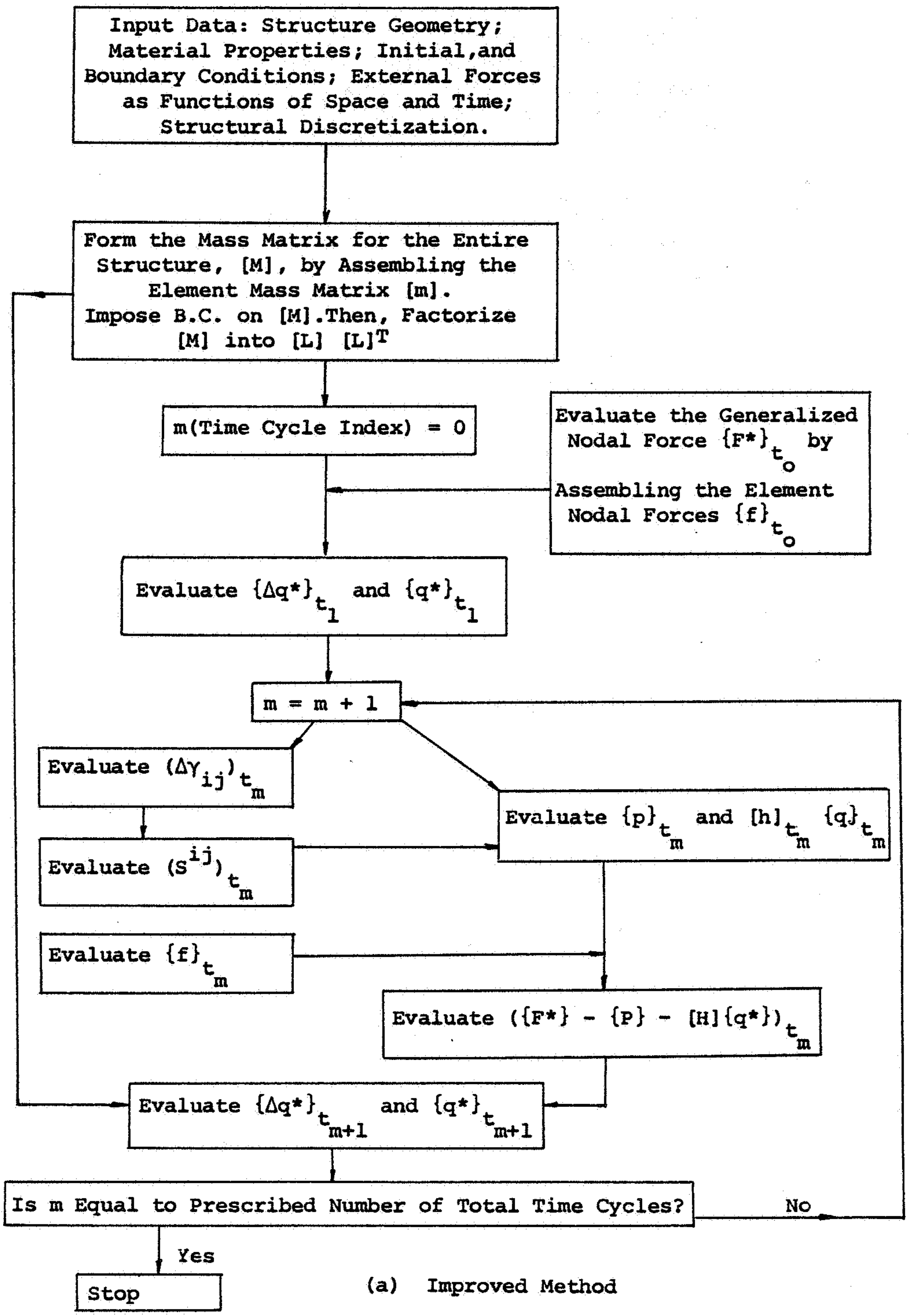
Input Data: Structure Geometry; Material Properties; Initial, and Boundary Conditions; External Forces as Functions of Space and Time; Structural Discretization.
Form the Mass Matrix for the Entire Structure, [M], by Assembling the Element Mass Matrix [m]. Impose B.C. on [M]. Then, Factorize [M] into [L] $[L]^T$
m(Time Cycle Index) = 0
Evaluate the Generalized Nodal Force $\{F^*\}_{t_o}$ by Assembling the Element Nodal Forces $\{f\}_{t_o}$
Evaluate $\{\Delta q^*\}_{t_1}$ and $\{q^*\}_{t_1}$
m = m + 1
Evaluate $(\Delta\gamma_{ij})_{t_m}$
Evaluate $(S^{ij})_{t_m}$
Evaluate $\{f\}_{t_m}$
Evaluate $\{p\}_{t_m}$ and $[h]_{t_m}$ $\{q\}_{t_m}$
Evaluate $(\{F^*\} - \{P\} - [H]\{q^*\})_{t_m}$
Evaluate $\{\Delta q^*\}_{t_{m+1}}$ and $\{q^*\}_{t_{m+1}}$
Is m Equal to Prescribed Number of Total Time Cycles?
No
Yes
Stop

(a) Improved Method

FIG. 4 FLOW CHART FOR SOLUTION PROCESS OF STRUCTURAL LARGE DEFLECTION ELASTIC-PLASTIC TRANSIENT RESPONSES

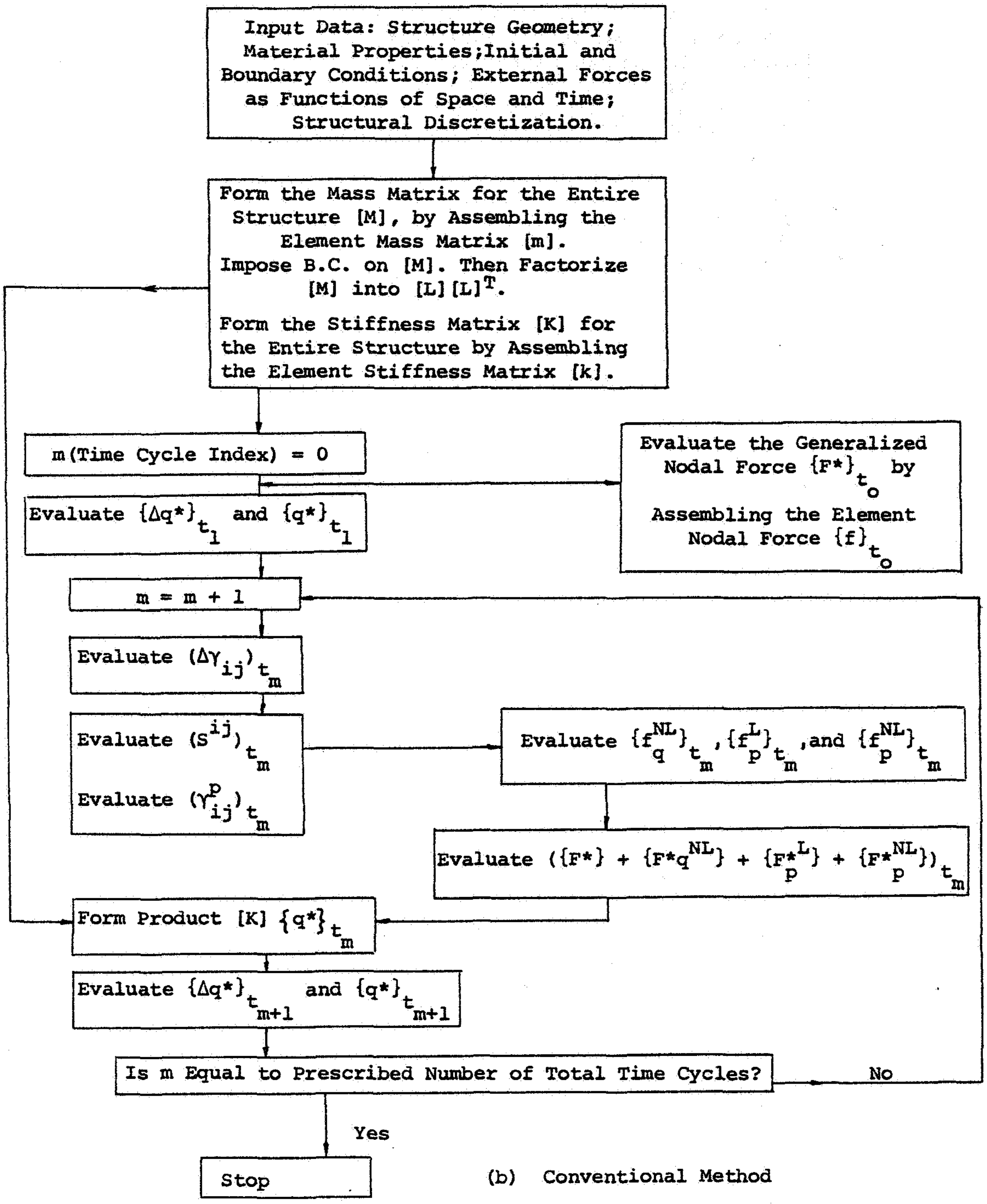
Input Data: Structure Geometry; Material Properties;Initial and Boundary Conditions; External Forces as Functions of Space and Time; Structural Discretization.
Form the Mass Matrix for the Entire Structure [M], by Assembling the Element Mass Matrix [m].
Impose B.C. on [M]. Then Factorize [M] into $[L][L]^T$.
Form the Stiffness Matrix [K] for the Entire Structure by Assembling the Element Stiffness Matrix [k].
m(Time Cycle Index) = 0
Evaluate the Generalized Nodal Force $\{F^*\}_{t_o}$ by Assembling the Element Nodal Force $\{f\}_{t_o}$
Evaluate $\{\Delta q^*\}_{t_1}$ and $\{q^*\}_{t_1}$
m = m + 1
Evaluate $(\Delta\gamma_{ij})_{t_m}$
Evaluate $(S^{ij})_{t_m}$
Evaluate $(\gamma^p_{ij})_{t_m}$
Evaluate $\{f_q^{NL}\}_{t_m}, \{f_p^L\}_{t_m}$, and $\{f_p^{NL}\}_{t_m}$
Evaluate $(\{F^*\} + \{F^*q^{NL}\} + \{F^{*L}_p\} + \{F^{*NL}_p\})_{t_m}$
Form Product $[K]\{q^*\}_{t_m}$
Evaluate $\{\Delta q^*\}_{t_{m+1}}$ and $\{q^*\}_{t_{m+1}}$
Is m Equal to Prescribed Number of Total Time Cycles?
No
Yes
Stop

(b) Conventional Method

FIG. 4 CONCLUDED

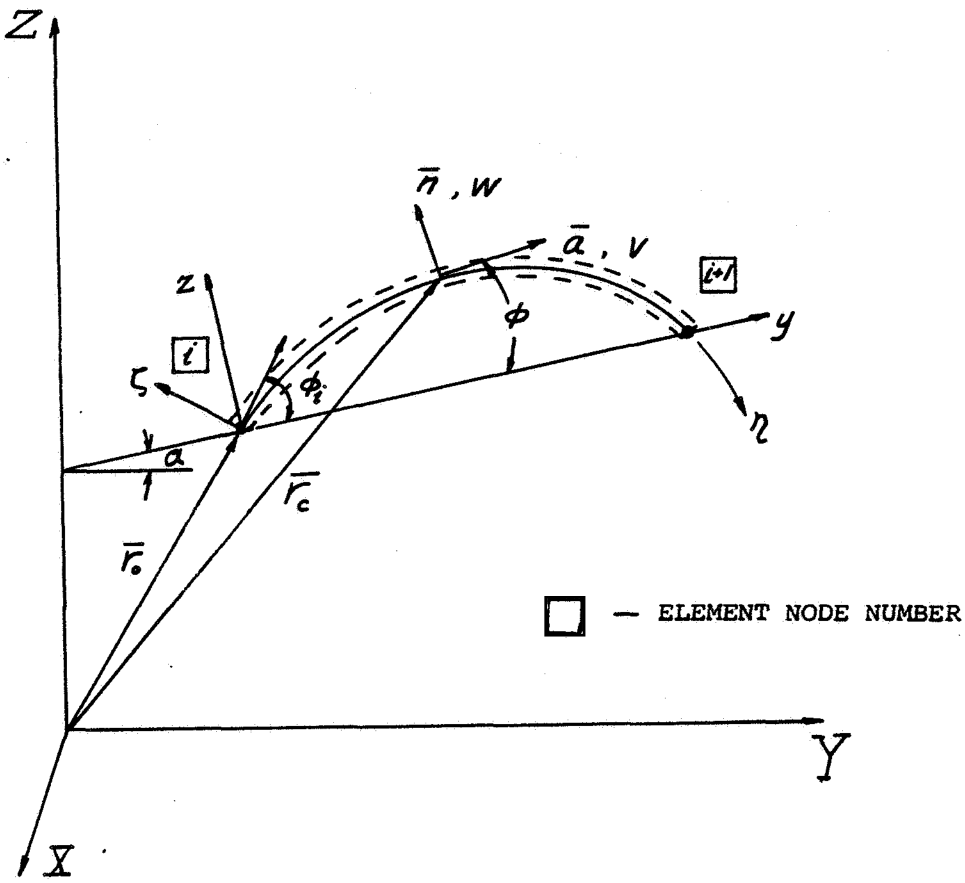
Z
n̄ , w
ā , v
z
i+1
y
i
ζ
φ
φ_i
η
α
r̄_c
r̄_o
□ — ELEMENT NODE NUMBER
Y
X

FIG.5 NOMENCLATURE FOR GEOMETRY,COORDINATES,AND DISPLACEMENTS OF A CURVED-BEAM FINITE ELEMENT

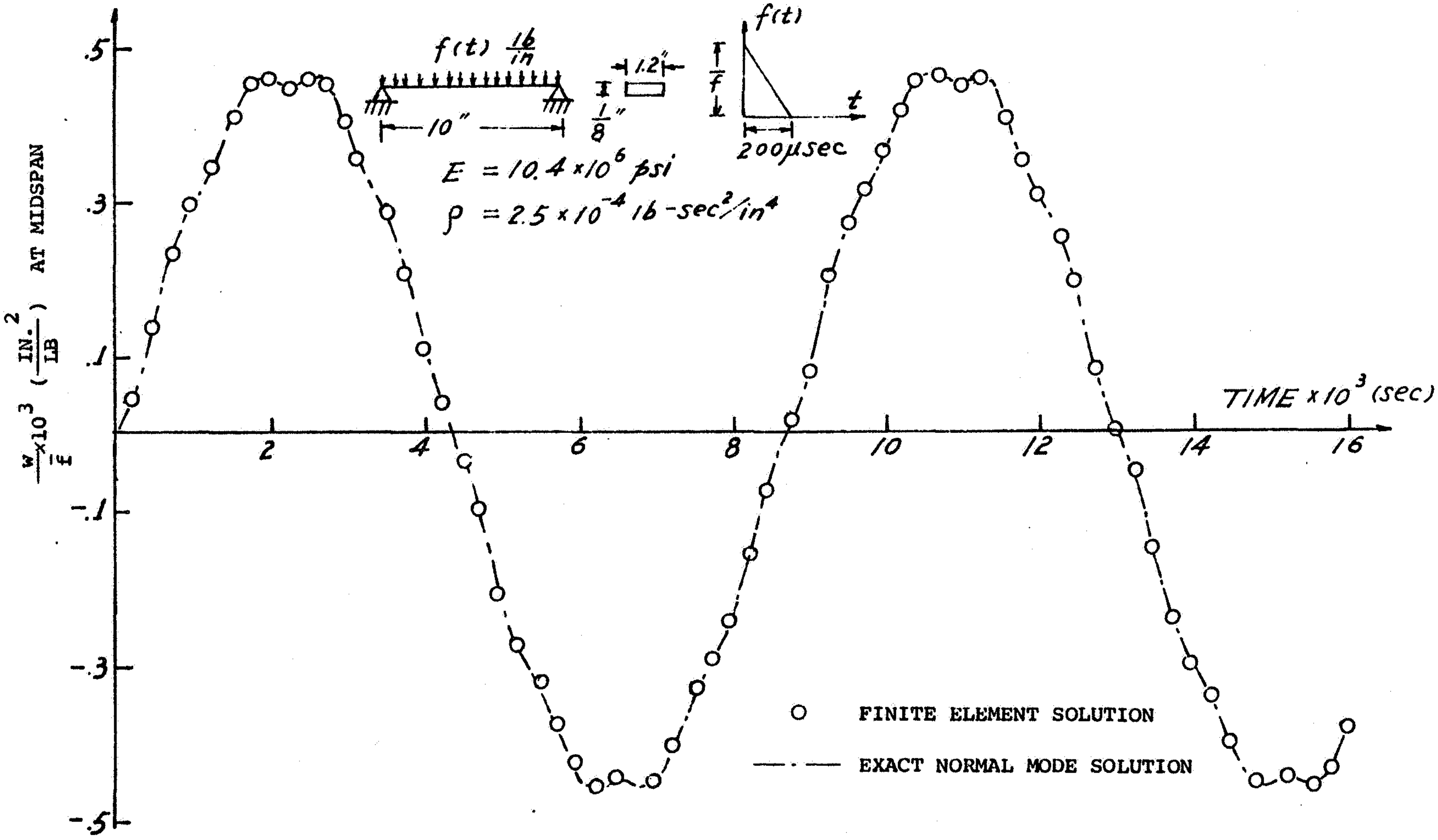

FIG.6 COMPARISON OF FINITE-ELEMENT WITH EXACT NORMAL MODE SOLUTION FOR THE SMALL-DEFLECTION RESPONSE OF A MECHANICALLY LOADED LINEAR-ELASTIC SIMPLY-SUPPORTED BEAM

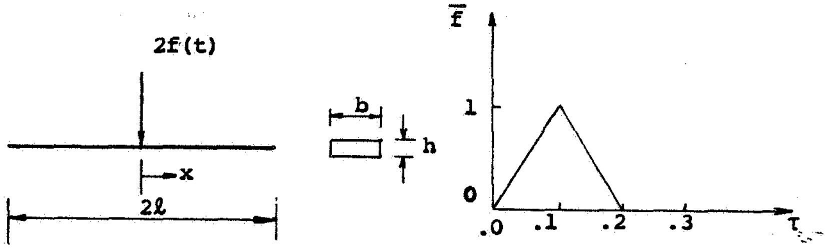

$$\frac{\ell}{h} = 2.887$$

$$k_s = \frac{1}{\ell}\sqrt{\frac{EI}{A_s G}} = 0.2$$

$$\tau = \frac{t}{\ell^2}\sqrt{\frac{EI}{\rho bh}} \quad , \quad \bar{f}(\tau) = \frac{f\ell^2}{EI} \quad , \quad \xi = \frac{x}{\ell}$$

$$\tilde{w} = \frac{w}{\ell} \quad , \quad \tilde{M} = \frac{M\ell}{EI} \quad , \quad \tilde{S} = \frac{S\ell^2}{EI} = \frac{1}{k_s^2}\left(\frac{\partial\tilde{w}}{\partial\xi} + \theta\right)$$

where

$A_s$ = effective shear carrying area of beam cross section

w = transverse deflection

M = bending moment

S = transverse shear force

FIG. 7 GEOMETRY AND NONDIMENSIONAL QUANTITIES FOR A FREE-FREE BEAM SUBJECTED TO AN APPLIED CONCENTRATED TRANSIENT LOAD AT ITS MIDSPAN

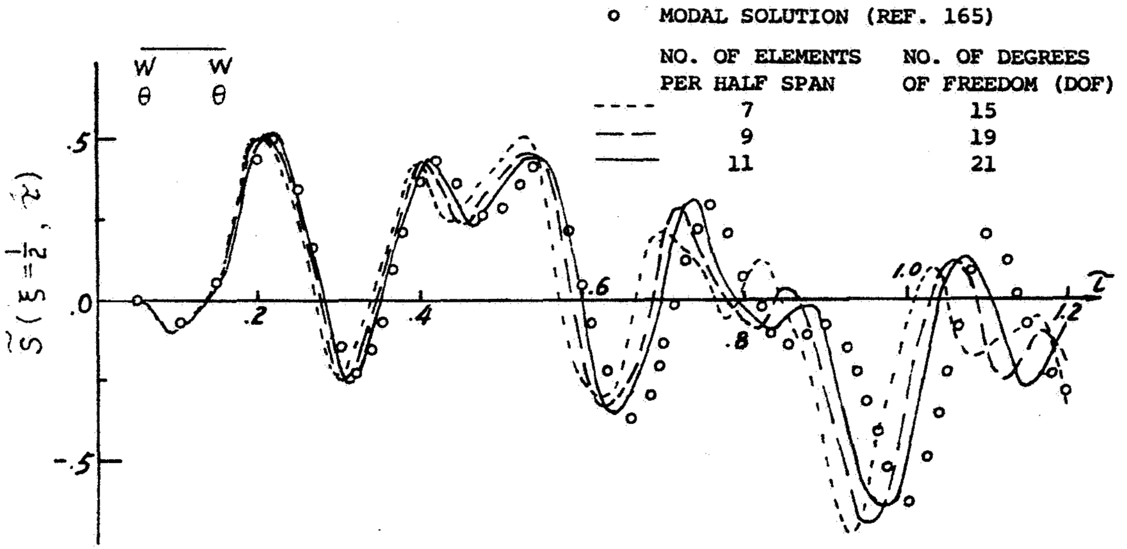

(a) T1 (Timoshenko-Type FE Solutions)

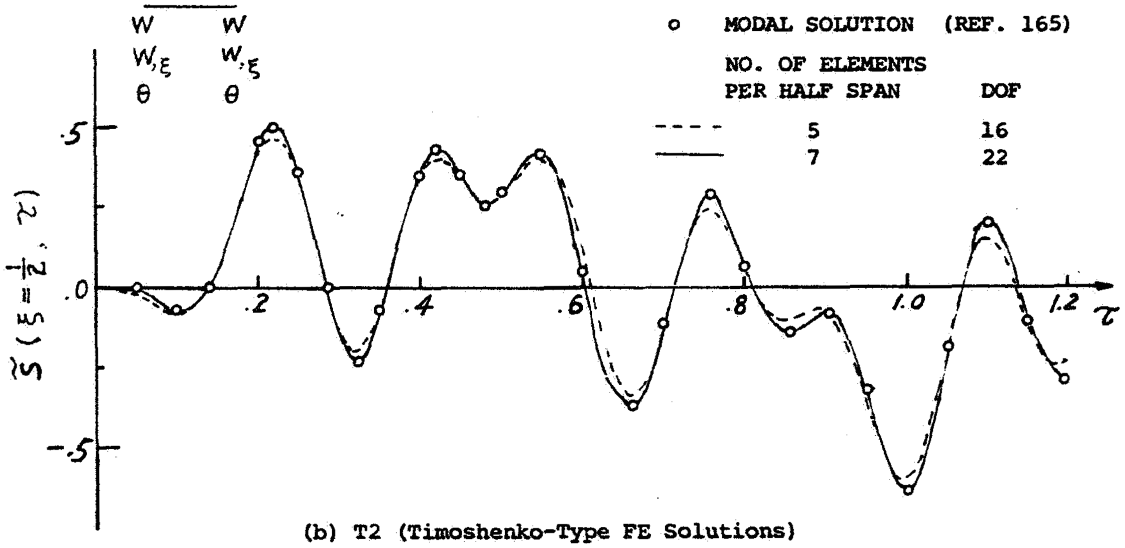

(b) T2 (Timoshenko-Type FE Solutions)

FIG.8 TRANSVERSE SHEAR RESPONSES OF THE MECHANICALLY LOADED SMALL-DEFLECTION LINEAR-ELASTIC FREE-FREE BEAM

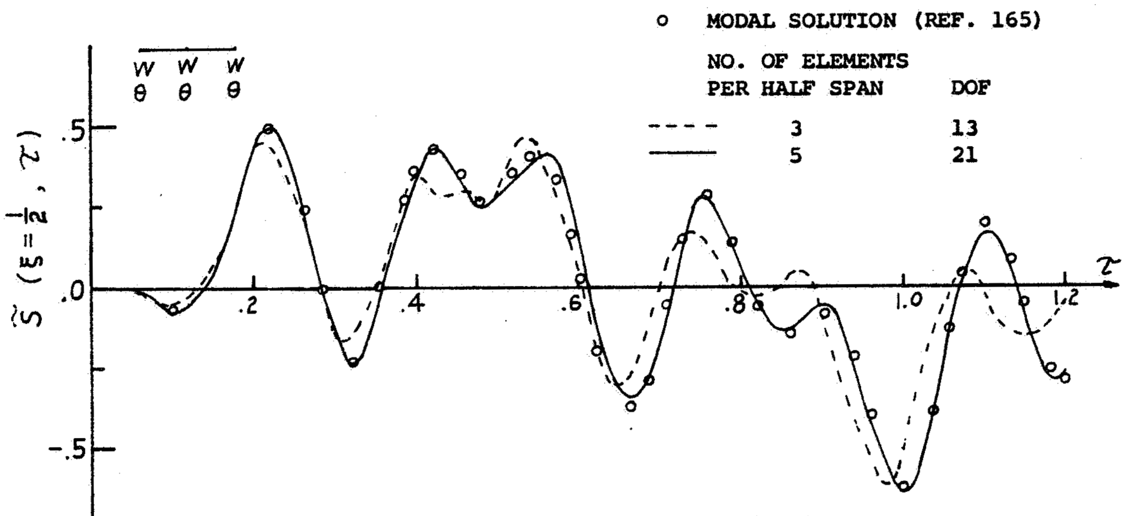

(c) T3 (Timoshenko-Type FE Solutions)

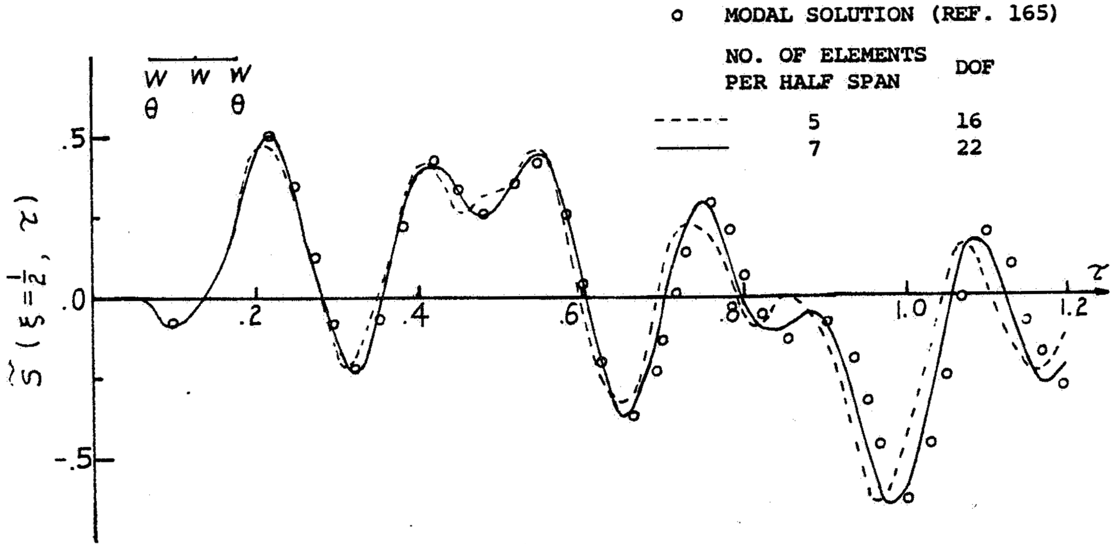

(d) T4 (Timoshenko-Type FE Solutions)

FIG.8 CONCLUDED

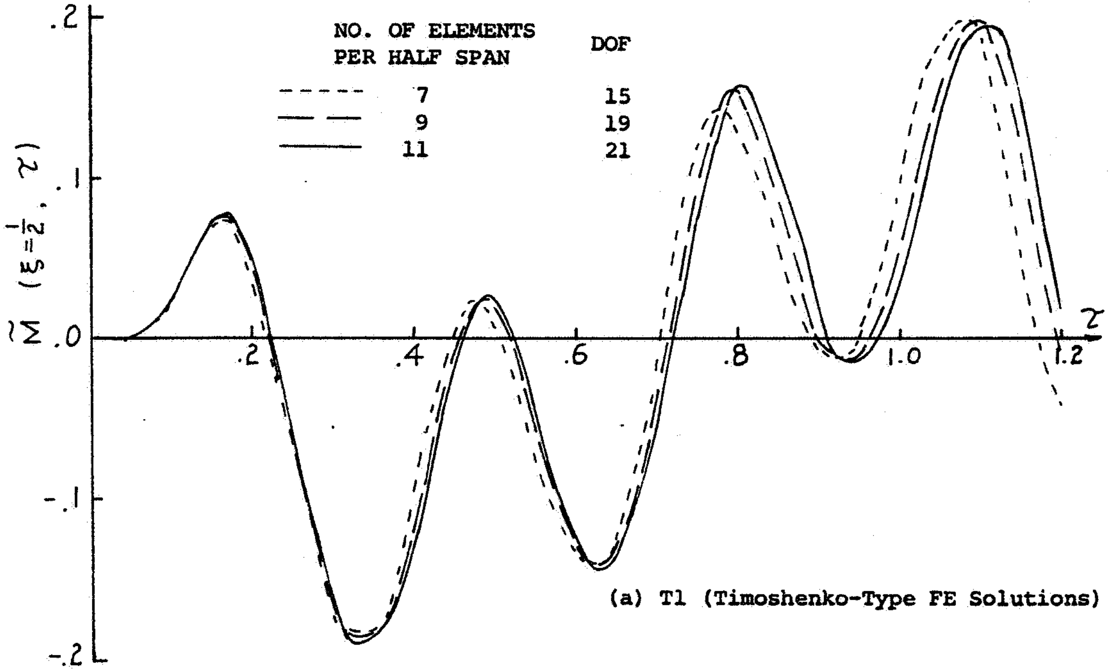

(a) T1 (Timoshenko-Type FE Solutions)

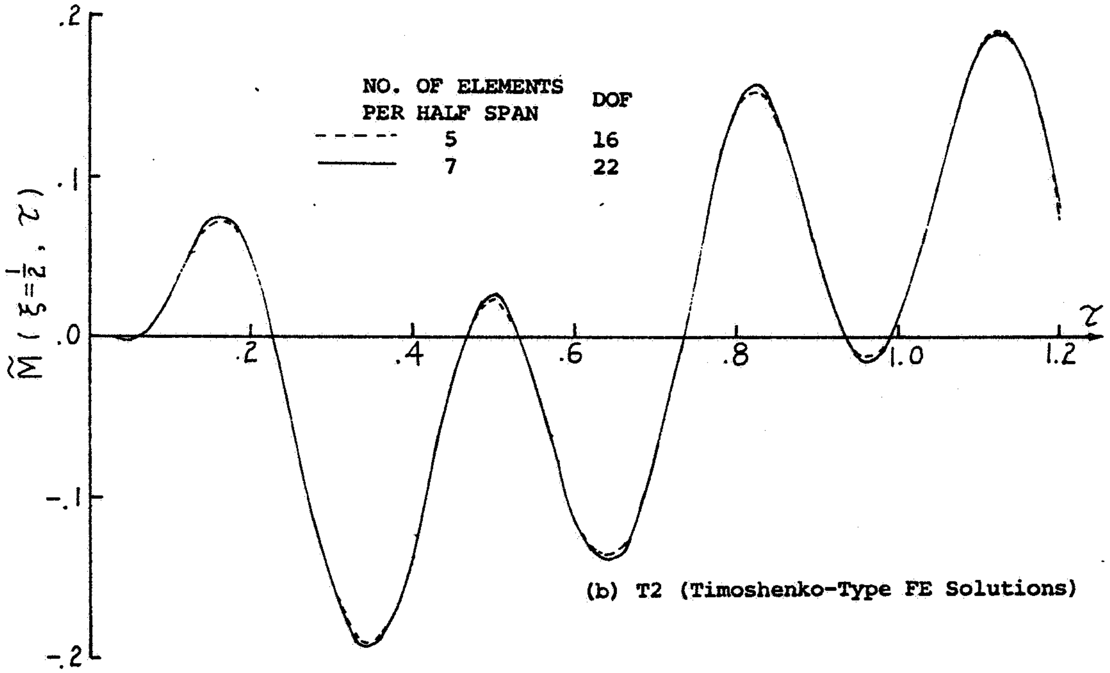

(b) T2 (Timoshenko-Type FE Solutions)

FIG.9 MOMENT RESPONSES OF THE MECHANICALLY LOADED SMALL-DEFLECTION LINEAR-ELASTIC FREE-FREE BEAM

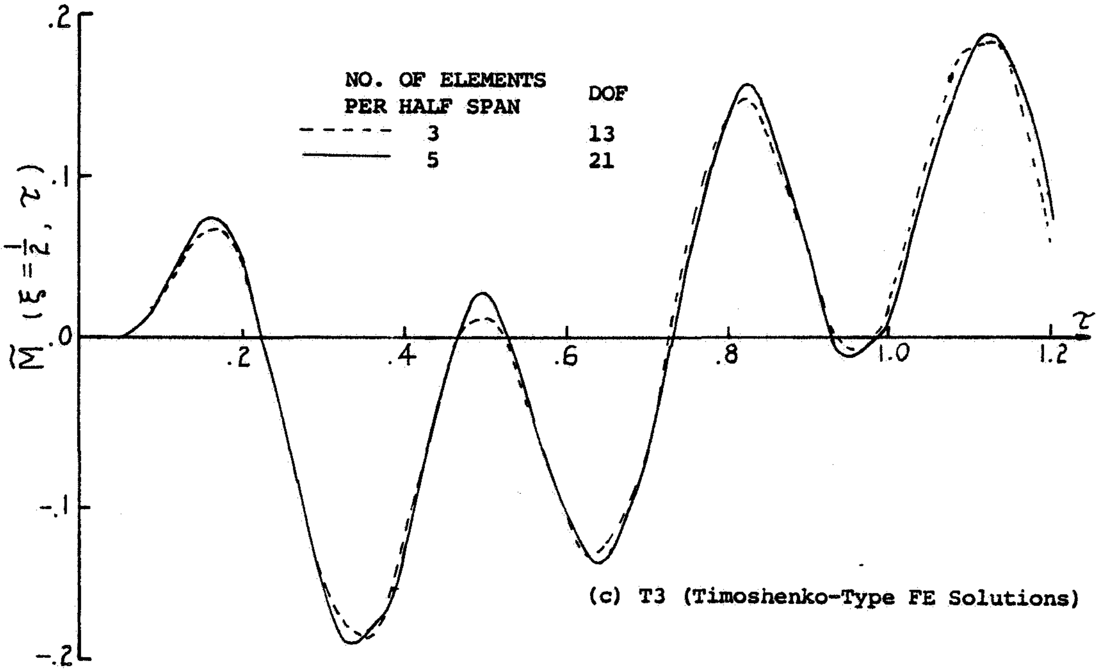

(c) T3 (Timoshenko-Type FE Solutions)

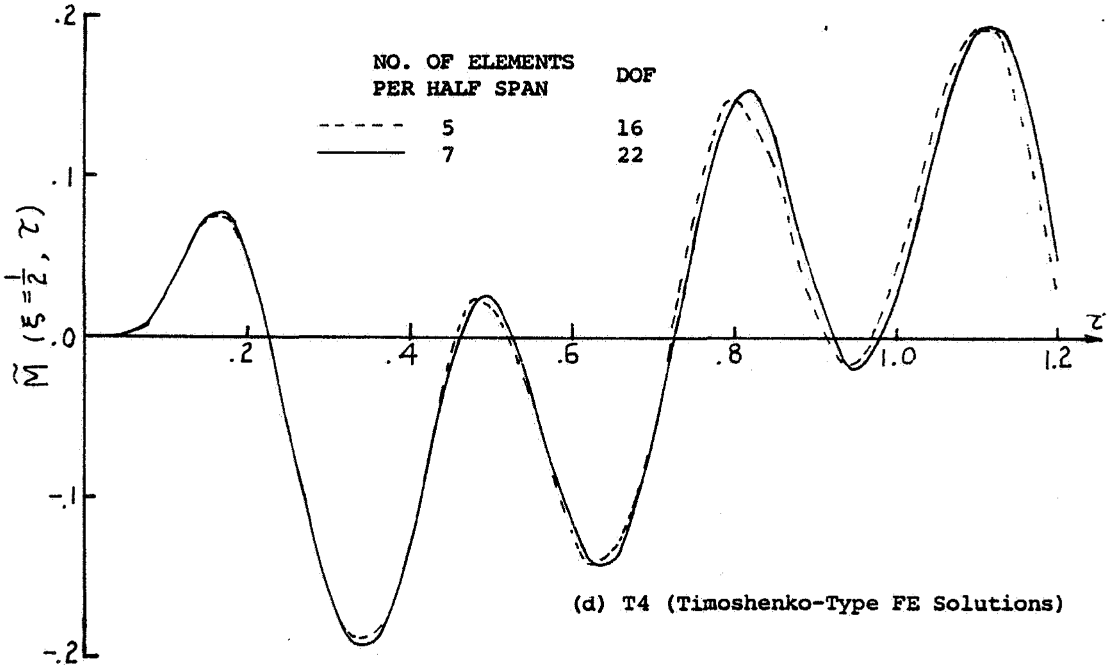

(d) T4 (Timoshenko-Type FE Solutions)

FIG.9 CONCLUDED

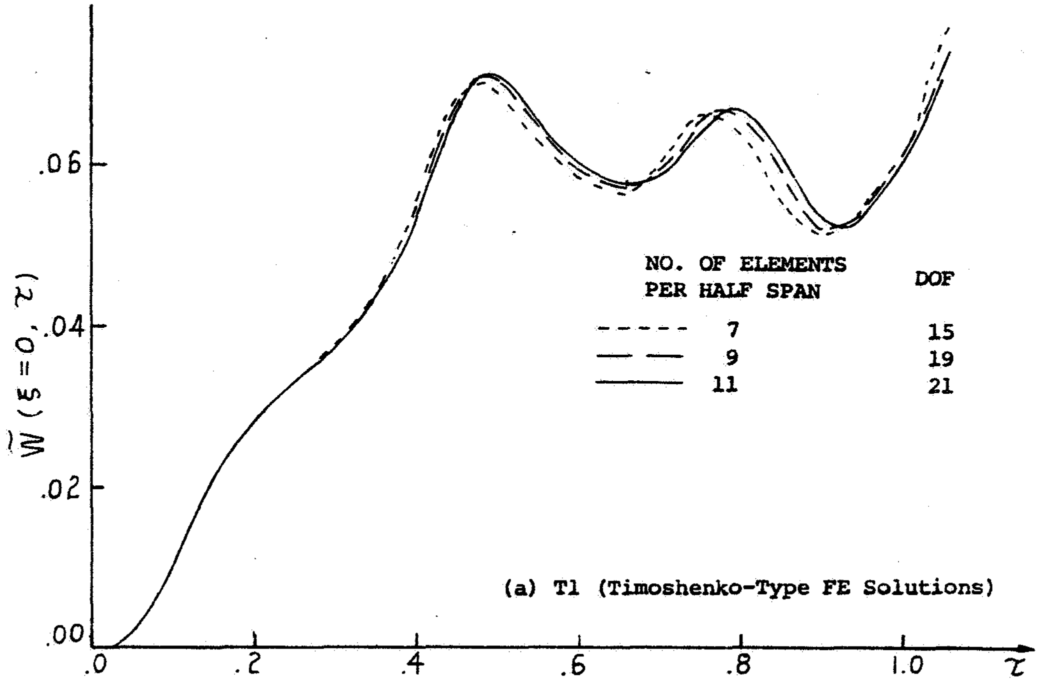

(a) T1 (Timoshenko-Type FE Solutions)

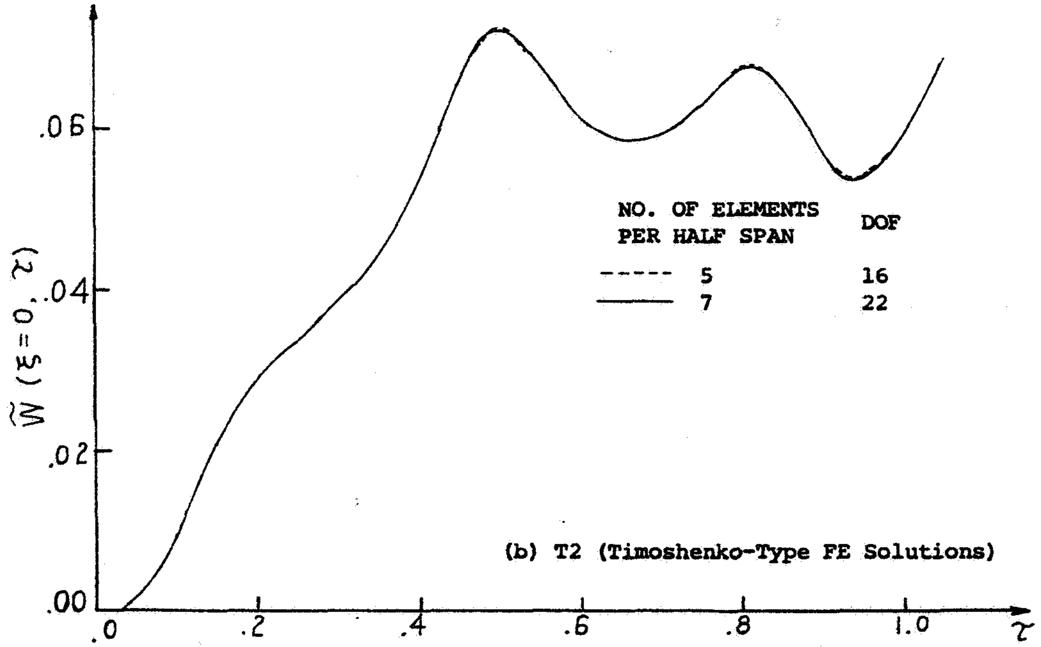

(b) T2 (Timoshenko-Type FE Solutions)

FIG.10 TRANSVERSE DEFLECTION RESPONSES OF THE MECHANICALLY LOADED SMALL-DEFLECTION LINEAR-ELASTIC FREE-FREE BEAM

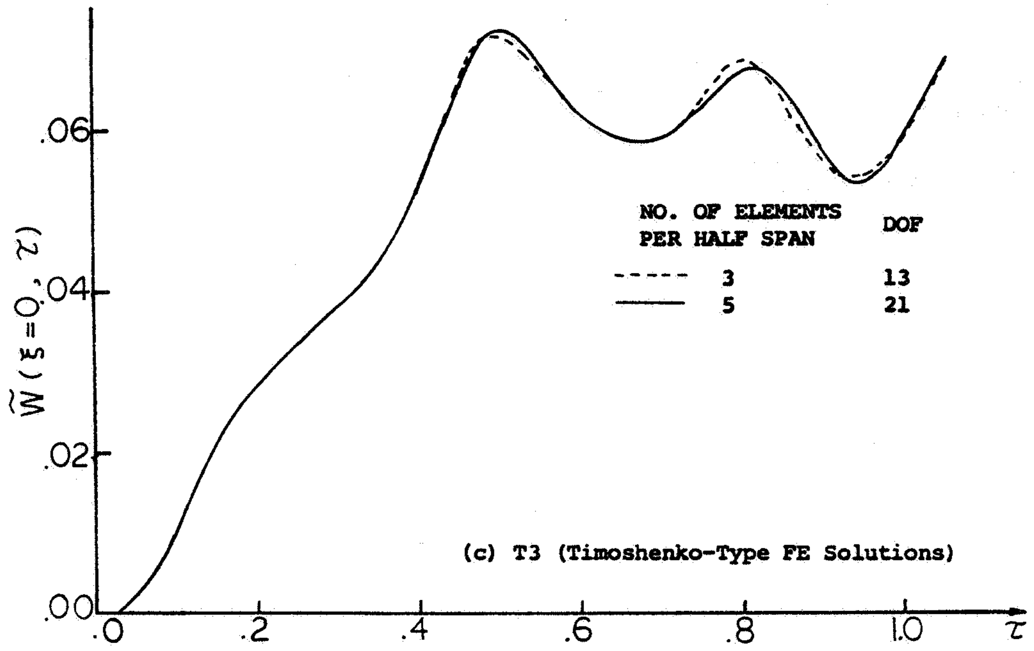

(c) T3 (Timoshenko-Type FE Solutions)

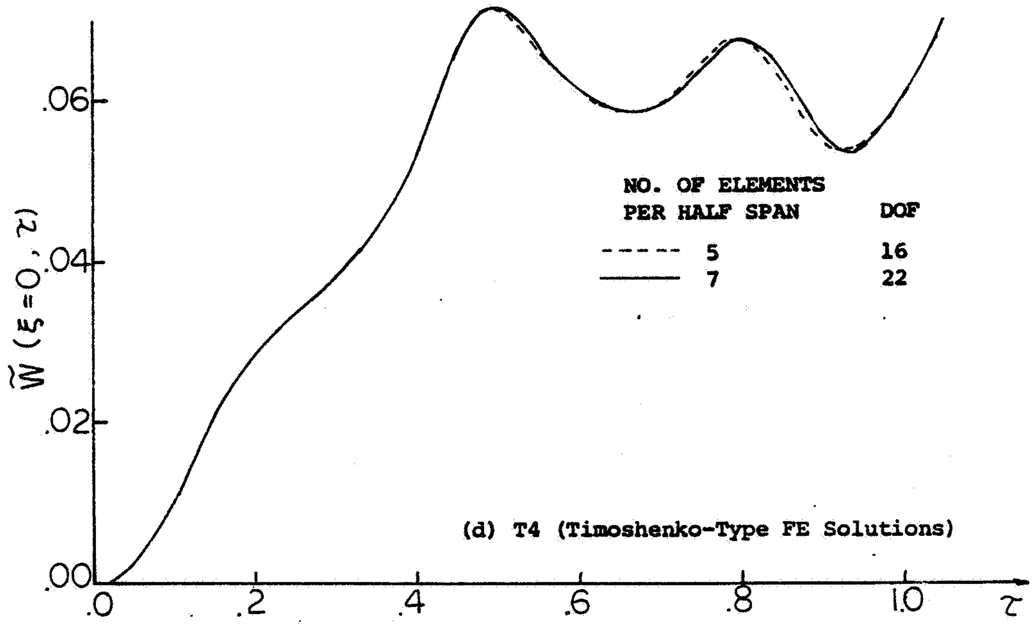

(d) T4 (Timoshenko-Type FE Solutions)

FIG.10 CONCLUDED

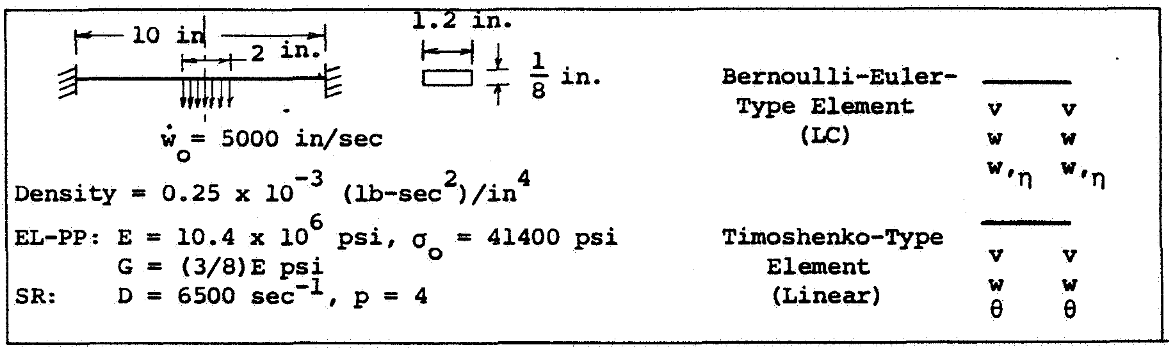
10 in
2 in.
1.2 in.
1/8 in.
$\dot{w}_o$ = 5000 in/sec
Density = $0.25 \times 10^{-3}$ (lb-sec$^2$)/in$^4$
EL-PP: E = $10.4 \times 10^6$ psi, $\sigma_o$ = 41400 psi
G = (3/8)E psi
SR: D = 6500 sec$^{-1}$, p = 4
Bernoulli-Euler-Type Element (LC)
v v
w w
$w,_\eta$ $w,_\eta$
Timoshenko-Type Element (Linear)
v v
w w
θ θ

(a) Clamped Beam

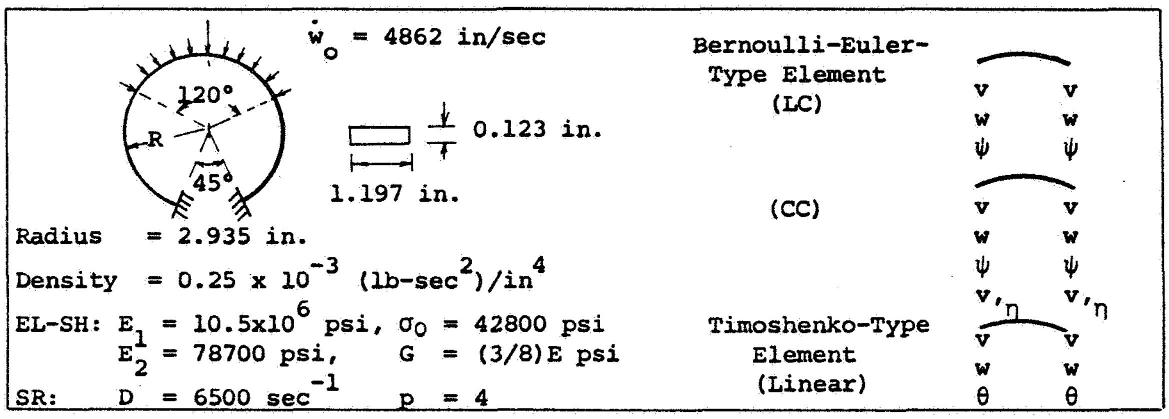
$\dot{w}_o$ = 4862 in/sec
120°
R
45°
0.123 in.
1.197 in.
Radius = 2.935 in.
Density = $0.25 \times 10^{-3}$ (lb-sec$^2$)/in$^4$
EL-SH: $E_1$ = $10.5 \times 10^6$ psi, $\sigma_O$ = 42800 psi
$E_2$ = 78700 psi, G = (3/8)E psi
SR: D = 6500 sec$^{-1}$ p = 4
Bernoulli-Euler-Type Element (LC)
v v
w w
ψ ψ
(CC)
v v
w w
ψ ψ
$v,_\eta$ $v,_\eta$
Timoshenko-Type Element (Linear)
v v
w w
θ θ

(b) Clamped Ring

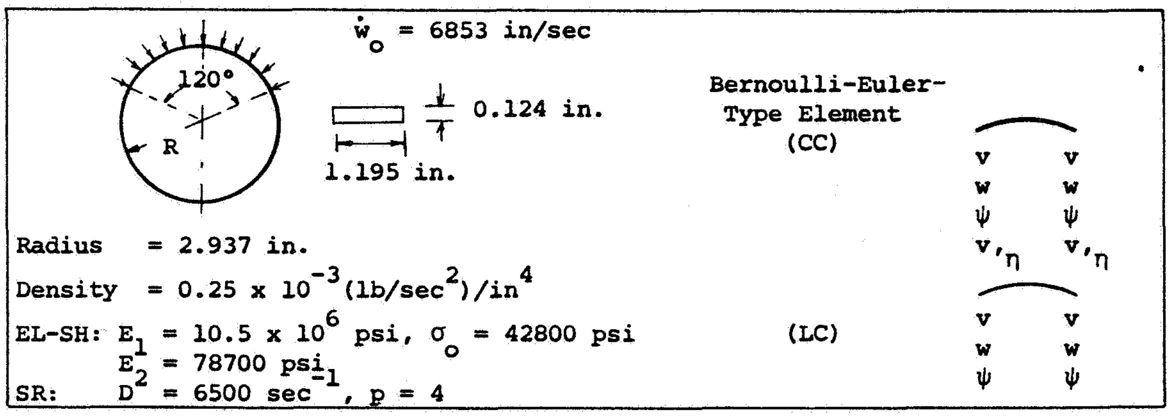
$\dot{w}_o$ = 6853 in/sec
120°
R
0.124 in.
1.195 in.
Radius = 2.937 in.
Density = $0.25 \times 10^{-3}$(lb/sec$^2$)/in$^4$
EL-SH: $E_1$ = $10.5 \times 10^6$ psi, $\sigma_o$ = 42800 psi
$E_2$ = 78700 psi
SR: D = 6500 sec$^{-1}$, p = 4
Bernoulli-Euler-Type Element (CC)
v v
w w
ψ ψ
$v,_\eta$ $v,_\eta$
(LC)
v v
w w
ψ ψ

(c) Free Ring

FIG. 11 TEST STUDIES OF LARGE-DEFLECTION ELASTIC-PLASTIC TRANSIENT RESPONSES OF IMPULSIVELY-LOADED SIMPLE STRUCTURES

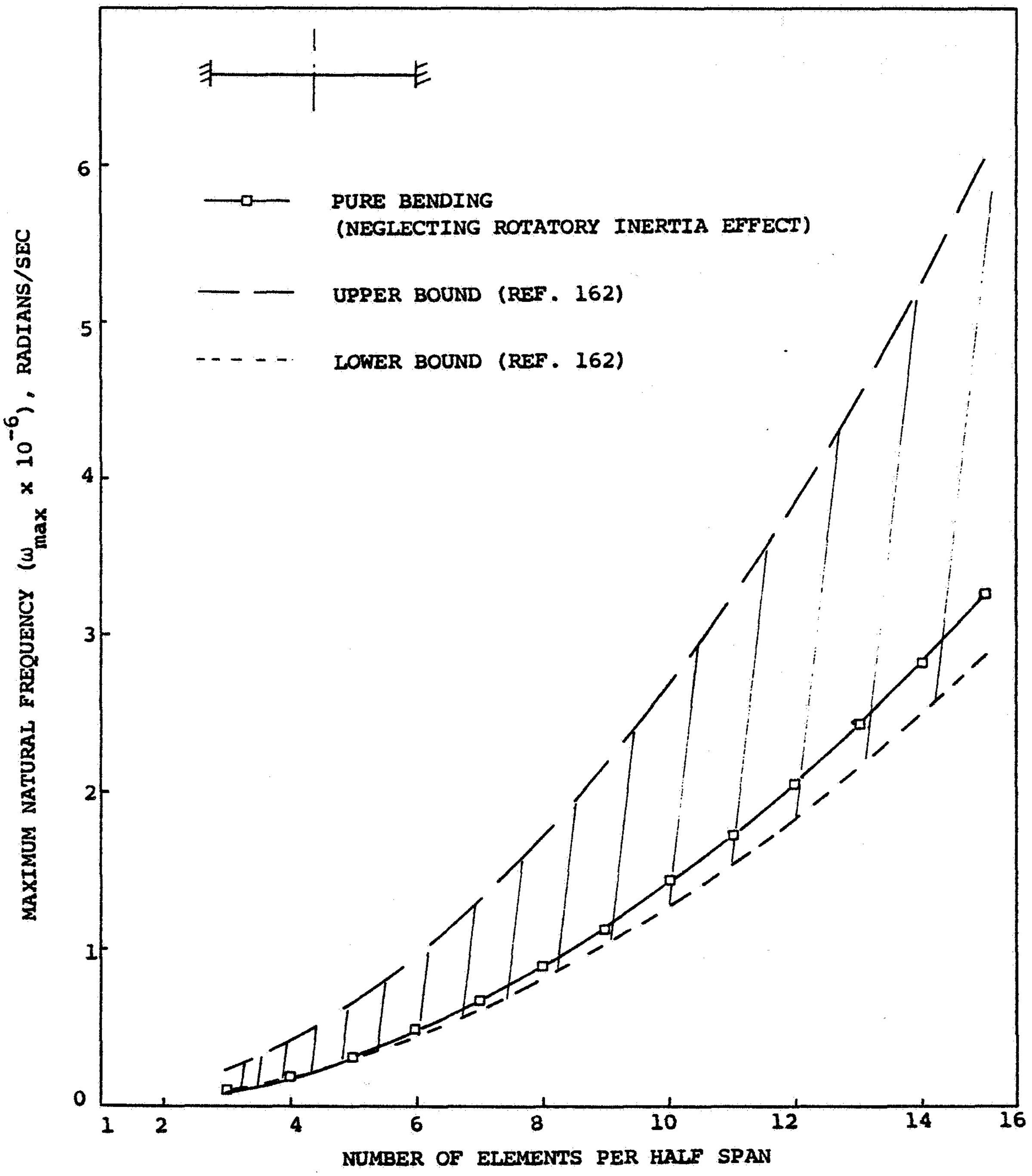

(b) Bounds of $\omega_{max}$ For Pure Bending Behavior

FIG.12 CONCLUDED

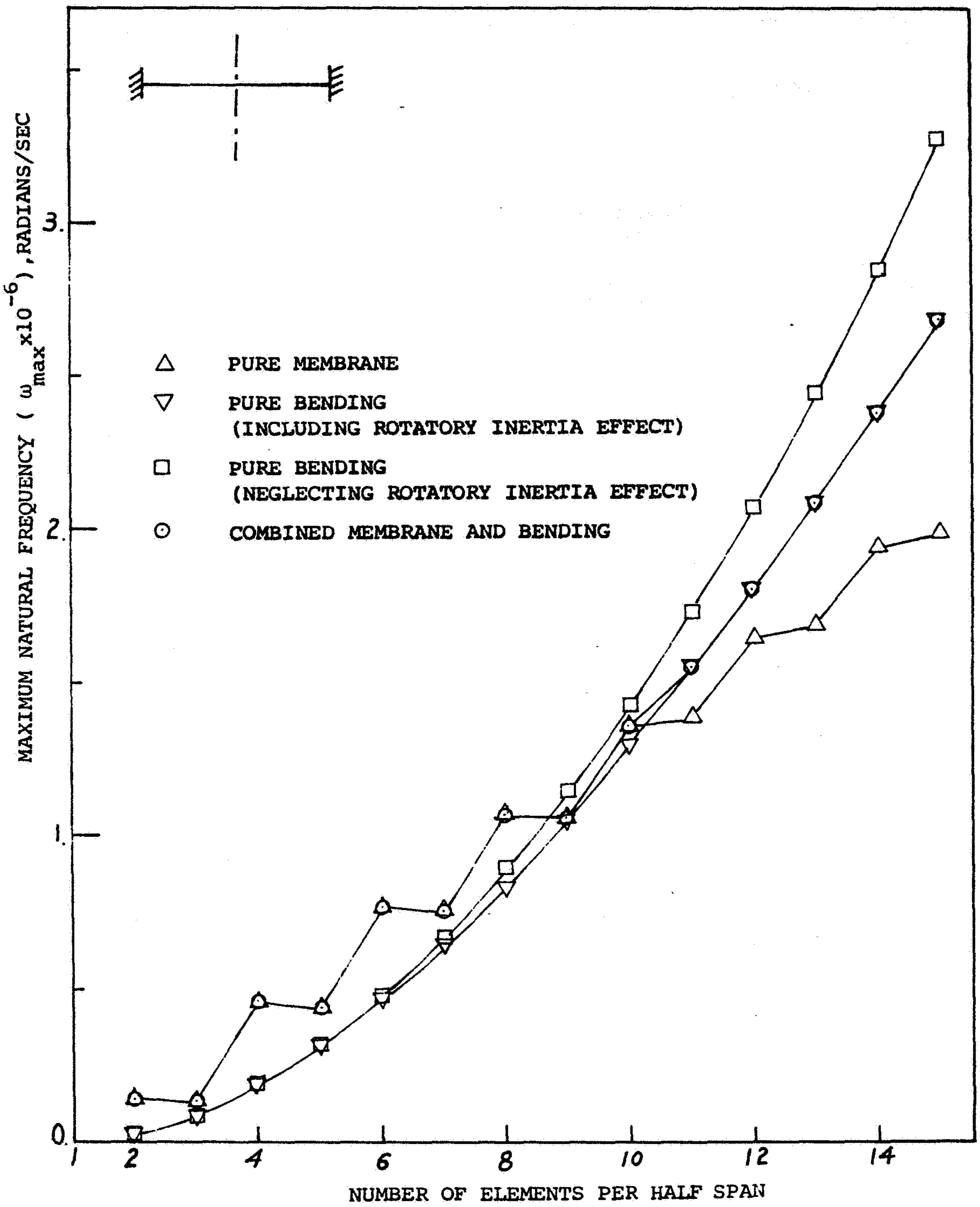

(a) The Maximum Natural Frequency

FIG.12 MAXIMUM NATURAL FREQUENCIES FOR SMALL VIBRATIONS OF THE CLAMPED BEAM

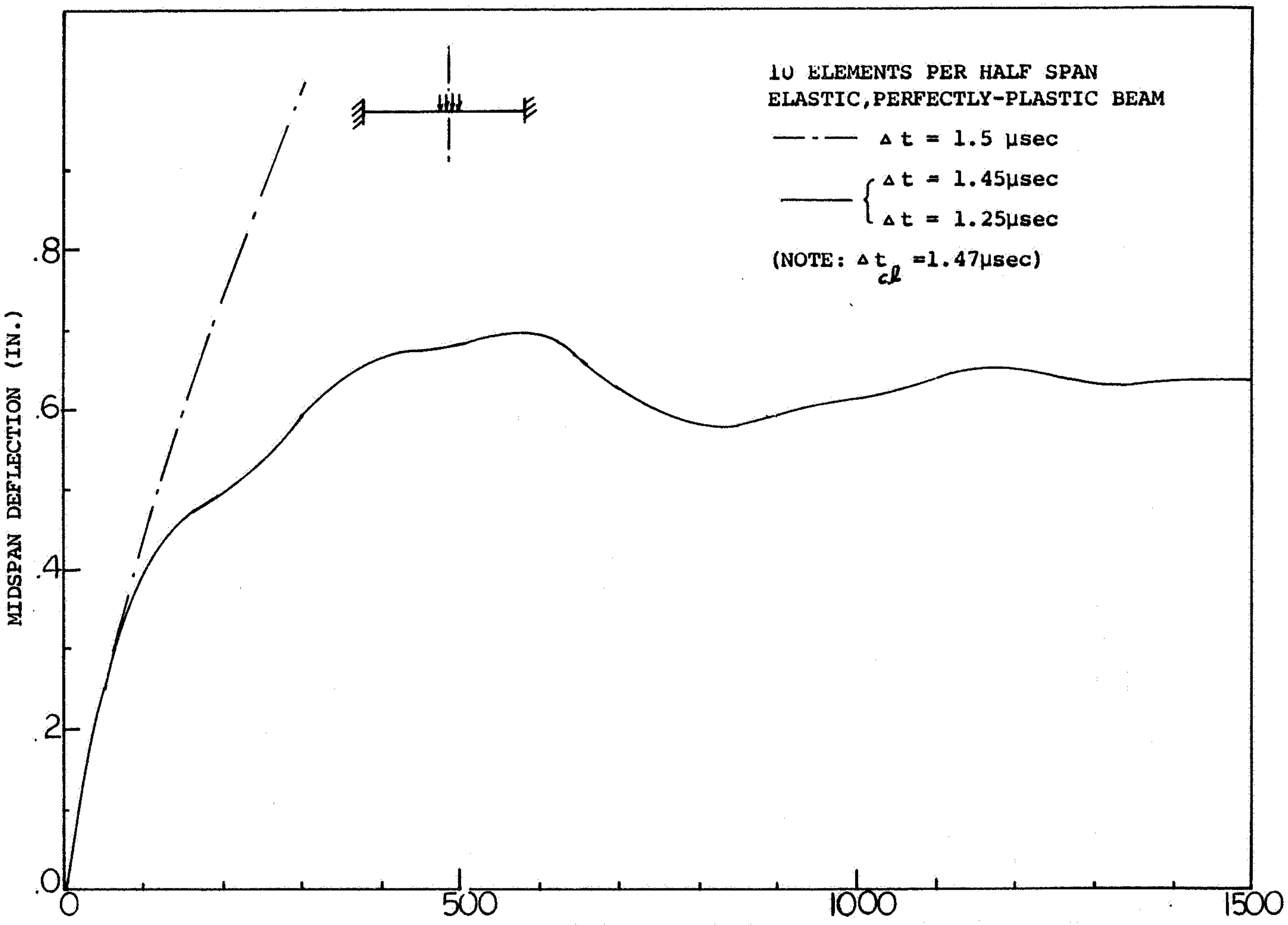

(a) Central-Difference Method

FIG.13 COMPARISON OF DYNAMIC RESPONSES OF THE CLAMPED BEAM CALCULATED BY USING VARIOUS TEMPORAL FINITE-DIFFERENCE OPERATORS: CENTRAL-DIFFERENCE,HOUBOLT'S,AND NEWMARK'S

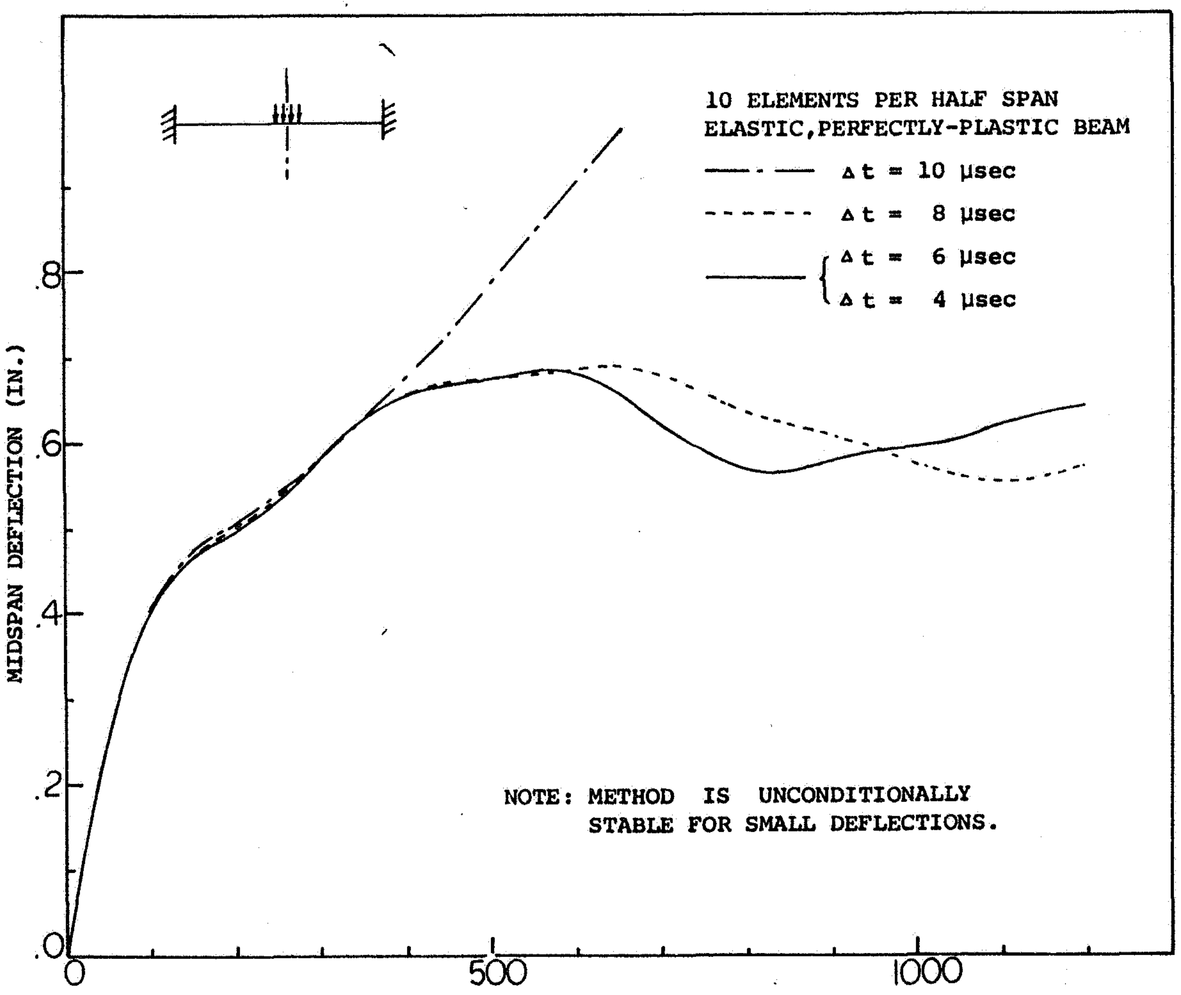

(b) Houbolt's Method

FIG.13 CONTINUED

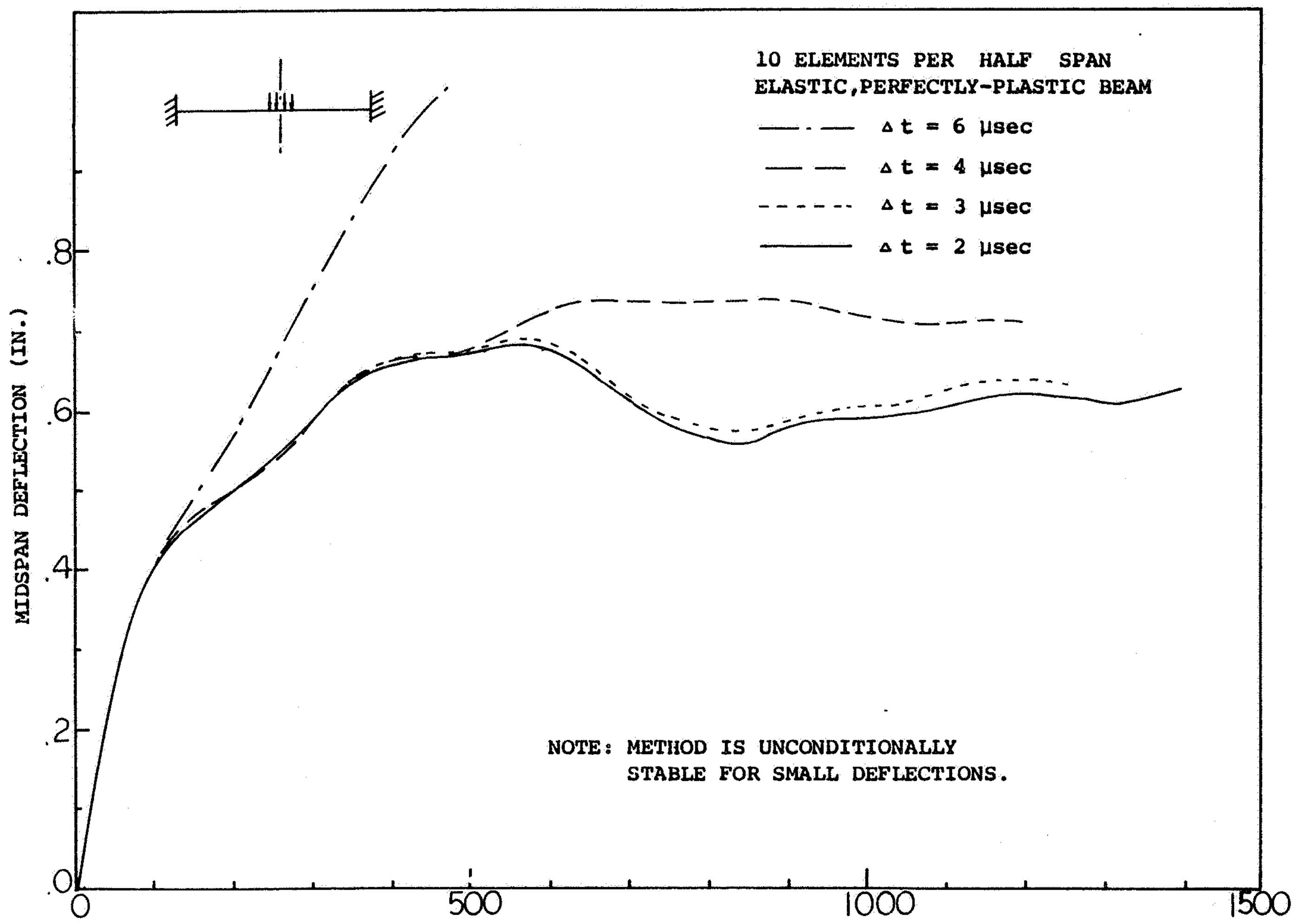

(c) Newmark's Method

FIG.13 CONCLUDED

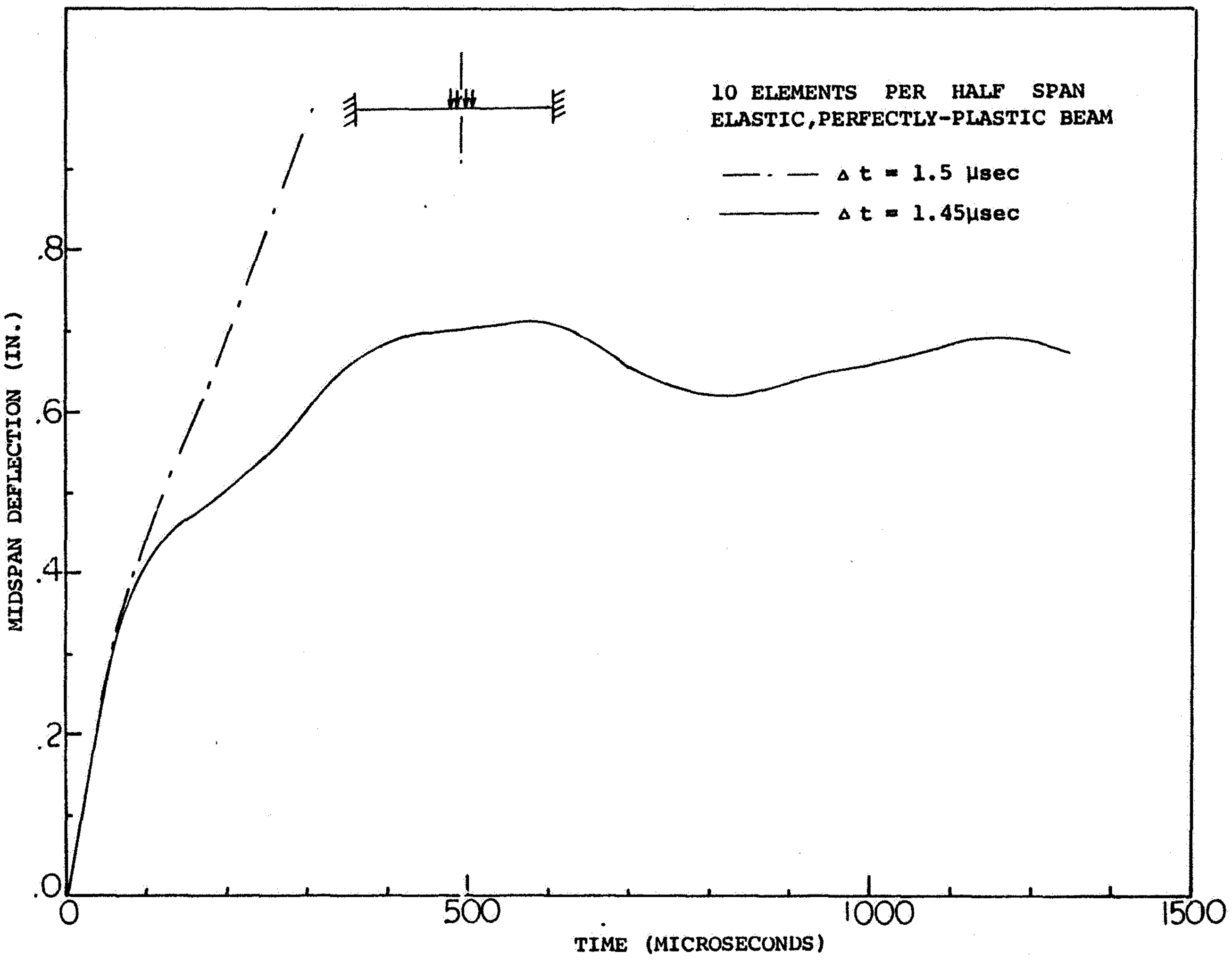

(a) Central-Difference Method

**FIG.14 EFFECTS OF USING INEXACT STRAIN INCREMENTS ON THE PREDICTED DYNAMIC RESPONSES OF THE CLAMPED BEAM**

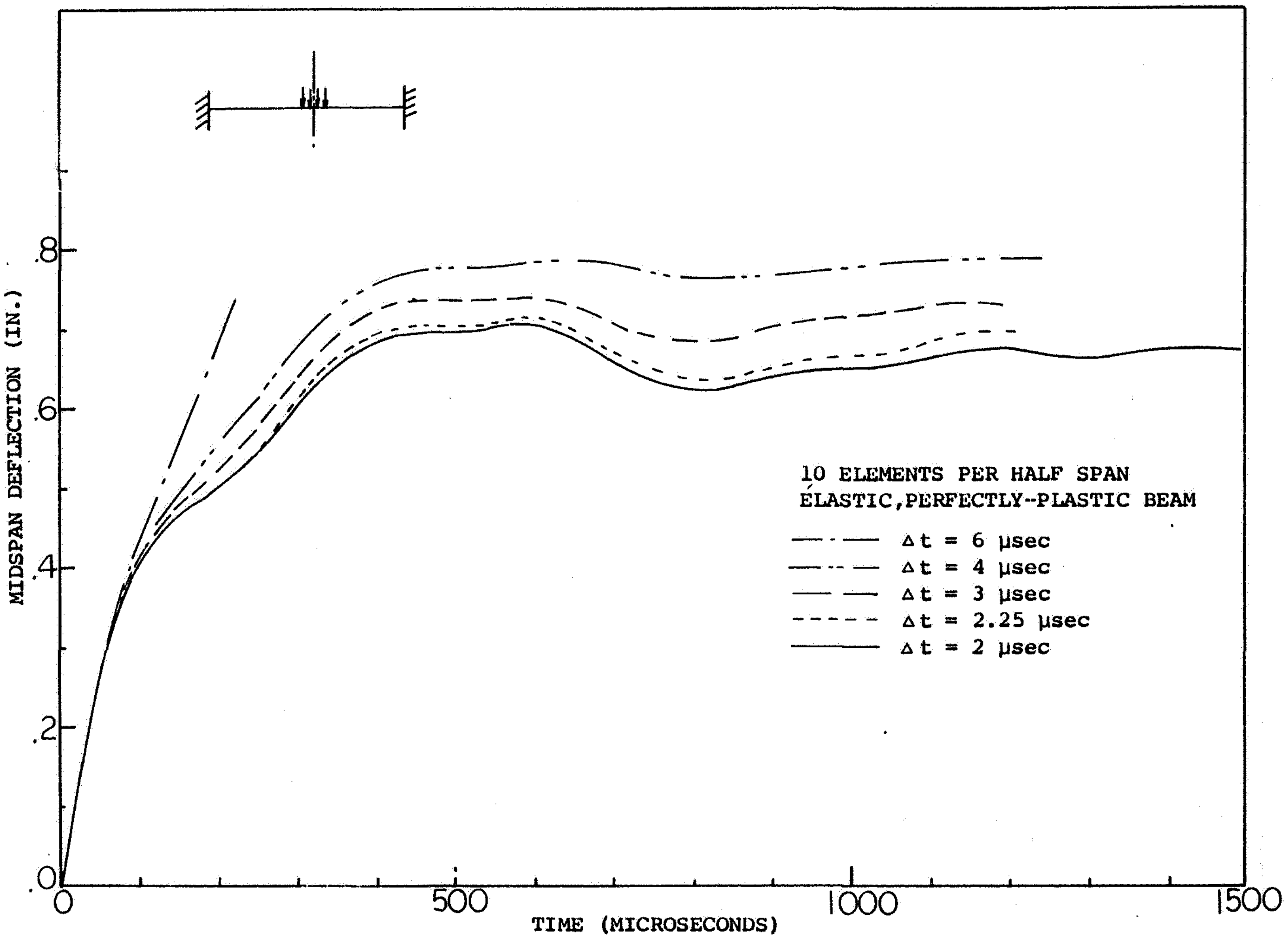

(b) Houbolt's Method

FIG.14 CONTINUED

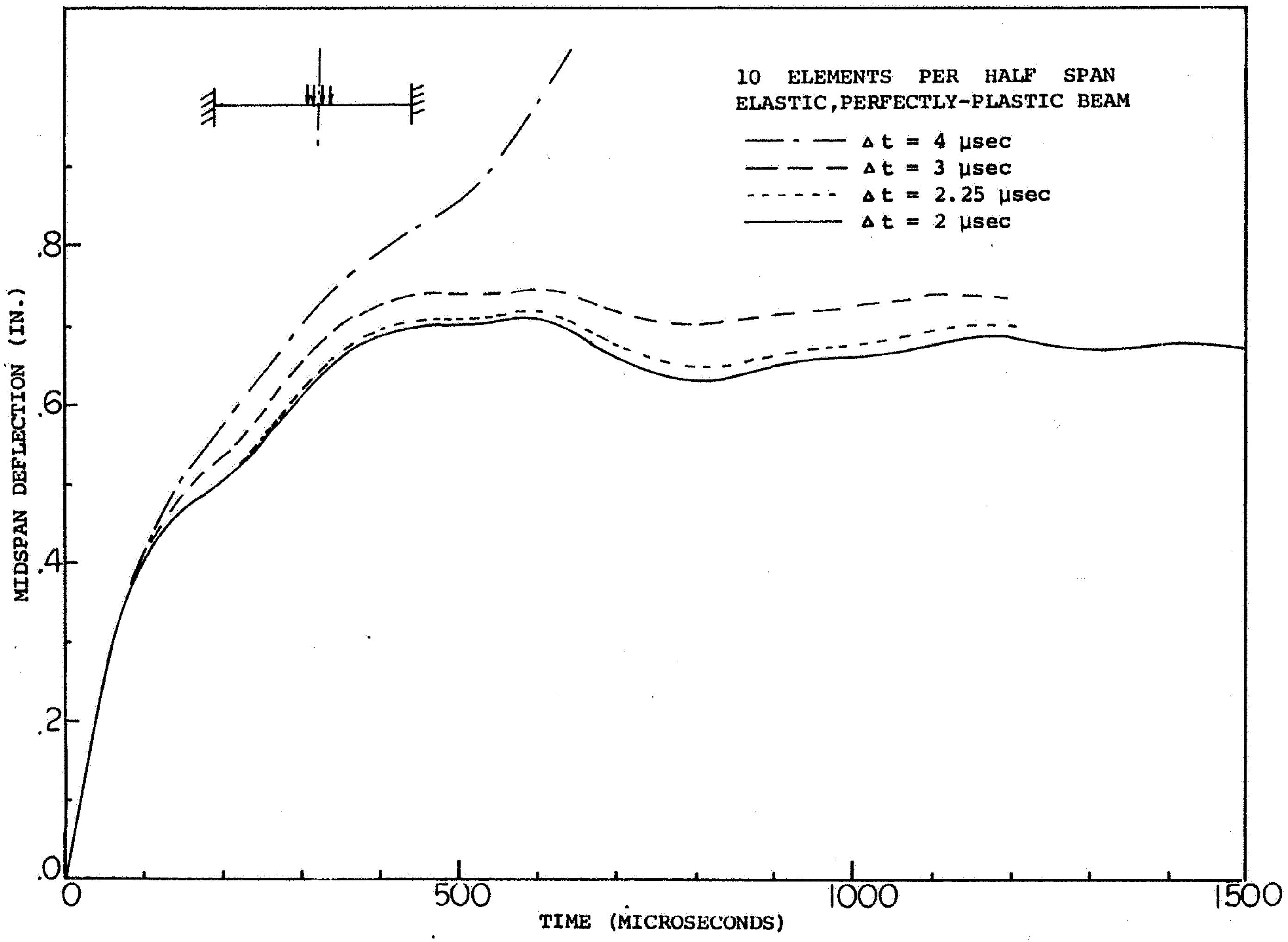

(c) Newmark's Method

FIG.14 CONCLUDED

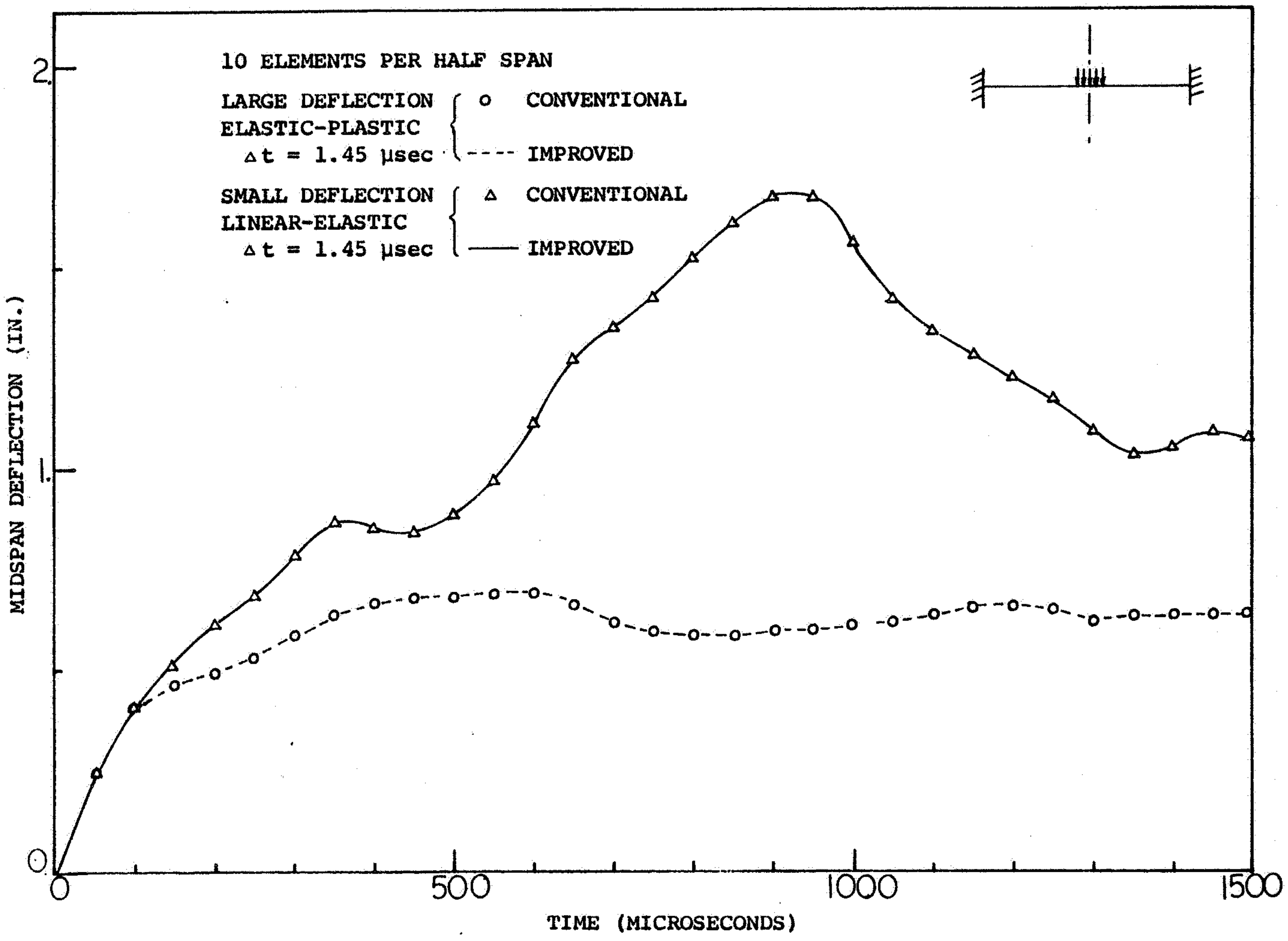

FIG.15 COMPARISON OF DYNAMIC RESPONSES OF THE CLAMPED BEAM CALCULATED BY THE CONVENTIONAL AND THE IMPROVED FORMULATION OF DYNAMIC EQUILIBRIUM

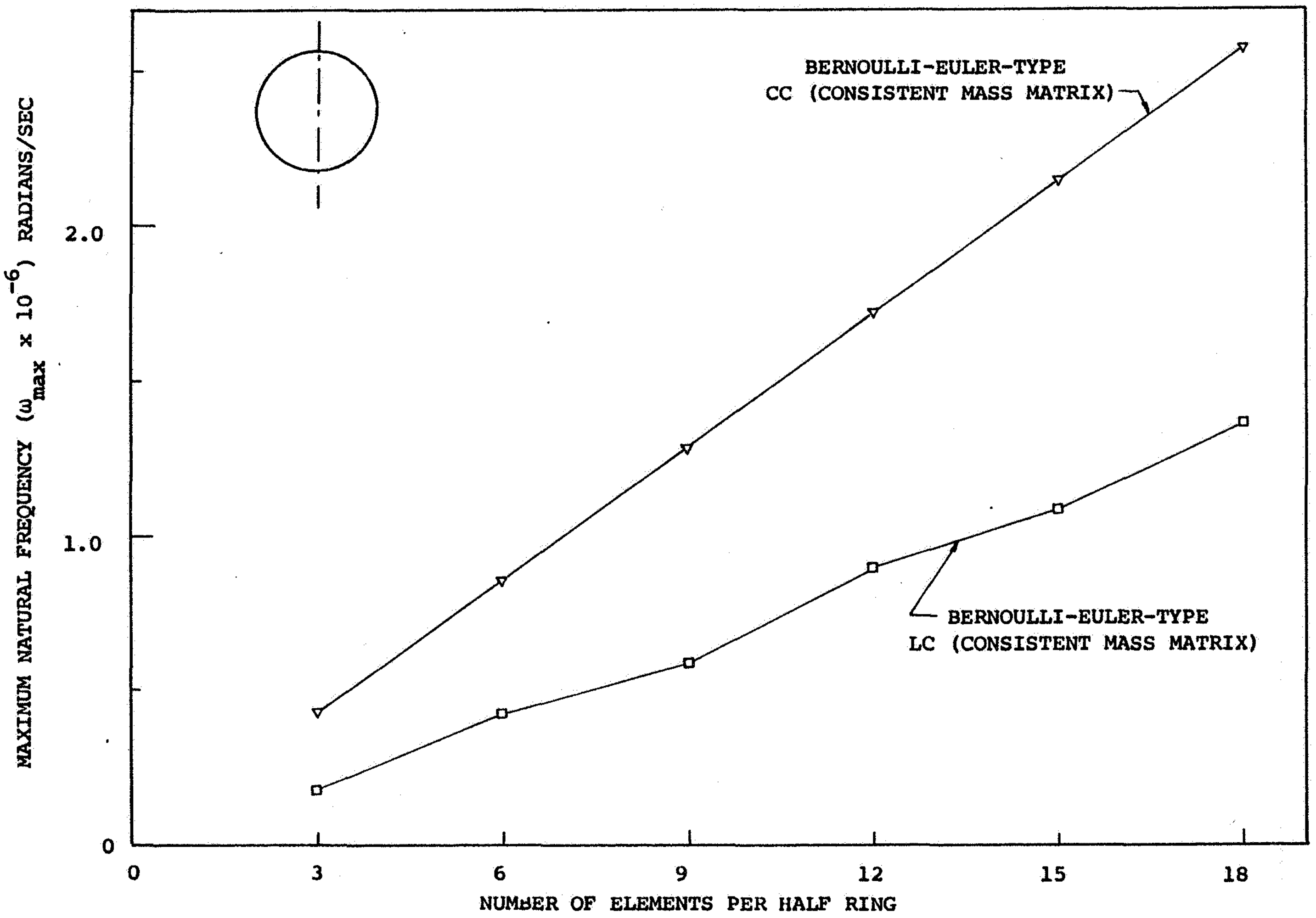

(a) MAXIMUM NATURAL FREQUENCY

FIG. 16 COMPARISON OF DYNAMIC RESPONSES OF THE FREE RING OBTAINED BY USING CC VERSUS LC ASSUMED DISPLACEMENT FUNCTIONS

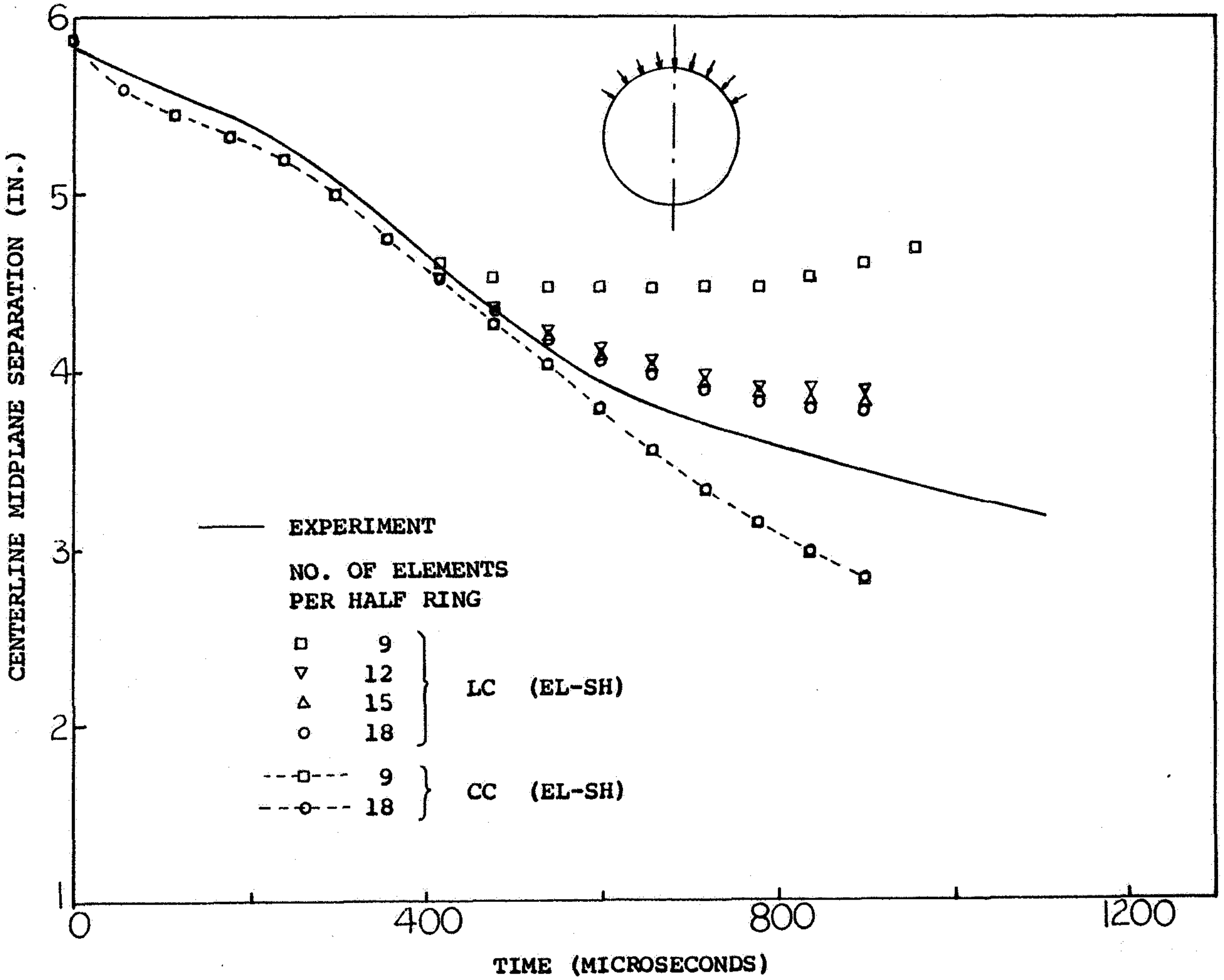

(b) Centerline Midplane Separation Responses

FIG.16 CONTINUED

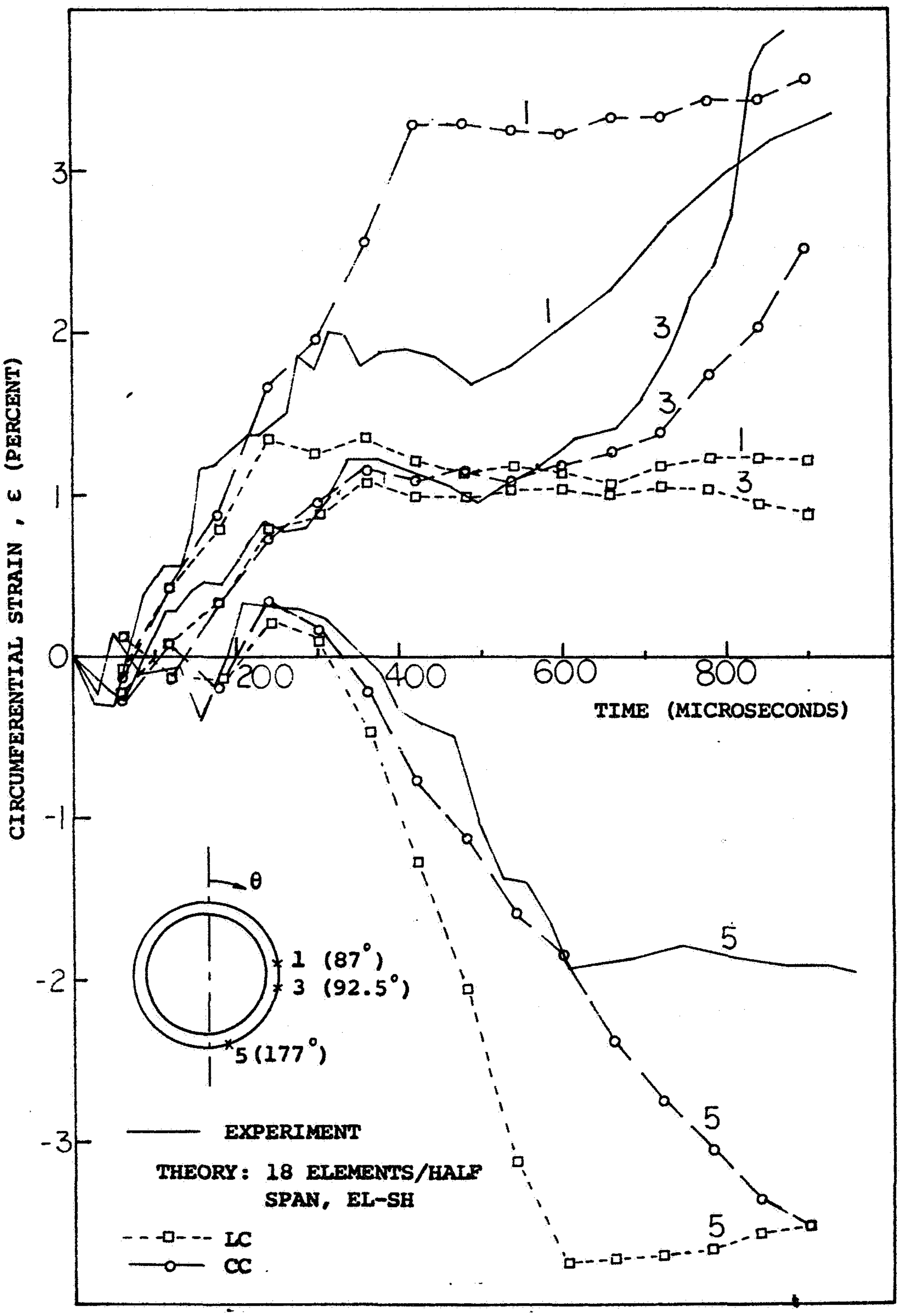

(c) Outer Surface Strain Responses

FIG.16 CONCLUDED

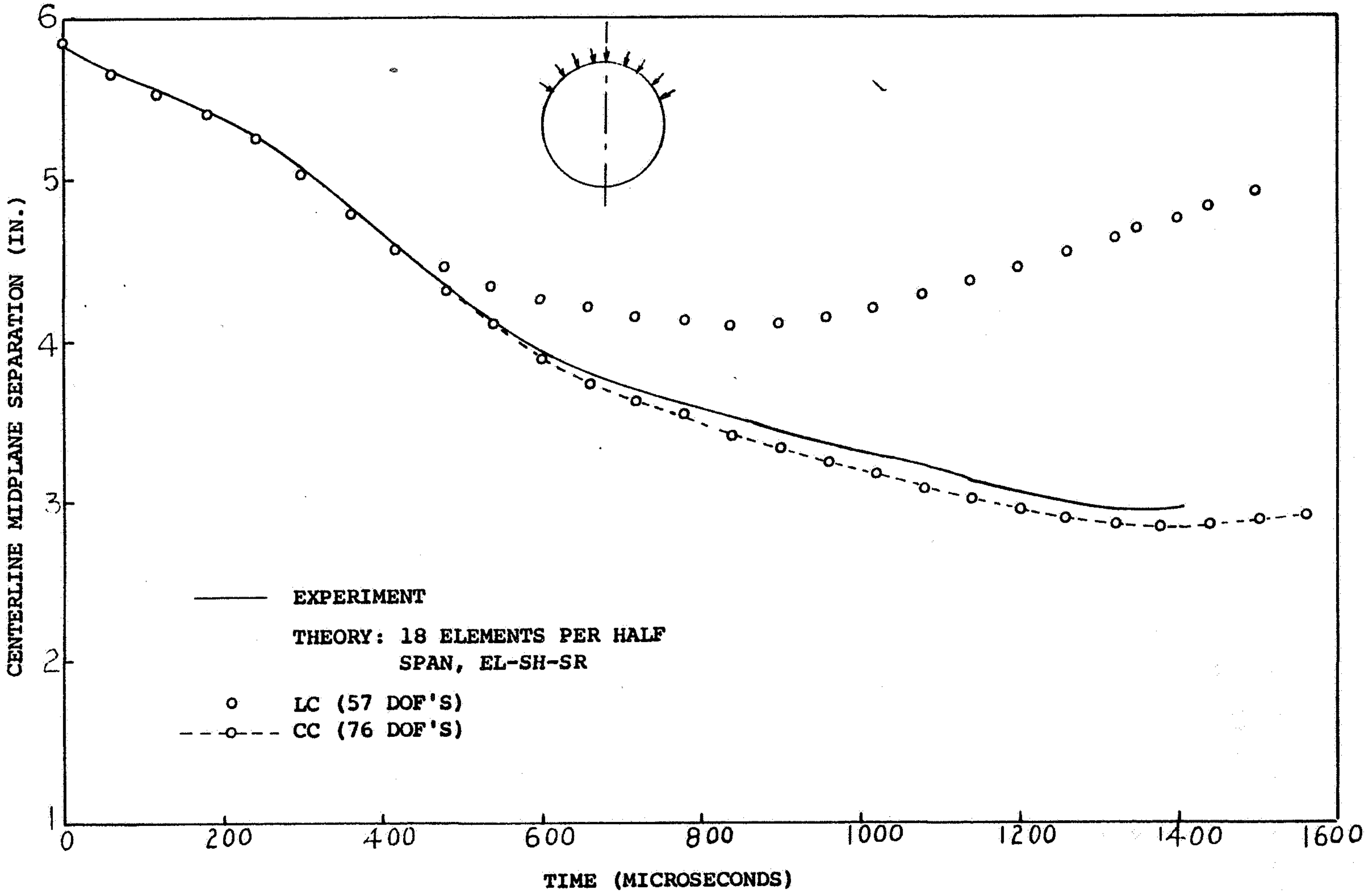

(a) Centerline Midplane Separation Responses

FIG.17 COMPARISON OF DYNAMIC RESPONSES OF THE FREE RING (INCLUDING STRAIN-RATE EFFECT) OBTAINED BY USING LC VERSUS CC ASSUMED DISPLACEMENT FUNCTIONS

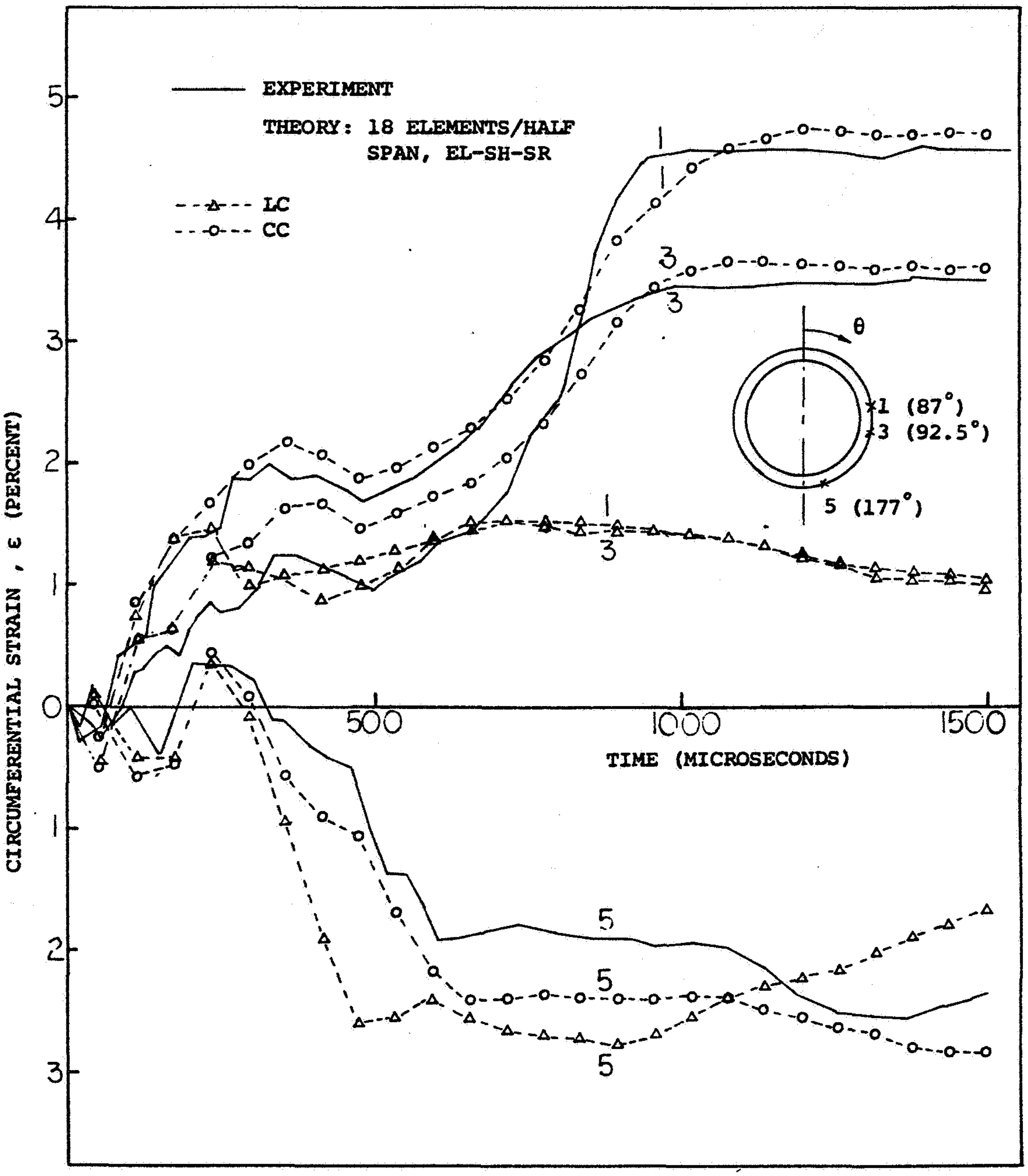

(b) Outer Surface Strain Responses

FIG.17. CONCLUDED

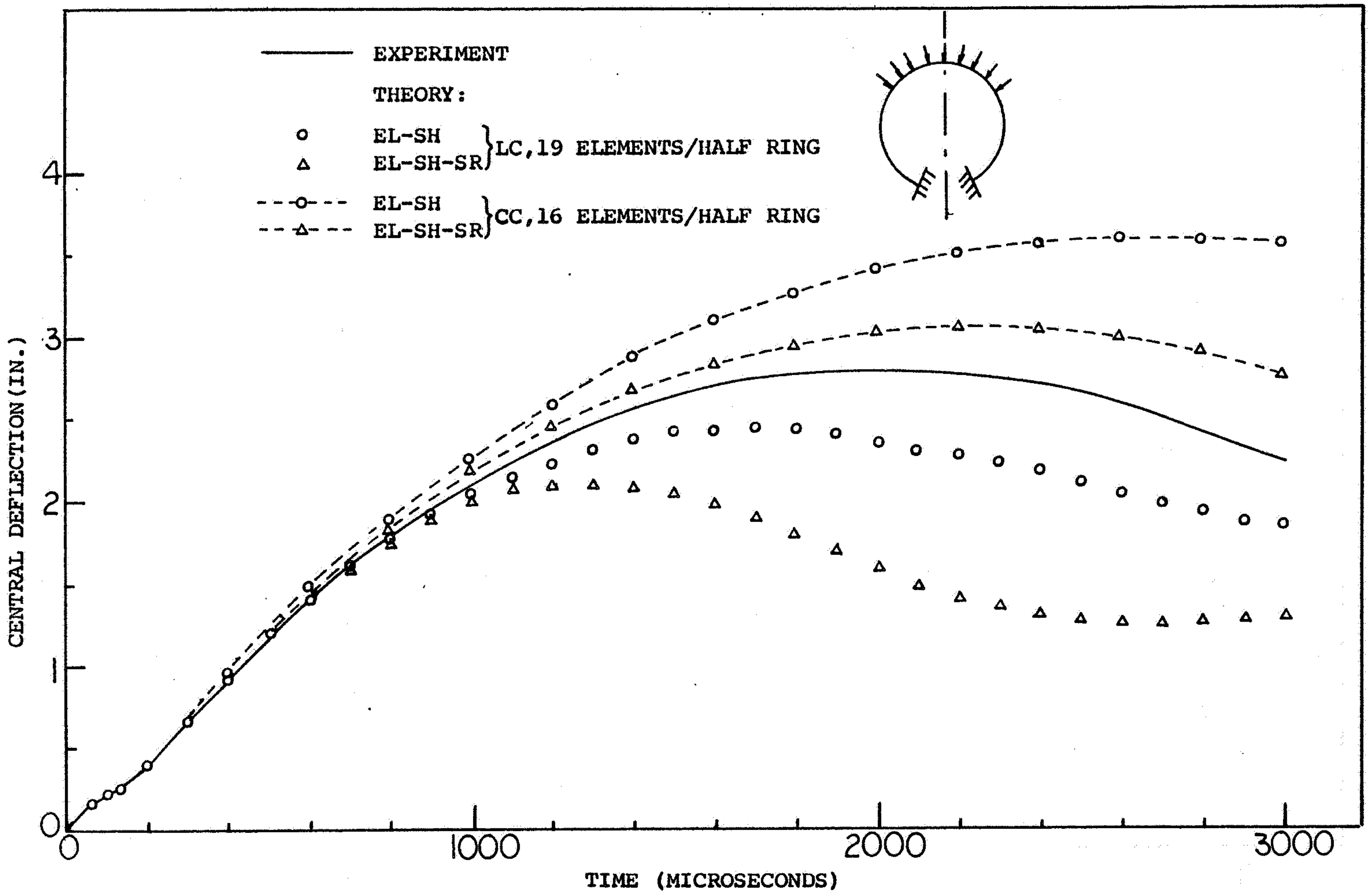

FIG.18 COMPARISON OF DYNAMIC RESPONSES OF THE CLAMPED RING CALCULATED BY USING CC VERSUS LC ASSUMED DISPLACEMENT FUNCTIONS

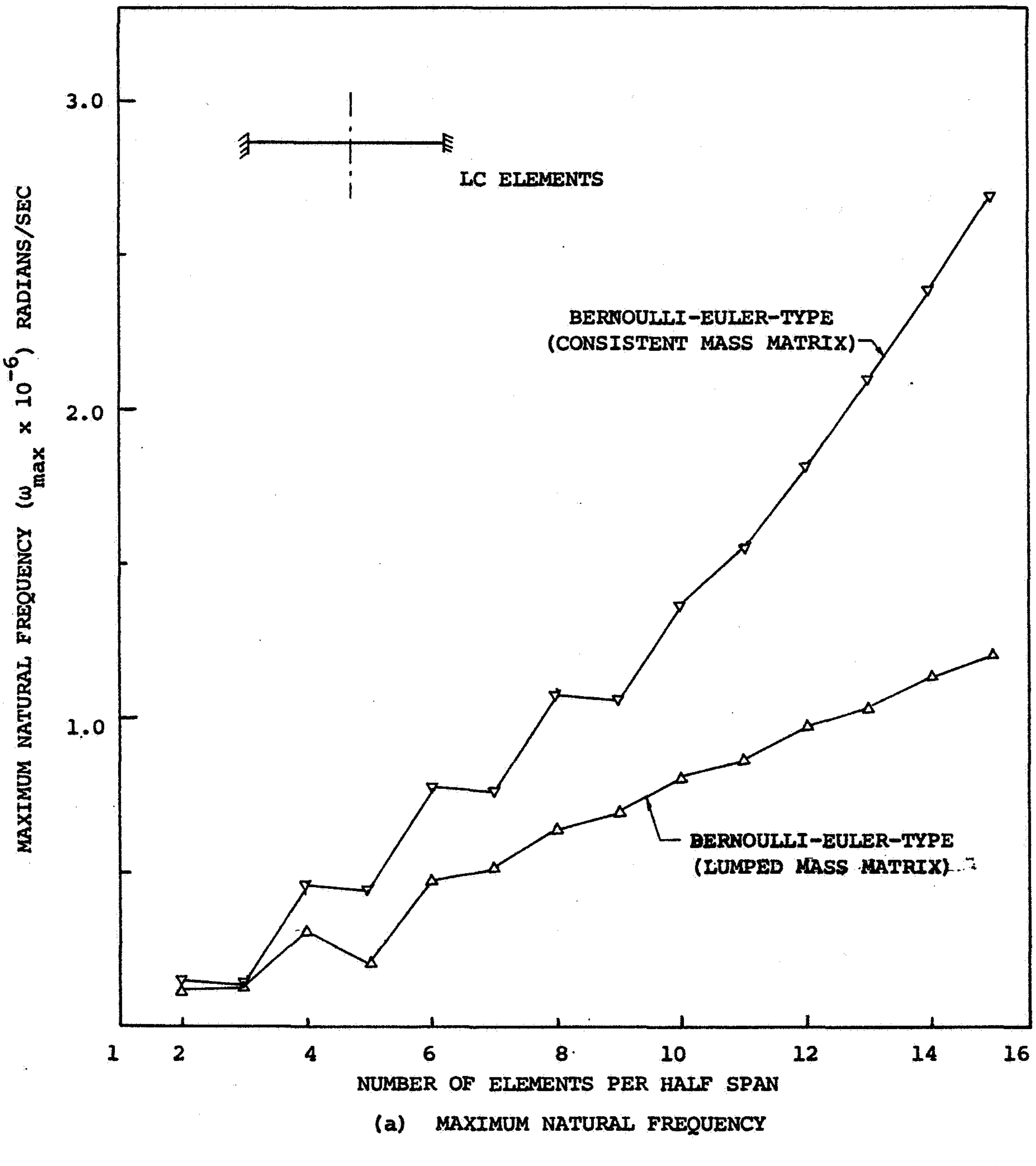

(a) MAXIMUM NATURAL FREQUENCY

FIG. 19 COMPARISON OF DYNAMIC RESPONSES OF THE CLAMPED BEAM CALCULATED BY USING THE LUMPED MASS MATRIX AND THE CONSISTENT MASS MATRIX

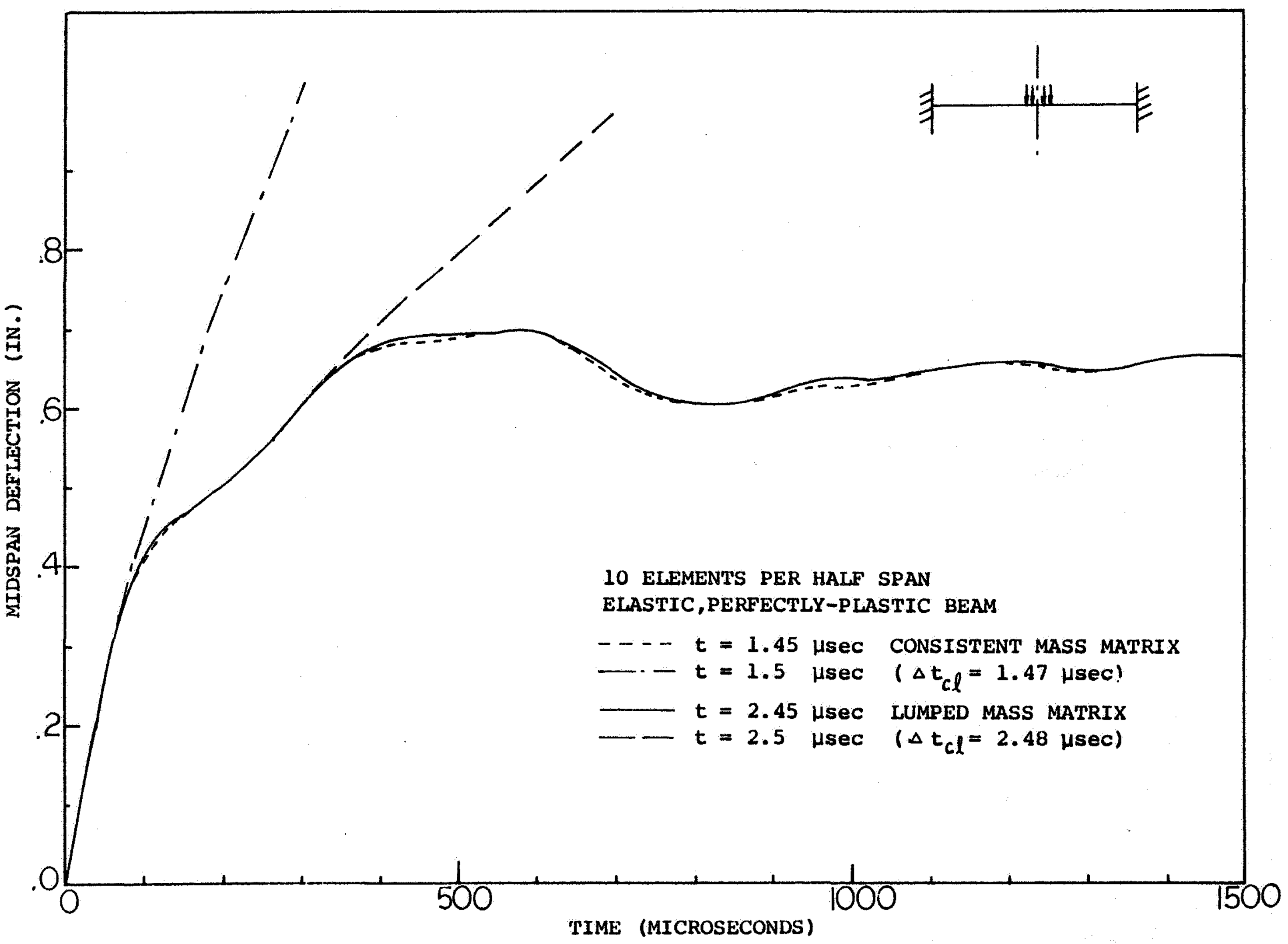

(b) Midspan Deflection Responses

FIG.19 CONCLUDED

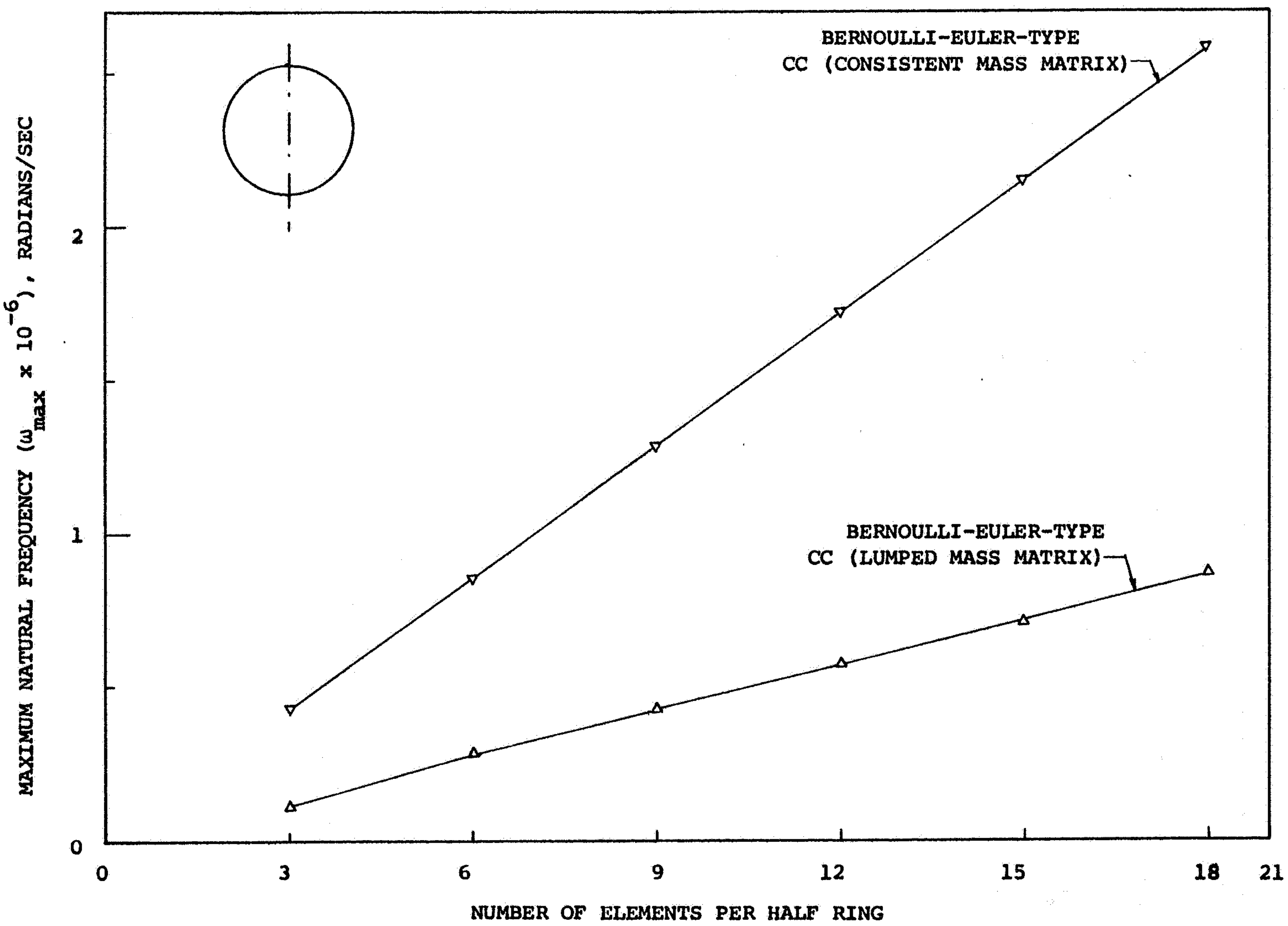

(a) MAXIMUM NATURAL FREQUENCY

FIG. 20 COMPARISON OF DYNAMIC RESPONSES OF THE FREE RING CALCULATED BY USING THE LUMPED MASS MATRIX AND THE CONSISTENT MASS MATRIX

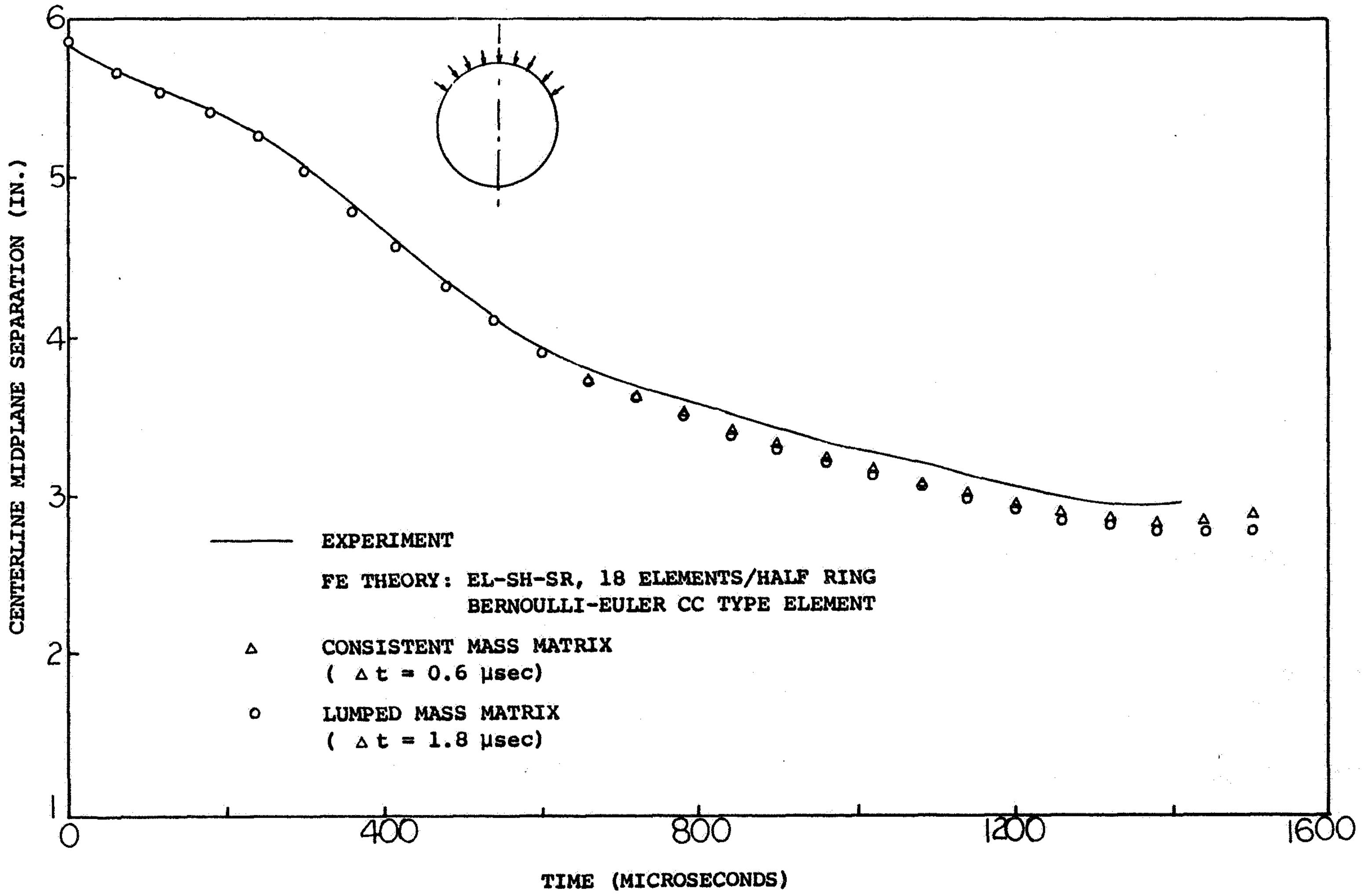

(b) Centerline Midplane Separation Responses

FIG.20 CONTINUED

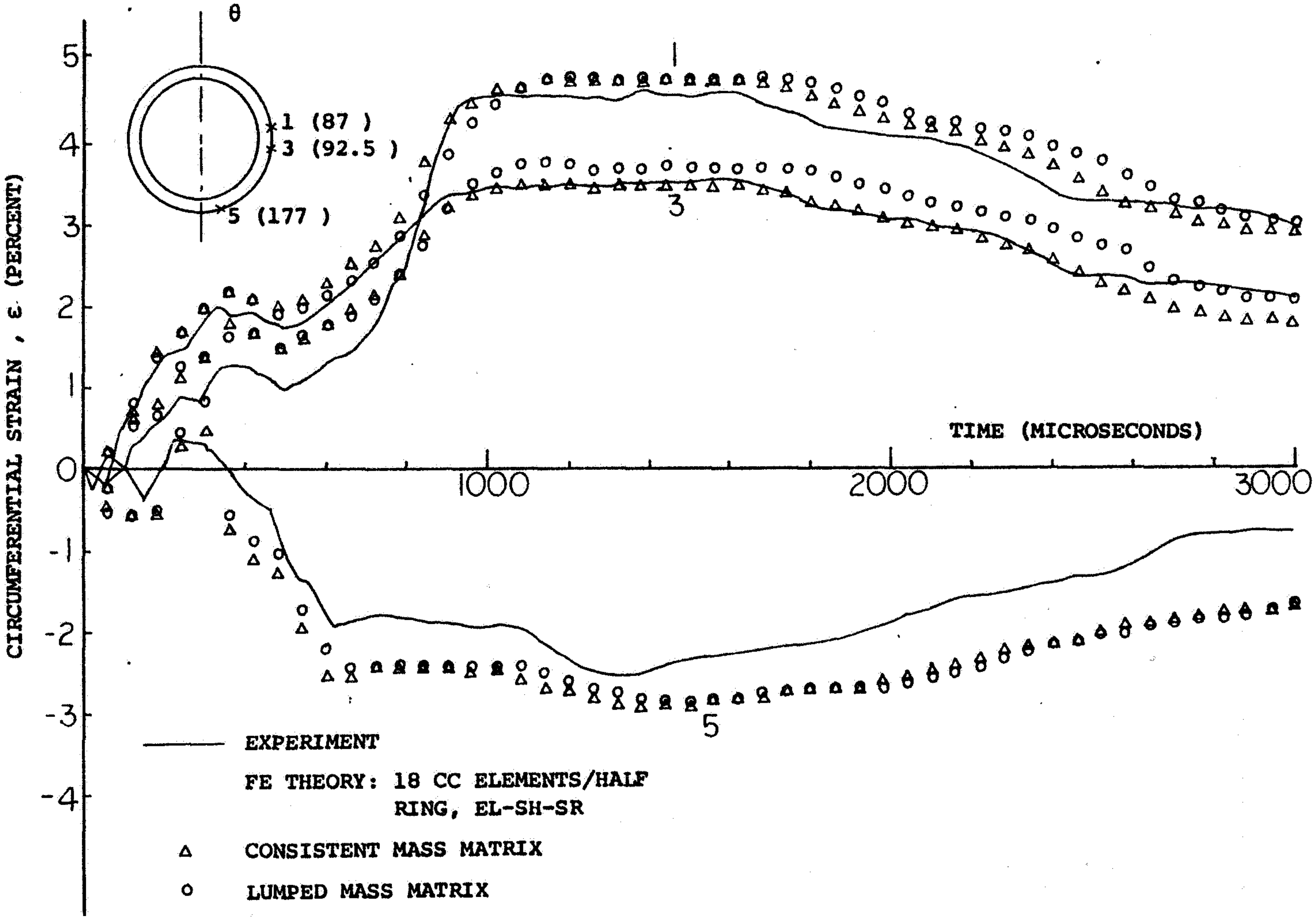

(c) Outer Surface Strain Responses

FIG.20 CONCLUDED

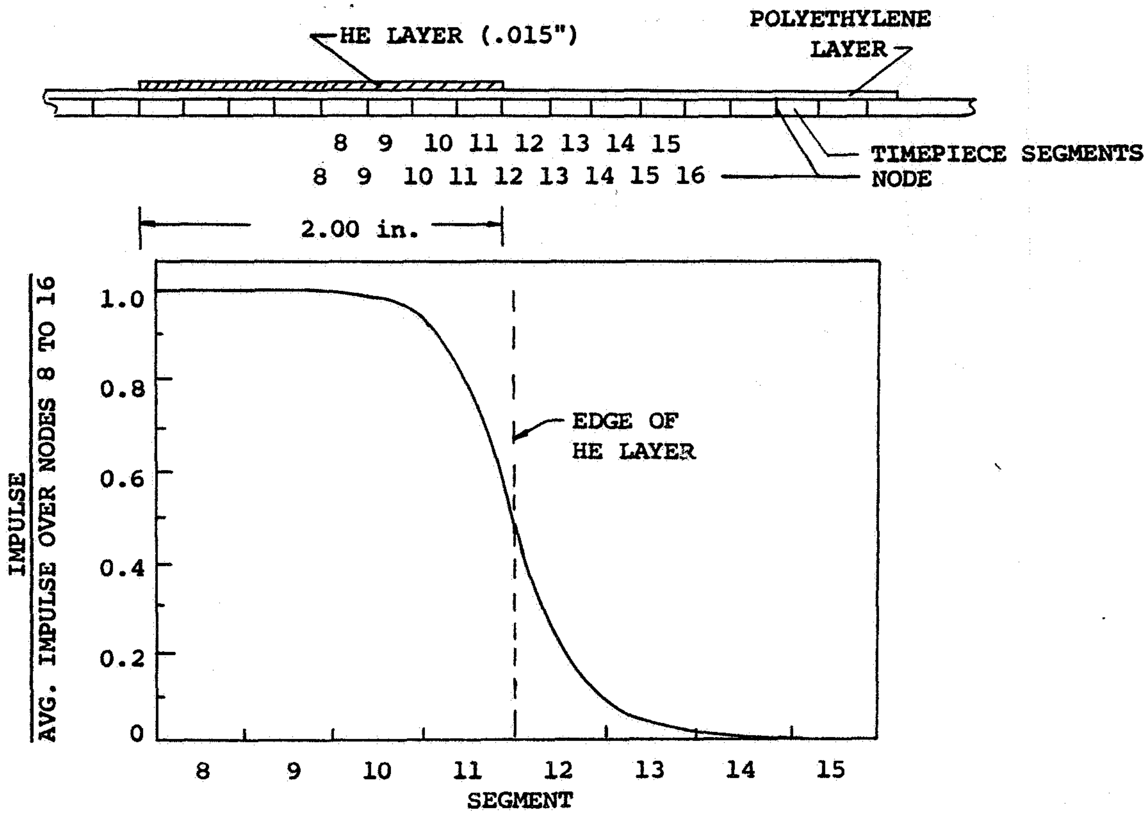

(a) Spanwise Distribution of Imparted Impulse (Ref. 55)

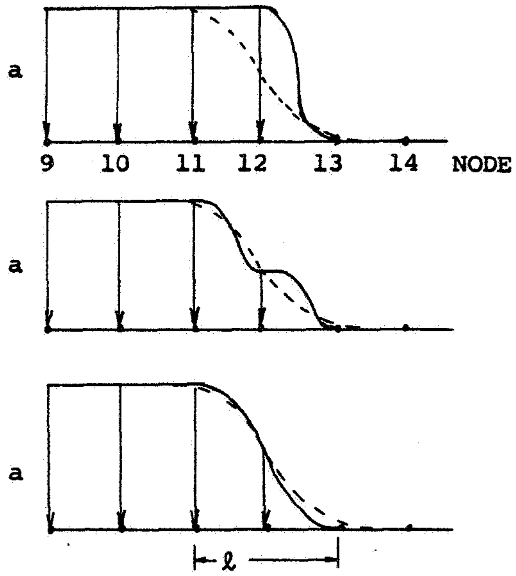

IV1: $\dot{w}_{11} = a$ $\dot{w}_{,\eta 11} = 0$
$\dot{w}_{12} = a$ $\dot{w}_{,\eta 12} = 0$
$\dot{w}_{13} = 0$ $\dot{w}_{,\eta 13} = 0$

IV2: $\dot{w}_{11} = a$ $\dot{w}_{,\eta 11} = 0$
$\dot{w}_{12} = a/2$ $\dot{w}_{,\eta 12} = 0$
$\dot{w}_{13} = 0$ $\dot{w}_{,\eta 13} = 0$

IV3: $\dot{w}_{11} = a$ $\dot{w}_{,\eta 11} = 0$
$\dot{w}_{12} = a/2$ $\dot{w}_{,\eta 12} = a/\ell$
$\dot{w}_{13} = 0$ $\dot{w}_{,\eta 13} = 0$

(b) Types of Initial Nodal Velocities to Approximate the Impulse Loading with Finite Span

FIG. 21 HIGH EXPLOSIVE EDGE EFFECTS ON THE DISTRIBUTION OF IMPARTED IMPULSE AND NODAL INITIAL VELOCITIES

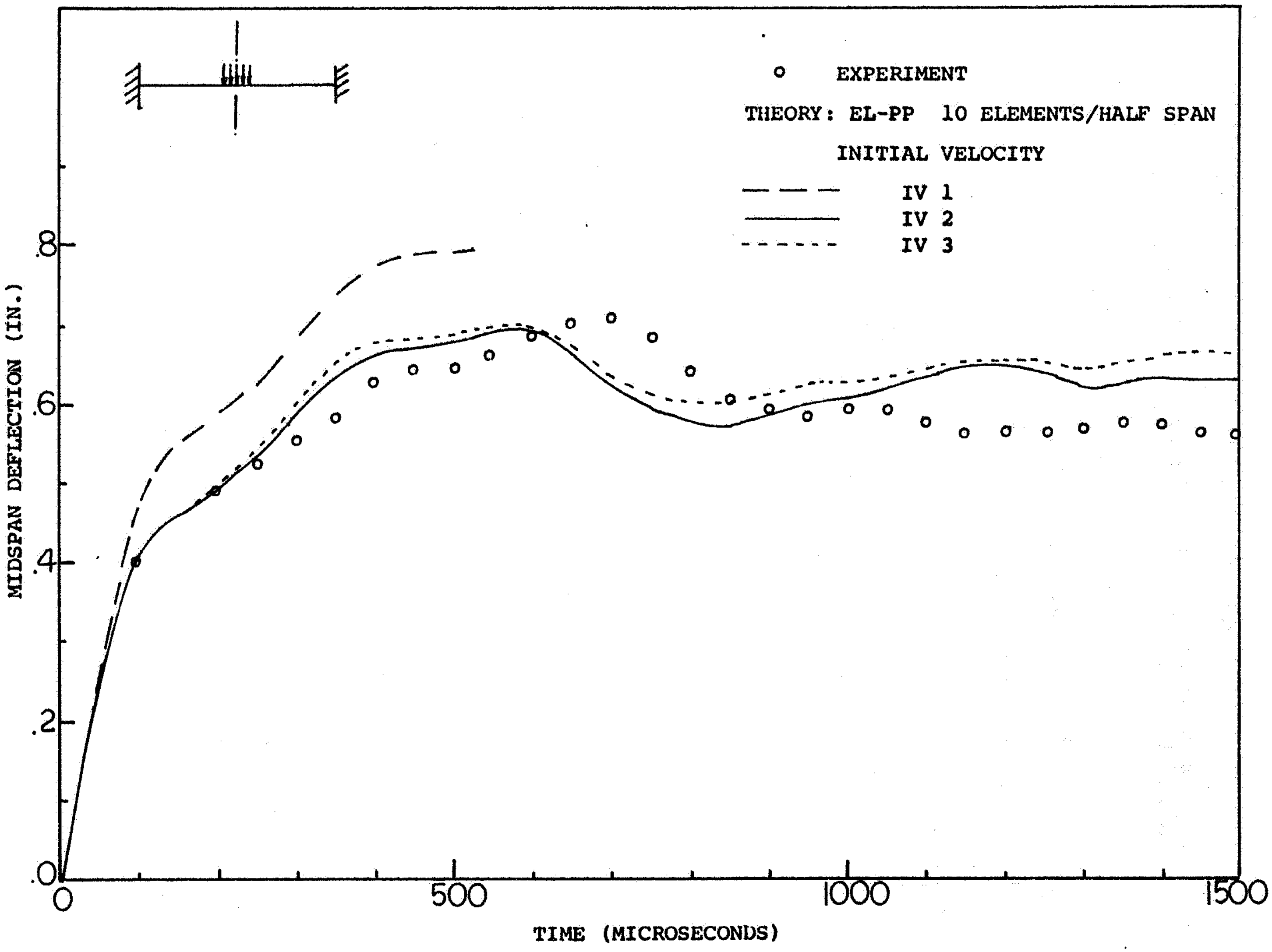

FIG.22 EFFECTS OF VARIOUS INITIAL NODAL VELOCITIES ON DYNAMIC RESPONSES OF THE CLAMPED BEAM

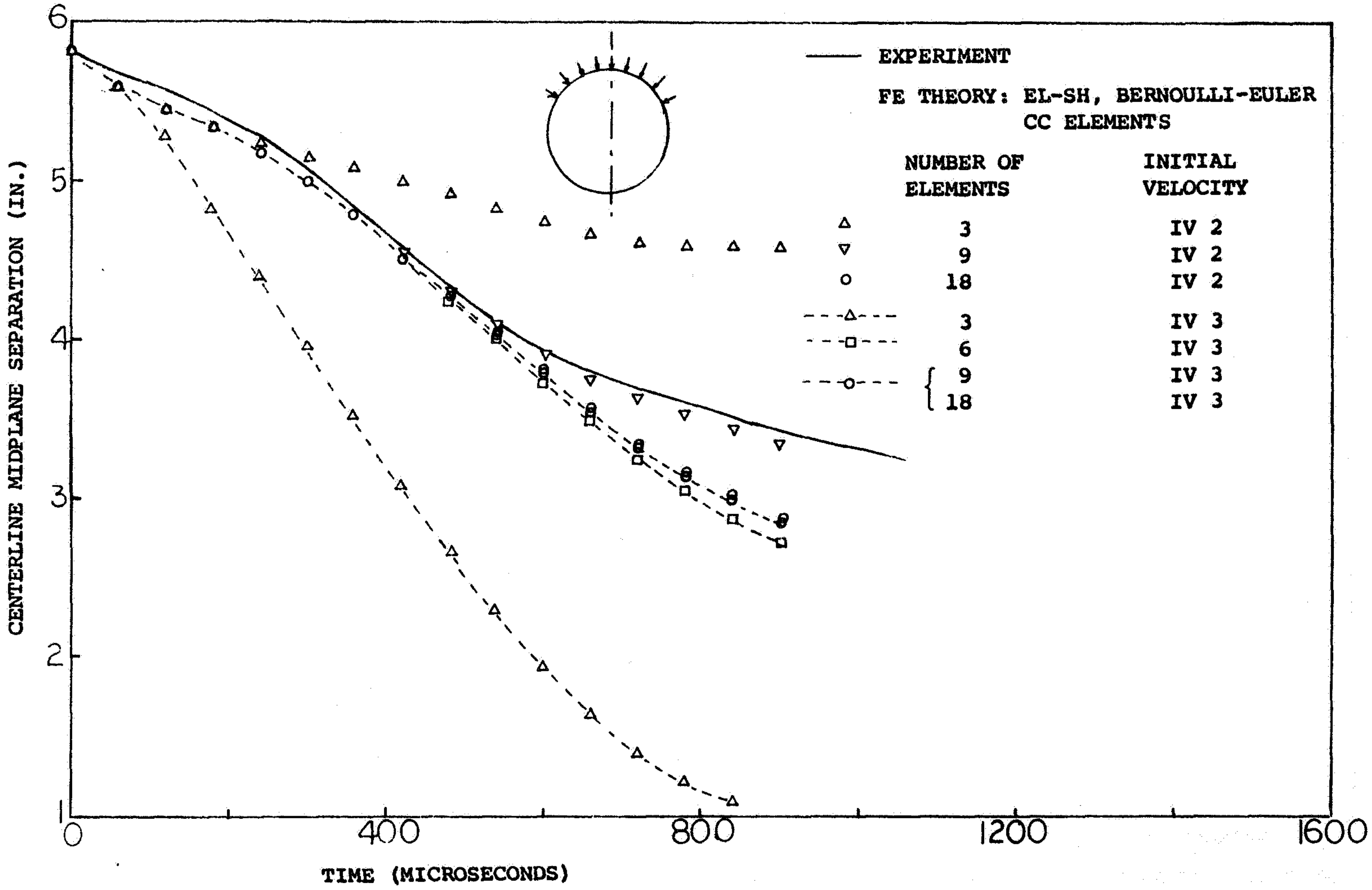

FIG.23 EFFECTS OF INITIAL NODAL VELOCITIES AND DISCRETE ELEMENT SIZE ON DYNAMIC RESPONSES OF THE FREE RING

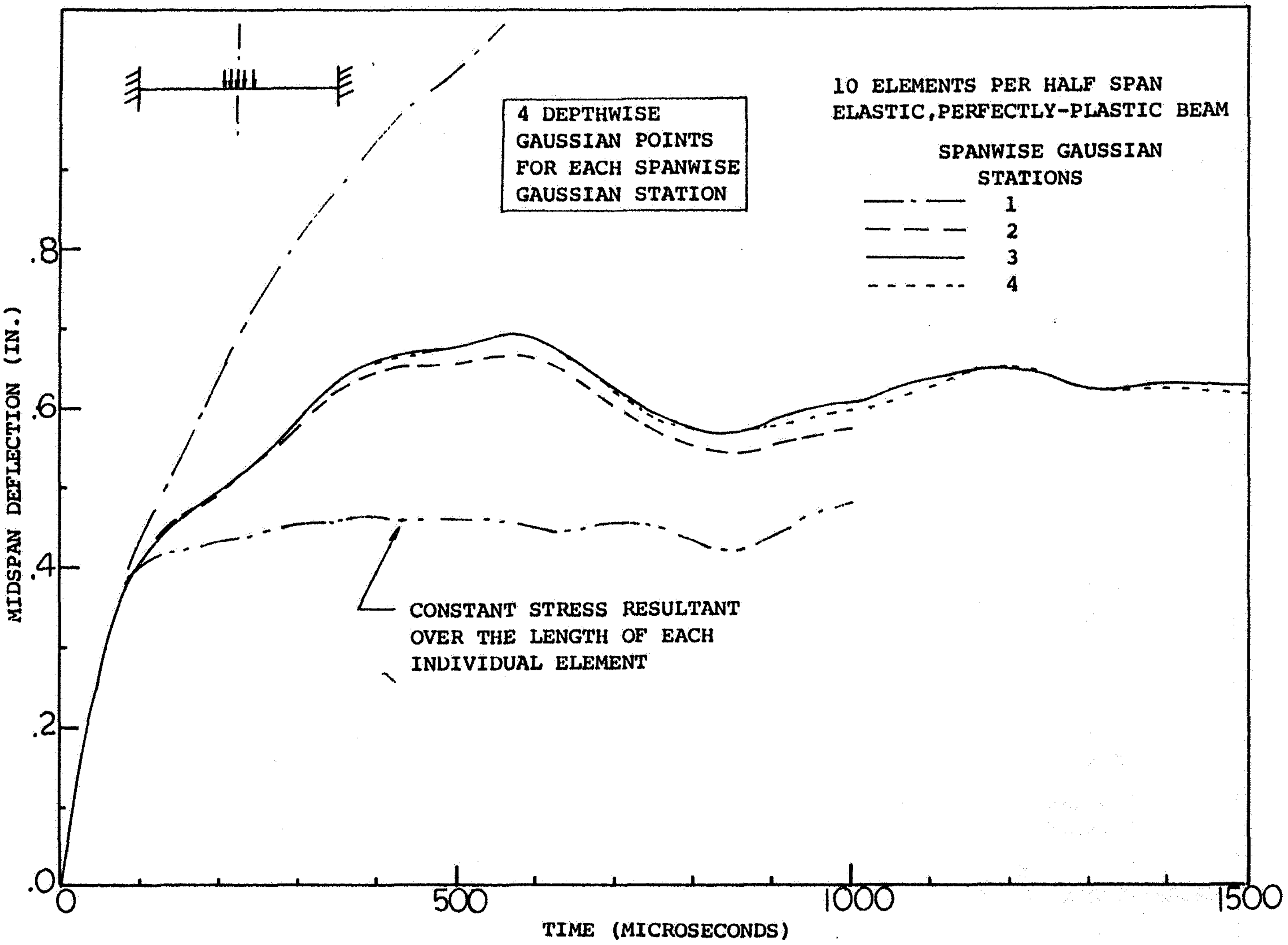

FIG.24 EFFECTS OF NUMBER OF SPANWISE GAUSSIAN INTEGRATION STATIONS ON DYNAMIC RESPONSES OF THE CLAMPED BEAM

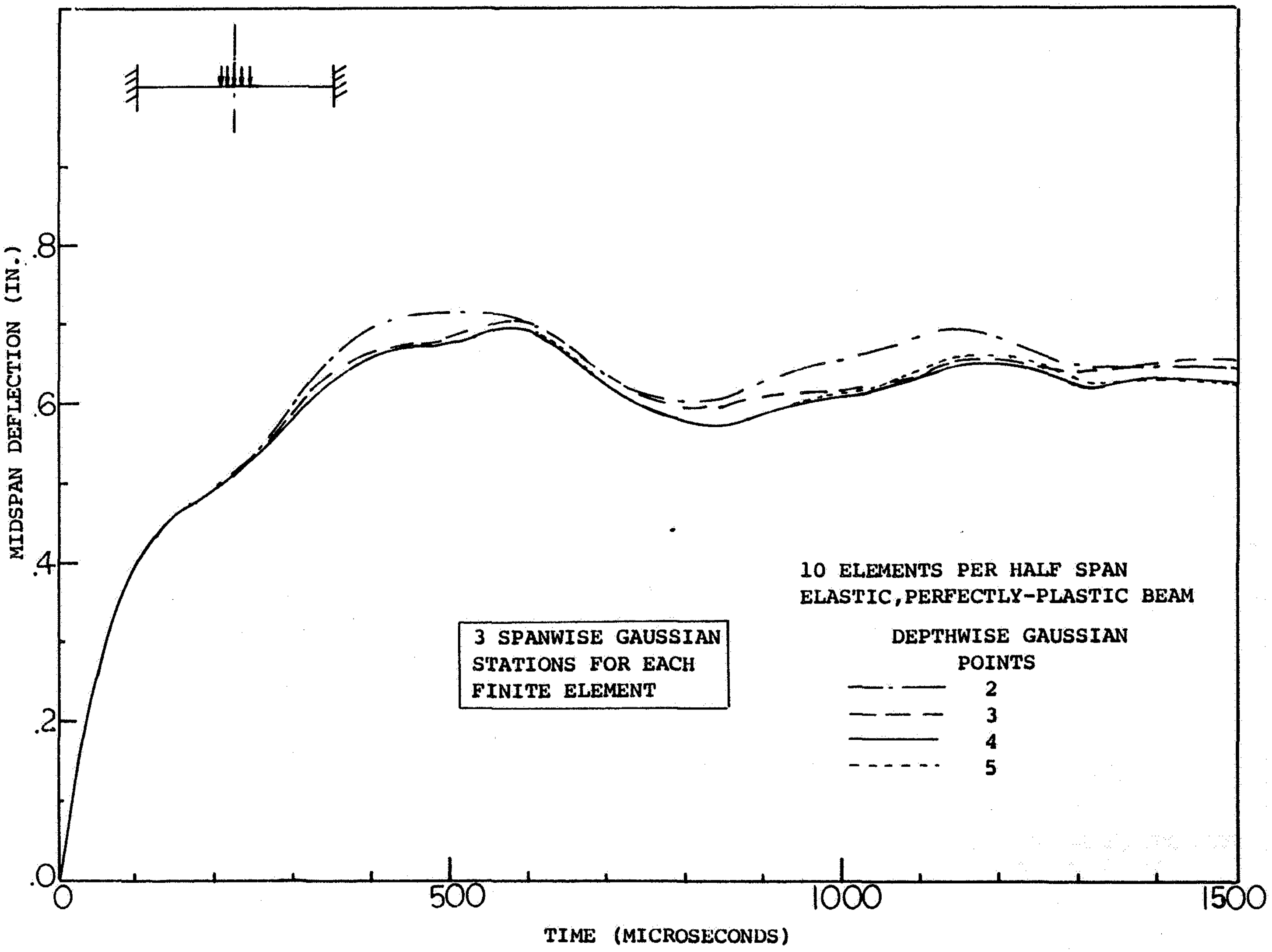

FIG.25 EFFECTS OF NUMBER OF DEPTHWISE GAUSSIAN INTEGRATION POINTS ON DYNAMIC RESPONSES OF THE CLAMPED BEAM

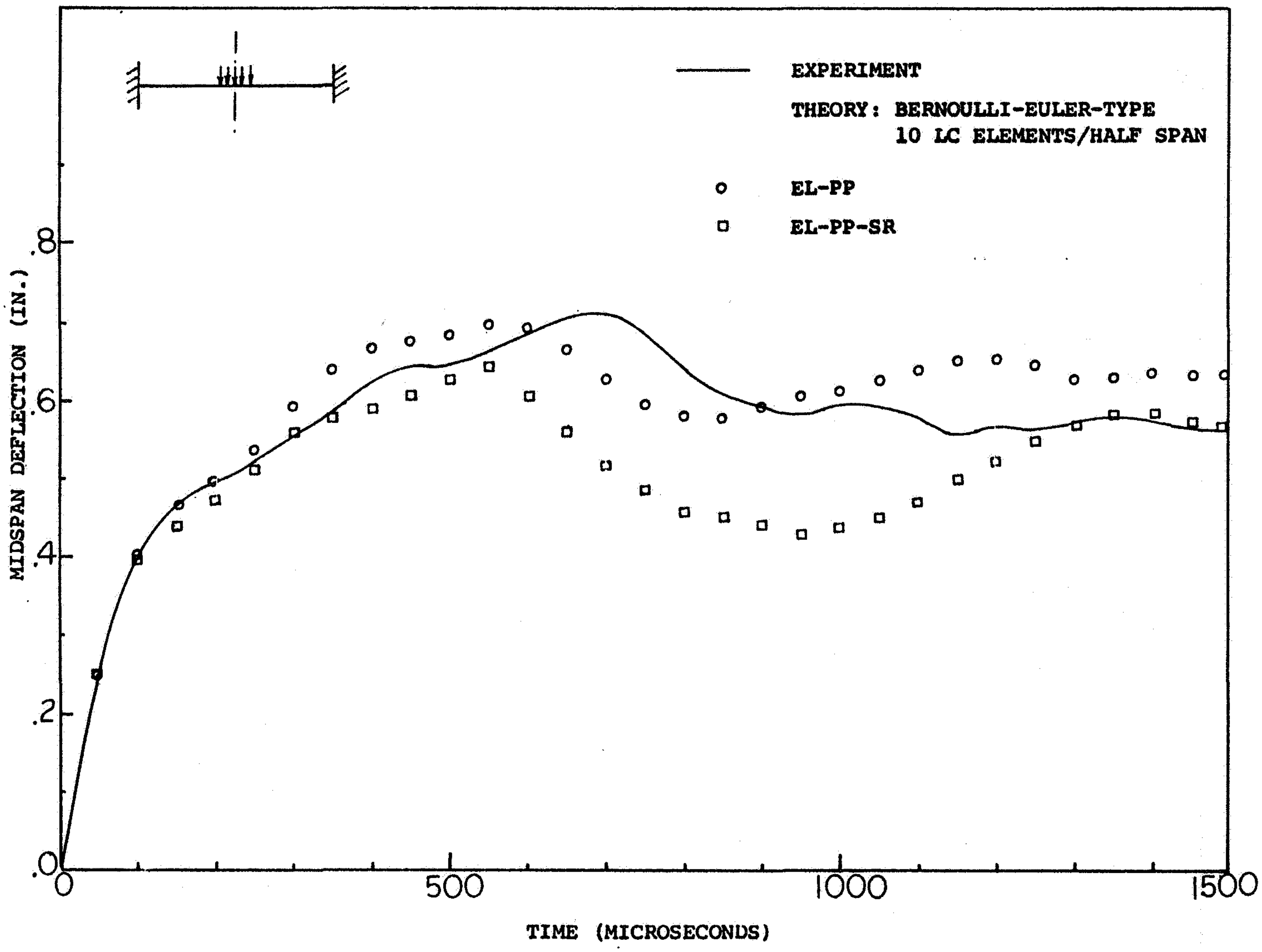

FIG.26 EFFECTS OF STRAIN-RATE ON DYNAMIC RESPONSES OF THE CLAMPED BEAM

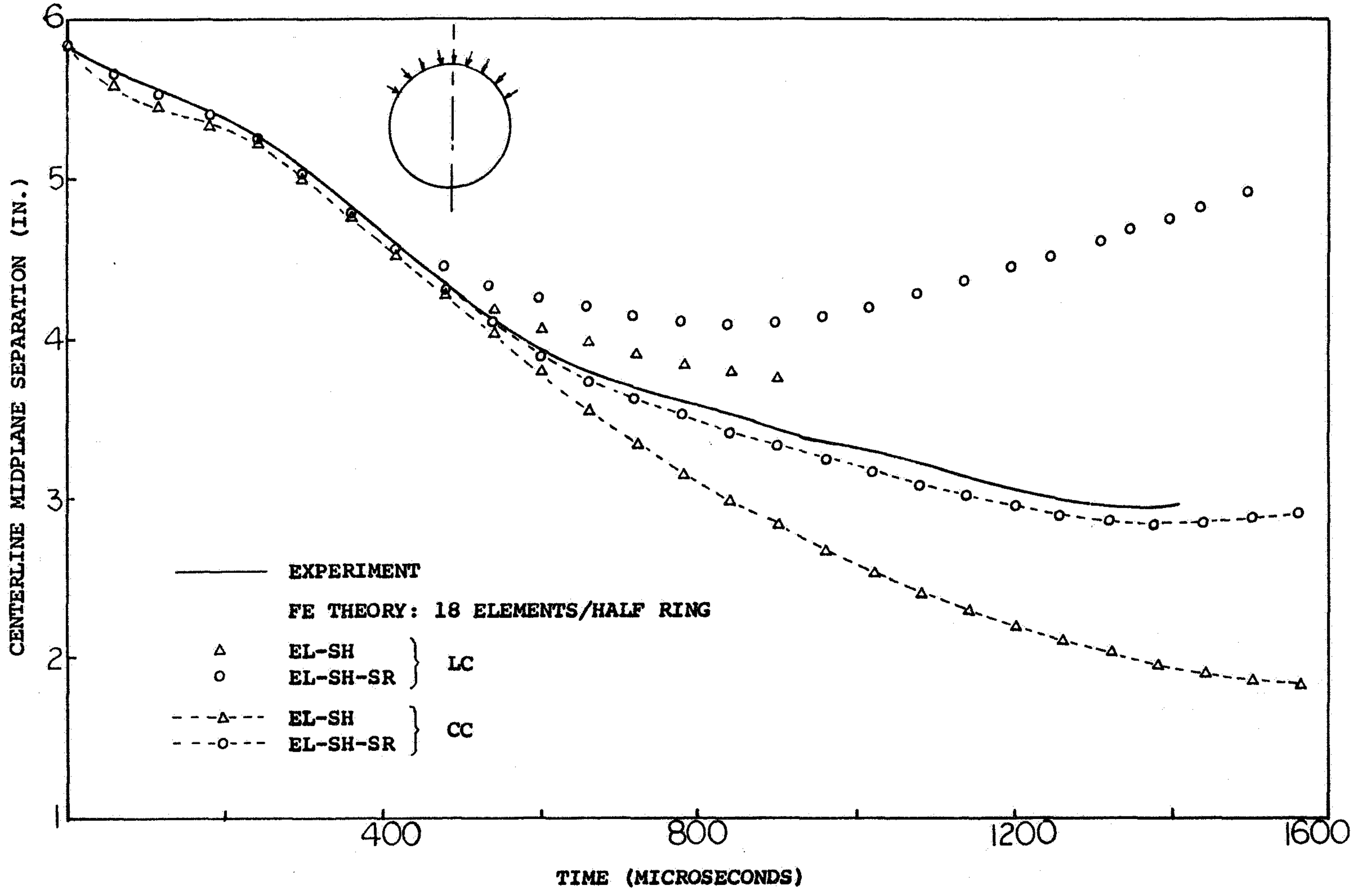

FIG.27 EFFECTS OF STRAIN-RATE ON DYNAMIC RESPONSES OF THE FREE RING

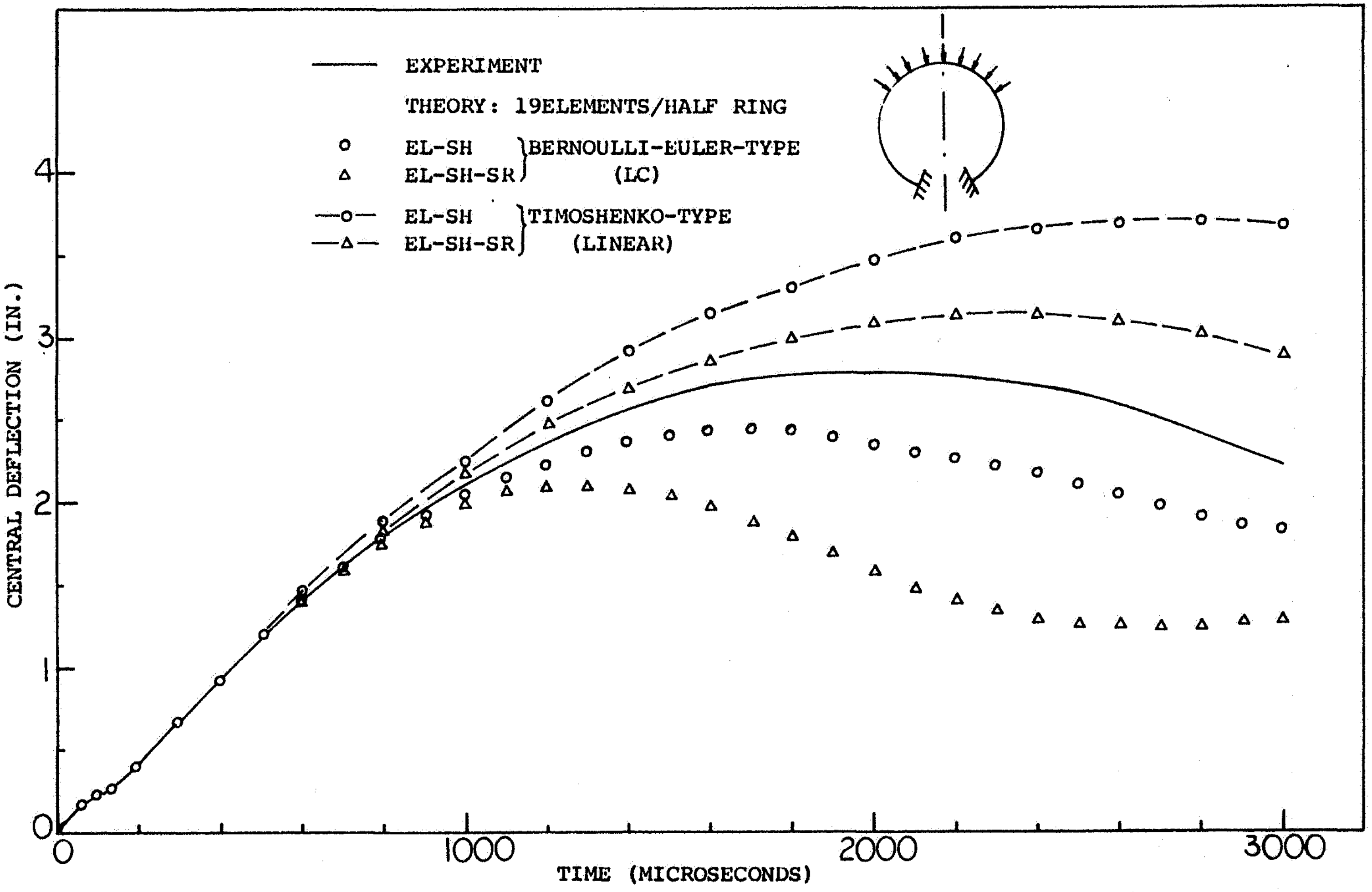

FIG.28 EFFECTS OF STRAIN-RATE ON DYNAMIC RESPONSES OF THE CLAMPED RING

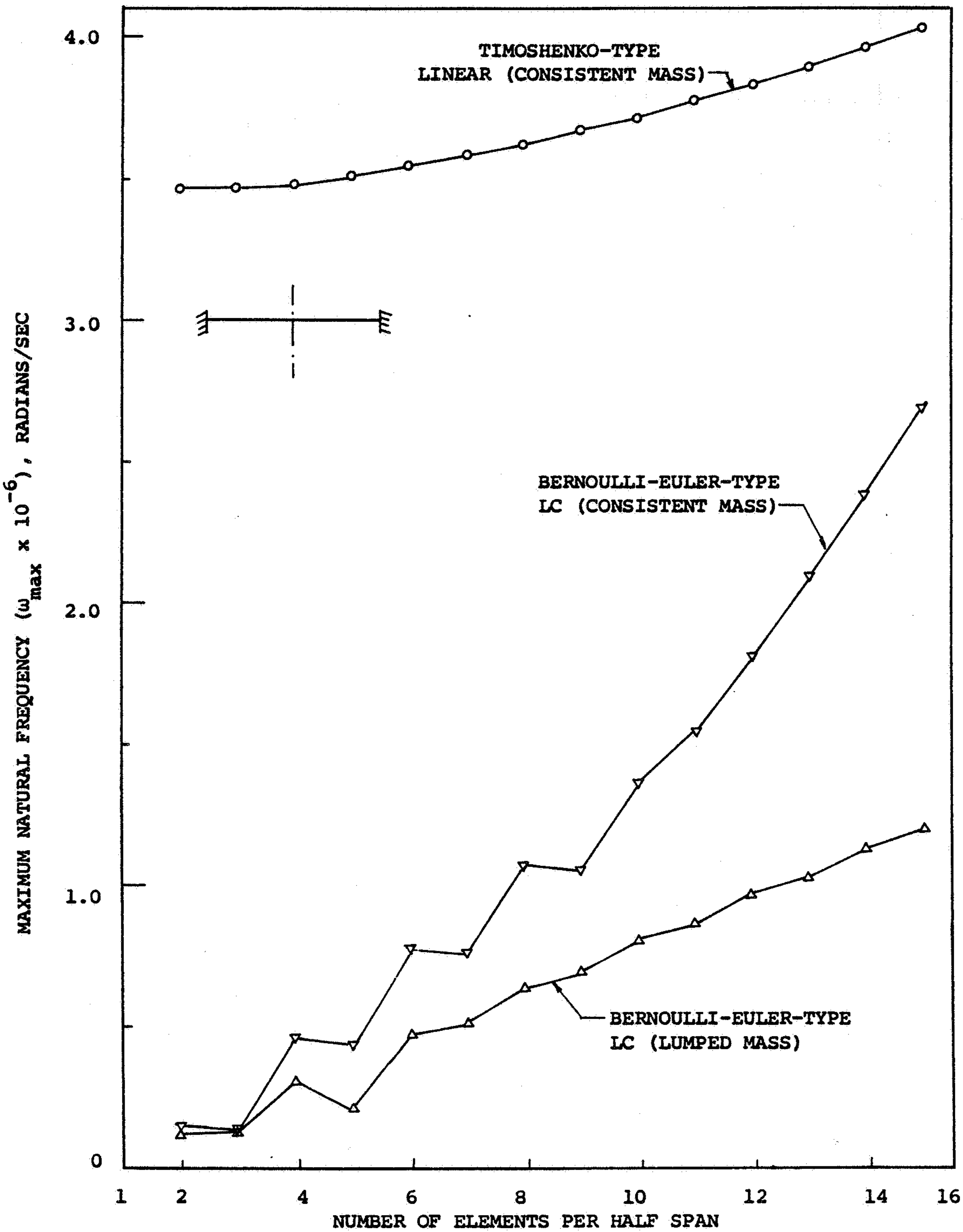

FIG. 29 COMPARISON OF THE MAXIMUM NATURAL FREQUENCY OF THE CLAMPED BEAM CALCULATED BY USING TIMOSHENKO-TYPE ELEMENTS VERSUS BERNOULLI-EULER-TYPE ELEMENTS

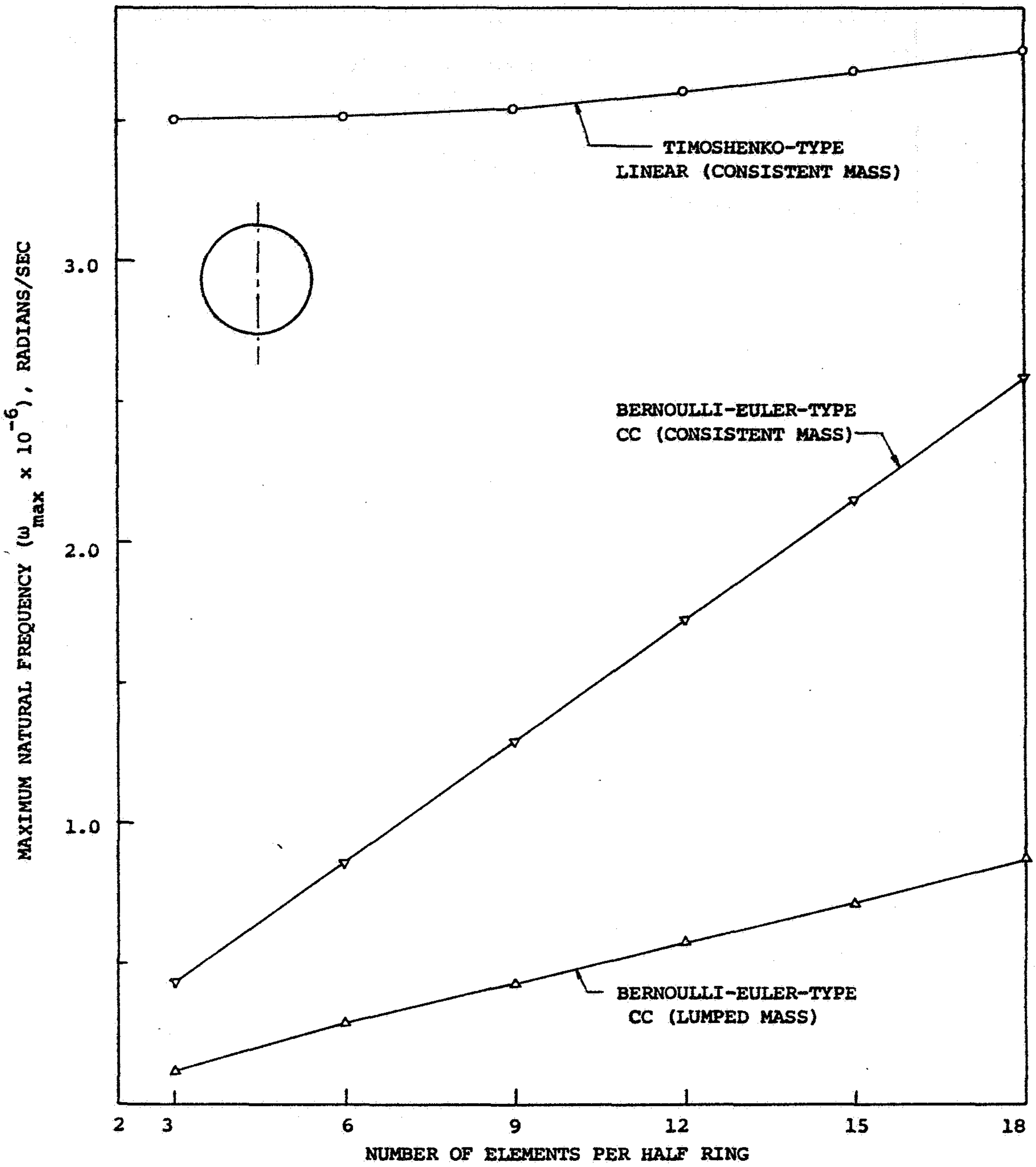

*FIG. 30* COMPARISON OF THE *MAXIMUM* NATURAL FREQUENCY OF THE FREE RING CALCULATED BY USING TIMOSHENKO-TYPE ELEMENTS VERSUS BERNOULLI-EULER-TYPE ELEMENTS

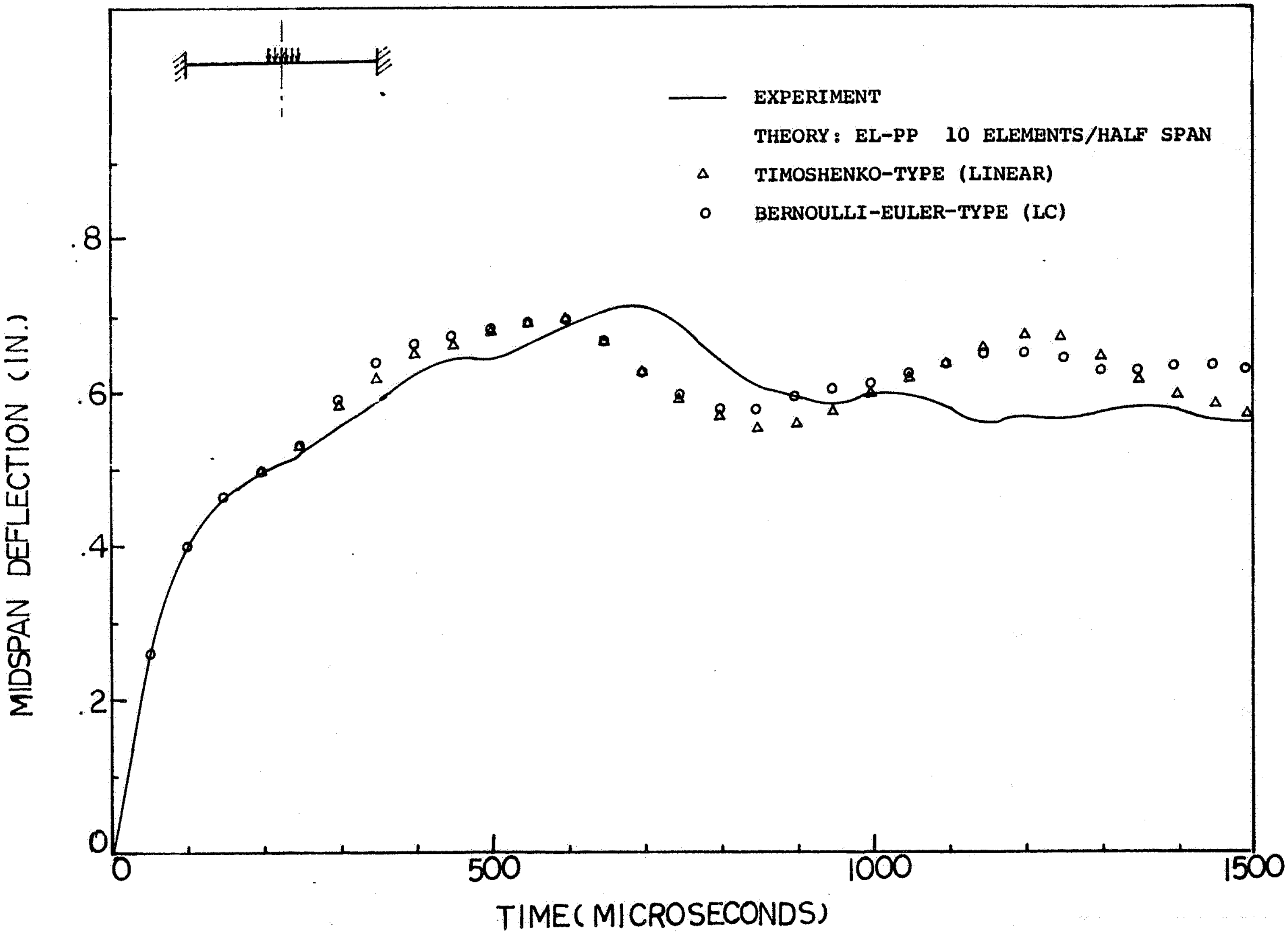

FIG.31 COMPARISON OF DYNAMIC RESPONSES OF THE CLAMPED BEAM CALCULATED BY USING THE TIMOSHENKO-TYPE ELEMENT VERSUS THE BERNOULLI-EULER-TYPE ELEMENT

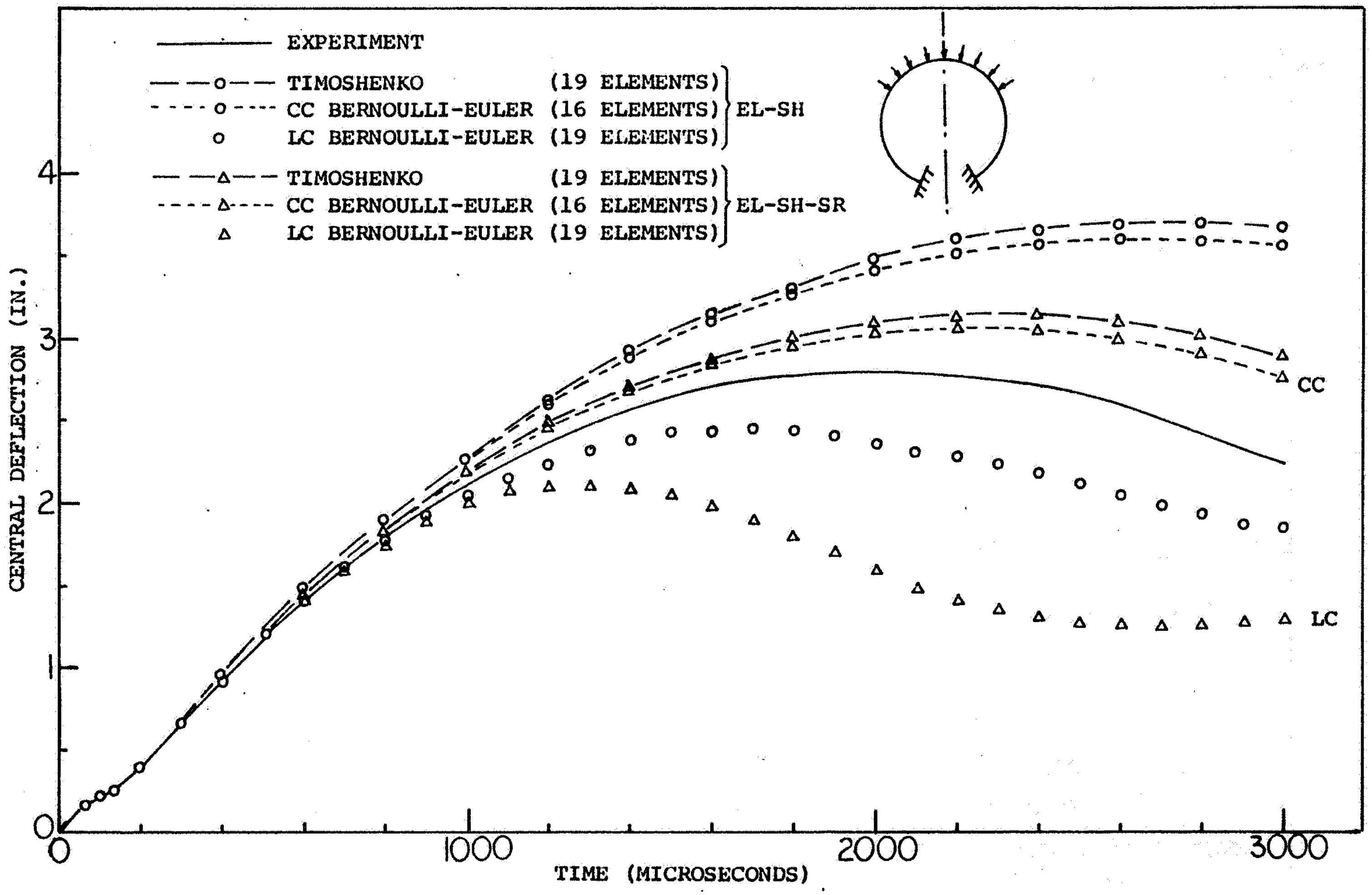

FIG. 32 COMPARISON OF DYNAMIC RESPONSES OF THE CLAMPED RING CALCULATED BY USING TIMOSHENKO-TYPE ELEMENTS VERSUS BERNOULLI-EULER-TYPE ELEMENTS

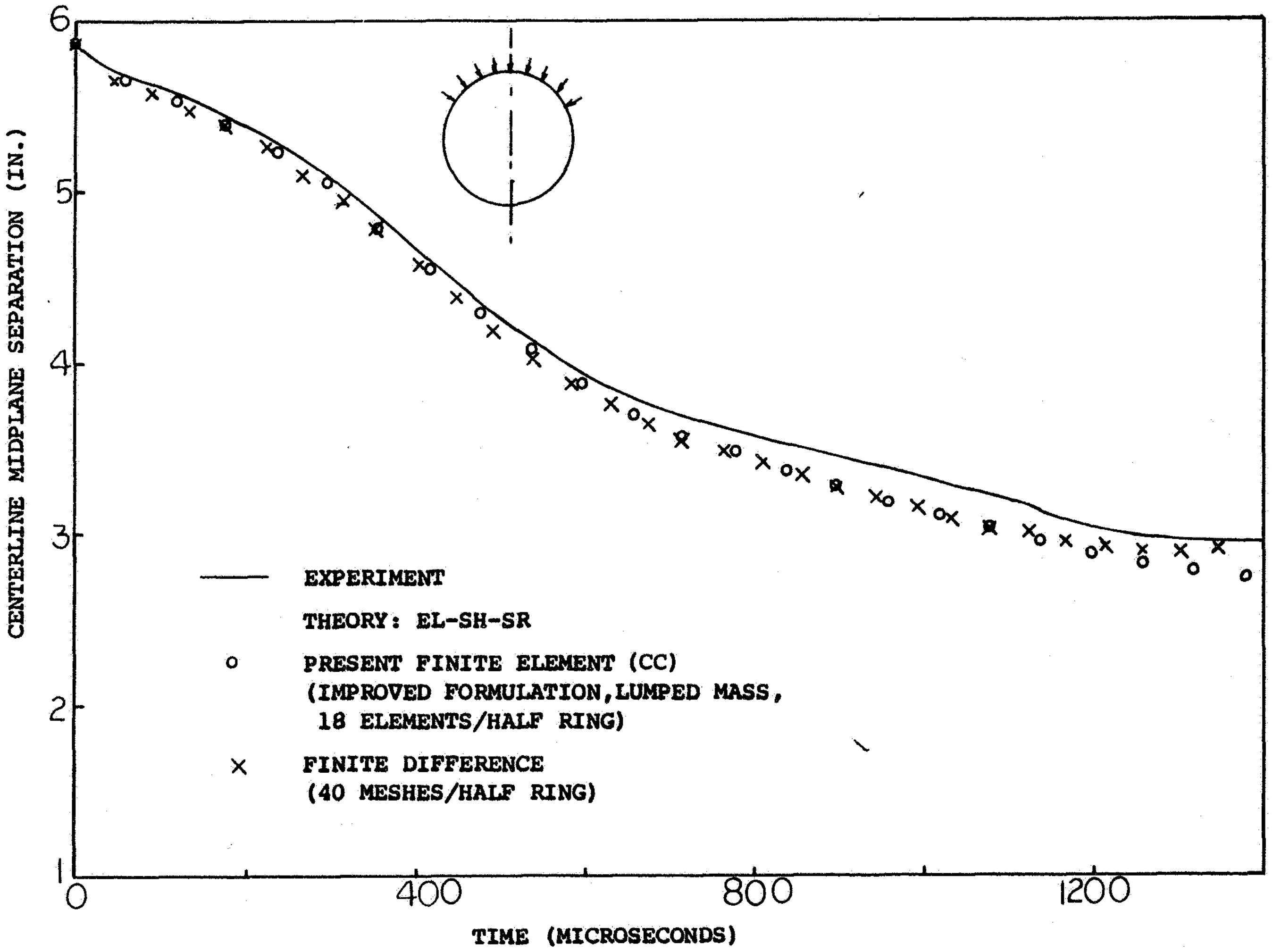

(a) Centerline Midplane Separation Responses

FIG.33 COMPARISON OF FINITE ELEMENT WITH FINITE DIFFERENCE PREDICTED TRANSIENT RESPONSES FOR THE IMPULSIVELY-LOADED FREE RING

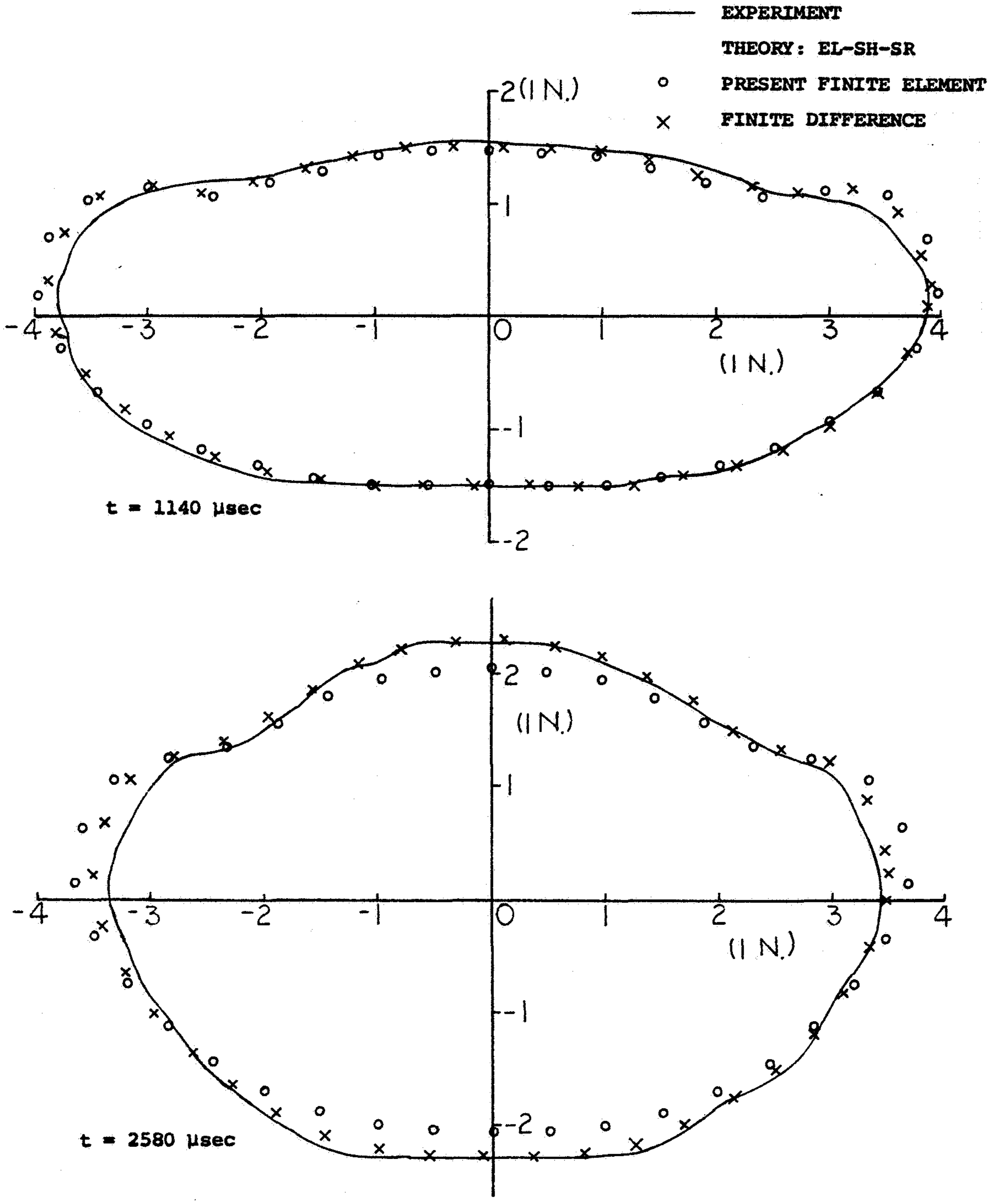

(b) Deformation Profiles

FIG.33 CONTINUED

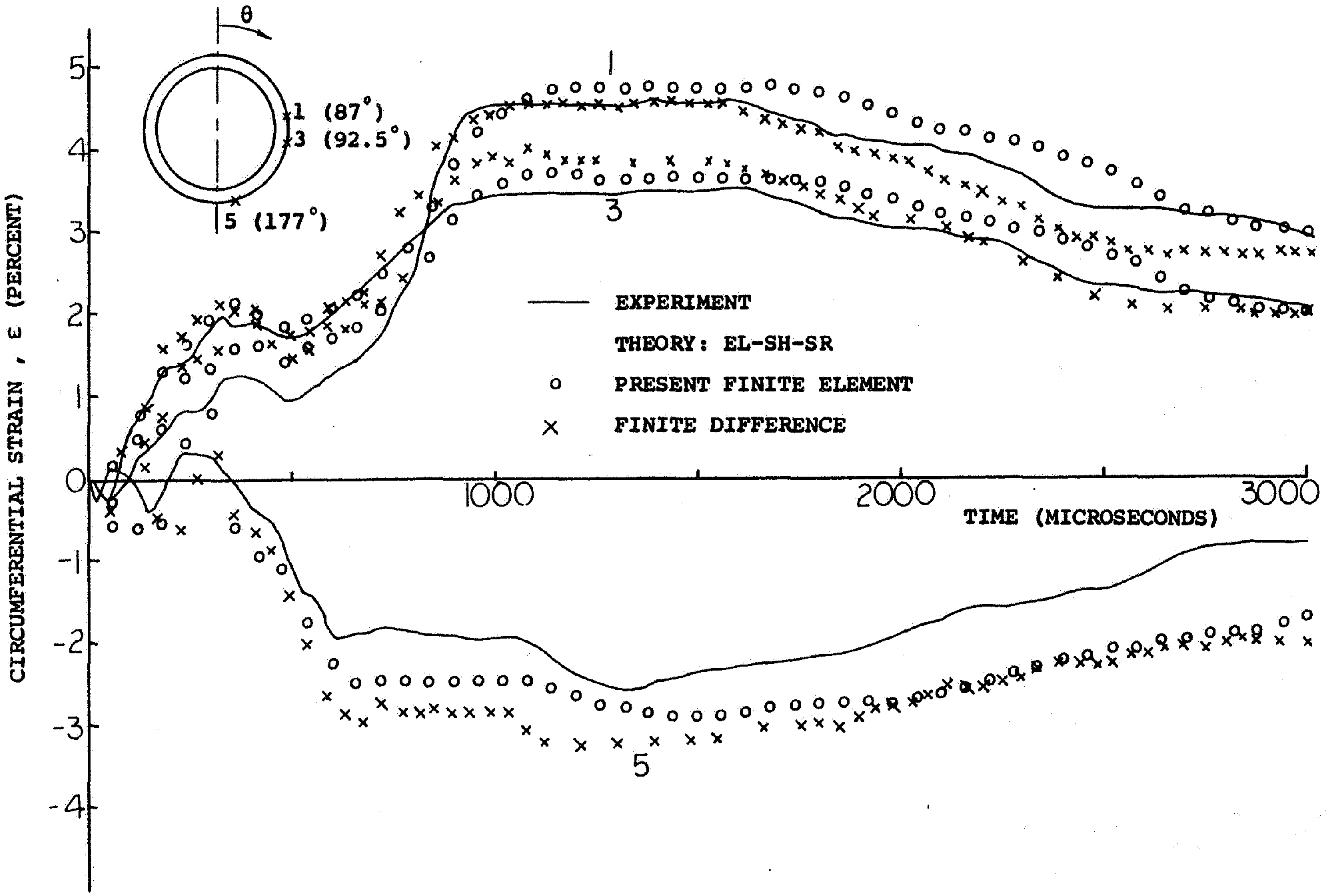

(c) Outer Surface Strain-Time Histories

FIG.33 CONTINUED

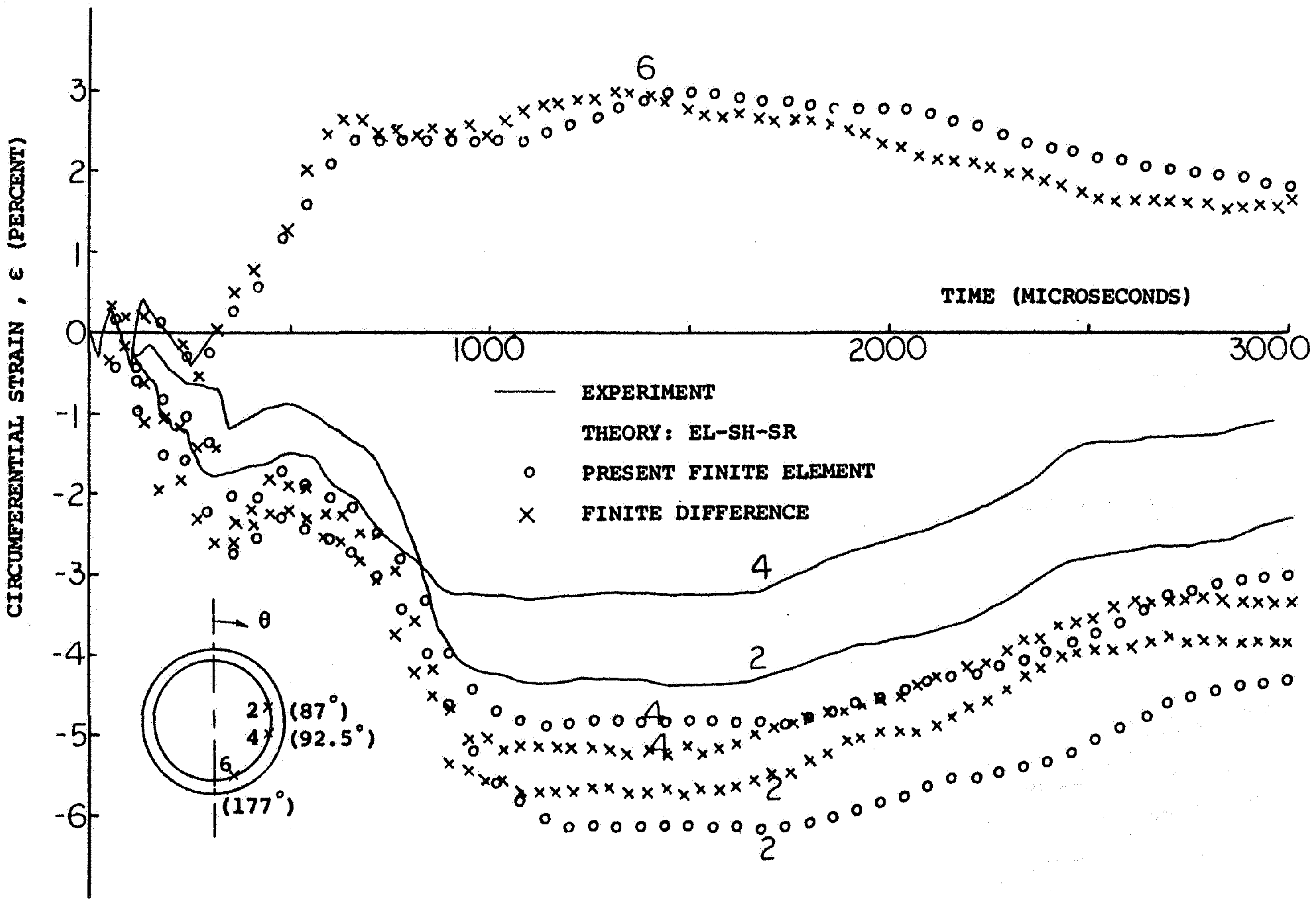

(d) Inner Surface Strain Histories

FIG.33 CONTINUED

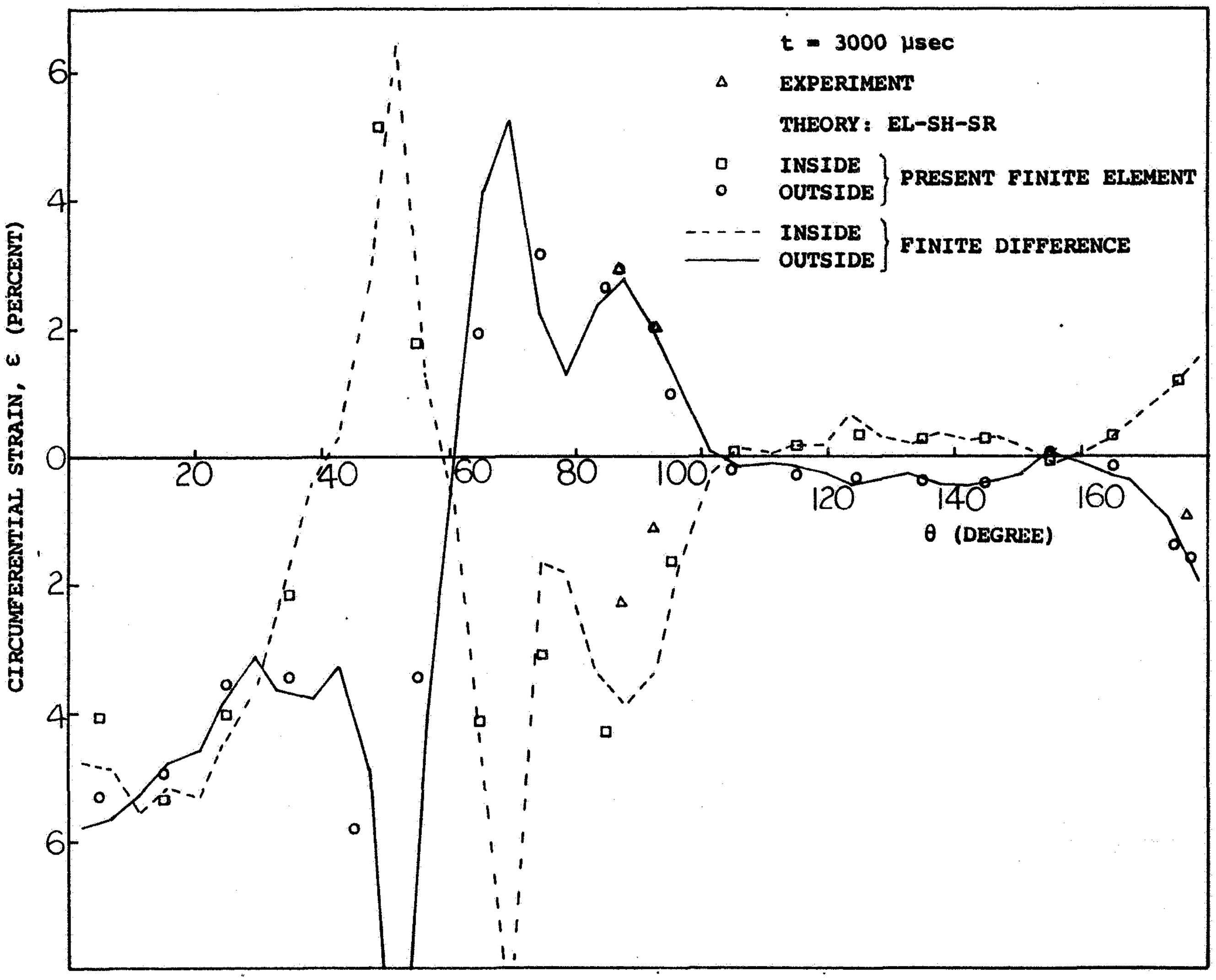

(e) Circumferential Strain Profiles

FIG.33 CONCLUDED

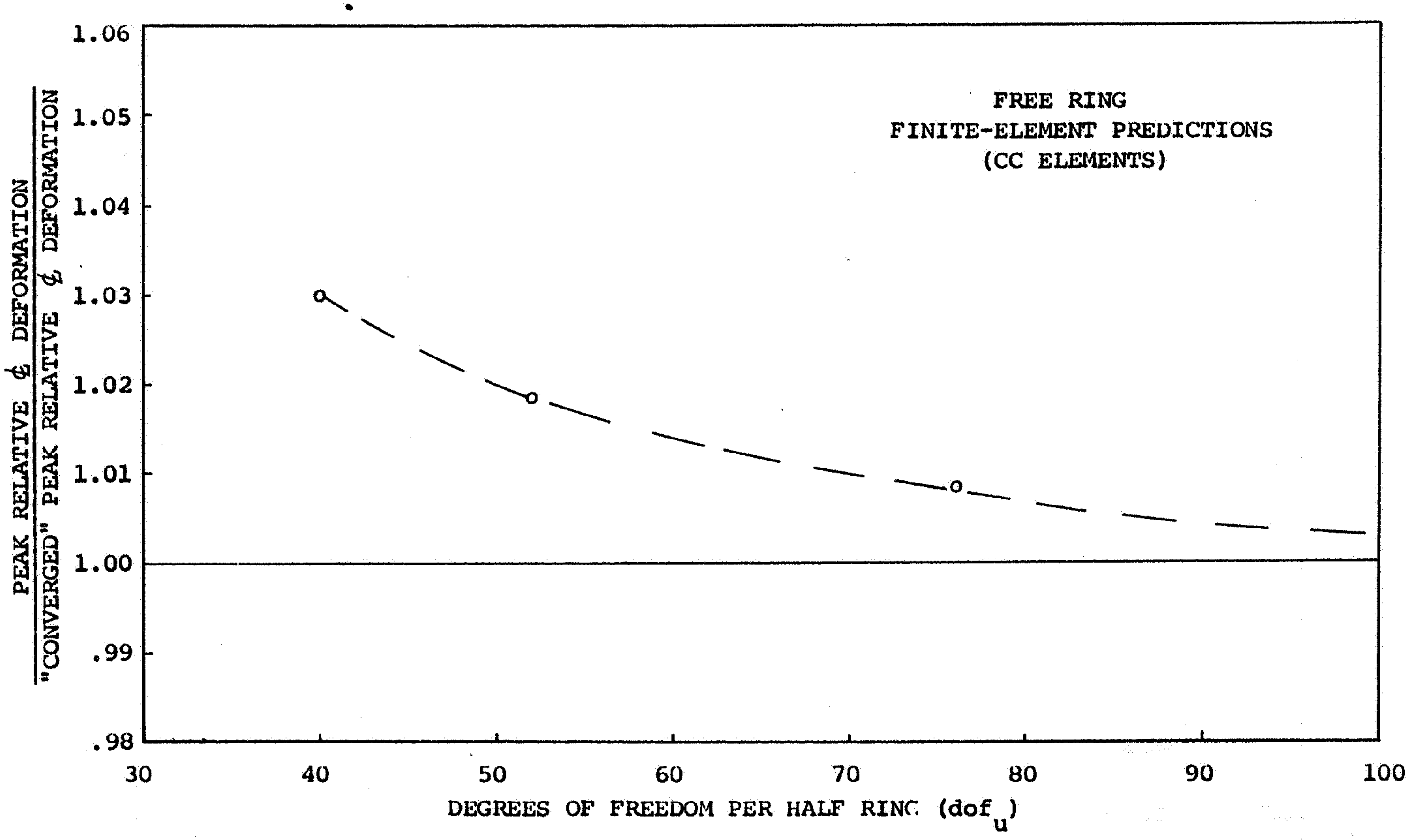

FIG. 34a CONVERGENCE BEHAVIOR OF FE-PREDICTED PEAK RELATIVE CENTERLINE DEFORMATION FOR THE FREE-RING EXAMPLE

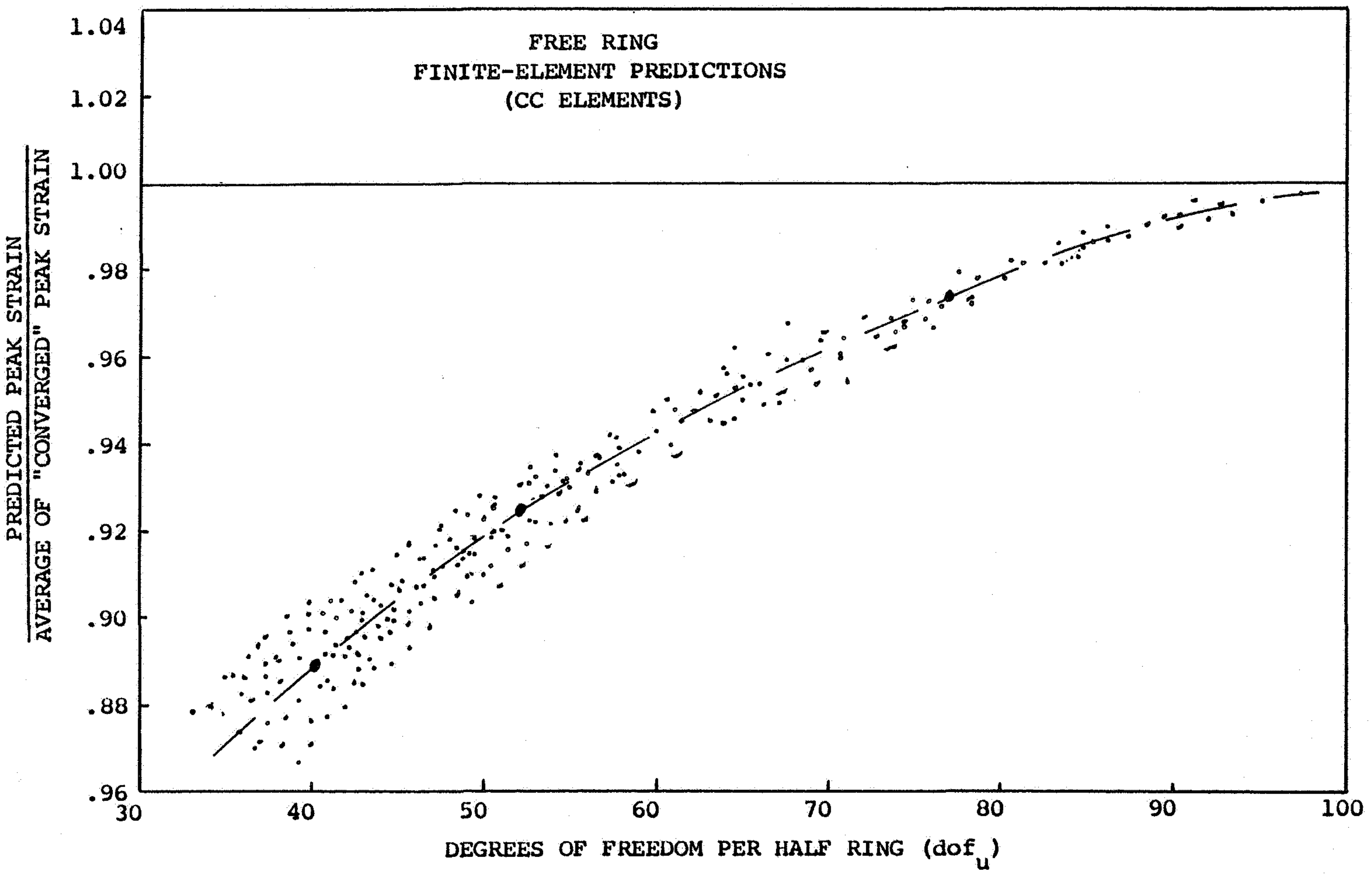

FIG. 34b APPROXIMATE CONVERGENCE BEHAVIOR OF FE-PREDICTED PEAK CIRCUMFERENTIAL STRAINS FOR THE FREE-RING EXAMPLE

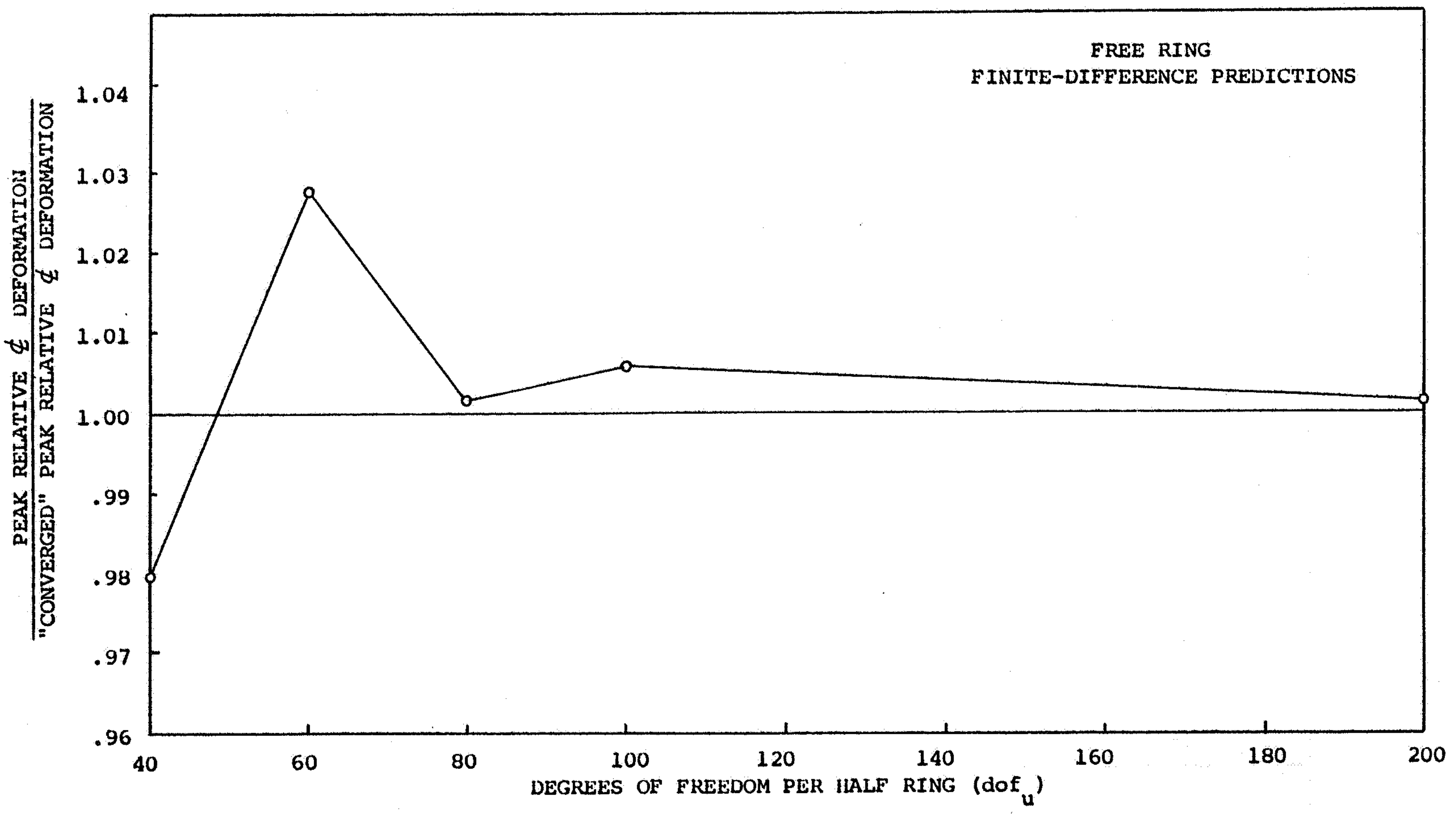

FIG. 35a CONVERGENCE BEHAVIOR OF FD-PREDICTED PEAK RELATIVE CENTERLINE DEFORMATION FOR THE FREE-RING EXAMPLE

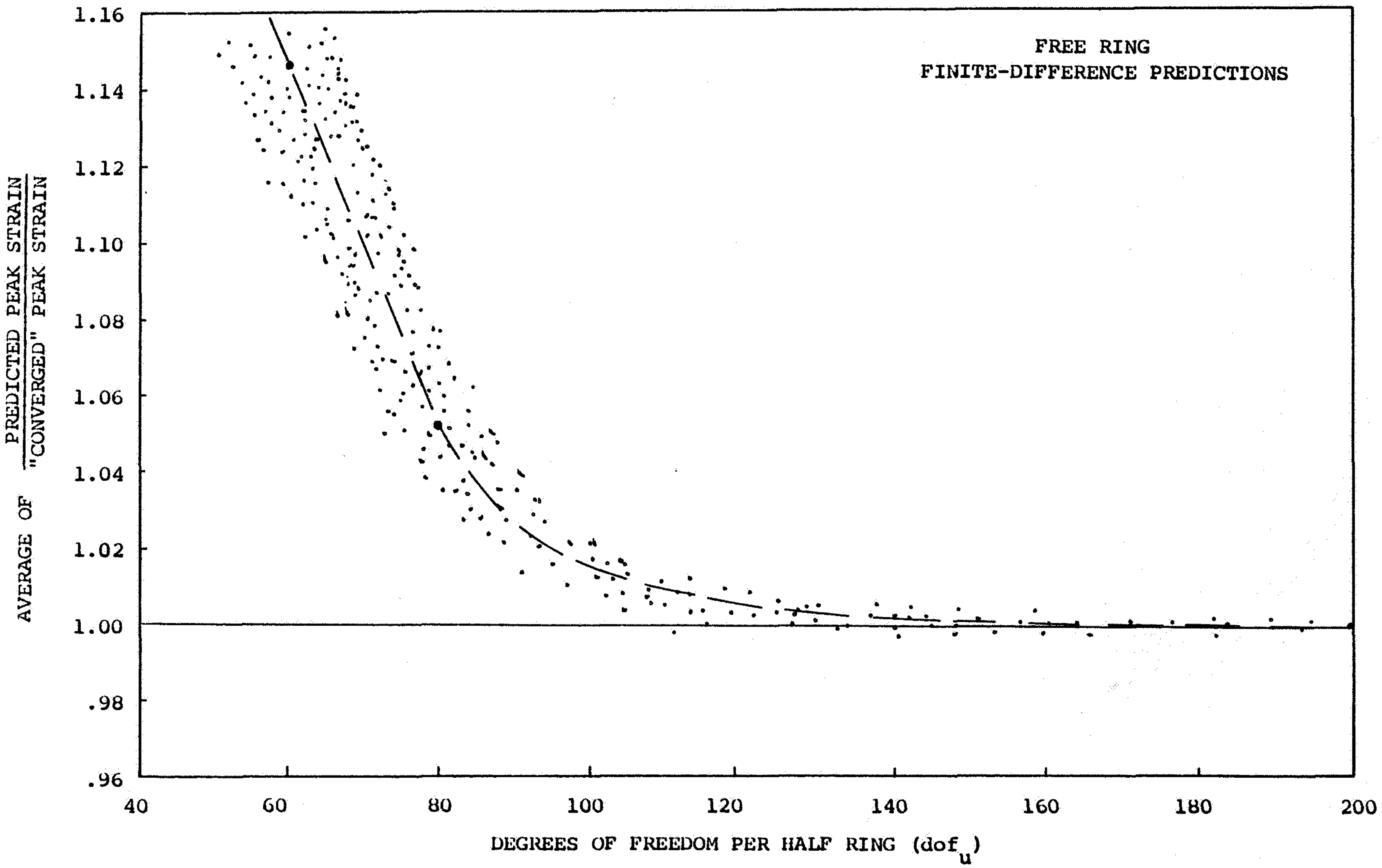

FIG. 35b APPROXIMATE CONVERGENCE BEHAVIOR OF FD-PREDICTED PEAK CIRCUMFERENTIAL STRAINS FOR THE FREE-RING EXAMPLE

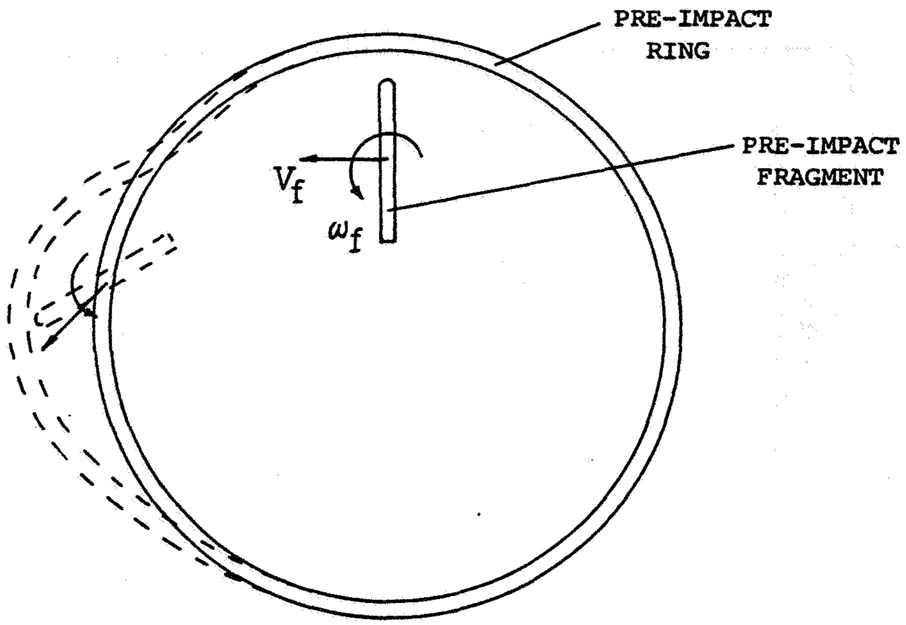
PRE-IMPACT
RING
PRE-IMPACT
FRAGMENT
$V_f$
$\omega_f$

(a) Complete Ring for Containment

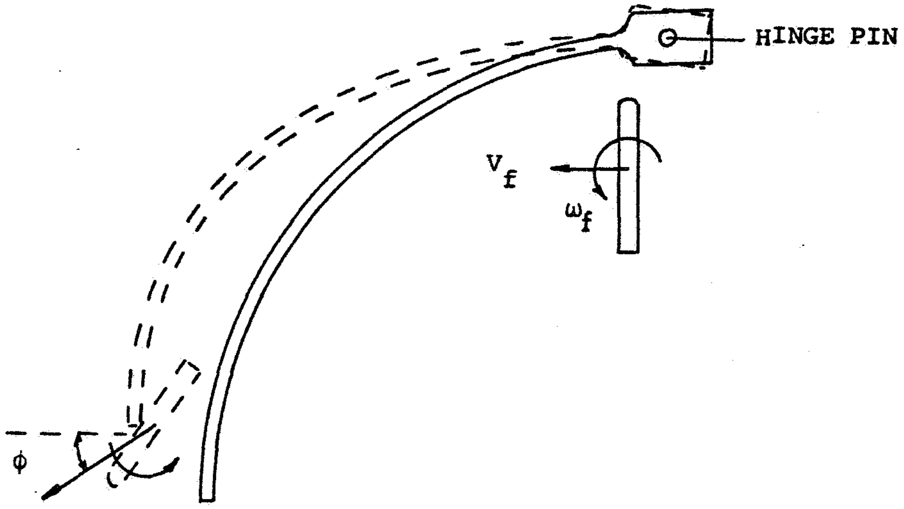
HINGE PIN
$V_f$
$\omega_f$
$\phi$

(b) Partial Ring as a Deflection Device

FIG. 36 SCHEMATICS OF THE FRAGMENT CONTAINMENT AND FRAGMENT DEFLECTION PROBLEMS

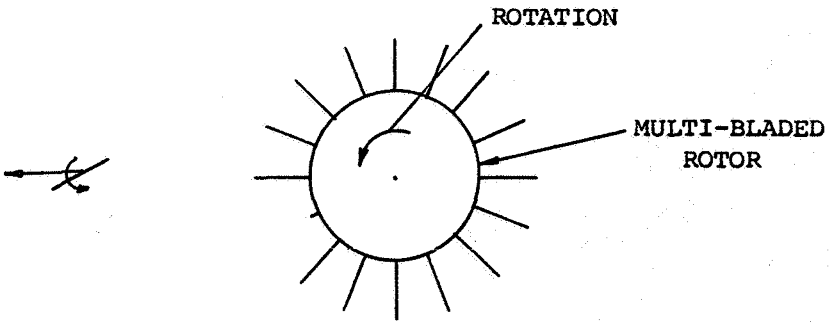
ROTATION
MULTI-BLADED ROTOR

(a) Single-Blade Fragment

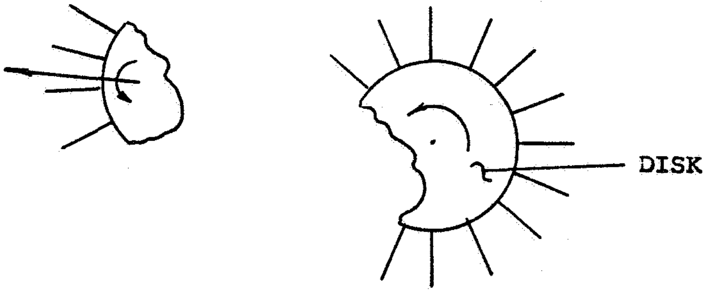

(b) Multi-Bladed Disk Fragment

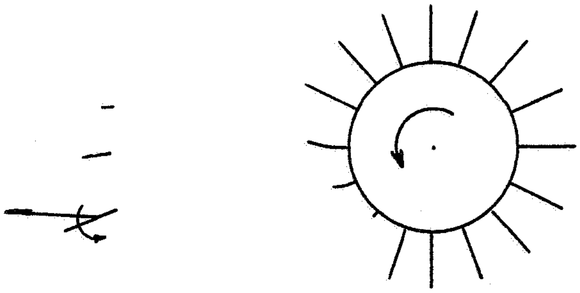

(c) Multiple-Blade Fragments

FIG. 37 SCHEMATICS OF SOME TYPES OF FAILED-ROTOR FRAGMENTS

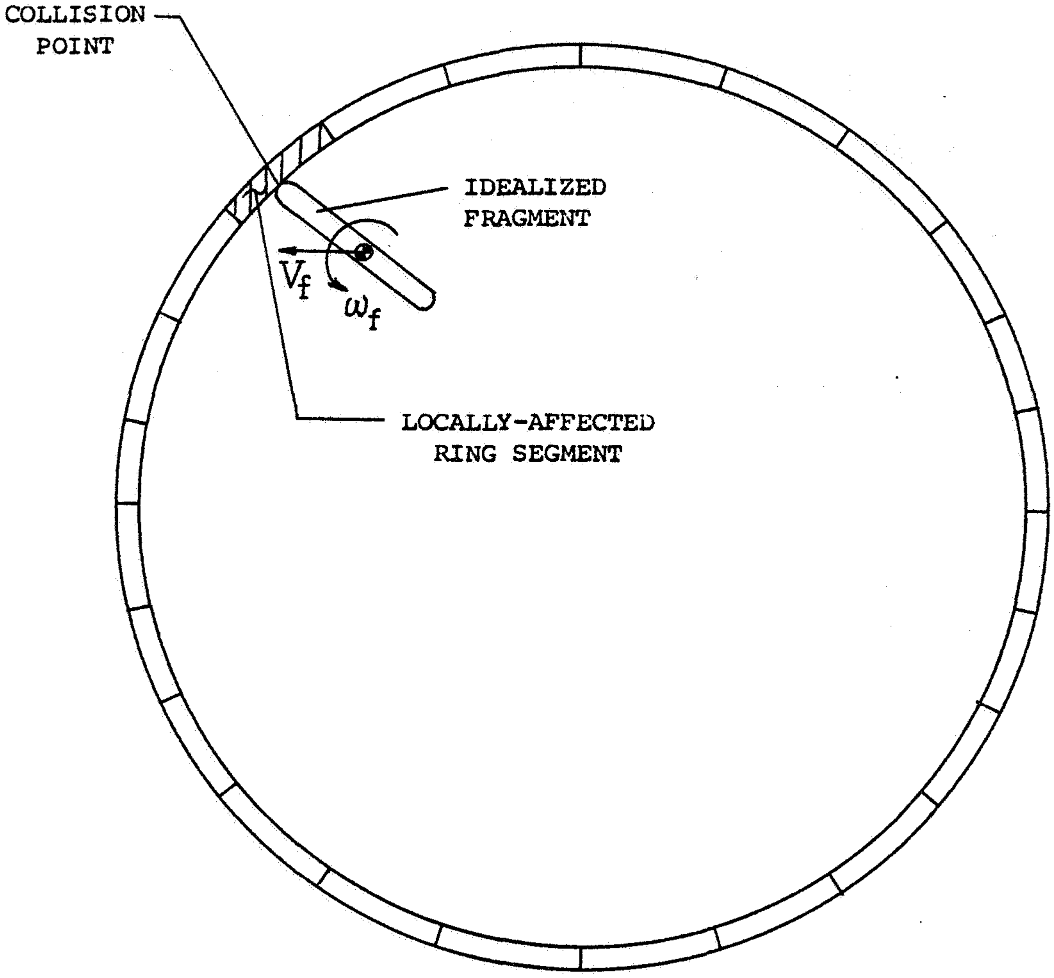

COLLISION POINT
IDEALIZED FRAGMENT
$V_f$
$\omega_f$
LOCALLY-AFFECTED RING SEGMENT

RING DISCRETIZED INTO SEGMENTS FOR ANALYSIS

FIG. 38 SCHEMATIC OF A CONTAINMENT RING SUBJECTED TO SINGLE-FRAGMENT IMPACT

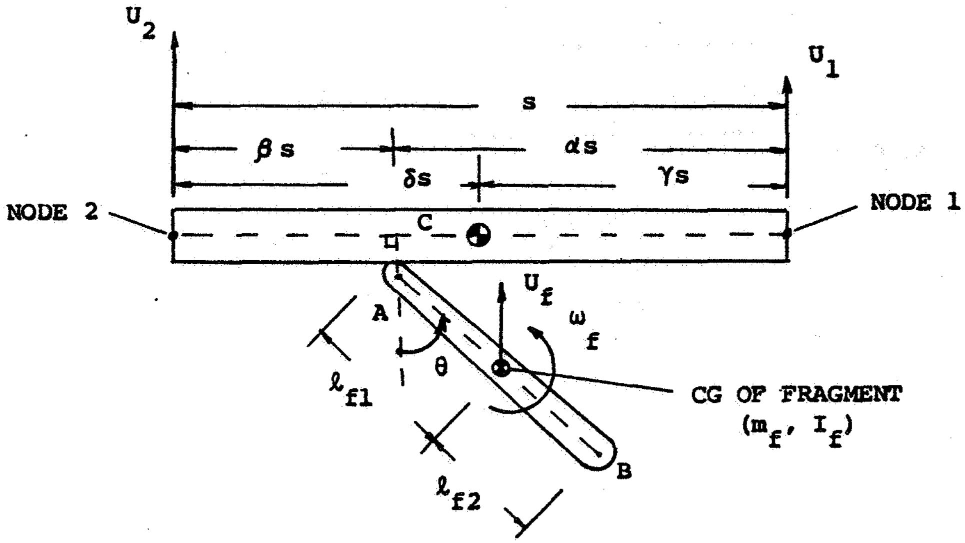
$U_2$
$U_1$
s
$\beta$ s
$\alpha$s
$\delta$s
$\gamma$s
NODE 2
NODE 1
C
$U_f$
$\omega_f$
A
$\theta$
$\ell_{f1}$
$\ell_{f2}$
B
CG OF FRAGMENT
$(m_f, I_f)$

(a) Fragment and Consistent-Mass Ring Segment

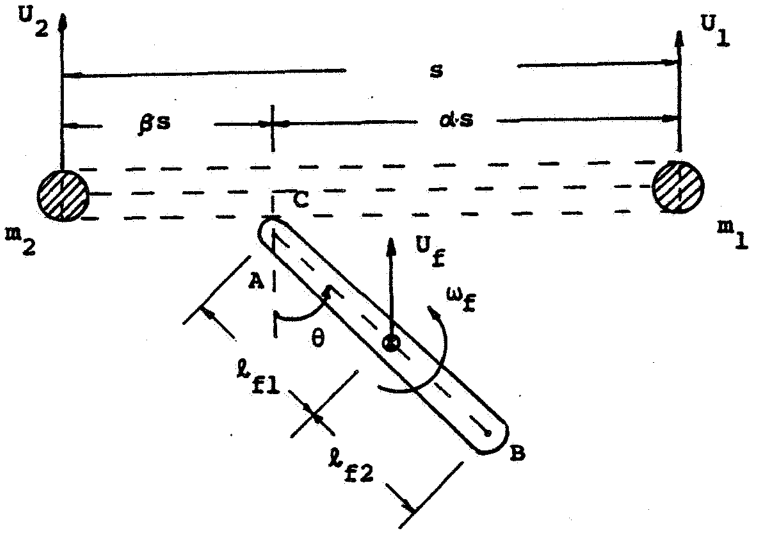
$U_2$
$U_1$
s
$\beta$s
$\alpha$·s
C
$m_2$
$m_1$
$U_f$
$\omega_f$
A
$\theta$
$\ell_{f1}$
$\ell_{f2}$
B

(b) Fragment and Lumped-Mass Ring Segment

NOTE: 1. $U_f$ represents only the component of fragment-c.g. velocity which is perpendicular to the (idealized-as-straight) ring segment immediately prior to impact.

2. $U_1$ and $U_2$ are, similarly, the perpendicular-direction components of the ring segment nodal velocities.

FIG. 39 SCHEMATICS OF FRAGMENT-RING COLLISION MODELS

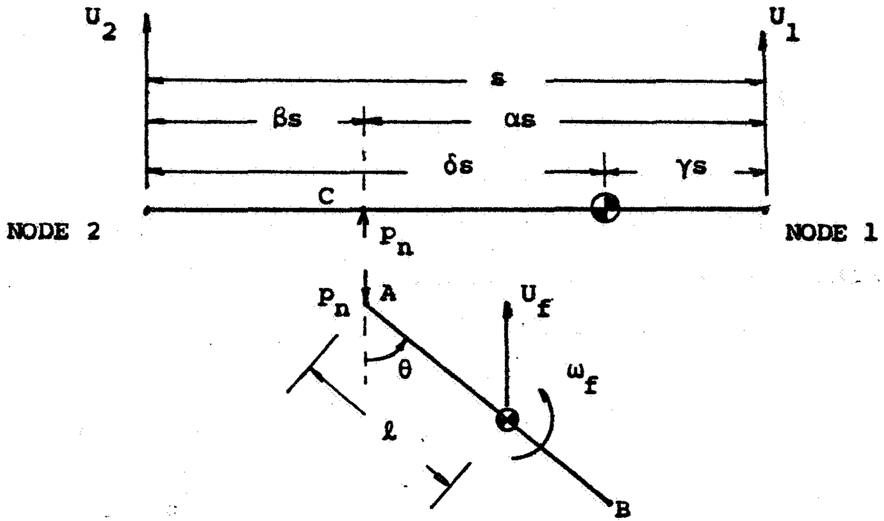
U2
U1
s
βs
αs
δs
γs
C
NODE 2
NODE 1
Pn
Pn
A
Uf
θ
ωf
ℓ
B

(a) Consistent-Mass Model

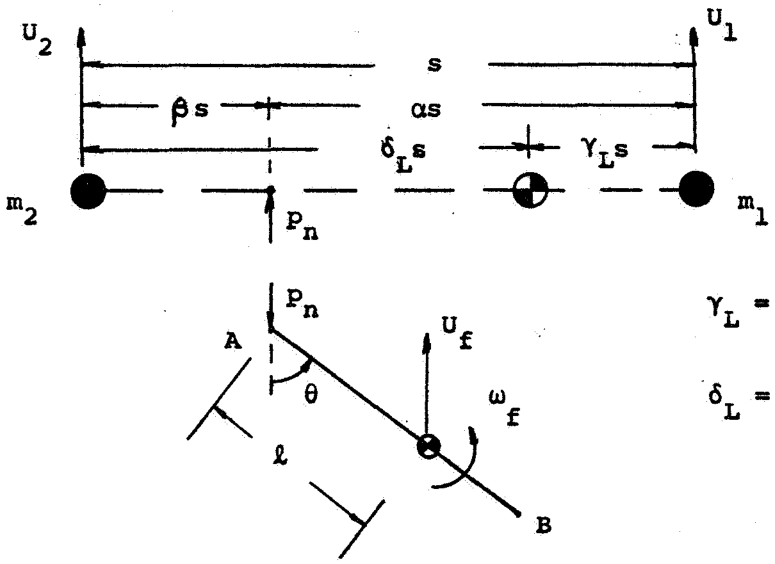
U2
U1
s
βs
αs
δLs
γLs
m2
m1
Pn
Pn
A
Uf
θ
ωf
ℓ
B

$$\gamma_L = \frac{m_2}{m_1 + m_2}$$

$$\delta_L = \frac{m_1}{m_1 + m_2}$$

(b) Lumped-Mass Model

FIG. 40 EXPLODED SCHEMATICS OF IDEALIZED COLLISION MODELS AT THE INSTANT OF IMPACT

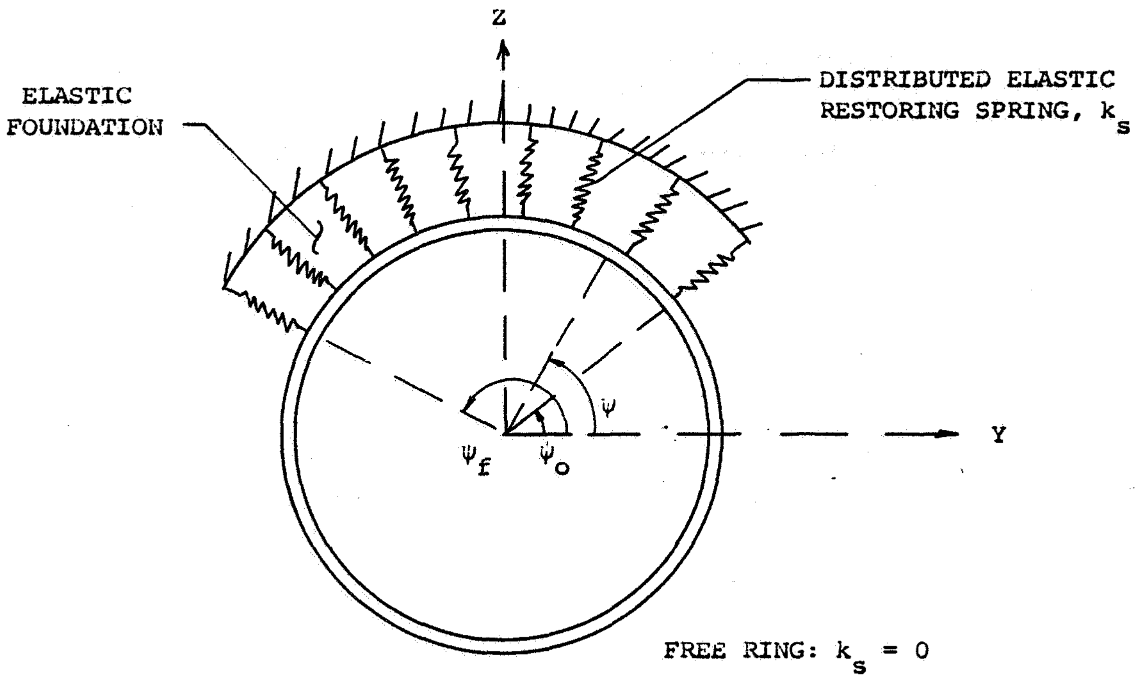
Z
ELASTIC FOUNDATION
DISTRIBUTED ELASTIC RESTORING SPRING, $k_s$
$\psi$
Y
$\psi_f$
$\psi_o$
FREE RING: $k_s = 0$

(a) Complete Ring

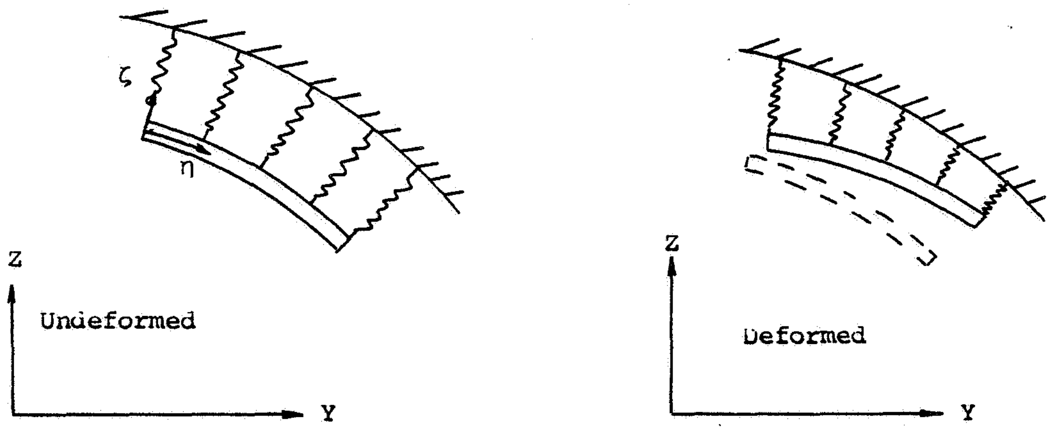
$\zeta$
$\eta$
Z
Undeformed
Y
Z
Deformed
Y

(b) Schematic of One Ring Segment

FIG. 41 SCHEMATICS FOR FREE AND RESTRAINED COMPLETE RINGS

(a) Free

(b) Smooth Hinge Support

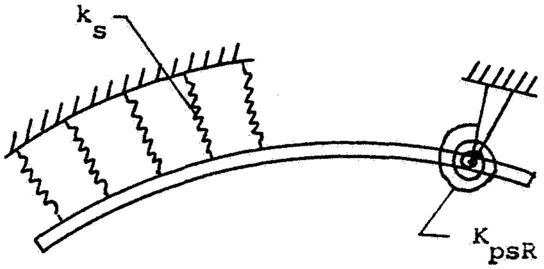

(c) Hinge-Restrained with Elastic Foundation

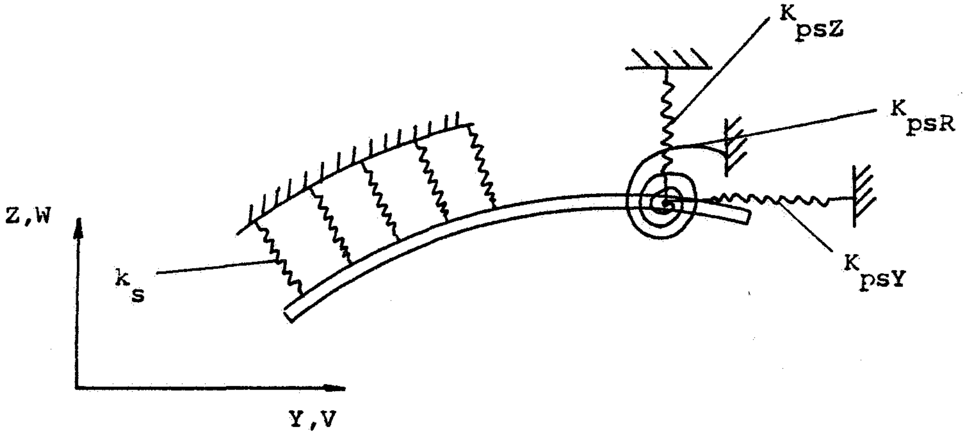

$K_{psZ}$
$K_{psR}$
Z,W
$k_s$
$K_{psY}$
Y,V

(d) Point Elastically Restrained plus Elastic Foundation

FIG. 42 SCHEMATICS FOR FREE AND RESTRAINED PARTIAL RINGS

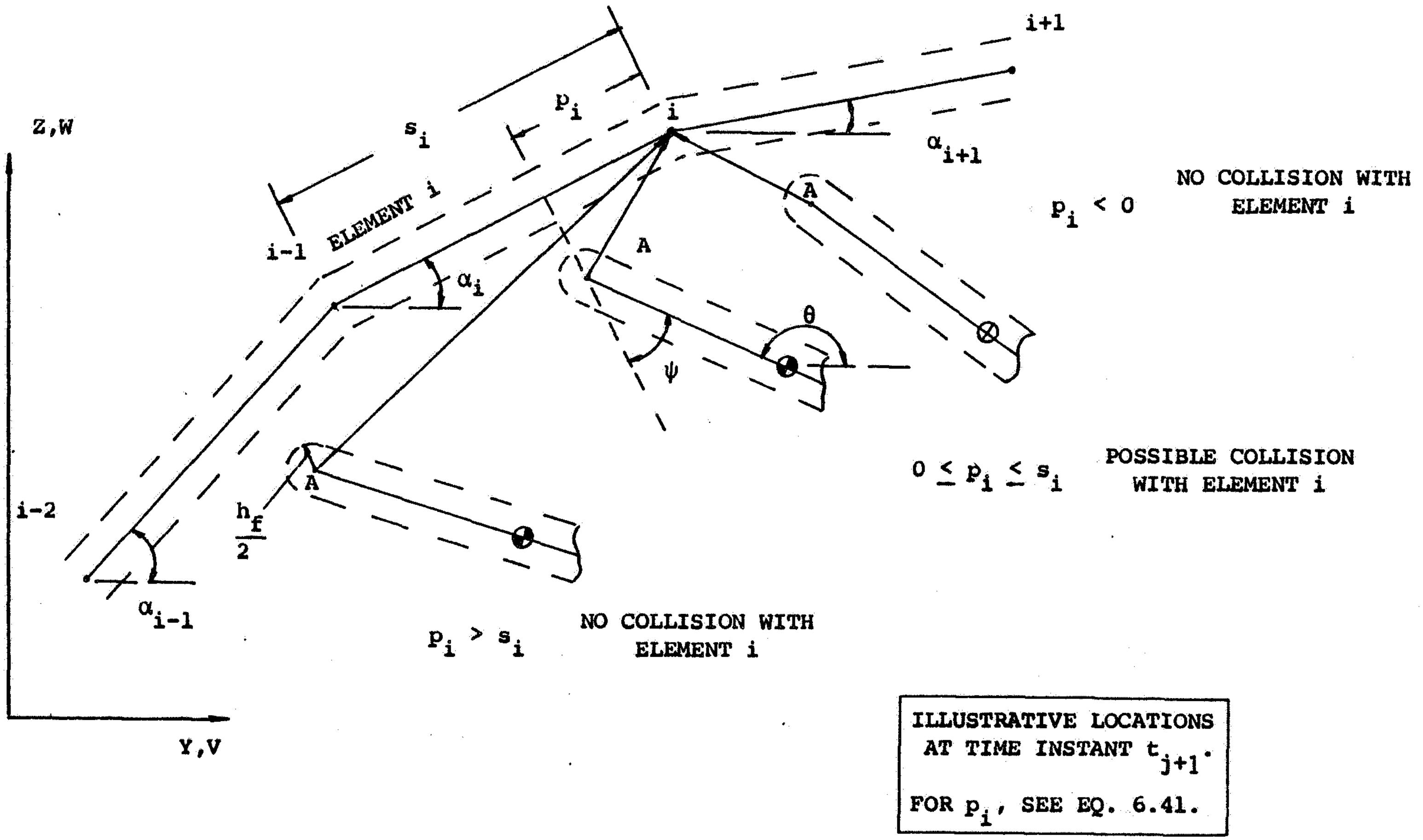
i+1
$s_i$
$p_i$
i
Z,W
$\alpha_{i+1}$
NO COLLISION WITH ELEMENT i
$p_i < 0$
ELEMENT i
i-1
A
A
$\alpha_i$
θ
ψ
$0 \leq p_i \leq s_i$
POSSIBLE COLLISION WITH ELEMENT i
i-2
A
$\frac{h_f}{2}$
$\alpha_{i-1}$
$p_i > s_i$
NO COLLISION WITH ELEMENT i
Y,V

ILLUSTRATIVE LOCATIONS AT TIME INSTANT $t_{j+1}$.

FOR $p_i$, SEE EQ. 6.41.

(a) Projection Inspection

FIG. 43 INSPECTION FOR DETERMINING A COLLISION OF THE FRAGMENT WITH THE RING

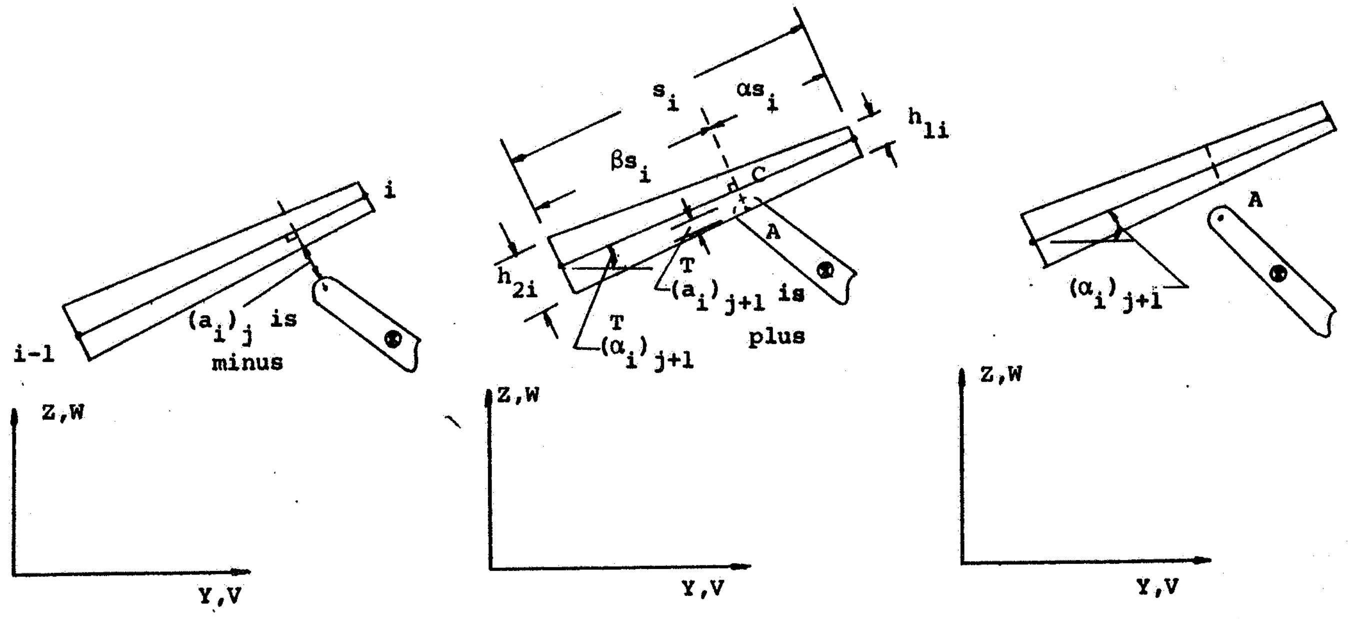
i
i-1
$(a_i)_j$ is minus
Z,W
Y,V
$s_i$
$\alpha s_i$
$\beta s_i$
$h_{1i}$
$h_{2i}$
C
A
$(\overset{T}{a_i})_{j+1}$ is plus
$(\overset{T}{\alpha_i})_{j+1}$
Z,W
Y,V
A
$(\alpha_i)_{j+1}$
Z,W
Y,V

$t = t_j$

$t_j < t \leq t_{j+1}$

"MAXIMUM PENETRATION CONDITION"

$t = t_{j+1}$

NOTE: 1. $(\overset{T}{p_i})_{j+1} = (\alpha s_i)_{j+1}$

2. $(\overset{T}{a_i})_{j+1} = [U_A - U_C]_j (\Delta t^*) \equiv [U_{R_i}]_j (\Delta t^*)$

where $\Delta t^*$ is the time interval from actual impact until $t_{j+1}$

(see Eq. 6.45a)

(b) Penetration Inspection

FIG. 43 CONCLUDED

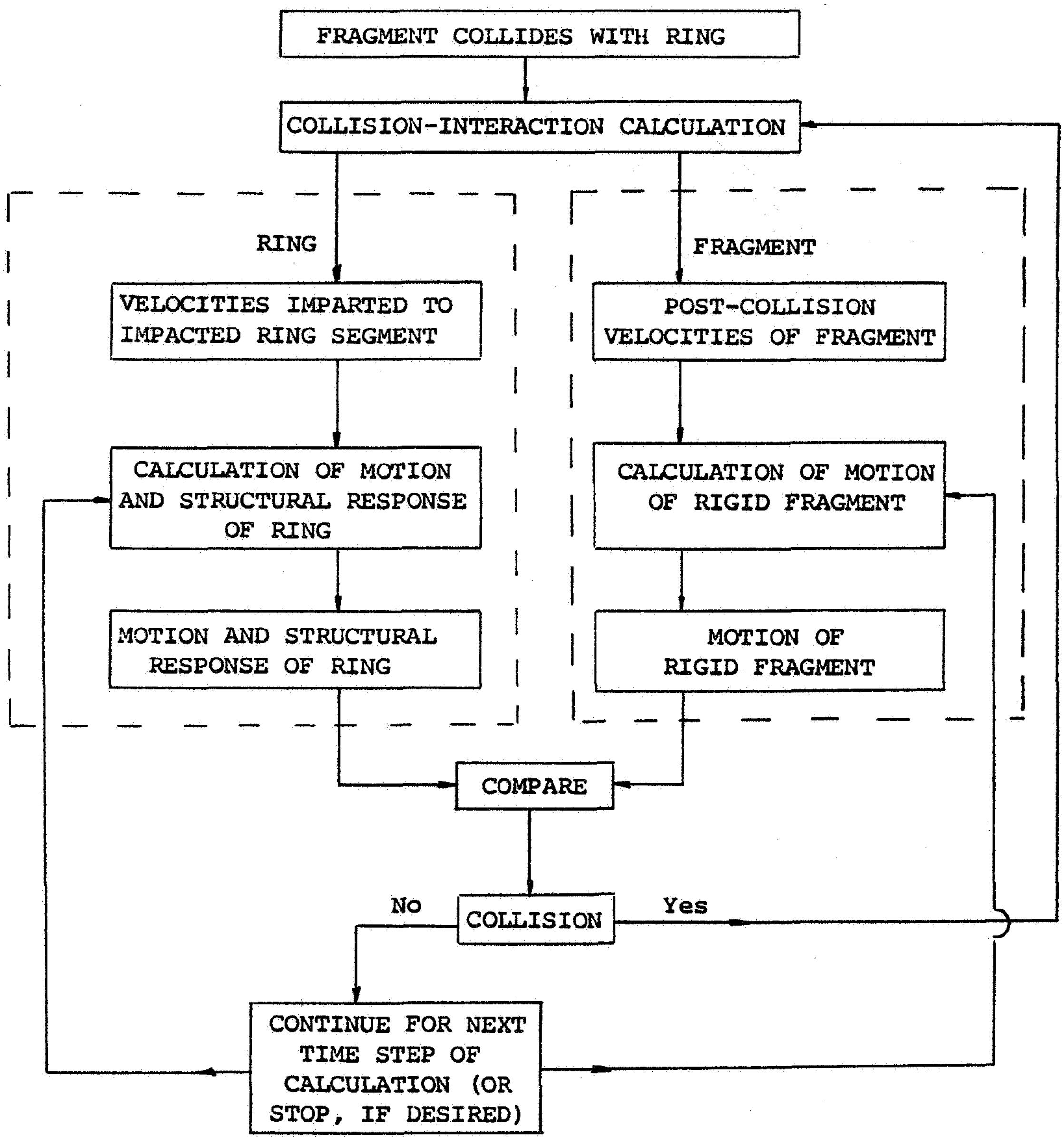
FRAGMENT COLLIDES WITH RING
COLLISION-INTERACTION CALCULATION
RING
VELOCITIES IMPARTED TO IMPACTED RING SEGMENT
CALCULATION OF MOTION AND STRUCTURAL RESPONSE OF RING
MOTION AND STRUCTURAL RESPONSE OF RING
FRAGMENT
POST-COLLISION VELOCITIES OF FRAGMENT
CALCULATION OF MOTION OF RIGID FRAGMENT
MOTION OF RIGID FRAGMENT
COMPARE
No
COLLISION
Yes
CONTINUE FOR NEXT TIME STEP OF CALCULATION (OR STOP, IF DESIRED)

FIG. 44 INFORMATION FLOW SCHEMATIC FOR PREDICTING RING AND FRAGMENT MOTIONS IN THE CIVM APPROACH

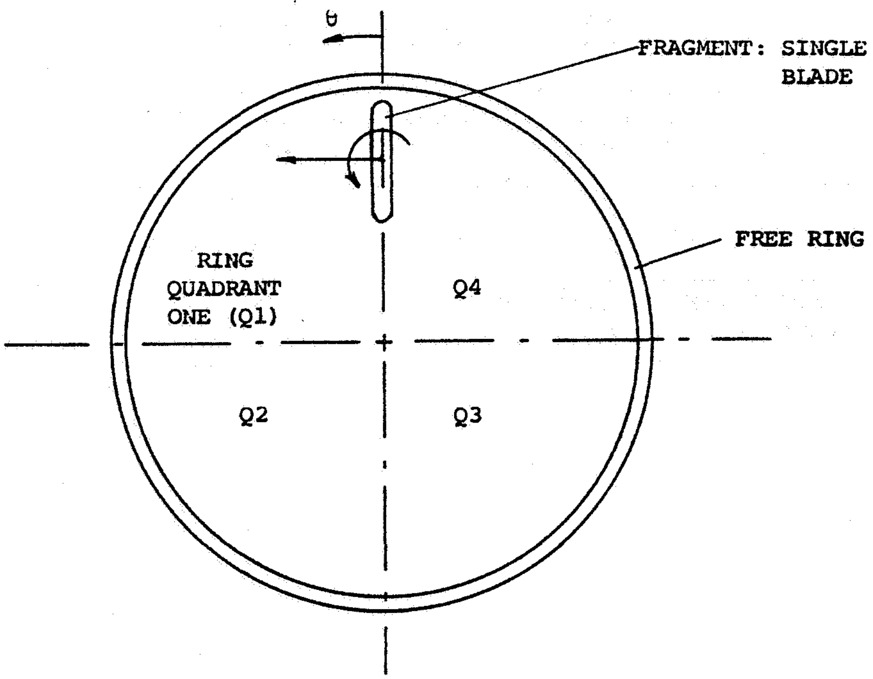
θ
FRAGMENT: SINGLE BLADE
FREE RING
RING QUADRANT ONE (Q1)
Q4
Q2
Q3

(a) Complete Ring (Containment Device)

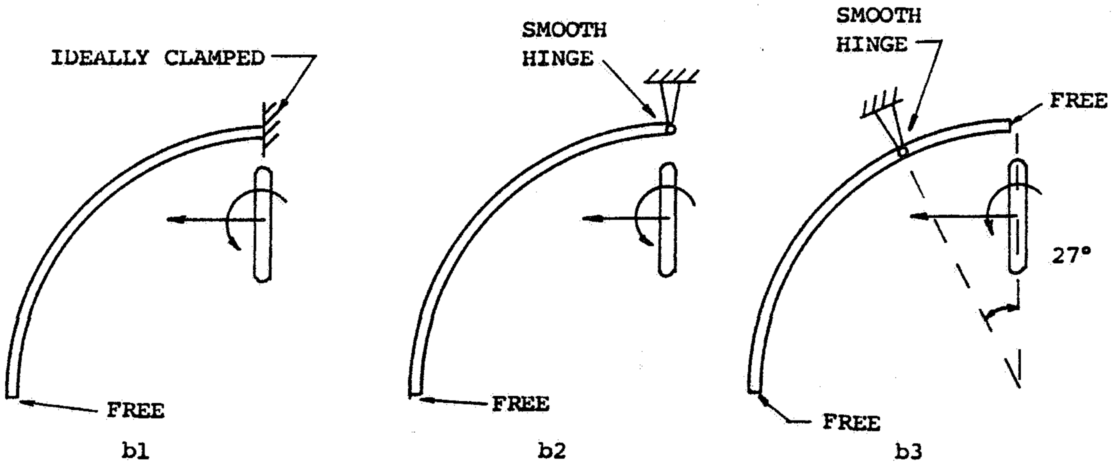
IDEALLY CLAMPED
SMOOTH HINGE
SMOOTH HINGE
FREE
27°
FREE
FREE
FREE
b1
b2
b3

(b) Ring Quadrant (Deflection Device)

FIG. 45 SCHEMATICS OF EXAMPLE PROBLEMS ANALYZED BY THE CIVM APPROACH

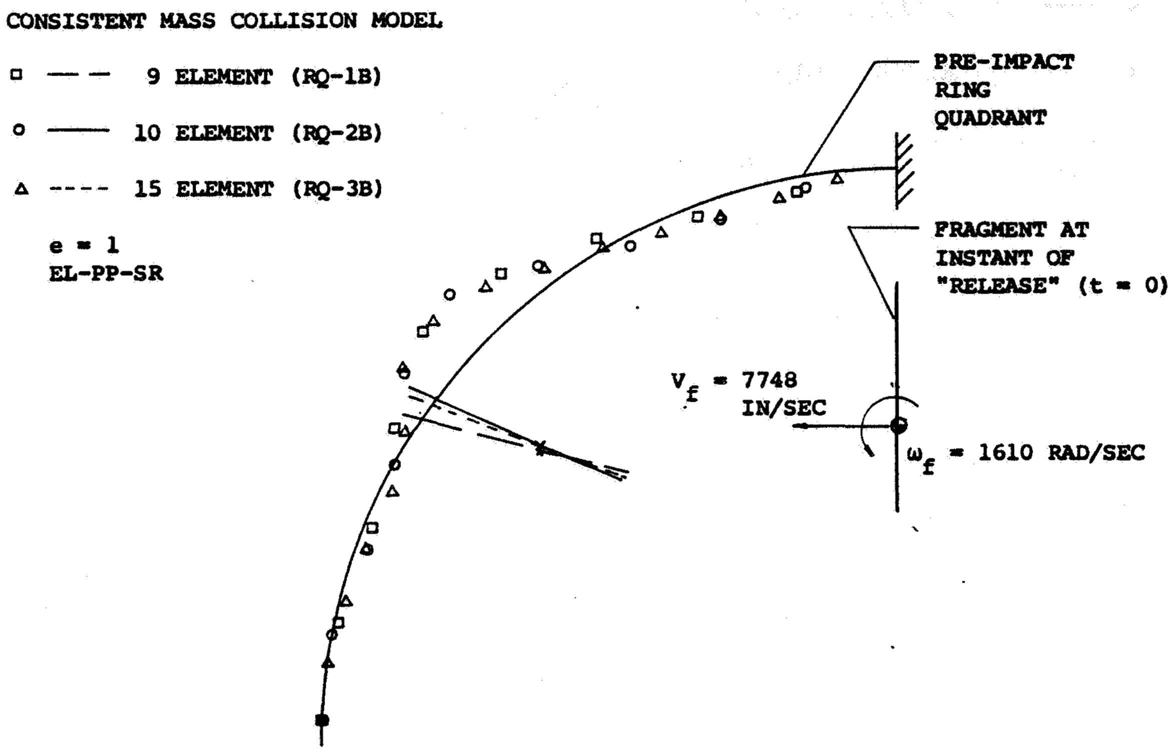

(a) t = 750 μsec

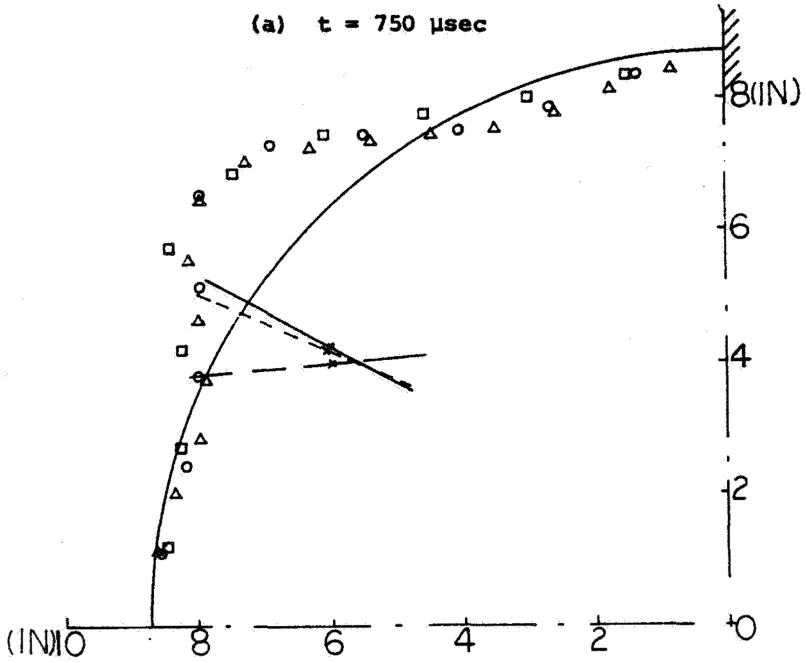

(b) t = 960 μsec

FIG. 46 RING QUADRANT AND BLADE-FRAGMENT RESPONSES PREDICTED BY USING THE CM COLLISION MODEL

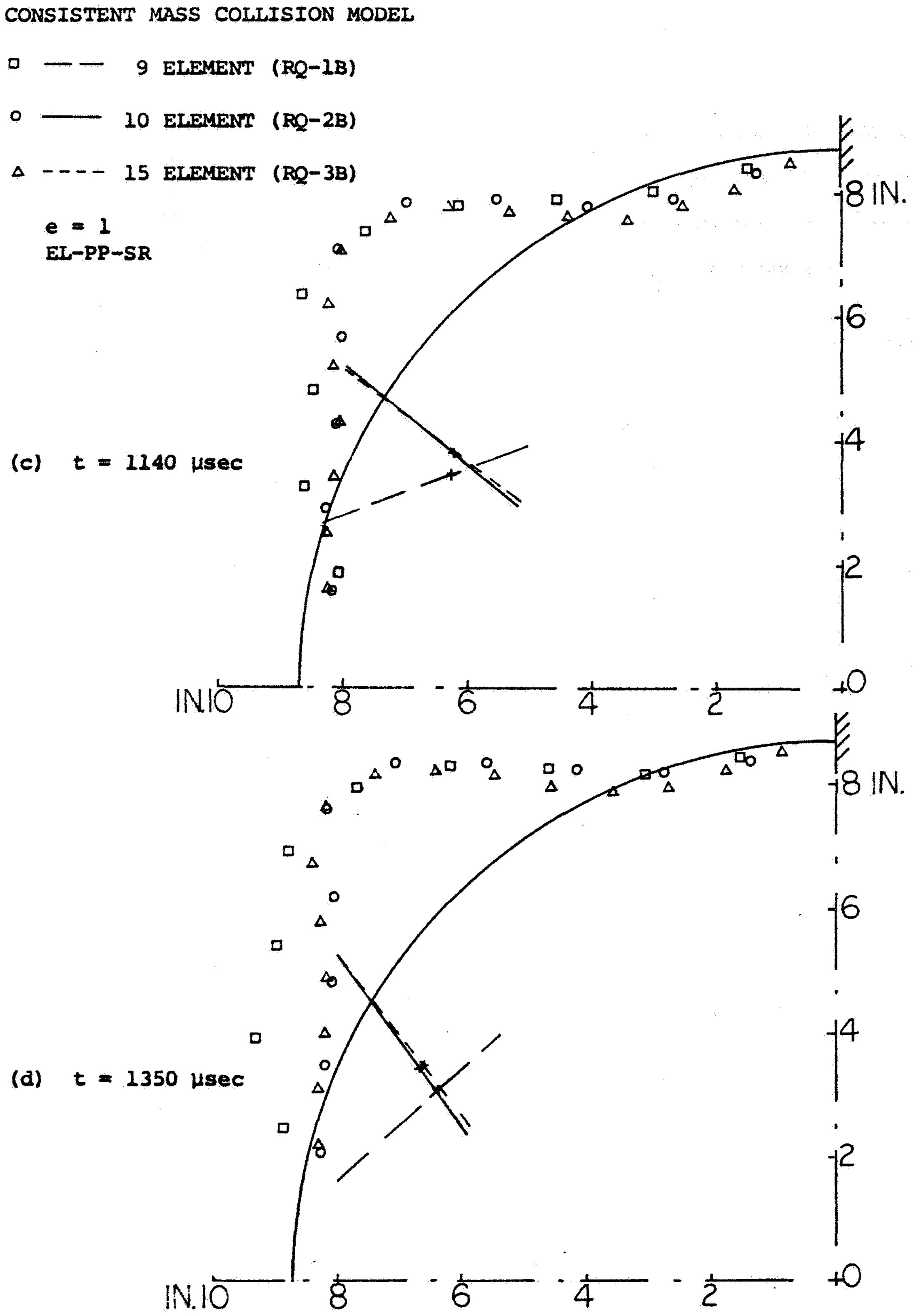

FIG. 46 CONCLUDED

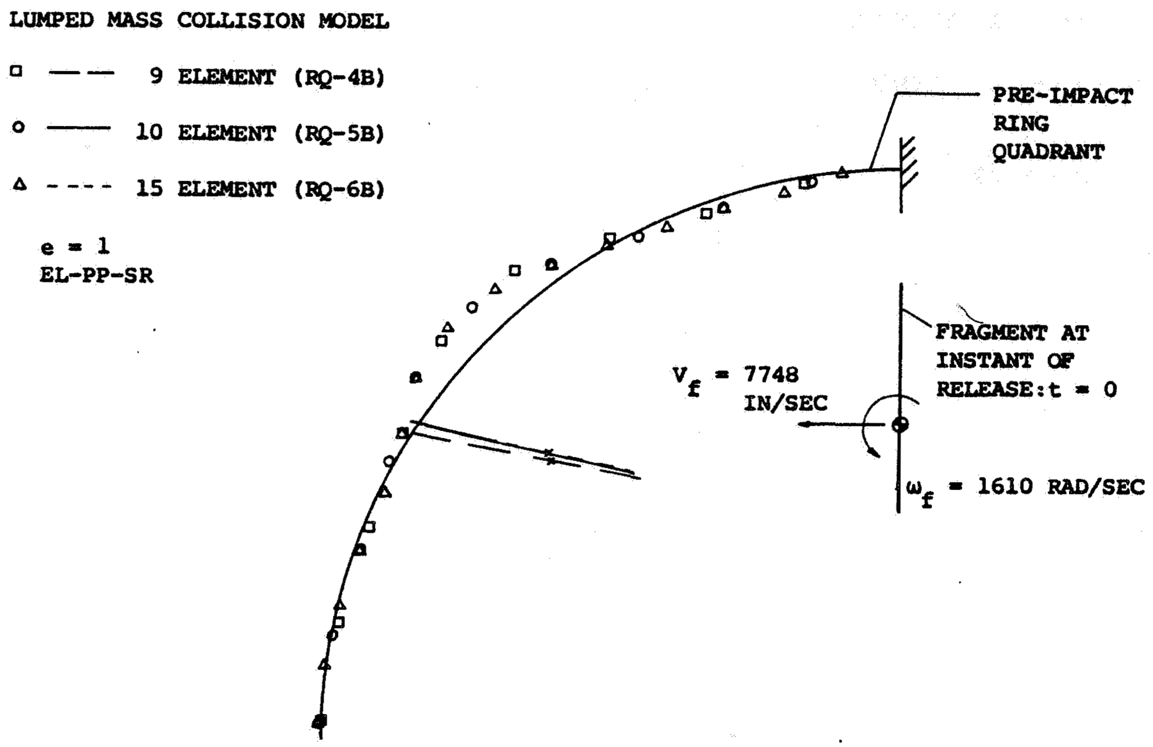

(a) t = 750 μsec

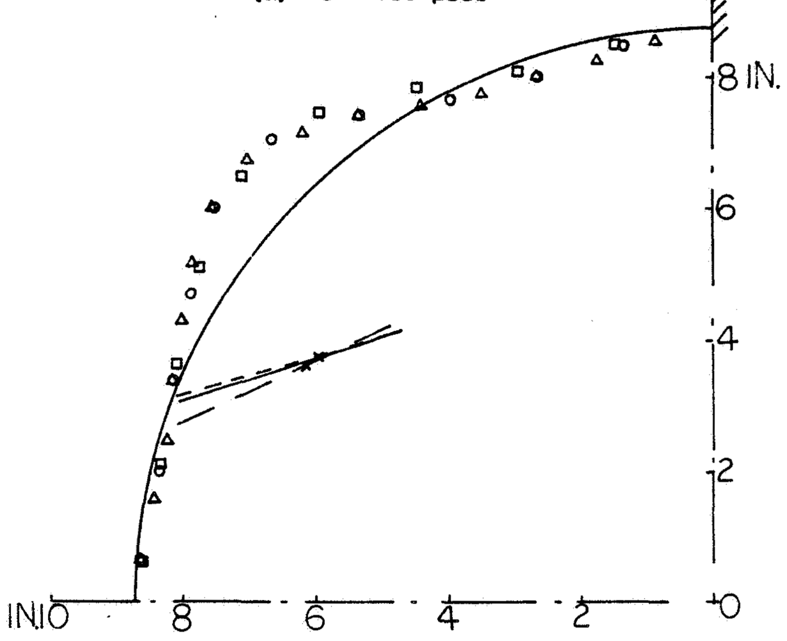

(b) t = 960 μsec

FIG. 47 RING QUADRANT AND BLADE FRAGMENT RESPONSES PREDICTED BY USING THE LM COLLISION MODEL

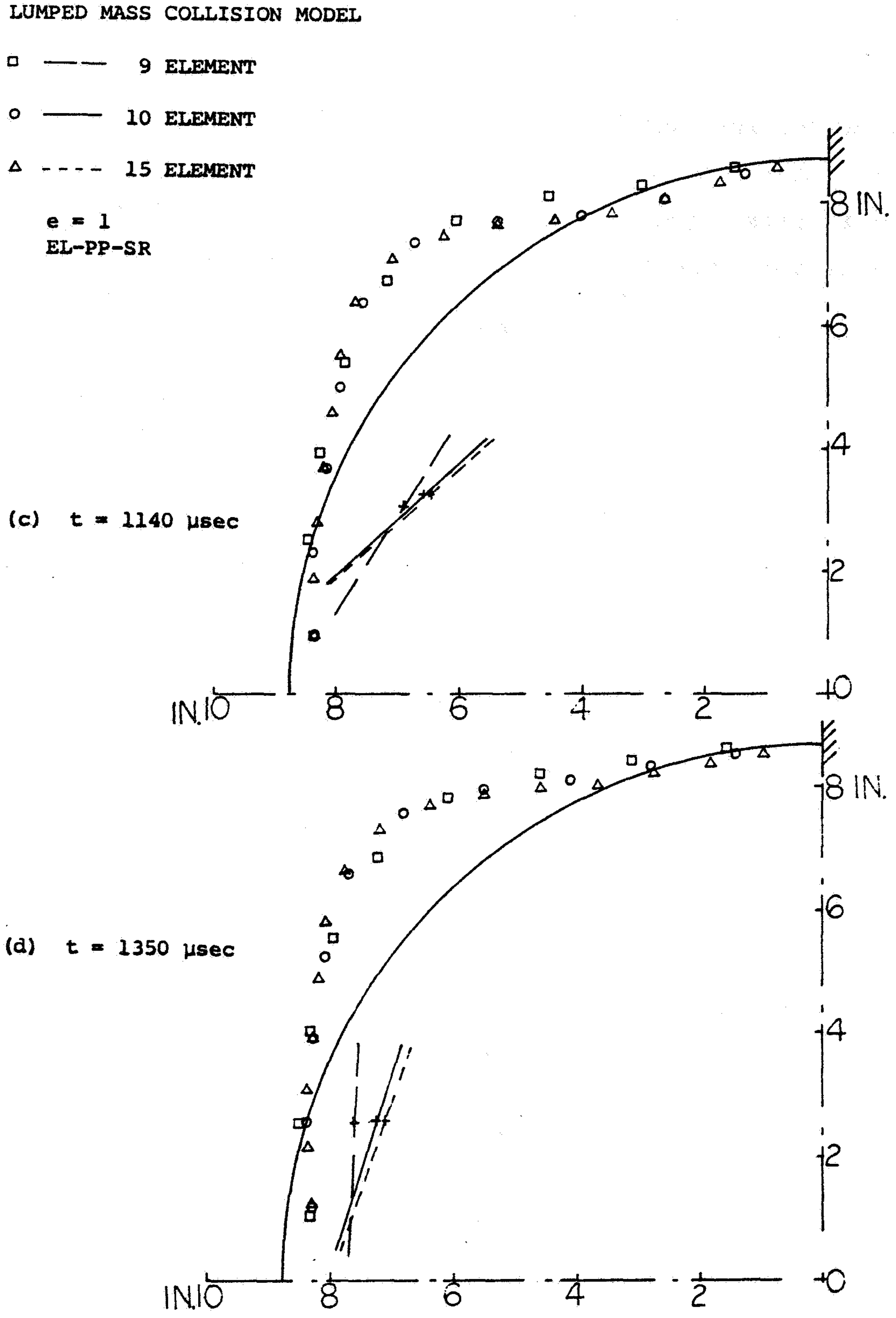

(c) t = 1140 μsec

(d) t = 1350 μsec

FIG. 47 CONCLUDED

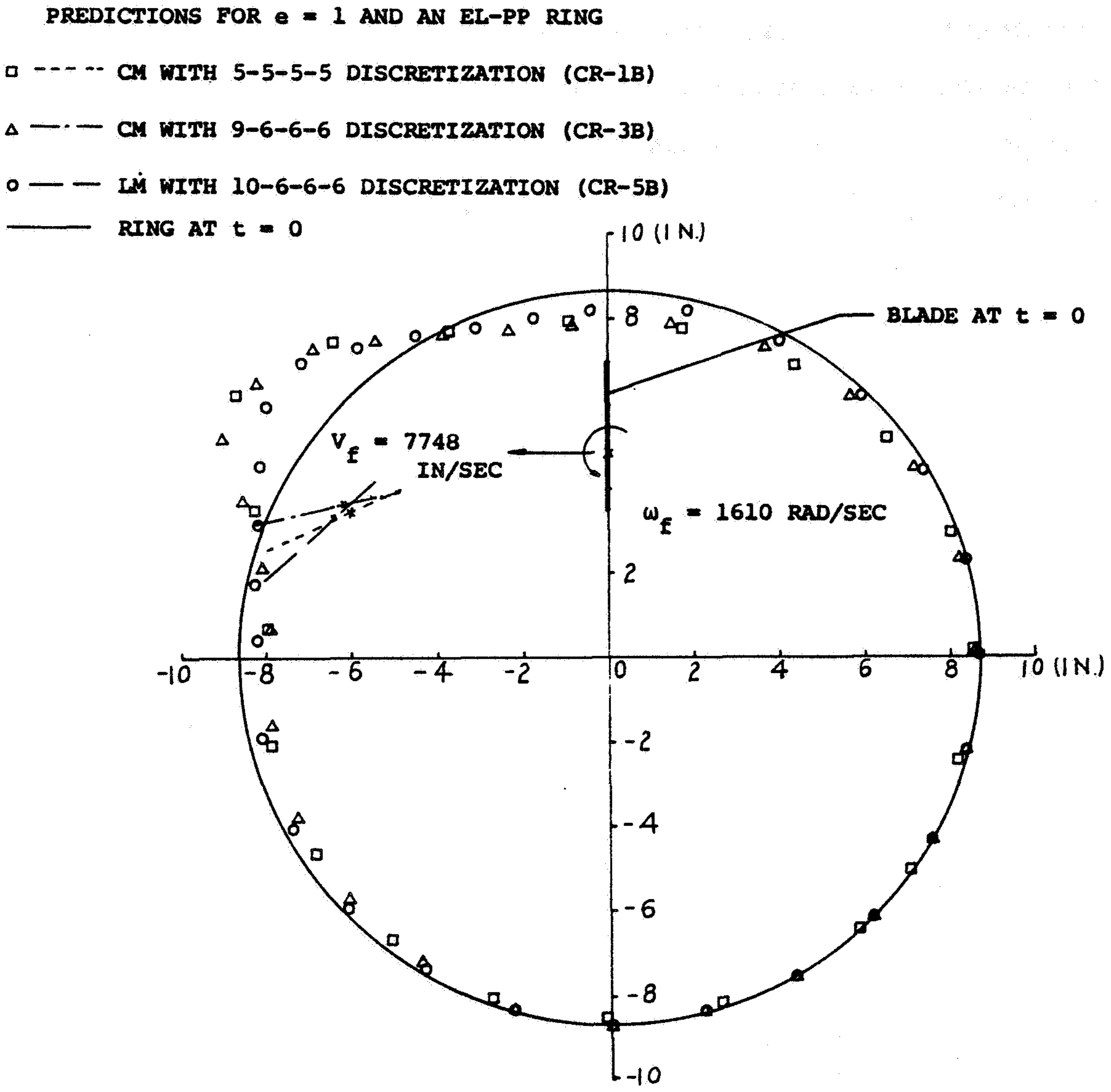

(a) t = 570 μsec

FIG. 48 COMPARISON OF CM WITH LM COLLISION MODEL PREDICTIONS FOR THE COMPLETE FREE RING SUBJECTED TO SINGLE-BLADE IMPACT

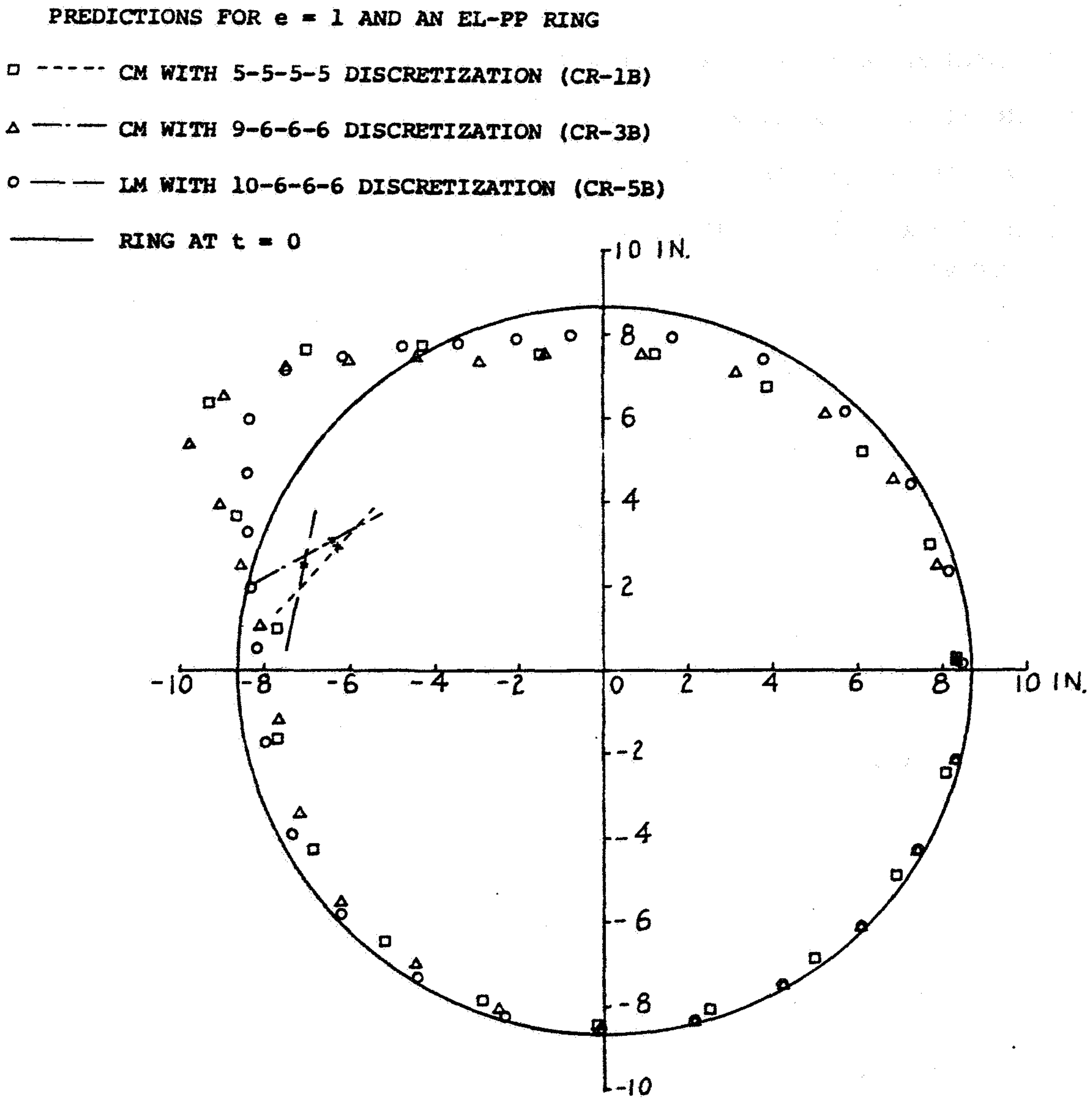

(b) t = 810 μsec

FIG. 48 CONCLUDED

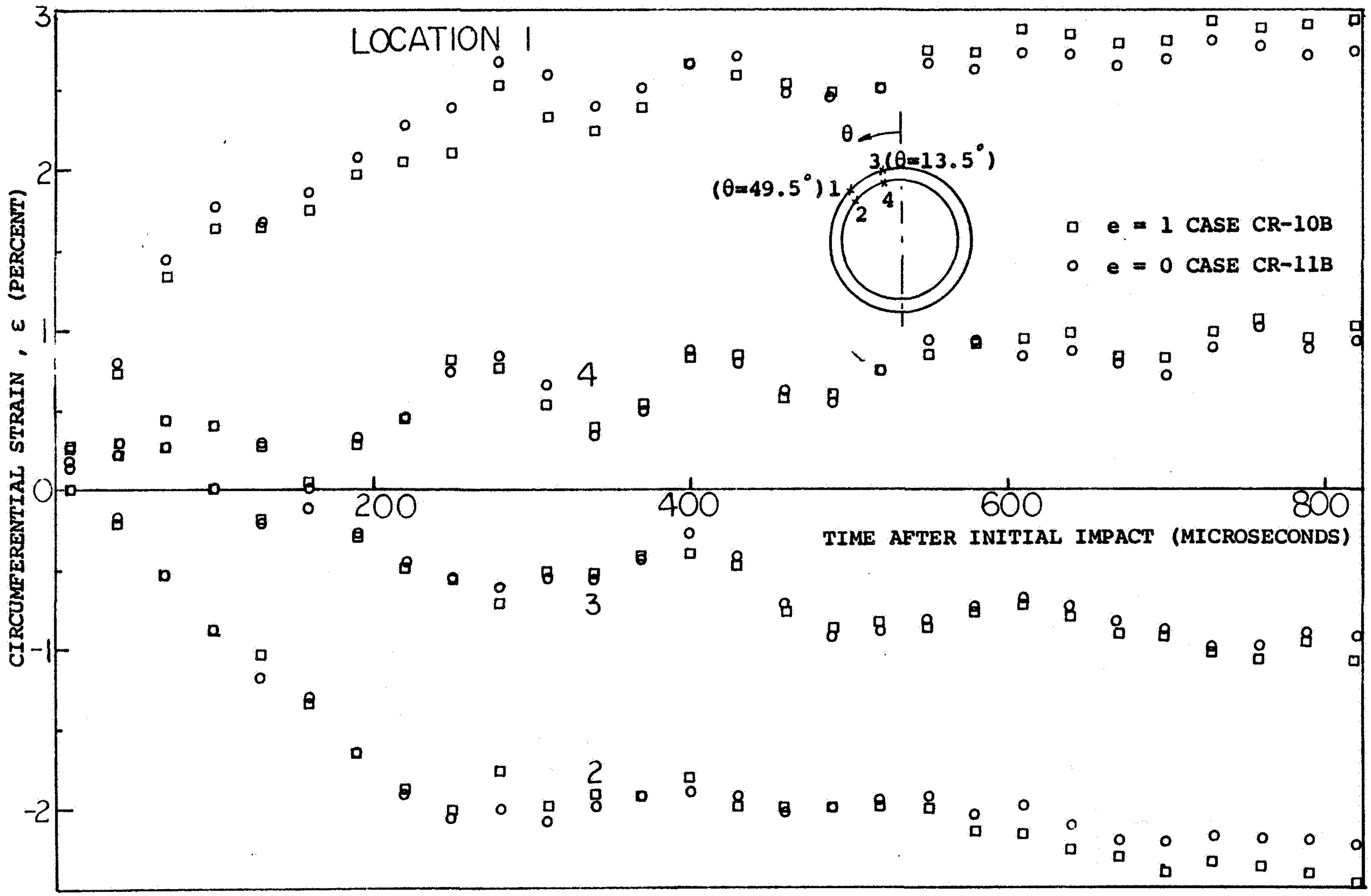

FIG. 49 EFFECT OF THE COEFFICIENT OF RESTITUTION ON THE PREDICTED INNER-SURFACE AND OUTER-SURFACE CIRCUMFERENTIAL STRAINS OF A BLADE-IMPACTED FREE COMPLETE RING

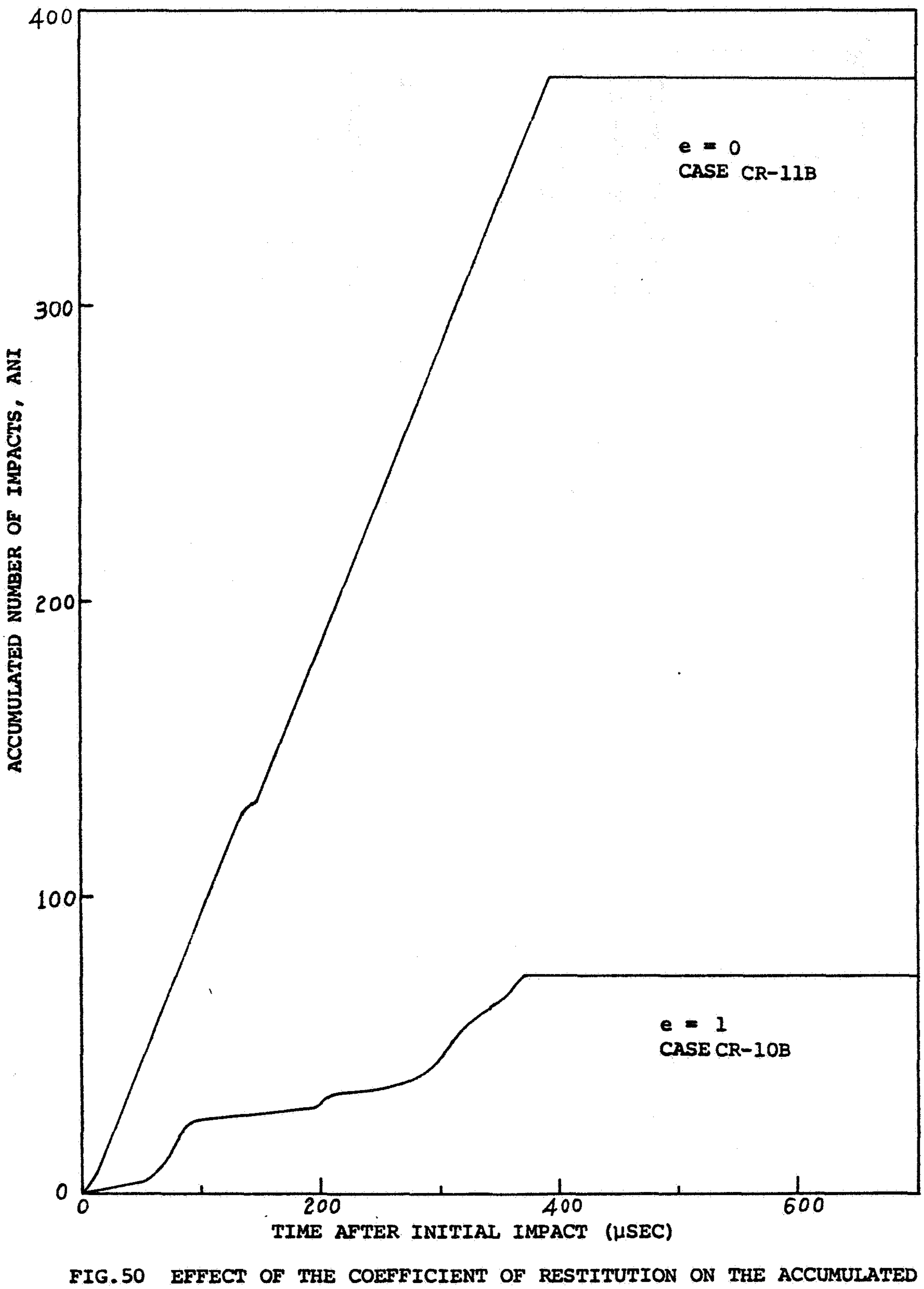

FIG.50 EFFECT OF THE COEFFICIENT OF RESTITUTION ON THE ACCUMULATED NUMBER OF IMPACTS OF A BLADE-IMPACTED FREE COMPLETE RING

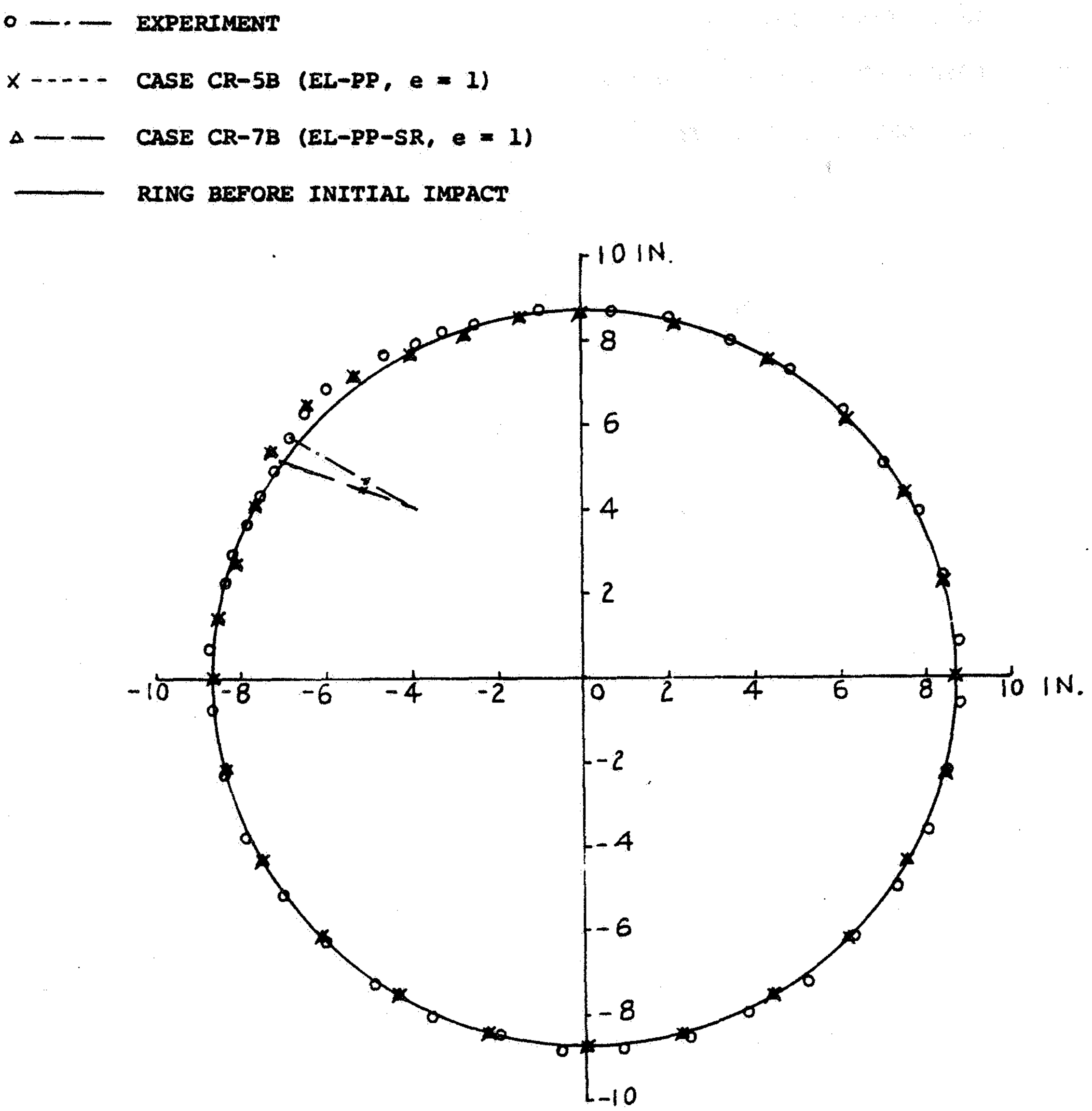

(a) Time after Initial Impact (TAII) = 150 μsec

FIG. 51 COMPARISON OF PREDICTIONS WITH EXPERIMENT FOR THE FREE COMPLETE RING SUBJECTED TO SINGLE-BLADE IMPACT IN NAPTC TEST 88

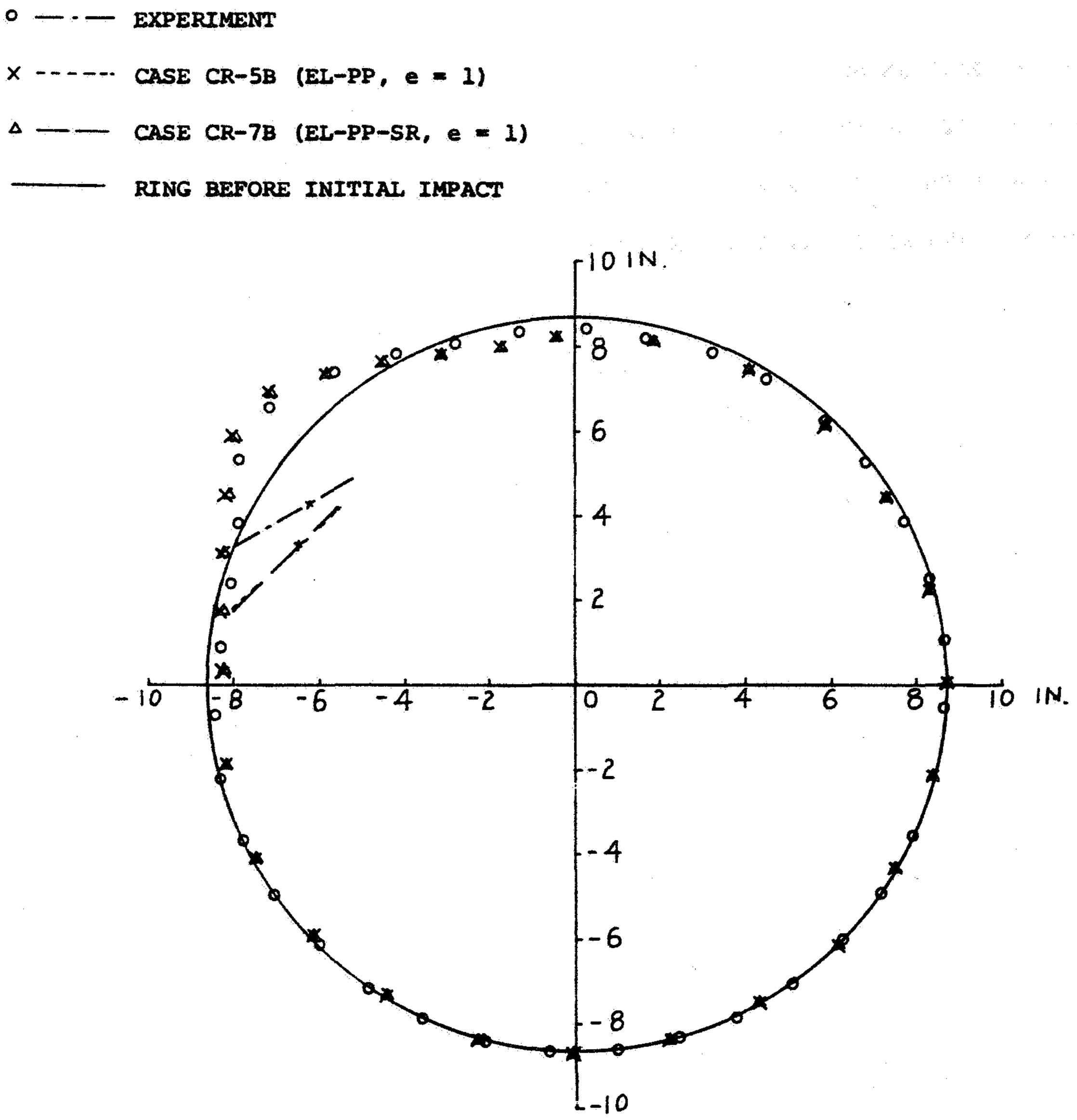

(b) TAII = 570 μsec

FIG. 51 CONTINUED

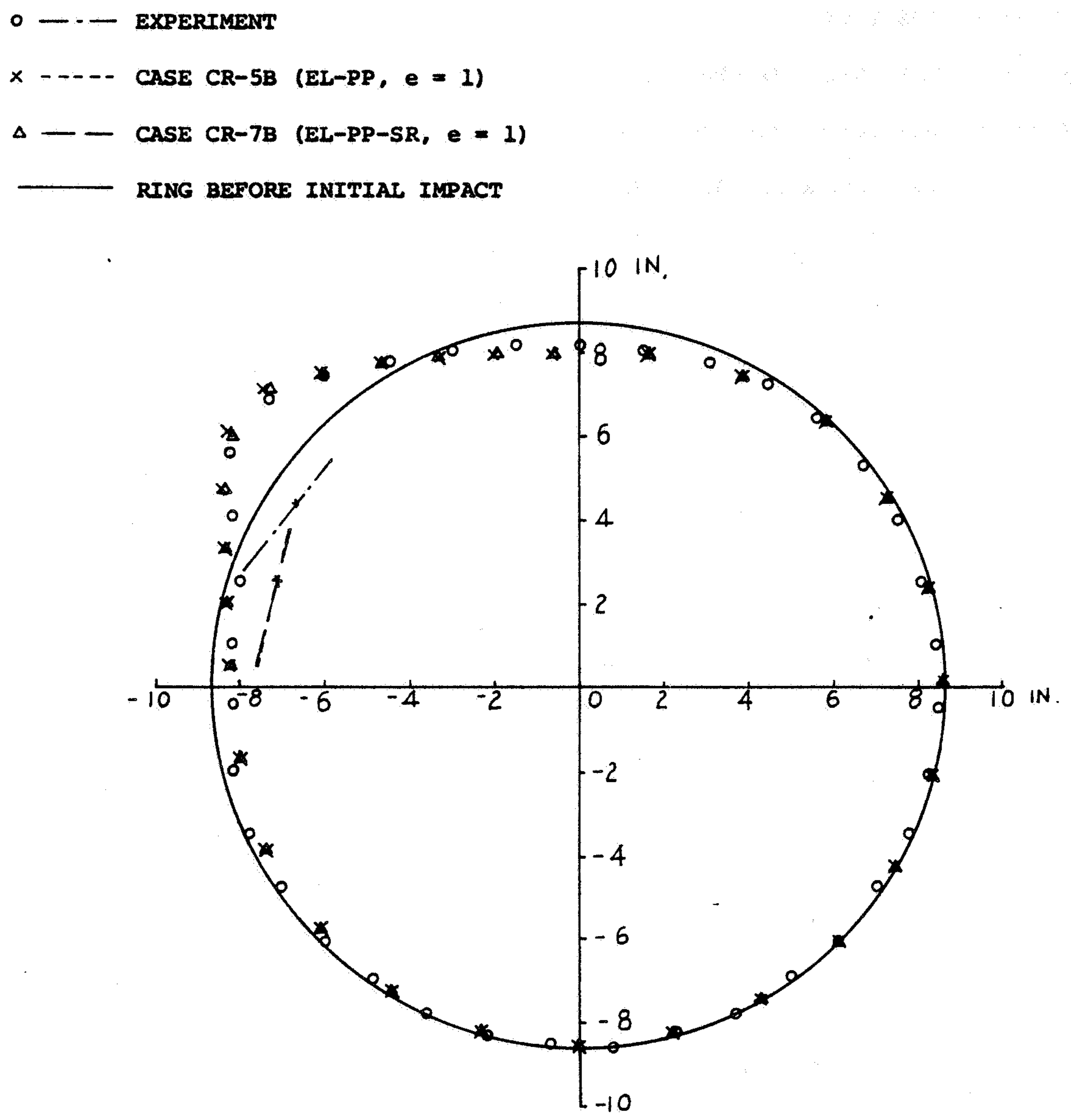

(c) TAII = 810 μsec

FIG. 51 CONCLUDED

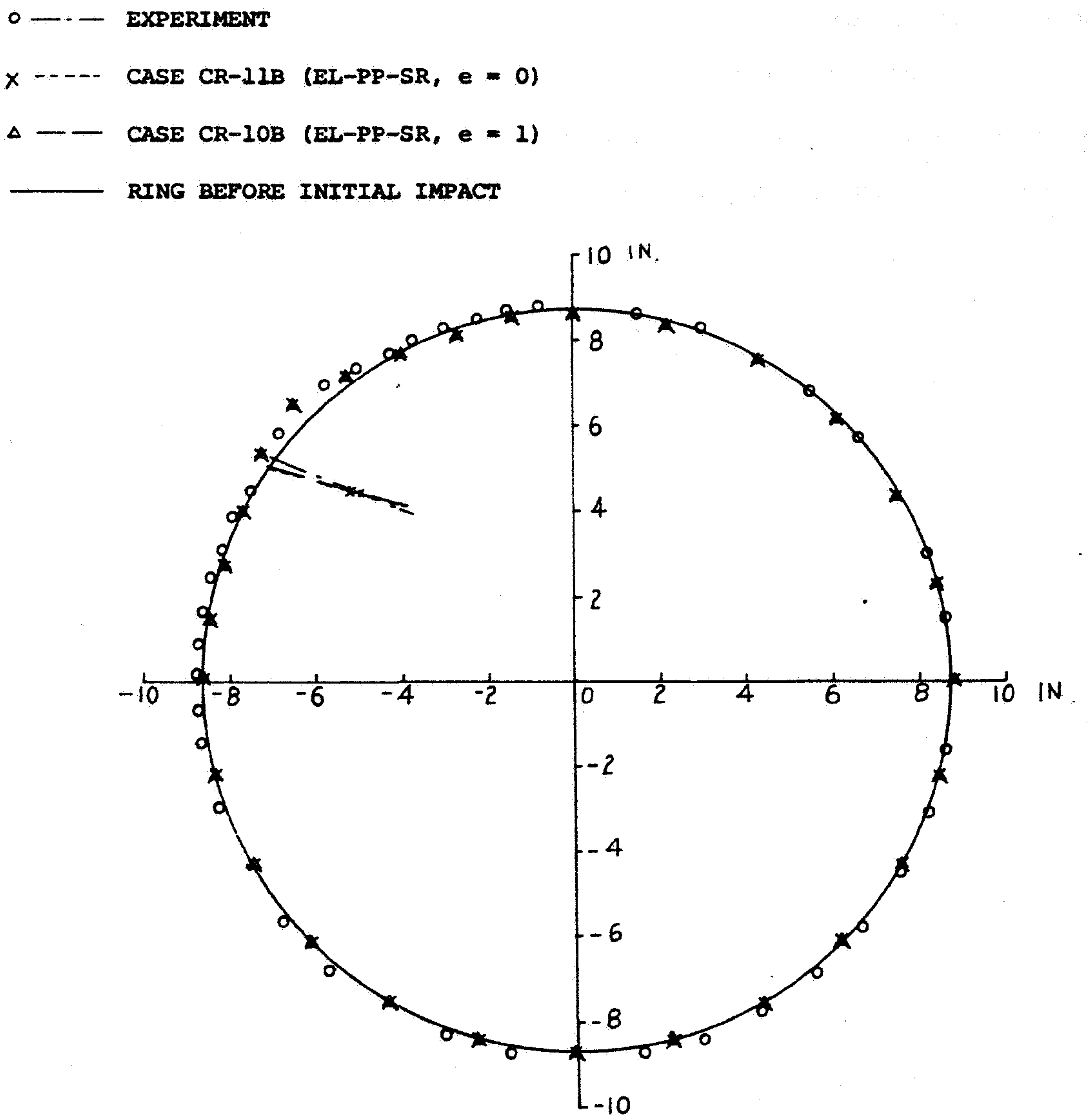

(a) TAII = 150 μsec

FIG. 52 COMPARISON OF PREDICTIONS WITH EXPERIMENT FOR THE FREE COMPLETE RING SUBJECTED TO SINGLE-BLADE IMPACT IN NAPTC TEST 91

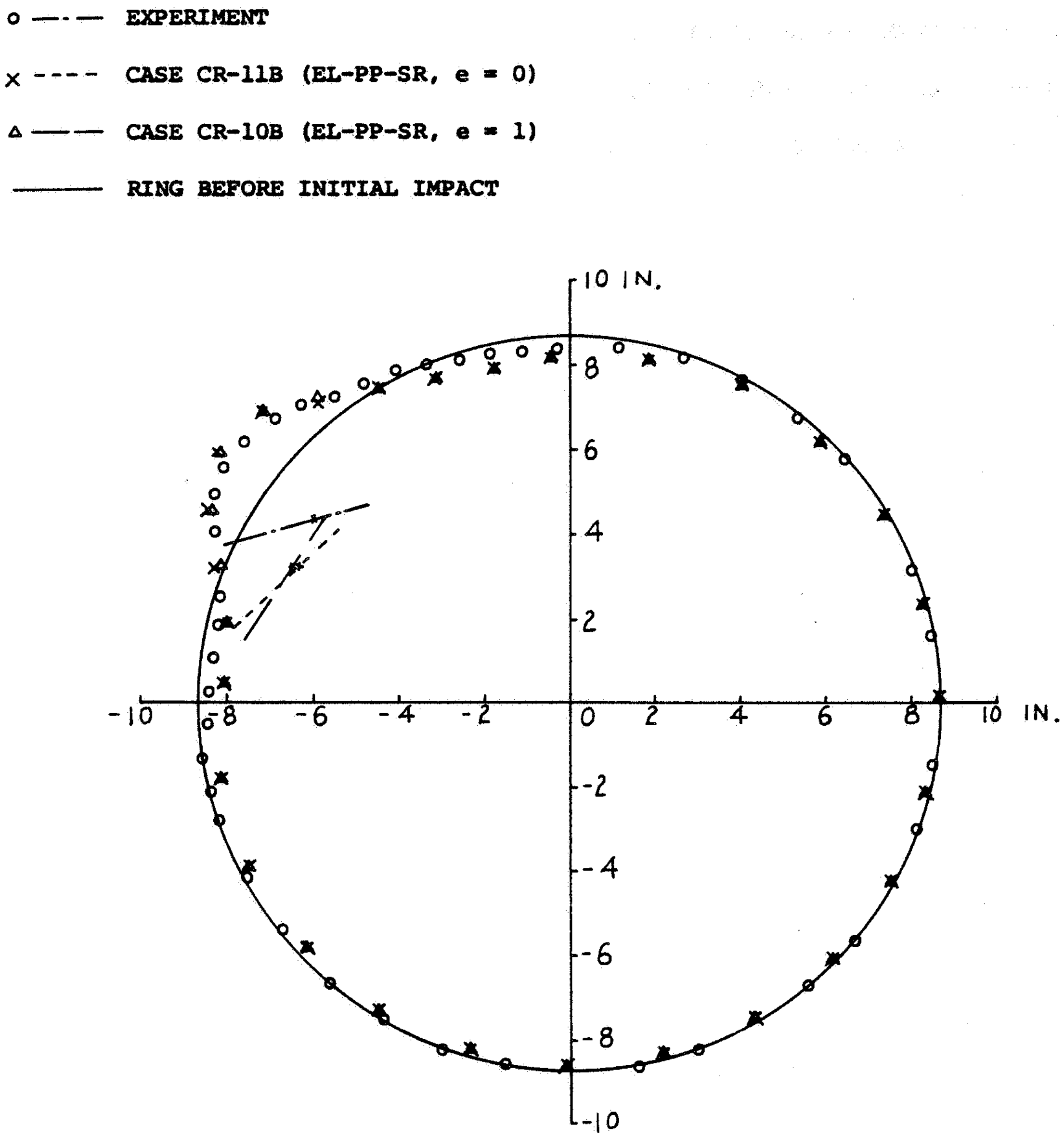

(b) TAII = 570 μsec

FIG. 52 CONTINUED

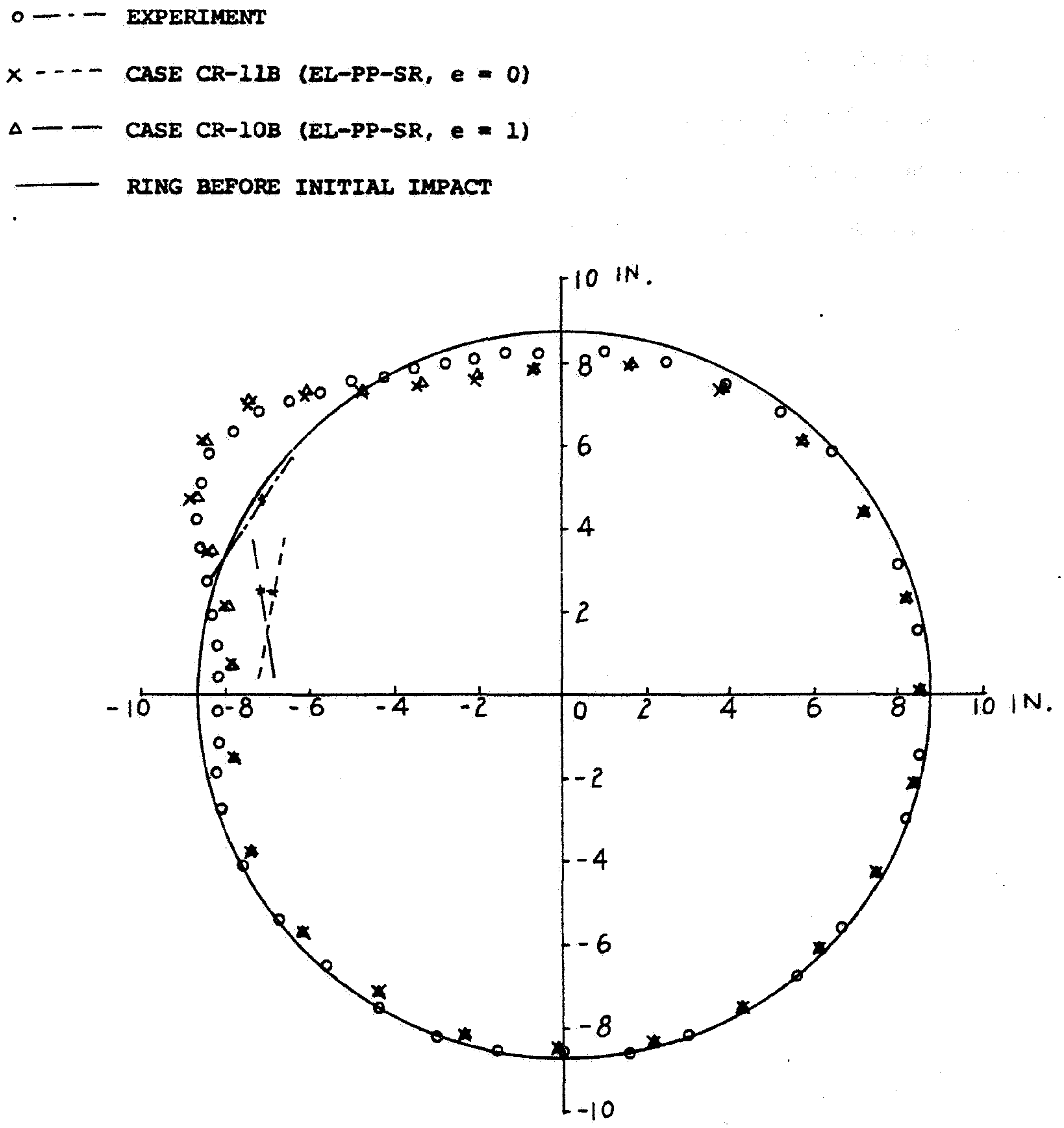

(c) TAII = 810 μsec

FIG. 52 CONCLUDED

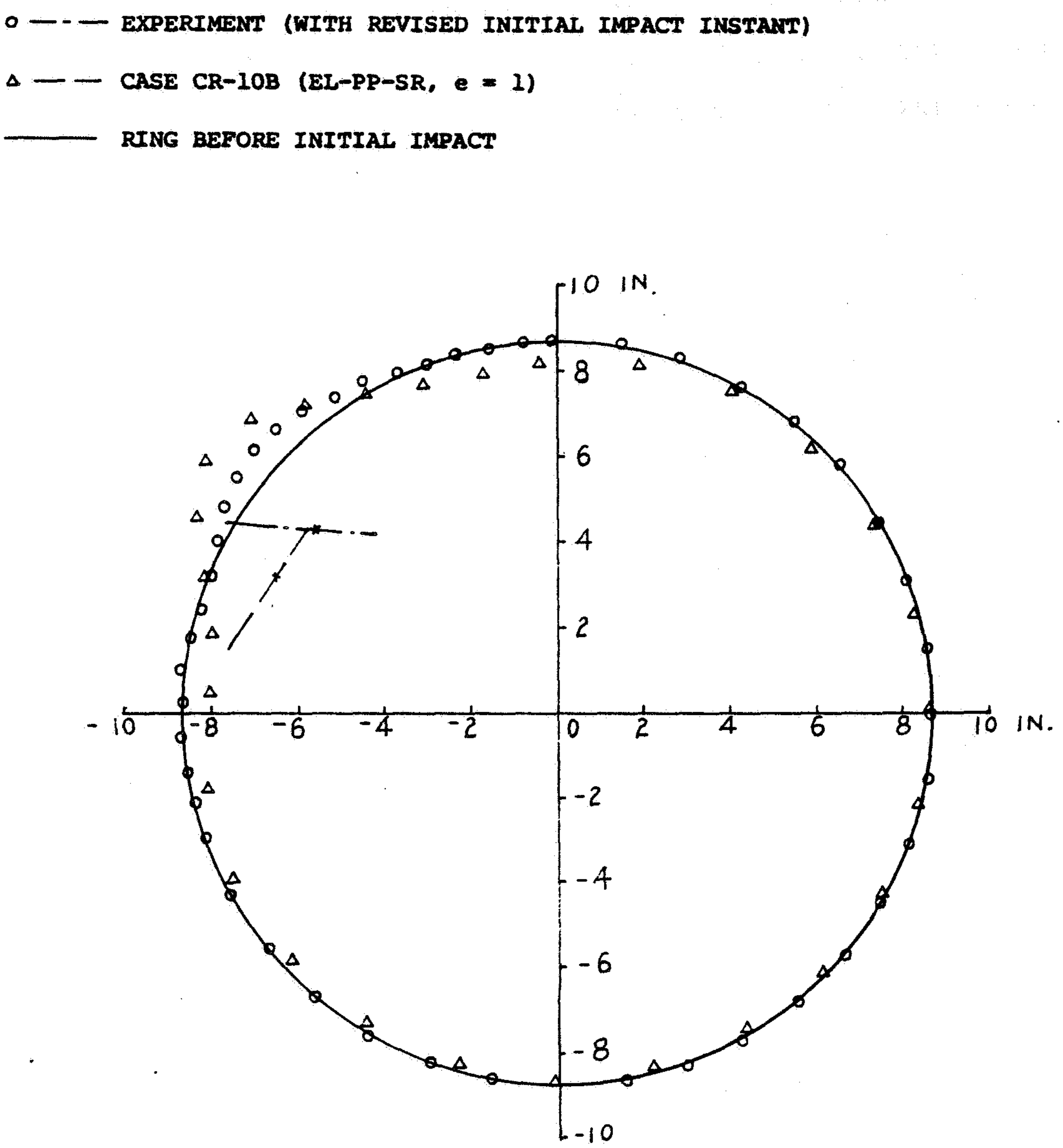

(a) TAII = 570 μsec

FIG. 53 COMPARISON OF PREDICTIONS WITH EXPERIMENT FOR THE FREE COMPLETE RING SUBJECTED TO SINGLE-BLADE IMPACT IN NAPTC TEST 91, WITH A REVISED INSTANT OF INITIAL IMPACT

o —·— EXPERIMENT (WITH REVISED INITIAL IMPACT INSTANT)

△ — — CASE CR-10B (EL-PP-SR, e = 1)

——— RING BEFORE INITIAL IMPACT

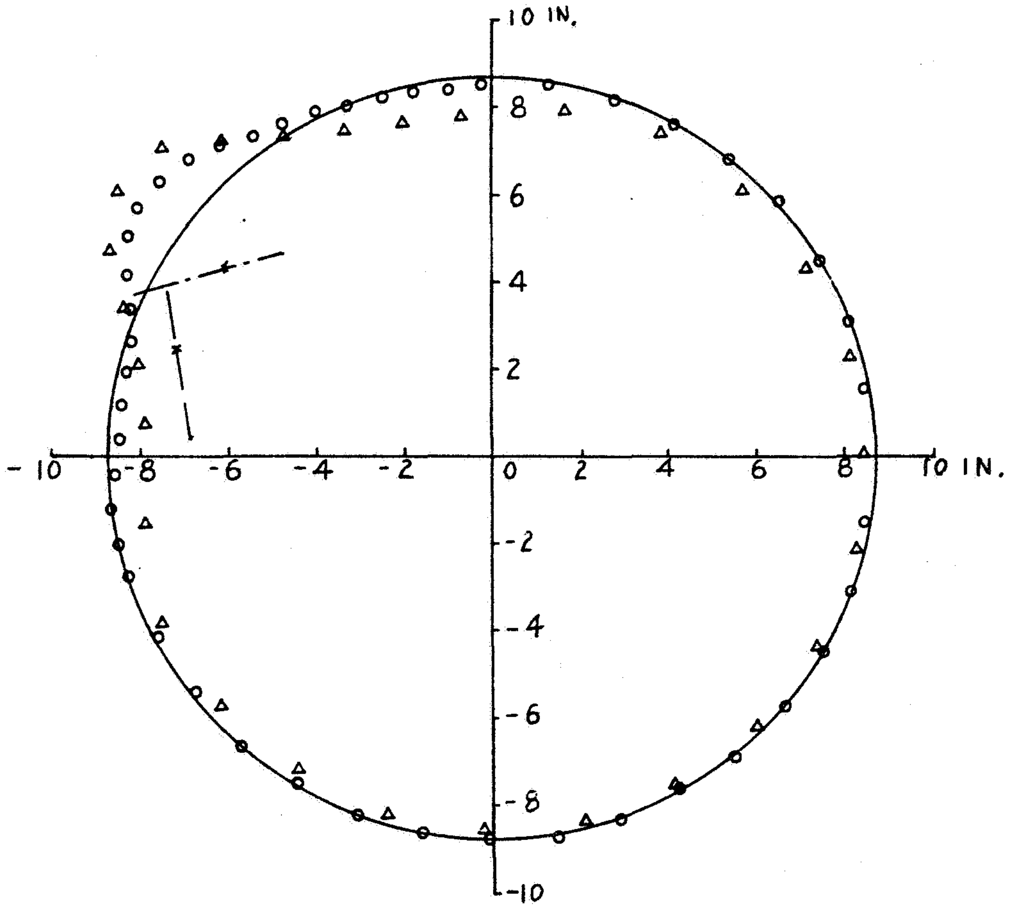

(b) TAII = 810 μsec

FIG. 53 CONCLUDED

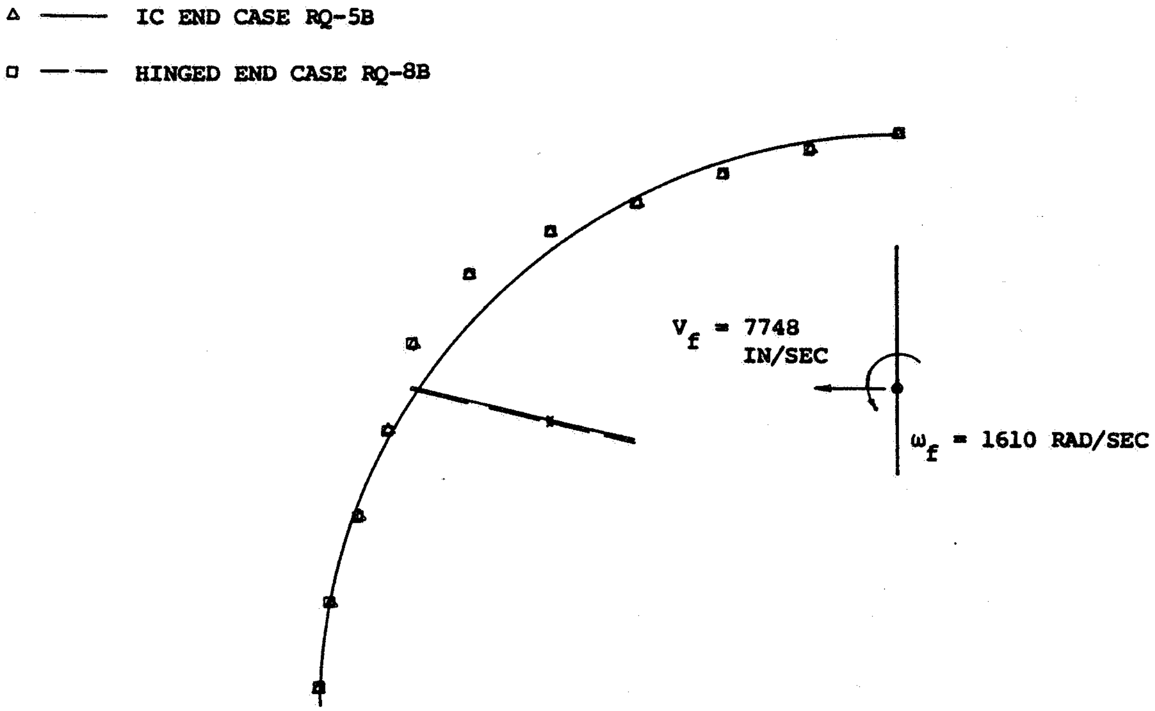

(a) Time t = 750 µsec

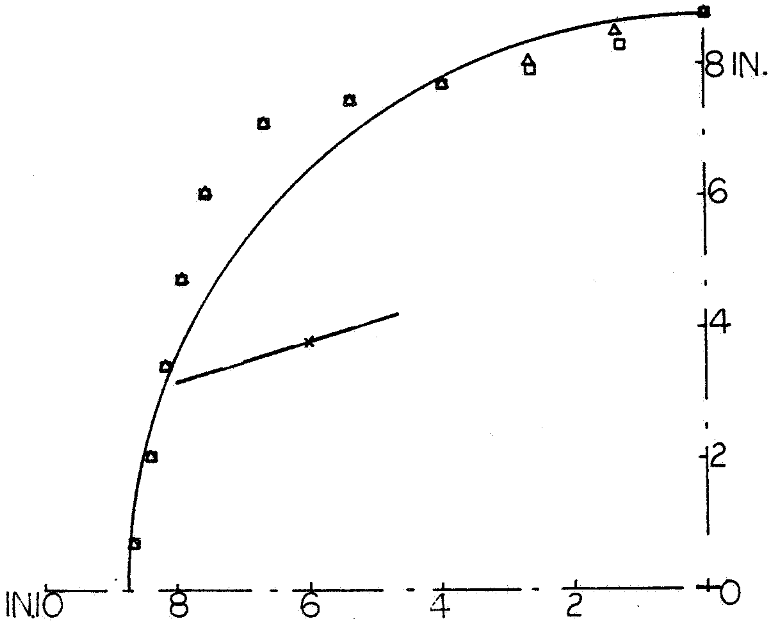

(b) t = 960 µsec

FIG. 54 COMPARISON OF THE RESPONSES OF RING QUADRANTS WITH IDEALLY-CLAMPED AND SMOOTH-HINGED ENDS TO SINGLE-BLADE IMPACT

(9)

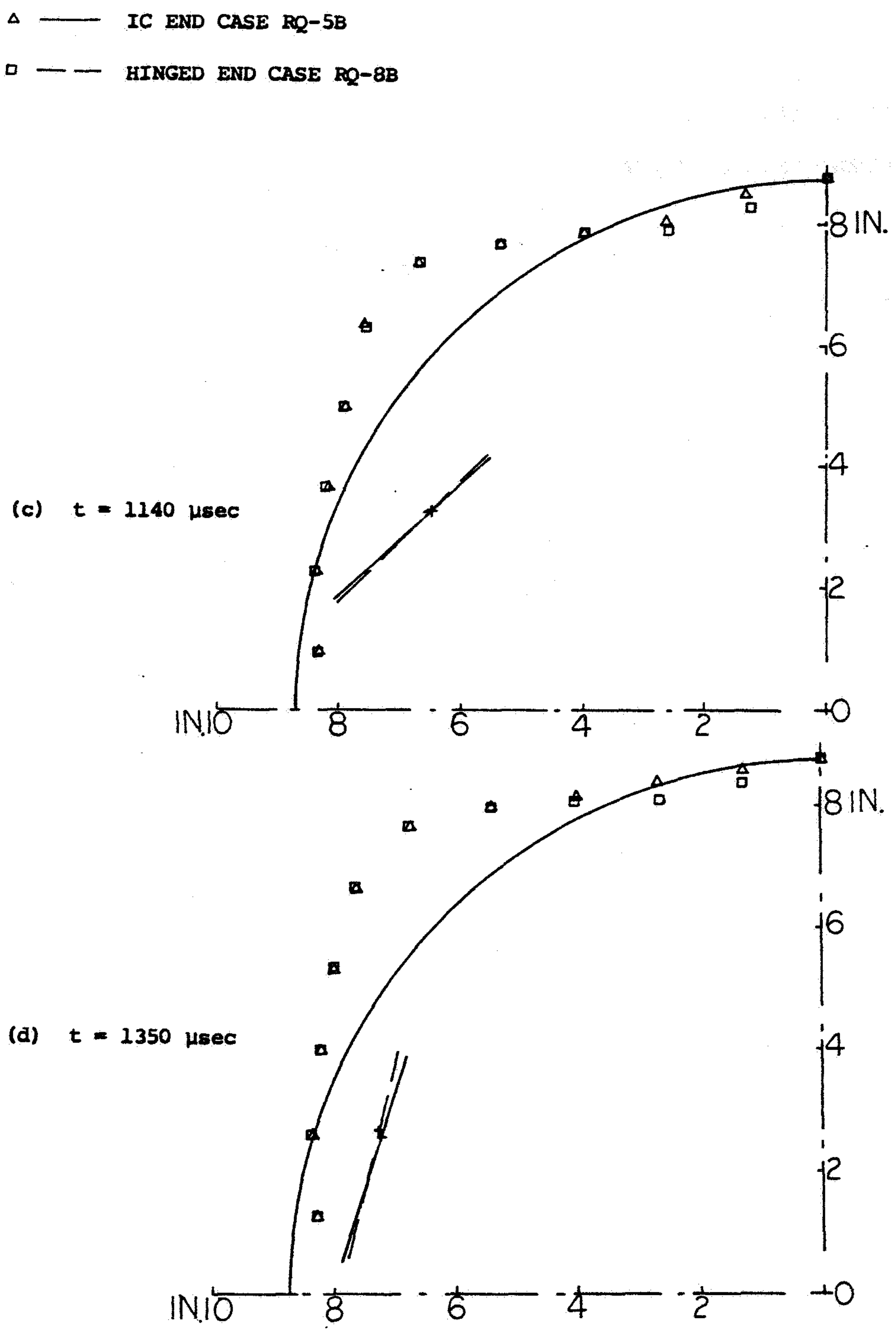

(c) t = 1140 μsec

(d) t = 1350 μsec

FIG. 54 CONCLUDED

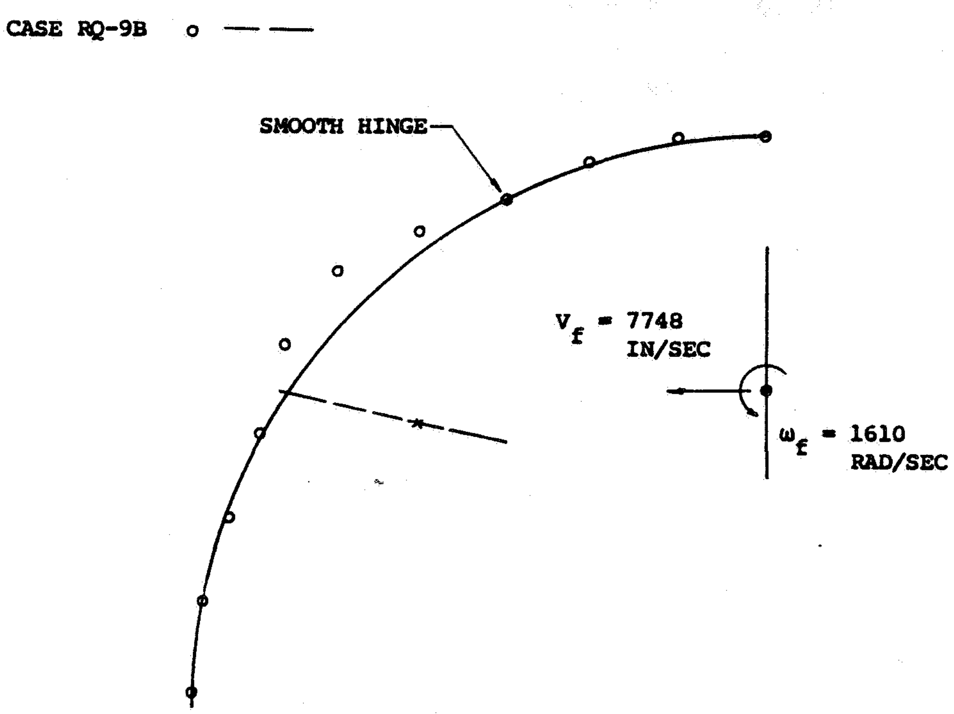

(a) t = 750 μsec

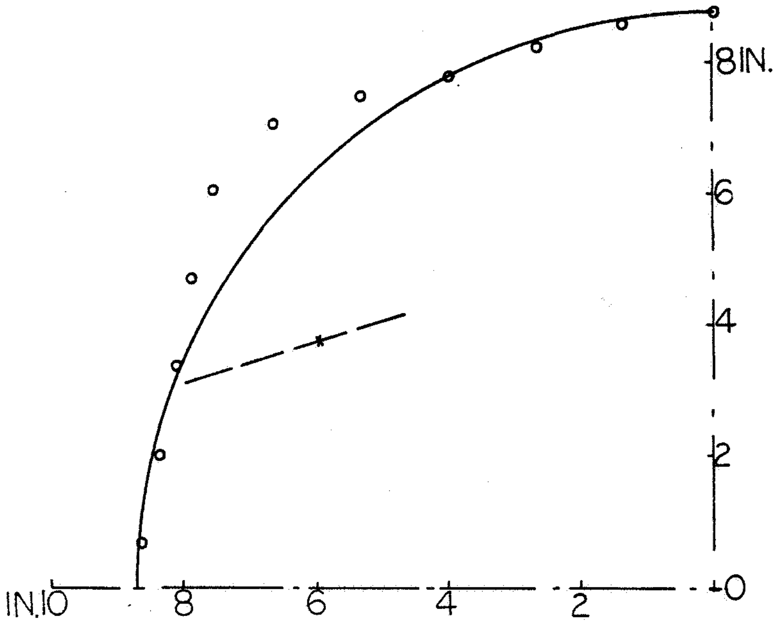

(b) t = 960 μsec

FIG. 55 ILLUSTRATION OF THE RESPONSE OF A QUADRANT RING SMOOTHLY HINGED AT θ = 27° TO SINGLE-BLADE IMPACT

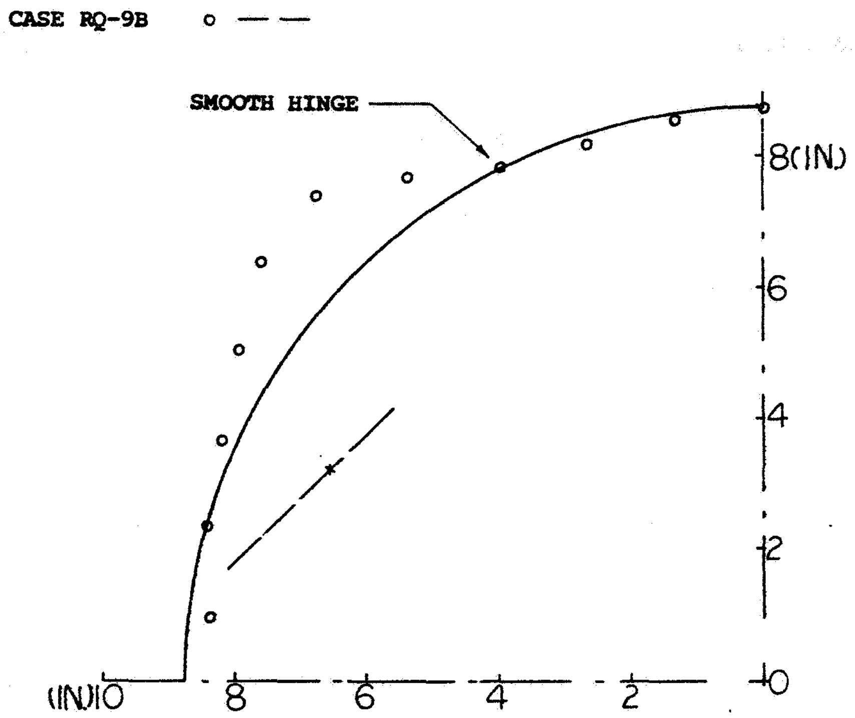

(c) t =1140 μsec

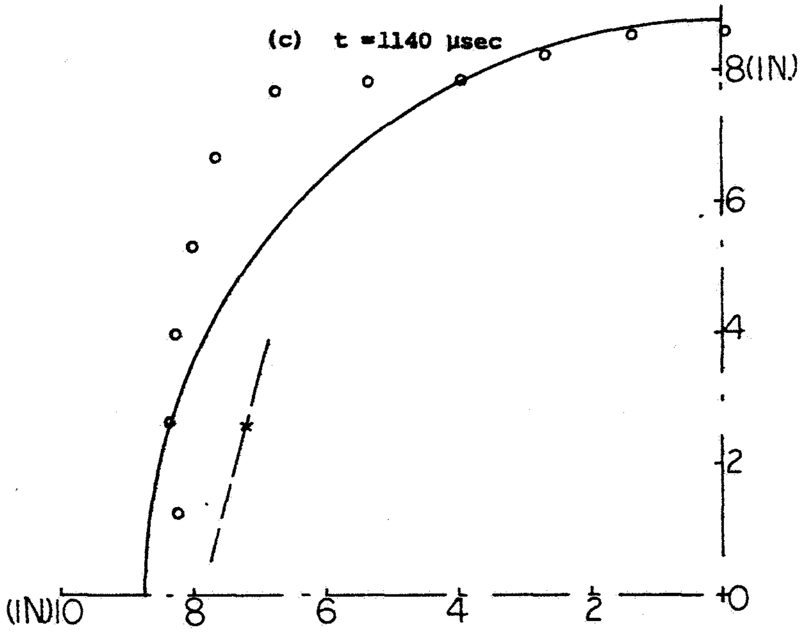

(d) t = 1350 μsec

FIG. 55 CONCLUDED

# APPENDIX A

## DESCRIPTION OF THE MECHANICAL SUBLAYER MODEL FOR STRAIN-HARDENING, STRAIN-RATE SENSITIVE MATERIAL BEHAVIOR

As discussed in Subsection 2.3.2, the yield surface of certain materials will change in case of continued straining beyond the initial yield. The change of the yield surface that characterizes the strain-hardening behavior of the material depends on the loading history. In the present analysis, the strain-hardening behavior of the material is accounted for by using the "mechanical sublayer model" (Ref. 20, 21, 46, and 48). In order that the present report be reasonably self-contained, the mechanical sublayer model is described in this appendix.

In the mechanical sublayer model, the uniaxial tension (or compression) test stress-strain curve of the material is first approximated by (n+1) piecewise-linear segments which are defined at coordinates $[(\sigma_k, \varepsilon_k), k = 1, 2, \ldots n]$, as depicted in Fig. A.1a. Next, the material is envisioned as consisting, at any point in the material, of n equally-strained "sublayers" of elastic, perfectly-plastic material, with each sublayer having the same elastic modulus E, but an appropriately different yield stress (see Fig. A.1b). For example, the yield stress of the kth sublayer is

$$\sigma_{0k} = E \varepsilon_k \quad , ( k = 1, 2, \cdots, n ) \tag{A.1}$$

Then, the stress value, $\sigma_k$, associated with the kth sublayer can be defined uniquely by the strain history and the value of strain and strain-rate present at that point. Taken collectively with an appropriate weighting factor $C_k$ for each sublayer, the stress, $\sigma$, at that point corresponding to strain $\varepsilon$ may be expressed as

$$\sigma = \sum_{k=1}^{n} C_k \sigma_k ( \varepsilon ) \tag{A.2}$$

where the weighting factor $C_k$ for the kth sublayer may readily be confirmed to be

$$C_k = \frac{E_k - E_{k-1}}{E} \tag{A.3}$$

where

$$E_1 = E \ , \quad E_k = \frac{\sigma_k - \sigma_{k-1}}{\varepsilon_k - \varepsilon_{k-1}} \quad (k = 2, 3, \cdots, n) \ , \quad E_{n+1} = 0 \tag{A.3a}$$

The elastic perfectly-plastic and linear strain-hardening constitutive relation may be treated as special cases. In the case of elastic perfectly-plastic behavior, there is only one sublayer, and in the case of linear strain-hardening material there are two sublayers and the yield limit of the second sublayer is taken sufficiently high so that the deformation in that sublayer remains elastic.

From the computational point of view, the use of the mechanical sublayer model is very convenient to analyze problems with general loading paths including loading, unloading, reloading, and cyclic loading. Its features include the "kinematic hardening rule" which takes the Baushinger effect into account (see Fig. A.1c). Also, this mechanical sublayer model may readily accommodate the strain-rate effect. Figure A.2a illustrates schematically the uniaxial stress-strain behavior for a strain-rate dependent, elastic, perfectly-plastic material whose rate dependence is described by Eq. 2.87,

$$\sigma_y = \sigma_0 \left( 1 + \left| \frac{\dot{\varepsilon}}{D} \right|^{\frac{1}{p}} \right) \tag{2.87}$$

while Fig. A.2b depicts the corresponding behavior for a strain-hardening material which is represented by the mechanical sublayer model, each sublayer of which has the same values for the strain-rate constants D and p. For this special type of rate-dependent strain-hardening material, the stress-strain curve at a given strain rate $\dot{\varepsilon}$ is simply a constant magnification of the static stress-strain curves along rays emanating from the origin. However, for strain-hardening material whose strain-rate behavior is not one of simple magnification, the strain-rate behavior can often be approximated adequately by employing appropriately different values of D and p for each sublayer; the resulting behavior is shown schematically in Fig. A.2c.

One may generalize this uniaxial behavior to the two- or three-dimensional stress case by adopting, for example, the Mises-Hencky yield condition, Eq. 2.79, and flow rule, Eq. 2.82, and applying them to each sublayer of the mechanical sublayer model. The strain-rate dependence may also be generalized by assuming that the $\dot{\varepsilon}$ of the one-dimensional case may be replaced by the second invariant of the deviatoric strain-rate tensor as defined by

$$\frac{2}{3}\,\dot{\varepsilon}^2 = \dot{\gamma}^i_j\,\dot{\gamma}^j_i - \frac{1}{3}\left(\dot{\gamma}^k_k\right)^2 \qquad (3.64)$$

In terms of the finite increments $\Delta\gamma^\alpha_\beta$ of strain determined in each timewise calculation step of the present procedure, the "replacement $\dot{\varepsilon}$" given by Eq. 3.64 becomes:

$$\dot{\varepsilon} = \frac{1}{\Delta t}\left[\frac{3}{2}\,\Delta\gamma^i_j\,\Delta\gamma^j_i - \frac{1}{2}\left(\Delta\gamma^k_k\right)^2\right]^{\frac{1}{2}} \qquad (A.4)$$

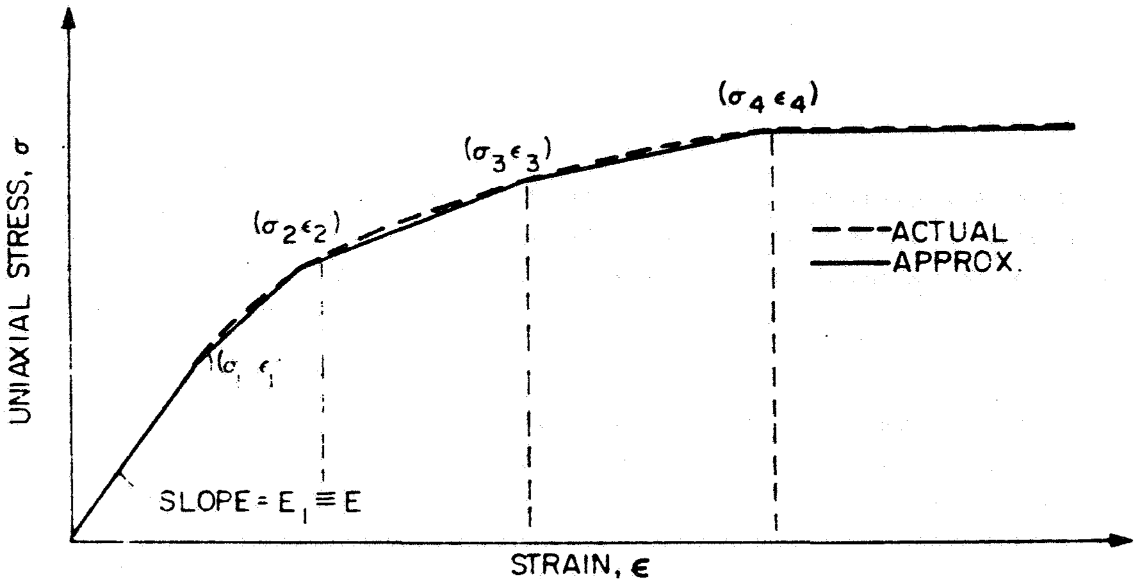

(a) ACTUAL AND APPROXIMATED CURVES

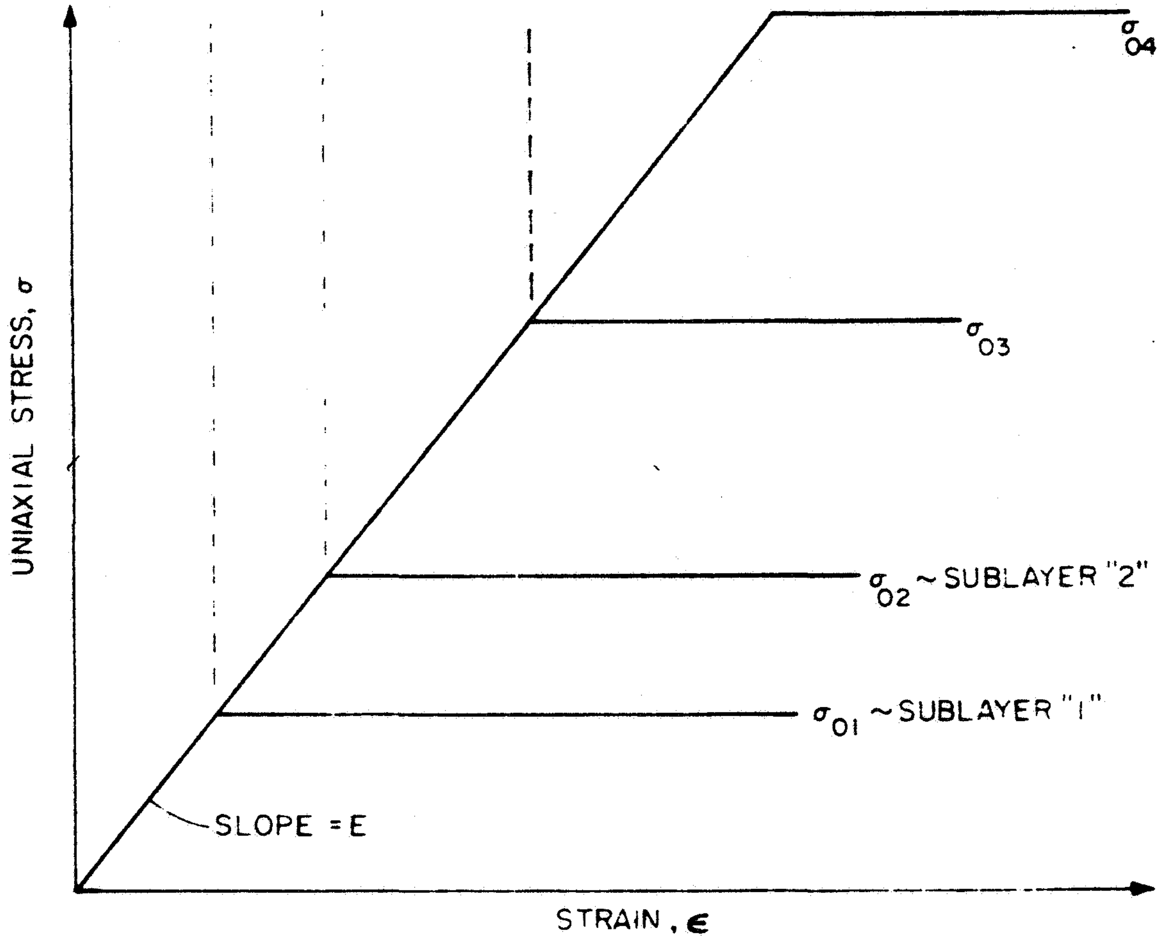

(b) PROPERTIES OF THE ELASTIC, PERFECTLY-PLASTIC SUBLAYERS

**FIG. A.1 APPROXIMATION OF A UNIAXIAL STRESS-STRAIN CURVE BY THE MECHANICAL SUBLAYER MODEL**

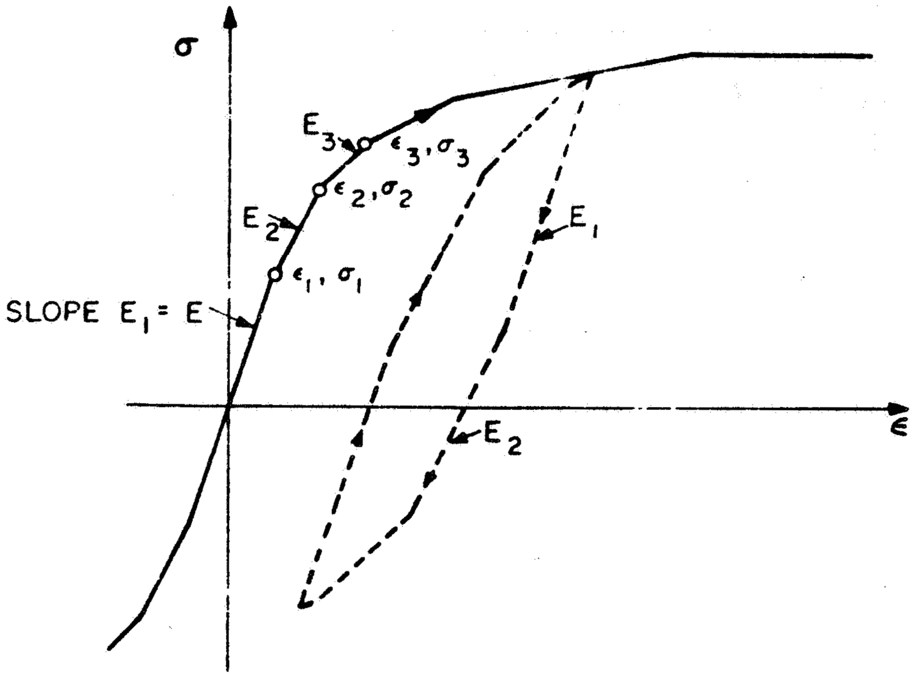
σ
E3
ε3, σ3
ε2, σ2
E2
ε1, σ1
SLOPE E1 = E
E1
E2
ε

(c) SCHEMATIC OF LOADING, UNLOADING, AND RELOADING PATHS

FIG. A.1 CONCLUDED

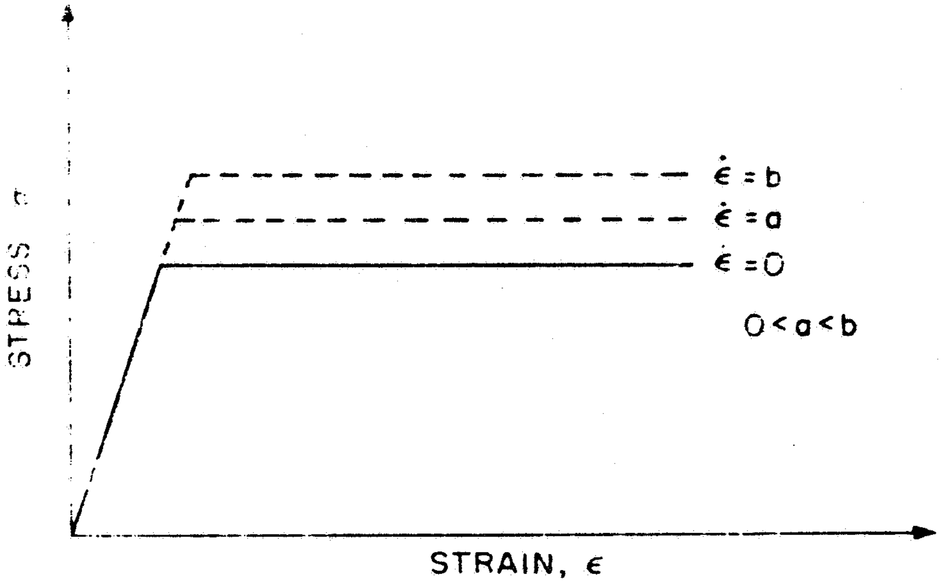

(a) ELASTIC, PERFECTLY-PLASTIC MATERIAL

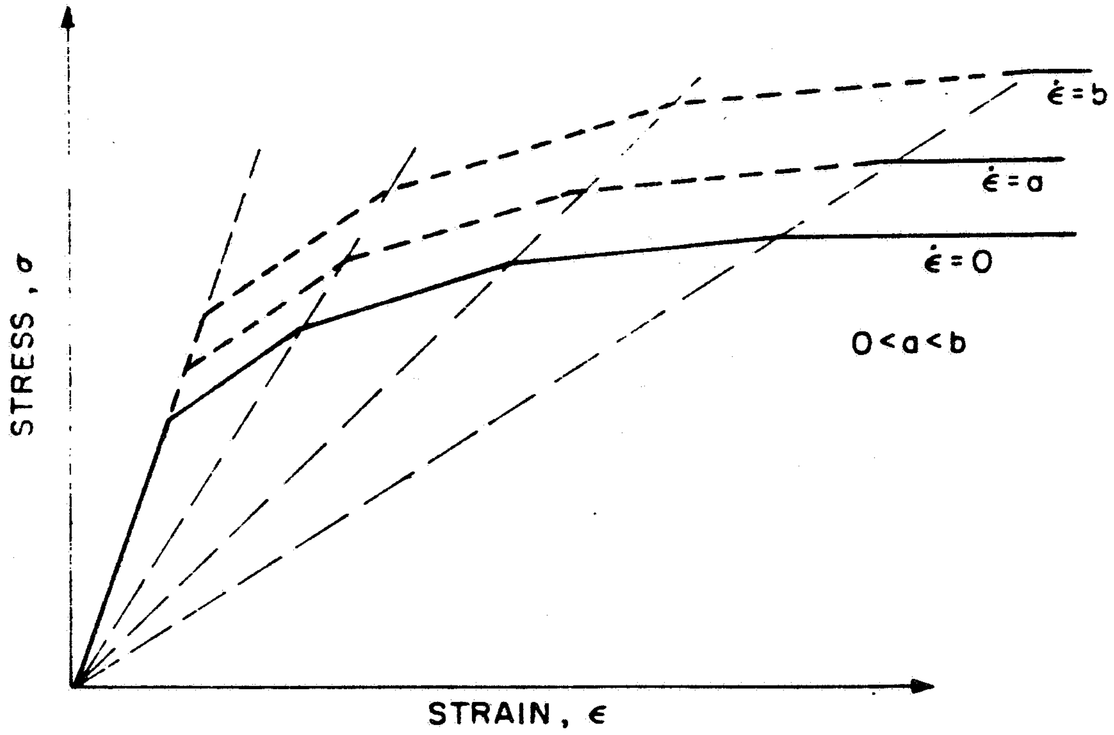

(b) SPECIAL STRAIN HARDENING MATERIAL

FIG. A.2 SCHEMATIC OF STRAIN-RATE DEPENDENT UNIAXIAL STRESS-STRAIN CURVES

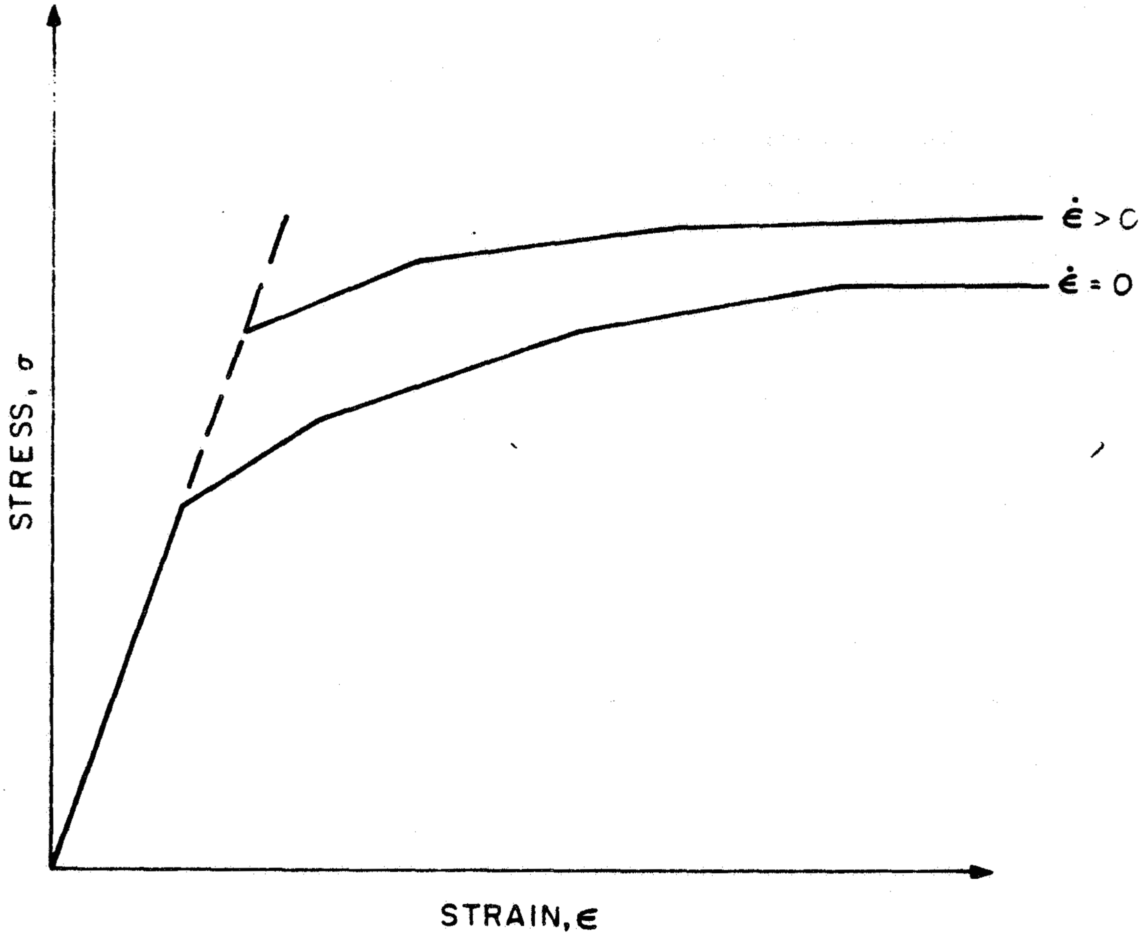

(c) MORE GENERAL STRAIN HARDENING MATERIAL

FIG. A.2 CONCLUDED

# APPENDIX B

## DEFINITION OF FINITE ELEMENT MATRICES INDICATED SYMBOLICALLY IN THE TEXT

The various matrices which are used symbolically in Section 4 for an arbitrarily curved beam element are documented in this appendix,and their specialization to represent simple circular ring and straight beam elements are also listed.

## B.1 Bernoulli-Euler Type Deformation Behavior

### B.1.1 Bernoulli-Euler Type Curved Beam Element with CC Assumed-Displacement Functions*

$$\{\underset{\sim}{u}\} = \begin{Bmatrix} v \\ w \end{Bmatrix} = [\underset{2\times 8}{U(\eta)}]\{\underset{8\times 1}{\beta}\} \tag{4.13a}$$

$$\{q\} = \lfloor v_i \quad w_i \quad \psi_i \quad v_{,\eta i} \quad v_{i+1} \quad w_{i+1} \quad \psi_{i+1} \quad v_{,\eta i+1}\rfloor^T = [\underset{8\times 8}{A}]\{\beta\} \tag{4.17}$$

$$\varepsilon_o = \lfloor \underset{1\times 8}{D_1} \rfloor \{q\} + \frac{1}{2}\lfloor q \rfloor \{\underset{8\times 1}{D_2}\}\lfloor \underset{1\times 8}{D_2}\rfloor \{q\} \tag{4.24}$$

$$\kappa = \lfloor \underset{1\times 8}{D_3} \rfloor \{q\} \tag{4.24}$$

$$[m] = \int_{\eta_i}^{\eta_{i+1}} [\underset{8\times 3}{N(\eta)}]^T [\underset{3\times 3}{B}] [\underset{3\times 8}{N(\eta)}]\, d\eta \tag{4.31b}$$

$$\{f\} = \int_{\eta_i}^{\eta_{i+1}} [N(\eta)]^T \begin{Bmatrix} F_v \\ F_w \\ \underset{\sim}{M} \end{Bmatrix} d\eta \tag{4.34a}$$

$$\{p\} = \int_{\eta_i}^{\eta_{i+1}} (\{D_1\} L + \{D_3\} M)\, d\eta \tag{4.37a}$$

$$[h] = \int_{\eta_i}^{\eta_{i+1}} \{D_2\}\lfloor D_2 \rfloor L\, d\eta \tag{4.37a}$$

$$[k] = \int_{\eta_i}^{\eta_{i+1}} (\{D_1\} E b h \lfloor D_1 \rfloor + \{D_3\} \frac{E b h^3}{12} \lfloor D_3 \rfloor)\, d\eta \tag{4.40a}$$

---

*Equations not numbered with a prefix B refer to pertinent equations in the text.

$$\{f_q^{NL}\} = -\left\langle \int_{\eta_i}^{\eta_{i+1}} Ebh\left(\tfrac{1}{2}\lfloor q \rfloor \{D_2\} \lfloor D_2 \rfloor \{q\}\right) \{D_1\}\, d\eta \right. \\ \left. + \int_{\eta_i}^{\eta_{i+1}} Ebh\left(\lfloor D_1 \rfloor \{q\} + \tfrac{1}{2}\lfloor q \rfloor \{D_2\} \lfloor D_2 \rfloor \{q\}\right) \{D_2\} \lfloor D_2 \rfloor\, d\eta\, \{q\} \right\rangle \tag{4.40d}$$

$$\{f_p^{L}\} = \iint_A \int_{\eta_i}^{\eta_{i+1}} \left( E\,\varepsilon^{p} \{D_1\} + \zeta\, E\,\varepsilon^{p} \{D_3\} \right) dV_n \tag{4.40b}$$

$$\{f_p^{NL}\} = \iint_A \int_{\eta_i}^{\eta_{i+1}} E\,\varepsilon^{p} \{D_2\} \lfloor D_2 \rfloor\, dV_n\, \{q\} \tag{4.40c}$$

In the following, the matrices $[U(\eta)]$, $[A]$, $(\lfloor D_i \rfloor,\ i=1,2,3)$, $[N(\eta)]$, and $[B]$ appearing in the above expressions are listed for an arbitrarily-curved beam element(see Fig. 5):

$$[U(\eta)] = \begin{bmatrix} \cos\phi & \sin\phi & -z\cos\phi + y\sin\phi & \eta & 0 & 0 & \eta^2 & \eta^3 \\ -\sin\phi & \cos\phi & z\sin\phi + y\cos\phi & 0 & \eta^2 & \eta^3 & 0 & 0 \end{bmatrix} \tag{4.13}$$

$$[A] = \begin{bmatrix} \cos\phi_i & \sin\phi_i & 0 & 0 & 0 & 0 & 0 & 0 \\ -\sin\phi_i & \cos\phi_i & 0 & 0 & 0 & 0 & 0 & 0 \\ 0 & 0 & 1 & 0 & 0 & 0 & 0 & 0 \\ \frac{\sin\phi_i}{R_i} & \frac{-\cos\phi_i}{R_i} & 0 & 1 & 0 & 0 & 0 & 0 \\ \cos\phi_{i+1} & \sin\phi_{i+1} & y_{i+1}\sin\phi_{i+1} & \eta_{i+1} & 0 & 0 & \eta_{i+1}^2 & \eta_{i+1}^3 \\ -\sin\phi_{i+1} & \cos\phi_{i+1} & y_{i+1}\cos\phi_{i+1} & 0 & \eta_{i+1}^2 & \eta_{i+1}^3 & 0 & 0 \\ 0 & 0 & 1 & -\frac{\eta_{i+1}}{R_{i+1}} & 2\eta_{i+1} & 3\eta_{i+1}^2 & \frac{-\eta_{i+1}^2}{R_{i+1}} & \frac{-\eta_{i+1}^3}{R_{i+1}} \\ \frac{\sin\phi_{i+1}}{R_{i+1}} & \frac{-\cos\phi_{i+1}}{R_{i+1}} & -y_{i+1}\frac{\cos\phi_{i+1}}{R_{i+1}} & 1 & 0 & 0 & 2\eta_{i+1} & 3\eta_{i+1}^2 \end{bmatrix} \tag{B.1}$$

$$\lfloor D_1 \rfloor = \lfloor 0 \quad 0 \quad 0 \quad 1 \quad \eta^2/R \quad \eta^3/R \quad 2\eta \quad 3\eta^2 \rfloor [A^{-1}] \tag{B.2}$$

$$\lfloor D_2 \rfloor = \lfloor 0 \quad 0 \quad 1 \quad -\eta/R \quad 2\eta \quad 3\eta^2 \quad -\eta^2/R \quad -\eta^3/R \rfloor [A^{-1}] \tag{B.3}$$

$$\lfloor D_3 \rfloor = \lfloor 0 \quad 0 \quad 0 \quad \frac{1}{R} - \eta\frac{\partial^2\phi}{\partial\eta^2} \quad -2 \quad -6\eta \quad \frac{2\eta}{R} - \eta^2\frac{\partial^2\phi}{\partial\eta^2} \quad \frac{3\eta^2}{R} - \eta^3\frac{\partial^2\phi}{\partial\eta^2} \rfloor [A^{-1}] \tag{B.4}$$

$$[N(\eta)] = \begin{bmatrix} \cos\phi & \sin\phi & -z\cos\phi + y\sin\phi & \eta & 0 & 0 & \eta^2 & \eta^3 \\ -\sin\phi & \cos\phi & z\sin\phi + y\cos\phi & 0 & \eta^2 & \eta^3 & 0 & 0 \\ 0 & 0 & 1 & -\frac{\eta}{R} & 2\eta & 3\eta^2 & -\frac{\eta^2}{R} & -\frac{\eta^3}{R} \end{bmatrix} [A^{-1}] \tag{B.5}$$

$$[B] = \begin{bmatrix} \tilde{m} & & 0 \\ & \tilde{m} & \\ 0 & & \tilde{I} \end{bmatrix} \tag{B.6}$$

where

$\tilde{m}$ = mass per unit length of the beam element

$\tilde{I}$ = mass moment of inertia of the beam cross section

Note that, in the above equations, only the matrix $[A]$ is given. In practice, one forms its inverse , $[A^{-1}]$ , by means of available standard computer subroutines. Also note that subscript i ( or i+1 ) is used to denote the value of the quantities at node i ( or node i+1 ).

For application to simple circular ring elements, the geometry and nomenclature of a typical circular ring element is shown in Fig. B.1 where the local and global coordinates are arranged to take advantage of the symmetry of the ring element's geometry. The matrices $[U(\eta)]$, $[A]$ , ( $\lfloor D_i \rfloor$, $i = 1, 2, 3$ ), $[N(\eta)]$, $[m]$ ,and $[k]$ for a simple circular ring element are listed in the following:

$$[U(\eta)] = \begin{bmatrix} \cos\lambda & -\sin\lambda & -R(1-\cos\lambda\cos\Lambda) & \eta & 0 & 0 & \eta^2 & \eta^3 \\ \sin\lambda & \cos\lambda & R\sin\lambda\cos\Lambda) & 0 & \eta^2 & \eta^3 & 0 & 0 \end{bmatrix} \tag{B.7}$$

$$[A] = \begin{bmatrix} \cos\Lambda & \sin\Lambda & -R(1-\cos^2\Lambda) & -\frac{S}{2} & 0 & 0 & \frac{S^2}{4} & -\frac{S^3}{8} \\ -\sin\Lambda & \cos\Lambda & -R\sin\Lambda\cos\Lambda & 0 & \frac{S^2}{4} & -\frac{S^3}{8} & 0 & 0 \\ 0 & 0 & 1 & \frac{S}{2R} & -S & \frac{3S^2}{4} & -\frac{S^2}{4R} & \frac{S^3}{8R} \\ \frac{\sin\Lambda}{R} & -\frac{\cos\Lambda}{R} & \sin\Lambda\cos\Lambda & 1 & 0 & 0 & -S & \frac{3S^2}{4} \\ \cos\Lambda & -\sin\Lambda & -R(1-\cos^2\Lambda) & \frac{S}{2} & 0 & 0 & \frac{S^2}{4} & \frac{S^3}{8} \\ \sin\Lambda & \cos\Lambda & R\sin\Lambda\cos\Lambda & 0 & \frac{S^2}{4} & \frac{S^3}{8} & 0 & 0 \\ 0 & 0 & 1 & -\frac{S}{2R} & S & \frac{3S^2}{4} & -\frac{S^2}{4R} & -\frac{S^3}{8R} \\ -\frac{\sin\Lambda}{R} & -\frac{\cos\Lambda}{R} & -\sin\Lambda\cos\Lambda & 1 & 0 & 0 & S & \frac{3S^2}{R} \end{bmatrix} \tag{B.8}$$

$$\lfloor D_1 \rfloor = \lfloor 0 \quad 0 \quad 0 \quad 1 \quad \eta^2/R \quad \eta^3/R \quad 2\eta \quad 3\eta^2 \rfloor \, [A^{-1}] \qquad \text{(B.9)}$$

$$\lfloor D_2 \rfloor = \lfloor 0 \quad 0 \quad 1 \quad -\eta/R \quad 2\eta \quad 3\eta^2 \quad -\eta^2/R \quad -\eta^3/R \rfloor \, [A^{-1}] \qquad \text{(B.10)}$$

$$\lfloor D_3 \rfloor = \lfloor 0 \quad 0 \quad 0 \quad 1/R \quad -2 \quad -6\eta \quad 2\eta/R \quad 3\eta^2/R \rfloor \, [A^{-1}] \qquad \text{(B.11)}$$

$$[N(\eta)] = \begin{bmatrix} \cos\lambda & -\sin\lambda & -R(1-\cos\lambda\cos\Lambda) & \eta & 0 & 0 & \eta^2 & \eta^3 \\ \sin\lambda & \cos\lambda & R\sin\lambda\cos\Lambda & 0 & \eta^2 & \eta^3 & 0 & 0 \\ 0 & 0 & 1 & -\frac{\eta}{R} & 2\eta & 3\eta^2 & \frac{-\eta^2}{R} & \frac{-\eta^3}{R} \end{bmatrix} [A^{-1}] \qquad \text{(B.12)}$$

$$[m] = [A^{-1}]^T \begin{bmatrix} m_{11} & & & & \text{SYMMETRIC} & & & \\ 0 & m_{22} & & & & & & \\ m_{31} & 0 & m_{33} & & & & & \\ 0 & m_{42} & 0 & m_{44} & & & & \\ 0 & m_{52} & 0 & m_{54} & m_{55} & & & \\ m_{61} & 0 & m_{63} & 0 & 0 & m_{66} & & \\ m_{71} & 0 & m_{73} & 0 & 0 & m_{76} & m_{77} & \\ 0 & m_{82} & 0 & m_{84} & m_{85} & 0 & 0 & m_{88} \end{bmatrix} [A^{-1}] \qquad \text{(B.13)}$$

where

$$m_{11} = \tilde{m} S$$

$$m_{31} = \tilde{m} R(-2R\sin\Lambda + S\cos\Lambda)$$

$$m_{61} = \tilde{m} R^4(-2\Lambda^3\cos\Lambda + 6\Lambda^2\sin\Lambda + 12\Lambda\cos\Lambda - 12\sin\Lambda)$$

$$m_{71} = \tilde{m} R^3(2\Lambda^2\sin\Lambda + 4\Lambda\cos\Lambda - 4\sin\Lambda)$$

$$m_{22} = \tilde{m} S$$

$$m_{42} = -\tilde{m} R^2(-2\Lambda\cos\Lambda + 2\sin\Lambda)$$

$$m_{52} = \tilde{m} R^3(2\Lambda^2\sin\Lambda + 4\Lambda\cos\Lambda - 4\sin\Lambda)$$

$$m_{82} = -\tilde{m} R^4(-2\Lambda^3\cos\Lambda + 6\Lambda^2\sin\Lambda + 12\Lambda\cos\Lambda - 12\sin\Lambda)$$

$$m_{33} = \widetilde{m}\, R^{2}(S + S\cos^{2}\Lambda - 2R\,\mathrm{SIN}\,2\Lambda) + \widetilde{I}\,S$$

$$m_{63} = \widetilde{m}\, R^{5}(-2\Lambda^{3}\cos\Lambda + 6\Lambda^{2}\mathrm{SIN}\Lambda + 12\Lambda\cos\Lambda - 12\,\mathrm{SIN}\Lambda)\cos\Lambda + \widehat{I}S^{3}/4$$

$$m_{73} = -\widetilde{m}\,R\left[(S^{3}/12) - R^{3}\cos\Lambda\,(2\Lambda^{2}\mathrm{SIN}\Lambda + 4\Lambda\cos\Lambda - 4\,\mathrm{SIN}\Lambda)\right] - \frac{\widetilde{I}S^{3}}{R\cdot 12}$$

$$m_{44} = \left(\widetilde{m} + \frac{\widetilde{I}}{R}\right)\frac{S^{3}}{12} \qquad , \qquad m_{54} = -\frac{\widetilde{I}S^{3}}{6R}$$

$$m_{84} = \left(\widetilde{m} + \frac{\widehat{I}}{R}\right)\frac{S^{3}}{80} \qquad , \qquad m_{55} = \frac{\widetilde{m}S^{5}}{80} + \frac{\widetilde{I}S^{3}}{3}$$

$$m_{85} = -\frac{\widehat{I}S^{5}}{40R} \qquad , \qquad m_{66} = \frac{\widetilde{m}S^{7}}{448} + \frac{9\widetilde{I}S^{5}}{80}$$

$$m_{76} = -\frac{3\widetilde{I}S^{5}}{80R} \qquad , \qquad m_{77} = \left(\widetilde{m} + \frac{\widetilde{I}}{R^{2}}\right)\frac{S^{5}}{80}$$

$$m_{88} = \left(\widetilde{m} + \frac{\widehat{I}}{R^{2}}\right)\frac{S^{7}}{448}$$

$$[k] = [A^{-1}]^{T}\left[\begin{array}{c|ccccc}
0_{3\times 3} & & & & \text{SYMMETRIC} & \\
\hline
 & \left(k_1 + \frac{k_2}{R^2}\right)S & & & & \\
0_{5\times 3} & \left(\frac{k_1S^3}{12R} - \frac{2k_2S}{R}\right) & \left(\frac{k_1S^5}{80R^2} + 4k_2S\right) & & & \\
 & 0 & 0 & \left(\frac{k_1S^7}{448R^2} + 3k_2S^3\right) & & \\
 & 0 & 0 & \left(\frac{k_1S^5}{40R} - \frac{k_2S^3}{R}\right) & \left(k_1 + \frac{k_2}{R^2}\right)\frac{S^3}{3} & \\
 & \left(k_1 + \frac{k_2}{R^2}\right)\frac{S^3}{4} & \left(\frac{3k_1S^5}{80R} - \frac{k_2S^3}{12R}\right) & 0 & 0 & \left(k_1 + \frac{k_2}{R^2}\right)\frac{9S^5}{80}
\end{array}\right][A^{-1}] \qquad \text{(B.14)}$$

where, in Eqs. B.13 and B.14 , $\widetilde{m} = \rho_0\, b\, h$, $\widehat{I} = \rho_0 \frac{bh^3}{12}$ , $k_1 = E\,b\,h$, and $k_2 = \frac{Ebh^3}{12}$

$\rho_0$ = mass density per unit volume of the undeformed beam

$b$ =the width of the beam

$h$ =the thickness of the beam

$E$ =Young's modulus

### B.1.2 Bernoulli-Euler Type Curved Beam Element with LC Assumed-Displacement Functions

$$\{\underline{u}\} = \begin{Bmatrix} v \\ w \end{Bmatrix} = \underset{2\times 6}{[U(\eta)]}\; \underset{6\times 1}{\{\beta\}} \tag{B.15}$$

$$\{q\} = \lfloor v_i \quad w_i \quad \psi_i \quad v_{i+1} \quad w_{i+1} \quad \psi_{i+1} \rfloor^T = \underset{6\times 6}{[A]}\,\{\beta\} \tag{B.16}$$

$$\varepsilon_o = \underset{1\times 6}{\lfloor D_1 \rfloor}\,\{q\} + \frac{1}{2}\lfloor q \rfloor \underset{6\times 1}{\{D_2\}}\, \underset{1\times 6}{\lfloor D_2 \rfloor}\,\{q\} \tag{B.17}$$

$$\kappa = \underset{1\times 6}{\lfloor D_3 \rfloor}\,\{q\} \tag{B.18}$$

$$[m] = \int_{\eta_i}^{\eta_{i+1}} \underset{6\times 3}{[N(\eta)]^T}\, \underset{3\times 3}{[B]}\, \underset{3\times 6}{[N(\eta)]}\, d\eta \tag{B.19}$$

$$\{f\} = \int_{\eta_i}^{\eta_{i+1}} [N(\eta)]^T \begin{Bmatrix} F_v \\ F_w \\ \underset{\sim}{M} \end{Bmatrix} d\eta \tag{B.20}$$

$$\{p\} = \int_{\eta_i}^{\eta_{i+1}} (\{D_1\} L + \{D_3\} M)\, d\eta \tag{B.21}$$

$$[h] = \int_{\eta_i}^{\eta_{i+1}} \{D_2\} \lfloor D_2 \rfloor L \, d\eta \tag{B.22}$$

$$[k] = \int_{\eta_i}^{\eta_{i+1}} \left( \{D_1\} Ebh \lfloor D_1 \rfloor + \{D_3\} \frac{Ebh^3}{12} \lfloor D_3 \rfloor \right) d\eta \tag{B.23}$$

$$\begin{aligned} \{f_q^{NL}\} = -\Big\langle & \int_{\eta_i}^{\eta_{i+1}} Ebh \left( \frac{1}{2} \lfloor q \rfloor \{D_2\} \lfloor D_2 \rfloor \{q\} \right) \{D_1\}\, d\eta \\ & + \int_{\eta_i}^{\eta_{i+1}} Ebh \left( \lfloor D_1 \rfloor \{q\} + \frac{1}{2} \lfloor q \rfloor \{D_2\} \lfloor D_2 \rfloor \{q\} \right) \{D_2\} \lfloor D_2 \rfloor\, d\eta \{q\} \Big\rangle \end{aligned} \tag{B.24}$$

$$\{f_p^L\} = \iint_A \int_{\eta_i}^{\eta_{i+1}} \left( E\varepsilon^p \{D_1\} + \zeta E \varepsilon^p \{D_3\} \right) dV_n \tag{B.25}$$

$$\{f_p^{NL}\} = \iint_A \int_{\eta_i}^{\eta_{i+1}} E\varepsilon^p \{D_2\} \lfloor D_2 \rfloor \, dV_n \{q\} \tag{B.26}$$

In the folowing, the matrices $[U(\eta)]$, $[A]$, $(\lfloor D_i \rfloor, i = 1, 2, 3)$, $[N(\eta)]$,and $[B]$ appearing in the above expressions are listed for an arbitrarily-curved beam element ( see Fig. 5 ) :

$$[U(\eta)]=\begin{bmatrix} \cos\phi & \sin\phi & -z\cos\phi+y\sin\phi & \eta & 0 & 0 \\ -\sin\phi & \cos\phi & z\sin\phi+y\cos\phi & 0 & \eta^2 & \eta^3 \end{bmatrix} \tag{B.27}$$

$$[A]=\begin{bmatrix} \cos\phi_i & \sin\phi_i & 0 & 0 & 0 & 0 \\ -\sin\phi_i & \cos\phi_i & 0 & 0 & 0 & 0 \\ 0 & 0 & 1 & 0 & 0 & 0 \\ \cos\phi_{i+1} & \sin\phi_{i+1} & y_{i+1}\sin\phi_{i+1} & \eta_{i+1} & 0 & 0 \\ -\sin\phi_{i+1} & \cos\phi_{i+1} & y_{i+1}\cos\phi_{i+1} & 0 & \eta_{i+1}^2 & \eta_{i+1}^3 \\ 0 & 0 & 1 & -\frac{\eta_{i+1}}{R_{i+1}} & 2\eta_{i+1} & 3\eta_{i+1}^2 \end{bmatrix} \tag{B.28}$$

$$\lfloor D_1 \rfloor = \lfloor 0 \quad 0 \quad 0 \quad 1 \quad \eta^2/R \quad \eta^3/R \rfloor [A^{-1}] \tag{B.29}$$

$$\lfloor D_2 \rfloor = \lfloor 0 \quad 0 \quad 1 \quad -\frac{\eta}{R} \quad 2\eta \quad 3\eta^2 \rfloor [A^{-1}] \tag{B.30}$$

$$\lfloor D_3 \rfloor = \lfloor 0 \quad 0 \quad 0 \quad \frac{1}{R}-\eta\frac{\partial^2\phi}{\partial\eta^2} \quad -2 \quad -6\eta \rfloor [A^{-1}] \tag{B.31}$$

$$[N(\eta)]=\begin{bmatrix} \cos\phi & \sin\phi & -z\cos\phi+y\sin\phi & \eta & 0 & 0 \\ -\sin\phi & \cos\phi & z\sin\phi+y\cos\phi & 0 & \eta^2 & \eta^3 \\ 0 & 0 & 1 & -\eta/R & 2\eta & 3\eta^2 \end{bmatrix} [A^{-1}] \tag{B.32}$$

$$[B]=\begin{bmatrix} \tilde{m} & & 0 \\ & \tilde{m} & \\ 0 & & \tilde{I} \end{bmatrix} \tag{B.33}$$

For application to a circular ring element ( see Fig. B.1 ), the matrices $[U(\eta)]$, $[A]$, $(\lfloor D_i \rfloor, i=1,2,3)$, $[N(\eta)]$, $[m]$ , and $[k]$ are listed in the following:

$$[U(\eta)]=\begin{bmatrix} \cos\lambda & -\sin\lambda & -R(1-\cos\lambda\cos\Lambda) & \eta & 0 & 0 \\ +\sin\lambda & \cos\lambda & R\sin\lambda\cos\Lambda & 0 & \eta^2 & \eta^3 \end{bmatrix} \tag{B.34}$$

$$[A] = \begin{bmatrix} \cos\Lambda & \sin\Lambda & -R(1-\cos^2\Lambda) & -S/2 & 0 & 0 \\ -\sin\Lambda & \cos\Lambda & -R\sin\Lambda\cos\Lambda & 0 & S^2/4 & -S^3/8 \\ 0 & 0 & 1 & \frac{S}{2R} & -S & 3S^2/4 \\ \cos\Lambda & -\sin\Lambda & -R(1-\cos^2\Lambda) & S/2 & 0 & 0 \\ \sin\Lambda & \cos\Lambda & +R\sin\Lambda\cos\Lambda & 0 & S^2/4 & S^3/8 \\ 0 & 0 & 1 & -\frac{S}{2R} & S & 3S^2/4 \end{bmatrix} \tag{B.35}$$

$$\lfloor D_1 \rfloor = \lfloor 0 \quad 0 \quad 0 \quad 1 \quad \eta^2/R \quad \eta^3/R \rfloor [A^{-1}] \tag{B.36}$$

$$\lfloor D_2 \rfloor = \lfloor 0 \quad 0 \quad 1 \quad -\eta/R \quad 2\eta \quad 3\eta^2 \rfloor [A^{-1}] \tag{B.37}$$

$$\lfloor D_3 \rfloor = \lfloor 0 \quad 0 \quad 0 \quad 1/R \quad -2 \quad -6\eta \rfloor [A^{-1}] \tag{B.38}$$

$$[N(\eta)] = \begin{bmatrix} \cos\lambda & -\sin\lambda & -R(1-\cos\lambda\cos\Lambda) & \eta & 0 & 0 \\ \sin\lambda & \cos\lambda & R\sin\lambda\cos\Lambda & 0 & \eta^2 & \eta^3 \\ 0 & 0 & 1 & -\eta/R & 2\eta & 3\eta^2 \end{bmatrix} [A^{-1}] \tag{B.39}$$

$$[m] = [A^{-1}]^T \begin{bmatrix} m_{11} & & & & & \\ 0 & m_{22} & & \text{SYMMETRIC} & & \\ m_{31} & 0 & m_{33} & & & \\ 0 & m_{42} & 0 & m_{44} & & \\ 0 & m_{52} & 0 & m_{54} & m_{55} & \\ m_{61} & 0 & m_{63} & 0 & 0 & m_{66} \end{bmatrix} [A^{-1}] \tag{B.40}$$

where

$$m_{11} = \tilde{m} S$$

$$m_{31} = \tilde{m} R(-2R\sin\Lambda + S\cos\Lambda)$$

$$m_{61} = \tilde{m} R^4(-2\Lambda^3\cos\Lambda + 6\Lambda^2\sin\Lambda + 12\Lambda\cos\Lambda - 12\sin\Lambda)$$

$$m_{22} = \tilde{m} S$$

$$m_{42} = -\tilde{m} R(-2\Lambda\cos\Lambda + 2\sin\Lambda)$$

$$m_{52} = \tilde{m} R^3(2\Lambda^2\sin\Lambda + 4\Lambda\cos\Lambda - 4\sin\Lambda)$$

$$m_{33} = \widetilde{m}\, R^2 (S + S\cos^2\Lambda - 2R\,\text{SIN}\, 2\Lambda\,) + \widetilde{I}\,S$$

$$m_{63} = \widetilde{m} R^5 \cos\Lambda\,( -2\Lambda^3 \cos\Lambda + 6\Lambda^2 \text{SIN}\Lambda + 12\Lambda\cos\Lambda - 12\,\text{SIN}\Lambda) + \widetilde{I} S^3/4$$

$$m_{44} = (\widetilde{m} + \widetilde{I}/R\,)\,S^3/12$$

$$m_{54} = -\,\widetilde{I}\,S^3/(6R)$$

$$m_{55} = \widetilde{m}\, S^5/80 \;+\; \widetilde{I}\,S^3/3$$

$$m_{66} = \widetilde{m}\, S^7/448 + 9\,\widetilde{I}\,S^5/80$$

$$[k] = [A^{-1}]^T \left[\begin{array}{c|ccc} 0_{3\times3} & & \text{SYMMETRIC} & \\ & (k_1 + \frac{k_2}{R^2})S & & \\ 0_{3\times3} & (\frac{k_1 S^3}{12R} - \frac{2k_2 S}{R}) & (\frac{k_1 S^5}{80R^2} + 4k_2 S) & \\ & 0 & 0 & (\frac{k_1 S^7}{448R^2} + 3k_2 S^3) \end{array}\right] [A^{-1}] \tag{B.41}$$

where

$$\widetilde{m} = \rho_0\, b\, h\,, \quad \widetilde{I} = \rho_0\, \frac{b h^3}{12}\,, \quad k_1 = E b h,$$

The corresponding quantities for a straight beam element (see Fig. B.2 ) can be obtained by setting $\frac{1}{R} = 0$, $\lambda = 0$, and $R d\lambda = dy$ in the preceeding equations. Thus, one obtains

$$[U(y)] = \begin{bmatrix} 1 & 0 & 0 & y & 0 & 0 \\ 0 & 1 & y & 0 & y^2 & y^3 \end{bmatrix} \tag{B.42}$$

$$[A] = \begin{bmatrix} 1 & 0 & 0 & -S/2 & 0 & 0 \\ 0 & 1 & -S/2 & 0 & S^2/4 & -S^3/8 \\ 0 & 0 & 1 & 0 & -S & 3S^2/4 \\ 1 & 0 & 0 & S/2 & 0 & 0 \\ 0 & 1 & S/2 & 0 & S^2/4 & S^3/8 \\ 0 & 0 & 0 & 0 & S & 3S^2/4 \end{bmatrix} \tag{B.43}$$

$$\lfloor D_1 \rfloor = \lfloor 0 \quad 0 \quad 0 \quad 1 \quad 0 \quad 0 \rfloor \, [A^{-1}] \tag{B.44}$$

$$\lfloor D_2 \rfloor = \lfloor 0 \quad 0 \quad 1 \quad 0 \quad 2y \quad 3y^2 \rfloor \, [A^{-1}] \tag{B.45}$$

$$\lfloor D_3 \rfloor = \lfloor 0 \quad 0 \quad 0 \quad 0 \quad -2 \quad -6y \rfloor \, [A^{-1}] \tag{B.46}$$

$$[N(\eta)] = \begin{bmatrix} 1 & 0 & 0 & y & 0 & 0 \\ 0 & 1 & y & 0 & y^2 & y^3 \\ 0 & 0 & 1 & 0 & 2y & 3y^2 \end{bmatrix} [A^{-1}] \tag{B.47}$$

$$[m] = [A^{-1}]^T \begin{bmatrix} \tilde{m}S & & & \text{SYMMETRIC} & & \\ 0 & \tilde{m}S & & & & \\ 0 & 0 & \frac{\tilde{m}S^3}{12} + \tilde{I}S & & & \\ 0 & 0 & 0 & \frac{\tilde{m}S^3}{12} & & \\ 0 & \frac{\tilde{m}S^3}{12} & 0 & 0 & \frac{\tilde{m}S^5}{80} + \frac{\tilde{I}S^3}{3} & \\ 0 & 0 & \frac{\tilde{m}S^5}{80} + \frac{\tilde{I}S^3}{4} & 0 & 0 & \frac{\tilde{m}S^7}{448} + \frac{9\tilde{I}S^5}{80} \end{bmatrix} [A^{-1}] \tag{B.48}$$

$$[k] = [A^{-1}]^T \left[ \begin{array}{c:ccc} 0_{3\times3} & & \text{SYMMETRIC} & \\ \hdashline & k_1 S & & \\ 0_{3\times3} & 0 & 4k_2 S & \\ & 0 & 0 & 3k_2 S^3 \end{array} \right] [A^{-1}] \tag{B.49}$$

## B.2 Timoshenko-Type Curved Beam Element

For the Timoshenko-type curved beam element, only the element properties with the linear displacement interpolation functions are presented here. The element properties with higher order assumed displacement functions may be derived in a similar manner as described in Subsection 4.4 .

$$\{\underline{u}\} = \begin{Bmatrix} v \\ w \\ \theta \end{Bmatrix} = [\underset{3\times 6}{U(\eta)}]\{\beta\} \qquad (4.54)$$

$$\{q\} = \lfloor v_i \quad w_i \quad \theta_i \quad v_{i+1} \quad w_{i+1} \quad \theta_{i+1} \rfloor^T = [\underset{6\times 6}{A}]\{\beta\} \qquad (4.55)$$

$$\varepsilon_o = \lfloor \underset{1\times 6}{D_1} \rfloor \{q\} + \frac{1}{2}\lfloor q \rfloor \{\underset{6\times 1}{D_2}\}\lfloor \underset{1\times 6}{D_2} \rfloor \{q\} \qquad (4.58)$$

$$\kappa = \lfloor \underset{1\times 6}{D_3} \rfloor \{q\} \qquad (4.58)$$

$$\gamma_o = \lfloor \underset{1\times 6}{D_4} \rfloor \{q\} \qquad (4.58)$$

$$[m] = \int_{\eta_i}^{\eta_{i+1}} [\underset{6\times 3}{N(\eta)}]^T [\underset{3\times 3}{B}] [\underset{3\times 6}{N(\eta)}]\, d\eta \qquad (4.61a)$$

$$\{f\} = \int_{\eta_i}^{\eta_{i+1}} [N(\eta)]^T \begin{Bmatrix} F_v \\ F_w \\ \underset{\sim}{M} \end{Bmatrix} d\eta \qquad (4.61a)$$

$$\{p\} = \int_{\eta_i}^{\eta_{i+1}} (\{D_1\}L + \{D_3\}M + \{D_4\}S)\, d\eta \qquad (4.61a)$$

$$[h] = \int_{\eta_i}^{\eta_{i+1}} \{D_2\}\lfloor D_2 \rfloor L\, d\eta \qquad (4.61a)$$

$$[k] = \int_{\eta_i}^{\eta_{i+1}} (\{D_1\}Ebh\lfloor D_1 \rfloor + \{D_3\}\frac{Ebh^3}{12}\lfloor D_3 \rfloor + \{D_4\}Gbh\lfloor D_4 \rfloor)\, d\eta \qquad (4.61a)$$

$$\begin{aligned} \{f_q^{NL}\} = -\langle &\int_{\eta_i}^{\eta_{i+1}} Ebh\left(\frac{1}{2}\lfloor q \rfloor \{D_2\}\lfloor D_2 \rfloor \{q\}\right)\{D_1\}\, d\eta \\ &+ \int_{\eta_i}^{\eta_{i+1}} Ebh\left(\lfloor D_1 \rfloor \{q\} + \frac{1}{2}\lfloor q \rfloor \{D_2\}\lfloor D_2 \rfloor \{q\}\right)\{D_2\}\lfloor D_2 \rfloor\, d\eta\, \{q\}\rangle \end{aligned} \qquad (4.62a)$$

$$\{f_p^L\} = \iint_A \int_{\eta_i}^{\eta_{i+1}} (E\varepsilon^p\{D_1\} + \zeta E\varepsilon^p\{D_3\} + G\gamma^p\{D_4\})\, dV_n \qquad (4.62a)$$

$$\{f_p^{NL}\} = \iint_A \int_{\eta_i}^{\eta_{i+1}} E\varepsilon^p\{D_2\}\lfloor D_2 \rfloor\, dV_n\, \{q\} \qquad (4.62a)$$

In the following, the matrices $[U(\eta)]$, $[A]$, $(\lfloor D_i \rfloor, i = 1, 2, 3, 4)$, $[N(\eta)]$, and $[B]$ appearing in the above expressions are listed for an arbitrarily-curved beam element ( see Fig. 5 ) :

$$[U(\eta)] = \begin{bmatrix} \cos\phi & \sin\phi & -z\cos\phi + y\sin\phi & \eta & 0 & 0 \\ -\sin\phi & \cos\phi & z\sin\phi + y\cos\phi & 0 & 0 & 0 \\ 0 & 0 & 0 & 0 & 1 & \eta \end{bmatrix} \qquad (4.54)$$

$$[A] = \begin{bmatrix} \cos\phi_i & \sin\phi_i & 0 & 0 & 0 & 0 \\ -\sin\phi_i & \cos\phi_i & 0 & 0 & 0 & 0 \\ 0 & 0 & 0 & 0 & 1 & 0 \\ \cos\phi_{i+1} & \sin\phi_{i+1} & y_{i+1}\sin\phi_{i+1} & \eta_{i+1} & 0 & 0 \\ -\sin\phi_{i+1} & \cos\phi_{i+1} & y_{i+1}\cos\phi_{i+1} & 0 & 0 & 0 \\ 0 & 0 & 0 & 0 & 1 & \eta_{i+1} \end{bmatrix} \tag{B.50}$$

$$\lfloor D_1 \rfloor = \lfloor 0 \quad 0 \quad 0 \quad 1 \quad 0 \quad 0 \rfloor \, [A^{-1}] \tag{B.51}$$

$$\lfloor D_2 \rfloor = \lfloor 0 \quad 0 \quad 1 \quad -\eta/R \quad 0 \quad 0 \rfloor \, [A^{-1}] \tag{B.52}$$

$$\lfloor D_3 \rfloor = \lfloor 0 \quad 0 \quad 0 \quad 0 \quad 0 \quad 1 \rfloor \, [A^{-1}] \tag{B.53}$$

$$\lfloor D_4 \rfloor = \lfloor 0 \quad 0 \quad 1 \quad -\eta/R \quad 1 \quad \eta \rfloor \, [A^{-1}] \tag{B.54}$$

$$[N(\eta)] = \begin{bmatrix} \cos\phi & \sin\phi & -z\cos\phi + y\sin\phi & \eta & 0 & 0 \\ -\sin\phi & \cos\phi & z\sin\phi + y\cos\phi & 0 & 0 & 0 \\ 0 & 0 & 0 & 0 & 1 & \eta \end{bmatrix} [A^{-1}] \tag{B.55}$$

$$[B] = \begin{bmatrix} \tilde{m} & & 0 \\ & \tilde{m} & \\ 0 & & \tilde{I} \end{bmatrix} \tag{B.56}$$

For application to a circular ring element ( see Fig. B.1 ), the matrices $[U(\eta)]$, $[A]$, $(\lfloor D_i \rfloor,\ i = 1, 2, 3, 4)$, $[m]$ ,and $[k]$ are listed in the following:

$$[U(\eta)] = \begin{bmatrix} \cos\lambda & -\sin\lambda & -R(1 - \cos\lambda\cos\Lambda) & \eta & 0 & 0 \\ \sin\lambda & \cos\lambda & R\sin\lambda\cos\Lambda & 0 & 0 & 0 \\ 0 & 0 & 0 & 0 & 1 & \eta \end{bmatrix} \tag{B.57}$$

$$[A] = \begin{bmatrix} \cos\Lambda & \sin\Lambda & -R(1-\cos^2\Lambda) & -\frac{S}{2} & 0 & 0 \\ -\sin\Lambda & \cos\Lambda & -R\sin\Lambda\cos\Lambda & 0 & 0 & 0 \\ 0 & 0 & 0 & 0 & 1 & -\frac{S}{2} \\ \cos\Lambda & -\sin\Lambda & -R(1-\cos^2\Lambda) & \frac{S}{2} & 0 & 0 \\ \sin\Lambda & \cos\Lambda & R\sin\Lambda\cos\Lambda & 0 & 0 & 0 \\ 0 & 0 & 0 & 0 & 1 & \frac{S}{2} \end{bmatrix} \tag{B.58}$$

$$\lfloor D_1 \rfloor = \lfloor 0 \quad 0 \quad 0 \quad 1 \quad 0 \quad 0 \rfloor \, [A^{-1}] \tag{B.59}$$

$$\lfloor D_2 \rfloor = \lfloor 0 \quad 0 \quad 1 \quad -\eta/R \quad 0 \quad 0 \rfloor \, [A^{-1}] \tag{B.60}$$

$$\lfloor D_3 \rfloor = \lfloor 0 \quad 0 \quad 0 \quad 0 \quad 0 \quad 1 \rfloor \, [A^{-1}] \tag{B.61}$$

$$\lfloor D_4 \rfloor = \lfloor 0 \quad 0 \quad 1 \quad -\eta/R \quad 1 \quad \eta \rfloor \, [A^{-1}] \tag{B.62}$$

$$[m] = [A^{-1}]^T \begin{bmatrix} m_{11} & & & & & \\ 0 & m_{22} & & \text{SYMMETRIC} & & \\ m_{31} & 0 & m_{33} & & & \\ 0 & m_{42} & 0 & m_{44} & & \\ 0 & 0 & 0 & 0 & m_{55} & \\ 0 & 0 & 0 & 0 & 0 & m_{66} \end{bmatrix} [A^{-1}] \tag{B.63}$$

where

$m_{11} = \tilde{m}\, s$

$m_{31} = \tilde{m} R(-2R\sin\Lambda + S\cos\Lambda)$

$m_{22} = \tilde{m}\, S$

$m_{42} = -\tilde{m} R^2(-2\Lambda\cos\Lambda + 2\sin\Lambda)$

$m_{33} = \tilde{m} R^2(S + S\cos^2\Lambda - 2R\sin 2\Lambda)$

$m_{44} = \tilde{m}\, S^3/12$

$m_{55} = \tilde{I}\, S$

$m_{66} = \tilde{I}\, S^3/12$

$$[k] = [A^{-1}]^{T} \left[\begin{array}{c:cccc} 0_{2\times 2} & & & \text{SYMMETRIC} & \\ & GbhS & & & \\ 0_{4\times 2} & 0 & \left(EbhS + \frac{Gbh}{R^2}\frac{S^3}{12}\right) & & \\ & GbhS & 0 & GbhS & \\ & 0 & Gbh\left(-\frac{S^3}{12R}\right) & 0 & \frac{Ebh^3S}{12} + \frac{GbhS^3}{12} \end{array}\right] [A^{-1}] \qquad \text{(B.64)}$$

For application to a straight beam element (see Fig. B.2), the matrices $[U(y)]$, $[A]$, $(\lfloor D_i \rfloor,\ i = 1,2,3,4)$, $[m]$, and $[k]$ are listed in the following:

$$[U(y)] = \begin{bmatrix} 1 & 0 & 0 & y & 0 & 0 \\ 0 & 1 & y & 0 & 0 & 0 \\ 0 & 0 & 0 & 0 & 1 & y \end{bmatrix} \qquad \text{(B.65)}$$

$$[A] = \begin{bmatrix} 1 & 0 & 0 & -S/2 & 0 & 0 \\ 0 & 1 & -S/2 & 0 & 0 & 0 \\ 0 & 0 & 0 & 0 & 1 & S/2 \\ 1 & 0 & 0 & S/2 & 0 & 0 \\ 0 & 1 & S/2 & 0 & 0 & 0 \\ 0 & 0 & 0 & 0 & 1 & S/2 \end{bmatrix} \qquad \text{(B.66)}$$

$$\lfloor D_1 \rfloor = \lfloor 0 \quad 0 \quad 0 \quad 1 \quad 0 \quad 0 \rfloor \, [A^{-1}] \qquad \text{(B.67)}$$

$$\lfloor D_2 \rfloor = \lfloor 0 \quad 0 \quad 1 \quad 0 \quad 0 \quad 0 \rfloor \, [A^{-1}] \qquad \text{(B.68)}$$

$$\lfloor D_3 \rfloor = \lfloor 0 \quad 0 \quad 0 \quad 0 \quad 0 \quad 1 \rfloor \, [A^{-1}] \qquad \text{(B.69)}$$

$$\lfloor D_4 \rfloor = \lfloor 0 \quad 0 \quad 1 \quad 0 \quad 1 \quad \eta \rfloor \, [A^{-1}] \qquad \text{(B.70)}$$

$$[m] = [A^{-1}]^{T} \begin{bmatrix} \tilde{m}S & & & & & \\ & \tilde{m}S & & & 0 & \\ & & \tilde{m}\frac{S^3}{12} & & & \\ & & & \tilde{m}\frac{S^3}{12} & & \\ & 0 & & & \tilde{I}S & \\ & & & & & \tilde{I}\frac{S^3}{12} \end{bmatrix} [A^{-1}] \qquad \textbf{(B.71)}$$

$$[k] = [A^{-1}]^{T} \left[ \begin{array}{c:cccc} 0_{2\times2} & & & \text{SYMMETRIC} & \\ & GbhS & & & \\ 0_{4\times2} & 0 & EbhS & & \\ & GbhS & 0 & GbhS & \\ & 0 & 0 & 0 & \left(\frac{Ebh^3}{12}S + \frac{GbhS^3}{12}\right) \end{array} \right] [A^{-1}] \qquad \textbf{(B.72)}$$

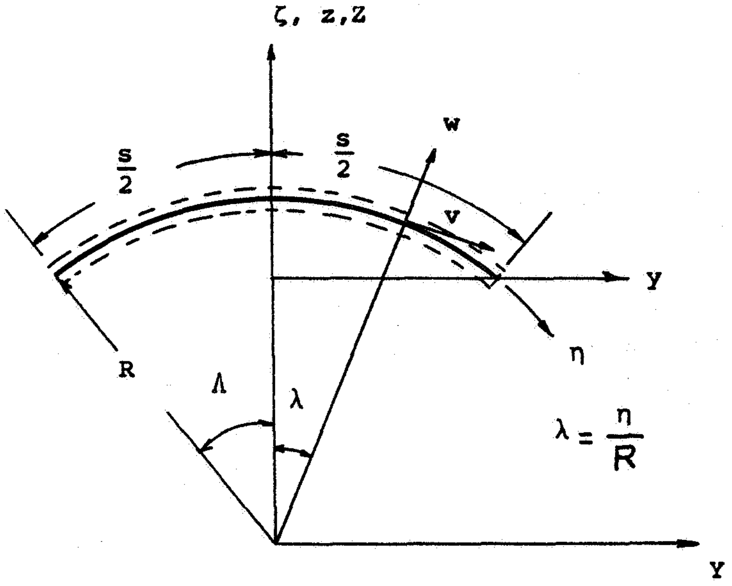
ζ, z,Z
s/2
s/2
w
v
y
η
R
Λ
λ
λ = η/R
Y

FIG. B.1 SIMPLE CIRCULAR RING ELEMENT

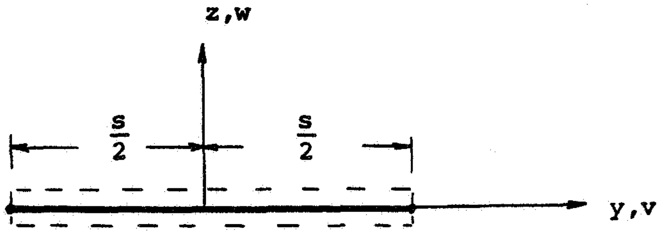

FIG. B.2 STRAIGHT BEAM ELEMENT

# APPENDIX C

## MIXED FINITE-ELEMENT MODEL BASED UPON REISSNER'S VARIATIONAL PRINCIPLE

This appendix contains, for the purpose of demonstrating the use of different variational principles, the formulation of the equation of motion based on a mixed finite-element model: (1) by assuming a displacement field which is continuous over the entire solid, (2) by assuming a stress field for each individual element. However, no evaluation of this model is made.

In the Principle of Virtual Work, the independent quantity which is subject to variation is the displacement; in Reissner's variational principle, the independent quantities which are subject to variation are stress and displacement. Reissner's variational principle may be stated mathematically as follows (Ref. 159):

$$\delta \Pi_R = \iiint_{V_o} \delta (S^{ij} \gamma_{ij})\, dV_o - \delta B - \delta W + \delta I - \iint_{A_{ov}} (v_i - \underset{\sim}{v_i})\, \delta T^i\, dA_o = 0 \tag{C.1}$$

where

$$\delta B = \iiint_{V_o} \gamma_{ij}\, \delta S^{ij}\, dV_o = \iiint_{V_o} (C_{ijkl} S^{kl} + \gamma^{p}_{ij})\, \delta S^{ij}\, dV_o$$

= the variation of the complementary work done in an arbitrary infinitesimal virtual stress $\delta S^{ij}$ increment (C.2)

$$\gamma_{ij} = \frac{1}{2} ( v_{i,j} + v_{j,i} + v_{a,i}\, v^{a}_{,j} ) \tag{C.3}$$

$A_{ov}$ = portion of $A_o$ over which the displacement $v_i$ is prescribed

$C_{ijkl}$ = elastic compliance tensor

and $\delta W, \delta I, S^{ij}, T^i, \gamma^{p}_{ij}$ are defined as previously stated in Section 2.

In applying Eq. C.1 to the finite-element analysis for a solid continuum which is conceptually subdivided into N discrete elements, one can write

$$\delta \Pi_R = \sum_{n=1}^{N} \left\{ \iiint_{V_n} \delta ( S^{ij} \gamma_{ij} ) \, dV_n - \delta B_n - \delta W_n + \delta I_n - \iint_{A_v} ( v_i - \underset{\sim}{v_i} ) \delta T^i dA_v - C_n \right\} \tag{C.4}$$

where the term $C_n$ arises from a possible jump function of the derivative of $v_i$ across the interelement boundaries. If the assumed displacement functions are such that $v_i$ and $v_{i,j}$ are continuous across the interelement boundaries, then $C_n = 0$ (Ref. 7).

The assumed approximate stress interpolation functions which need not satisfy the equilibrium condition for each individual element are expressed using a finite number of independent parameters $\{\alpha\}$:

$$S^{ij} = \lfloor R^{ij} \rfloor \{\alpha\} \tag{C.5}$$

and the displacements are approximated by interpolation functions [N] to satisfy the interelement displacement and slope compatibility conditions anchored to nodal generalized coordinates $\{q\}$:

$$\{v\} = [N] \{q\} \tag{C.6}$$

By applying Eq. C.6, Eq. C.3 becomes

$$\gamma_{ij} = \lfloor D_{ij} \rfloor \{q\} + \frac{1}{2} \lfloor q \rfloor \{D_{ai}\} \lfloor D_j^a \rfloor \{q\} \tag{C.7}$$

Using Eqs. C.5, C.6, and C.7, and if the boundary displacement can be made to satisfy the prescribed value, Eq. C.4 may be expressed in the form

$$
\begin{aligned}
\delta\Pi_R = \sum_{n=1}^{N}\Big\{ & \lfloor\delta\alpha\rfloor \Big\langle -\iiint_{V_n}\{R^{ij}\}\,C_{ijkl}\lfloor R^{kl}\rfloor\, dV_n\,\{\alpha\} - \iiint_{V_n}\{R^{ij}\}\,\gamma^{p}_{ij}\, dV_n \\
& + \iiint_{V_n}\{R^{ij}\}\left(\lfloor D_{ij}\rfloor\{q\} + \tfrac{1}{2}\lfloor q\rfloor\{D_{ai}\}\lfloor D^{a}_{j}\rfloor\{q\}\right) dV_n \Big\rangle \\
& + \lfloor\delta q\rfloor \Big\langle \iiint_{V_n}\{D_{ij}\}\left(\lfloor R^{ij}\rfloor\{\alpha\}\right) dV_n + \iiint_{V_n}\{D_{ai}\}\lfloor D^{a}_{j}\rfloor\{q\}\left(\lfloor R^{ij}\rfloor\{\alpha\}\right) dV_n \\
& - \iiint_{V_n}[N]^{T}\rho_o\{\underset{\sim}{f}\}\, dV_n - \iint_{A_n}[N_B]^{T}\{\underset{\sim}{T}\}\, dA_n + \iiint_{V_n}[N]^{T}\rho_o[N]\, dV_n\{\ddot{q}\}\Big\rangle\Big\} \\
= \sum_{n=1}^{N}\Big\{ & \lfloor\delta\alpha\rfloor \Big\langle -[r]\{\alpha\} + \{s\} + \{t\}\Big\rangle \\
& + \lfloor\delta q\rfloor \Big\langle \{p\} + [h]\{q\} - \{f\} + [m]\{\ddot{q}\}\Big\rangle\Big\} = 0
\end{aligned}
\tag{C.8}
$$

where the following quantities are evaluated for each finite element:

$$[r] = \iiint_{V_n}\{R^{ij}\}\,C_{ijkl}\lfloor R^{kl}\rfloor\, dV_n \tag{C.8a}$$

$$\{s\} = -\iiint_{V_n}\{R^{ij}\}\,\gamma^{p}_{ij}\, dV_n \tag{C.8b}$$

$$\{t\} = \iiint_{V_n}\{R^{ij}\}\left(\lfloor D_{ij}\rfloor\{q\} + \tfrac{1}{2}\lfloor q\rfloor\{D_{ai}\}\lfloor D^{a}_{j}\rfloor\{q\}\right) dV_n \tag{C.8c}$$

$$\{p\} = \iiint_{V_n}\{D_{ij}\}\left(\lfloor R^{ij}\rfloor\{\alpha\}\right) dV_n \tag{C.8d}$$

$$[h] = \iiint_{V_n} \{D_{ai}\} \lfloor D^{a}_{j} \rfloor \left( \lfloor R^{ij} \rfloor \{\alpha\} \right) dV_n \qquad \text{(C.8e)}$$

$$\{f\} = \iiint_{V_n} [N]^T \rho_0 \{\underset{\sim}{f}\}\, dV_n + \iint_{A_n} [N_B]^T \{\underset{\sim}{T}\}\, dA_n \qquad \text{(C.8f)}$$

$$[m] = \iiint_{V_n} [N]^T \rho_0 [N]\, dV_n \qquad \text{(C.8g)}$$

The quantities {α} can be varied independently for each finite element; hence, from Eq. C.8 it may be concluded that

$$[r]\{\alpha\} - \{s\} - \{t\} = 0 \qquad \text{(C.9)}$$

or

$$\{\alpha\} = [r]^{-1} \left( \{s\} + \{t\} \right) \qquad \text{(C.9a)}$$

and, hence, it follows from Eqs. C.9 and C.8 that

$$\sum_{n=1}^{N} \lfloor \delta q \rfloor \left( \{p\} + [h]\{q\} - \{f\} + [m]\{\ddot{q}\} \right) = 0 \qquad \text{(C.10)}$$

It is seen that Eq. C.10 is of the same form as Eq. 3.14 which is associated with the assumed-displacement type of finite-element model. Thus, transforming the element nodal displacements {q} to independent global displacements {q*} of the discrete-element assembly as described previously will lead to the same form of matrix expression as given by Eq. 3.17 which represents the "improved formulation" form of the dynamic equilibrium equations:

$$[M]\{\ddot{q}^*\} + \{P\} + [H]\{q^*\} = \{F^*\} \qquad \text{(C.11)}$$

However, it should be noted that the numerical values of the terms in [M], {P}, [H], and {F*} of Eq. C.11 can be, in general, different from the corresponding symbolic quantities in Eq. 3.17.

Given a set of initial conditions $\{q^*\}_0$, $\{\dot{q}^*\}_0$ and $\{F^*\}_0$ at time zero, and the proper boundary conditions, the system of second-order differential equations, Eq. C.11, together with Eq. C.9 may be solved in a step-by-step timewise fashion. Let it be assumed that at a typical time instant $t_m$, one knows the generalized nodal displacement $\{q^*\}_m$, the strain component $\{\gamma_{ij}\}_m$, and the plastic strain component $\{\gamma_{ij}^p\}_m$ at any station in each finite element. The stress parameter $\{\alpha\}_m$ for each individual finite element may be calculated from Eq. C.9, where $\{s\}_m$ and $\{t\}_m$ can be evaluated from Eqs. C.8b and C.8c, respectively. Having the stress parameter $\{\alpha\}$ at time $t_m$, one can calculate $\{p\}_m$ and $[h]_m$ for each finite element by using Eqs. C.8d and C.8e, respectively. Now, assemble this information for the discretized structure. Then Eq. C.11 together with the use of a proper timewise finite-difference operator to approximate $\{\ddot{q}\}_m$ can be employed to determine the displacements $\{q^*\}$ or the displacement increments $\{\Delta q^*\}$ at the next time instant $t_{m+1}$, since all quantities except $\{\ddot{q}^*\}_m$ in Eq. C.11 are known, and hence $\{\ddot{q}^*\}_m$ can be readily calculated. Having the displacements or displacement increments at time $t_{m+1}$, the strain (or strain increment) at any station in each element may be found from Eq. C.7. With the displacement and strain available, the desired stress parameter at time instant $t_{m+1}$ can be determined through the use of proper elastic-plastic constitutive relations, and Eqs. C.5 and C.9. Then Eq. C.11 can furnish the displacements for the next time step. The process is cyclic thereafter.

It should be noted that the application of the mixed finite-element model in this form does not provide any particular advantage over the assumed-displacement finite-element model since the interelement boundary compatibility is still required. However, the use of the mixed finite-element model has its merit in the elastic analysis of plates and shells (Ref. 7). But for the elastic-plastic analysis, the proper interaction (yielding) surface between stress and moment resultants has not been found; such information, however, would be needed in this mixed method.

Finally, it can be expected that assumed-stress finite-element models, such as the assumed-stress hybrid model, the equilibrium model, etc., (Ref. 7) will not be as accurate as the assumed displacement finite-element model for elastic-plastic transient structural analyses, unless the time-step size is made sufficiently small, since the stress-strain curves for many structural materials are usually very flat in the plastic range; thus, a small error in the strain will produce a small error in the stress, but on the other hand, a small error in the stress will result in a much larger error in the strain.